THE FLORIDA STATE UNIVERSITY

COLLEGE OF ARTS AND SCIENCES

A SEARCH FOR EXOTIC MESONS IN $\gamma p \to \pi^+\pi^+\pi^- n$ WITH CLAS AT JEFFERSON LAB

By

CRAIG BOOKWALTER

A Dissertation submitted to the
Department of Physics
in partial fulfillment of the
requirements for the degree of
Doctor of Philosophy

Degree Awarded:
Spring Semester, 2012

Craig Bookwalter defended this dissertation on April 5, 2012.

The members of the supervisory committee were:

Paul Eugenio
Professor Directing Thesis

Tomek Plewa
University Representative

Susan Blessing
Committee Member

Simon Capstick
Committee Member

Volker Crede
Committee Member

Stepan Stepanyan
Committee Member

The Graduate School has verified and approved the above-named committee members, and certifies that the dissertation has been approved in accordance with the university requirements.

ACKNOWLEDGMENTS

I've never done drugs and I'm not a hard drinker, so take this with a grain of salt, but writing a thesis is probably the most unhealthy thing I've ever done. I've spent about three months parked in my office, eating Chunky Soup and Chef Boyardee at every meal. I've gotten little to no exercise and I've gained about fifteen pounds. I haven't had much social interaction either; at parties I feel like Tom Hanks in Castaway when he returns to civilization, talking too loud, laughing at the wrong moments, crazed look in the eye from too much computer-monitor staring. Thus the recipients of this tract must forgive me if this reads like a message in a bottle; I've been on a long voyage, and writing these acknowledgments is the first sight of land.

Lonely as the writing may be, the execution of the science underlying this document is by no means a one-man job. To this end I must thank the Hall B staff scientists at Jefferson Lab for keeping CLAS operational during the experiment, and the members of the CLAS collaboration for manning shifts. After experiment was complete, g12 graduate students Johann Goetz, Diane Schott, Mukesh Saini and post-doc Michael Paolone worked long hours to prepare the g12 dataset for reconstruction. The vast knowledge of Eugene Pasyuk, Valery Kubarovsky, Stepan Stepanyan, and Mac Mestayer were instrumental in this effort, and a special thanks to Dr. Stepanyan for agreeing to serve on my committee. A special thanks is in order for Paul Mattione, who put up with a lot of pesky questions from me while I was calibrating the time-of-flight. Sandy Philpott was especially helpful in getting us the computing resources required to reconstruct one of CLAS's largest datasets in a timely manner. Once analysis began, I relied heavily on the physics knowledge and partial-wave analysis experience of my de-facto adviser at JLab, Dennis Weygand. Matt Bellis and Mike Williams deserve a special thanks in this regard as well; you guys were both wonderfully patient with my slow pace learning the minutiae of performing a partial-wave analysis. During the writing of this document, my office-mate Alexander Ostrovidov has also been uniformly patient and kind to me while enduring endless questions about the finer points of partial-wave analysis techniques as well as details of the E852 3π analysis. I would also like to thank my other committee members: Susan Blessing, Volker Crede, Simon Capstick, and Tomasz Plewa for their careful reading and editing of this document.

For my personal and my professional development, all credit goes to my adviser, Paul Eugenio. Paul, you've been exceedingly generous with your time and funding, sending me to conferences all over the world, writing letters of introduction and recommendation, networking with other professors on my behalf. You seemed always to put my success first– many, many students out there do not get the benefit of such selfless advising. I travel through doors which you have opened for me.

Figure 1: The glorious Goetz Caesar salad, replete with from-scratch dressing and homemade croutons.

To Raffaella De Vita, working with you in Genoa was the most satisfying experience of my career; you were a fantastic colleague and friend in a strange land.

I must also thank my undergraduate adviser, Ed Brash, who left no stone unturned in getting me involved at Jefferson Lab as an undergrad. Ed, I would have never made it to grad school if it weren't for you opening doors for me at JLab.

Also from the undergraduate days, I must thank John Hardie. You are without a doubt my physicist role model, John, even though you are a physicist no more.

Without the love of my friends and family and that of the good Lord watching over me, this journey would have ground me into dust.

Mom, thank you for the endless encouragement and cheerleading and care packages stuffed with cookies. Dad, thank you for helping me to navigate the murky waters of business relationships, for finding so many ways to help me succeed in this endeavor, and for always wondering what the hell the practical application is for all this stuff. To you both, your pride in me will always be my greatest reward.

To Alana and David, thank you for being the best brother and sister a guy could as for. I miss you guys terribly.

Grandma Katzy, thank you for so many weekends of peaceful refuge with you in the Father's company; from your kitchen table over a cup of coffee, the vast number of blessings I've received have never been so clear.

To Justin: whenever someone tells me that I don't look/sound/act like a physicist, I rejoice and say thank you to you. To the rest of the Askew family, thank you. No matter how long I'm gone, I come to your home and you welcome me like a son and a brother and there is no greater gift.

To Johann and Katherine, you too have welcomed me as family, so often in fact that

the room upstairs in your house is now known as "Craig's Room", and have treated me to innumerable delicious treats far beyond the ability of my palette to comprehend: Swedish gløgg, beeves Wellington, homemade ice cream, and braised beef fajitas were all on the menu at various times, along with of course Goetz Caesar salads (see Figure 1).

To Mike Paolone, the good memories are too many to count. Thank you for providing just what I needed so many times: an objective point of view, Internet-based distractions, enigmatic and awesome music.

To the Fits and Starts, thank you for the memories. Making music with you guys was such a blessing.

To Diane, I can't count how many times we'd be driving to the climbing gym and I'd find myself sharing with you things I never realized I needed to share. Thank you for listening.

To Mukesh, thank you for commiserating with me about so many of the doldrums of grad school.

To Joe, thanks so much for all the long walks around campus to blow off steam, and to Michelle, thank you for being so damned adorable all the time and for sparking so many enlightening beer-fueled debates. You two drew me back to Tallahassee to end this journey.

And to Christina, she that I found when I returned here. I am so thankful that it is you that I have found, and that now found, I hope to keep.

These and all my blessings are given by the Lord; foremost among those blessings is his Son, without whom I could not have come to know my Father.

April 13, 2012

Tallahassee, FL

TABLE OF CONTENTS

LIST OF TABLES

LIST OF FIGURES

ABSTRACT

In addition to ordinary $q\bar{q}$ pairs, quantum chromodynamics (QCD) permits many other possibilities in meson spectra, such as gluonic hybrids, glueballs, and tetraquarks. Experimental discovery and study of these exotic states provides insight on the nonperturbative regime of QCD. Over the past twenty years, some searches for exotic mesons have met with controversial results, especially those obtained in the three-pion system. Prior theoretical work suggests that in photoproduction, gluonic hybrids might be found at enhanced levels relative to that found in pion production. To that end, the E004-05 experiment at Jefferson Lab's CEBAF Large Acceptance Spectrometer (CLAS) has recently acquired a high statistics photoproduction dataset, using a liquid hydrogen target and tagged photons from a 5.71 GeV electron beam. The CLAS experimental apparatus was modified to maximize forward acceptance for peripheral production of mesons. The resulting data contain the world's largest 3π photoproduction dataset. A sample of 510K $\gamma p \to \pi^+\pi^+\pi^- n$ events have been subjected to a partial-wave analysis in search of the spin-parity exotic $\pi_1(1600)$ meson. Results show strong evidence for the production of the well-known nonexotic $a_2(1320)$ and $\pi_2(1670)$, as well as some evidence for the $a_1(1260)$. However, we find no evidence of $\pi_1(1600)$ production in $\gamma p \to \pi^+\pi^+\pi^- n$. Possible explanations include misinterpretation of previous analyses claiming the existence of the $\pi_1(1600)$, or a preference for production mechanisms forbidden to charge-exchange photoproduction.

CHAPTER 1

INTRODUCTION

The desire to understand matter at its most fundamental level has become one of the most demanding and fascinating quests in physics. Beginning with Ernest Rutherford's work a century ago, the pursuit of this objective has been driven by scattering experiments, where a target of some suitable material is inundated with a beam of energetic particles, and the recoiling byproducts are measured by a system of detectors. Using beams of helium nuclei (also called α particles) to irradiate a gold foil target, Rutherford was able to deduce that the positive charge of an atom was concentrated in a tiny area in the center, thus giving rise to the planetary model of the atom [1]. Then in 1932, results from James Chadwick's experiments with a beam of α particles incident on a sample of beryllium led him to propose the existence of the neutron [2]. Combined with Rutherford's studies, the atomic picture was complete, with protons and neutrons concentrated in the nucleus, and clouds of electrons orbiting beyond.

However, the questions did not end there. The dense concentration of positive charges in the atomic nucleus implied a new and powerful force of nature at work. Hideki Yukawa formulated an elegant theory of a force between the nucleons [3], mediated by the exchange of a new neutral particle, the pion, or π. The muon (or μ) was discovered in 1936, shortly after Yukawa's theory was published, but carried the same electric charge as the electron [4]. Indeed, the muon seemed to be not much more than a electron but with two hundred times the mass. Yukawa's pion was finally seen in 1947 [5], [6], but that year brought the additional observation of a new and long-lived "strange" meson (called the kaon or K) [7]. With these discoveries, the landscape consisted of nearly a dozen so-called "elementary" particles, all of which were required to describe experimental results. Thus suspicions were mounting that these states were the expression of a more fundamental physics.

1.1 The Quark Model and Quantum Chromodynamics

The fundamental nature of these new discoveries could only be tested by experimentally probing to smaller and smaller distance scales. This motivated a rapid expansion of the energy scales of experimental apparatus, and by the 1960s, particle accelerators operating across the world had uncovered a bonafide ecology of sub-atomic particles. In the midst of this diverse array of particles, classification schemes became of principal interest to theorists of this era, and many of them are still useful today.

Perhaps the most obvious ordering is by mass. The electron, muon, and their associated neutrinos became classified as *leptons*, due to their lightweight nature. Later, the τ lepton and its associated neutrino were discovered, thus completing the group of leptons. Protons, neutrons, pions, and kaons all fall into a complementary class called *hadrons*, from the Greek word for thick or bulky. The large number of hadrons invites further classification, and thus hadrons with integer spin, such as pions and kaons, are termed *mesons* from the Greek prefix *meso-*, meaning middle, due to their tendency to be of medium weight. Hadrons with half-integer spin, such as the proton and neutron are termed *baryons*, from the Greek prefix *bary*, meaning weight, as they tend to be the heaviest. Compared to just six leptons known today (or the four known in the 1960s), the diverse spectrum of hadrons observed in experiments implied that their identities must be an expression of some more fundamental phenomena. However, a deeper understanding of Nature's organization of the panoply of hadrons remained elusive. The fulcrum of the mystery proved to be their modes of decay, specifically decays according to the weak nuclear force.

Neglecting gravity, as it has a infinitesimal influence on particles so small, hadrons decay via three of the four fundamental forces of nature: the weak nuclear force, the strong nuclear force, and electromagnetism. Leptons, by comparison, interact only via electromagnetism and the weak nuclear force. The strong nuclear force, so-named because it is the strongest fundamental force of nature, binds protons and neutrons together in the atomic nucleus. Decays via the strong force occur quickly (on the order of 10^{-24} s) and more frequently than other decays. The electromagnetic force, which binds electrons to atomic nuclei and is responsible for atomic spectra, accounts for *radiative decays*, or decays involving photons. Finally the weak nuclear force, which governs the decays of many radioactive nuclei, permits the lightest hadrons to decay into lepton-antilepton pairs, or for flavored hadrons, such as the kaon, to decay into ordinary mesons or leptons. The kaon is not alone in its refusal to decay via the strong force; the Λ and Σ baryons also share this tendency, hinting that they each contain something in common that is different than in ordinary hadronic matter. A revolutionary answer came in the *quark model*, proposed by Murray Gell-Mann in 1962 [8].

In the quark model, Gell-Mann posited that hadrons were composed of smaller entities called *quarks*. There were three *flavors* of quark, up (u), down (d), and strange (s), each carrying a fractional unit of charge. In this model, quarks are governed an underlying symmetry which can be described mathematically by group theory, specifically as a discrete realization of the special unitary group in three dimensions (the group of all 3×3 unitary matrices with determinant equal to one). This group is labeled as $SU(3)_F$, with F to remind us that flavor is the symmetric property. Group theory was not unknown to quantum mechanics during Gell-Mann's era; indeed, the coupling of angular momenta obeys the rules of $SU(2)$. Constructing the meson spectrum then becomes a matter of coupling a quark and antiquark according to the rules of $SU(3)_F$, in a fashion analogous to coupling two angular momenta:

$$3 \otimes \bar{3} = 8 \oplus 1 \tag{1.1}$$

Eq. 1.1 states that a quark and an antiquark will combine into a flavor singlet and a flavor octet. There is an $8 \oplus 1$ object for each meson spin-parity, or J^P combination. Figure 1.1 shows two nonets of mesons from the Gell-Mann quark model. On the basis of $SU(3)_F$, Gell-Mann predicted the existence of an as-yet unseen baryon, the Ω^- (sss), at a mass

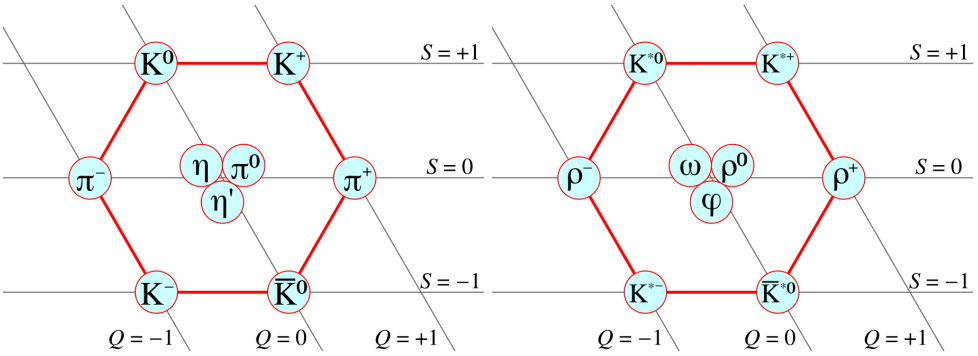

Figure 1.1: Illustration of the $SU(3)_F$ spectrum of $J^P = 0^-$ (left) and $J^P = 1^-$ (right) mesons. (Image sources: [11],[12])

of 1680 MeV [9]. The Ω^- was then observed during experiments at Brookhaven National Laboratory [10].

However, even as Gell-Mann's successful prediction made a powerful case for the quark model, unexplained difficulties remained. If $SU(3)_F$ was an exact symmetry of nature, it would allow for the exchange of any two flavors of quark without any change in mass. Examining the experimentally-measured masses of the members of any $SU(3)_F$ multiplet, one finds that particles with higher s-quark content tend to be heavier. In fact, modern measurements place the s quark mass at 150 MeV, while the u and d quarks weigh between 5 and 10 MeV. Thus, Nature does not strictly obey $SU(3)_F$, and possibilities arise for the existence of a more fundamental symmetry.

Another mystery left unexplained by the quark model was the existence of the doubly-charged Δ^{++}. The model describes the quark composition of the Δ^{++} as uuu, with all three spins aligned to give a total spin of $\frac{3}{2}$. However, such a system contains three fermions in the same quantum state, which violates the Pauli exclusion principle.

The Δ^{++}, as well as the Ω^- with its sss quark content, seemed to indicate another quantum number available to Nature in order to preserve the antisymmetric baryon wave function. This additional number, proposed by Han and Nambu [13], and also independently by Oscar Greenberg [14], is now known as *color*. Now, in addition to flavor, each quark is postulated to have its own color charge, selected from three possible values, commonly denoted as red, blue, and green. Quarks then combine in color-neutral combinations again according to the rules of the $SU(3)$ group, with baryons having one quark of each color, and mesons being composed of a color-anticolor pair. This theory of color, called quantum chromodynamics (QCD), is governed by the following Lagrangian:

$$\mathcal{L}_{QCD} = \bar{\psi}_i \left(i\gamma^\mu (D_\mu)_{ij} - m\,\delta_{ij} \right) \psi_j - \frac{1}{4} G^a_{\mu\nu} G^{\mu\nu}_a \tag{1.2}$$

where

- $\bar{\psi}_i$ and ψ_j are quark fields,
- D_μ is the covariant derivative containing a set of $SU(3)$ generators,

- $G^a_{\mu\nu}$ is the gluonic field tensor, defined as:

$$G^a_{\mu\nu} = \partial_\mu G^a_\nu - \partial_\nu G^a_\mu - g f^{abc} G^b_\mu G^c_\nu \tag{1.3}$$

- γ^μ and δ_{ij} are the Dirac matrices and Kronecker delta function, respectively.

Just as the photon communicates the presence of an electric field between two charged particles, the force associated with color charge is mediated by vector boson called *gluons*. QCD, like the quark model, obeys the rules of the $SU(3)$ group, albeit through color rather than flavor. This $SU(3)$ symmetry of QCD dictates that there are *eight* different gluons with unique and non-zero combinations of color and anticolor, performing a function analogous to the job the photon does in electromagnetism. In more detail, consider the electromagnetic field tensor from quantum electrodynamics (QED):

$$F_{\mu\nu} = \partial_\mu A_\nu - \partial_\nu A_\mu \tag{1.4}$$

which is similar in form to Eq. 1.3 except for the last term, $g f^{abc} G^b_\mu G^c_\nu$. This last term describes the ability of the gluon to interact not only with quarks and antiquarks, but also with itself. Gluonic self-interaction is a necessary component of the definitive feature of QCD: color confinement.

In practical terms, color confinement means that an infinite amount of force is required to separate two color-charged objects to infinity. The gluonic field between a given qq or $q\bar{q}$ acts like a string stretching tight as the two ends are separated. In practice, once the potential energy stored in the gluonic field exceeds the mass-energy of a new $q\bar{q}$ pair, the band "snaps" and a meson is produced while the original quark remains. This leads to the principle of confinement, which holds that hadrons exist in Nature solely as color singlet states. No free quarks have ever been observed; they are always encapsulated within hadrons.

The self-interactive nature of the gluon is also the cause of all troubles from the perspective of obtaining and solving the equations of motion. In QED the force between two charges at a distance is screened by the production of virtual lepton pairs, meaning that diagrams with increasing numbers of virtual lepton loops contribute less and less to a total cross-section. But in QCD, each additional $q\bar{q}$ loop *magnifies* the effect of the gluonic field, leading to a never-ending array of diagrams, each contributing more and more to the total cross-section. This means perturbative solutions to QCD are intractably complex in the hadronic regime. Low-energy difficulties aside, QCD has been so successful at predicting dynamics at high energy that the color force is now regarded as the strong force fundamental to Nature. The force between nucleons is now known as the *residual strong force* or the nucleon-nucleon force.

1.2 Exotic Mesons in Theory and Experiment

The community is not handcuffed by the complexity of low-energy QCD. Detours exist to extract useful results from the theory without dealing head-on with the nonperturbative regime. In any case, starting with $q\bar{q}$ seems logical, as the meson is the simplest strongly-interacting system in Nature. Furthermore, it is not very instructive to consider states

already well-described by the quark model. Instead, we would prefer to study states which exploit the new degrees of freedom permitted by QCD, as these states focus on the area of our greatest ignorance. QCD allows for many novel integer-spin systems:

- $q\bar{q}g$ or *hybrid* configurations, where g indicates a valence gluon,
- states consisting of only valence gluons, called glueballs,
- multi-quark states, such as tetraquarks ($q\bar{q}q\bar{q}$) or hexaquarks ($q\bar{q}q\bar{q}q\bar{q}$)

Collectively these non-$q\bar{q}$ states are sometimes referred to as "exotic" mesons. In collaboration between theory and experiment, it is helpful to focus on states which are easily distinguishable as exotic. In some cases, such an observation could prove elementary; for example, any meson with electric charge greater than 1 or less than -1 would be manifestly non-$q\bar{q}$. However, no charge-2 meson states have been predicted or observed to date. Also possible is the observation of *quark model overpopulation*, when more states are observed than the quark model can accommodate. One could also attempt to visually locate bumps or trends uncorrelated with any known state in some invariant-mass spectrum, but the spectrum of known states in the light quark regime makes most invariant-mass distributions crowded. In addition, as they are artifacts of the strong force, exotic states decay primarily via the strong force, meaning they will appear broad and overlapping in any mass distribution, making them difficult to identify by eye. Finally, exotic states could manifest themselves by unusual branching ratios or decay channels; however, this requires large statistical samples over a wide selection of decay channels, a luxury not yet available to the experimental community.

Aside from a hunt for exotic electric charge states or a simple mass-spectrum analysis, the most straightforward way to search experimentally for exotic states is to focus on the subset of exotic mesons with non-$q\bar{q}$ quantum numbers. In addition to mass, five quantum numbers are of primary importance for identifying a meson. They are the isospin quantum number I, the total angular momentum J, the intrinsic parity P, the charge-conjugation parity or C-parity and its generalized counterpart G-parity.

Isospin was first proposed by Werner Heisenberg in 1932 [15], where he formalized the common tendency to group the proton and neutron together under the title of *nucleon*. He postulated that the proton and neutron were merely two states of the same particle [15]. Indeed, except for their electric charge, the proton and neutron have almost identical masses and behave similarly in scattering experiments. Thus the proton and neutron became labeled as an *isospin* $I = \frac{1}{2}$ doublet, with the proton carrying $I_z = +\frac{1}{2}$ and the neutron with $I_z = -\frac{1}{2}$. The modern understanding of isospin instead assigns $I = \frac{1}{2}$ to quarks, and the isospin of hadrons then arises from the coupling of quark isospins. A $q\bar{q}$ pair can occupy either the isospin singlet (*isoscalar*) or isospin triplet (*isovector*) states; thus any state with charge greater than 1 or less than -1 would be exotic in terms of isospin as well.

The total angular momentum J of a meson is determined by the spins of its constituents and the relative angular momentum between them. As a meson must be of integer spin, any additional components beyond $q\bar{q}$ which cause it to have non-integer spin would cause it to be no longer considered a meson. In the case of a quark and antiquark, both are spin-$\frac{1}{2}$, and thus $q\bar{q}$ can have spin S equal to 0 or 1. The relative orbital angular momentum

L between the quark and antiquark can be zero or any positive integer value. The total angular momentum J of a meson can then take on one of the permitted values of the $SU(2)$ coupling $L \oplus S$.

The parity of a meson state depends on the intrinsic parity of its constituents, as well as the behavior of the spacial wavefunction under inversion of axes. A $q\bar{q}$ pair has opposite intrinsic parities, giving an overall minus sign. For a two-particle system with some angular momentum L, the parity of the spacial component of the wavefunction goes like $(-1)^L$. Thus the intrinsic parity P of a $q\bar{q}$ system is

$$P = (-1)^{L+1} \tag{1.5}$$

While the parity operation inverts the spacial coordinate axes, C-parity interchanges a particle with its antiparticle. Thus by definition only states which are their own antiparticle are C-parity eigenstates. In a two-particle system such as $q\bar{q}$, the C-parity operation is carried out by inverting the coordinates as in the parity operation *as well as* inverting the spin projections as well. For $q\bar{q}$ states in the spin triplet state, this inversion of spin projections makes no contribution to the C-parity eigenvalue, but for those in the spin singlet state, an overall minus sign is encountered. Thus the intrinsic C-parity of a $q\bar{q}$ system is

$$C = (-1)^{S+1}(-1)^{L+1} = (-1)^{L+S} \tag{1.6}$$

G-parity [16] is a useful extension of C-parity for non-strange charged isovector mesons. The G-parity operator combines the C-parity operation with a 180° rotation in isospin space,

$$G = C \exp\left[i\pi I_y\right] \tag{1.7}$$

where C is the C-parity of the neutral member of the isospin triplet and I_y is the y-component of the isospin operator. The eigenvalues of G for a given state are related to the C-parity eigenvalues of the neutral partner by:

$$\eta_G = \eta_C(-1)^I \tag{1.8}$$

$$\eta_G\left[q\bar{q}\right] = (-1)^{S+L+I} \tag{1.9}$$

All of these quantities are conserved by the strong force. We commonly combine them in a standard notation of $I^G J^{PC}$, and along with the mass, they are sufficient to uniquely define a meson state. However, we have defined these quantum numbers for a $q\bar{q}$ system; specifically the spin, parity, and C-parity J^{PC} can take on only certain values for a $q\bar{q}$ pair with some relative orbital angular momentum. These values are shown in Table 1.1. Through enumeration, several J^{PC} combinations are forbidden to $q\bar{q}$ states:

$$J^{PC}_{Non-QM} = J^{PC}(QM) = 0^{--}, 0^{+-}, 1^{-+}, 2^{+-}, 3^{-+}... \tag{1.10}$$

Thus J^{PC} combinations listed in Eq. 1.10 represent states that cannot be described by $q\bar{q}$ and make for an ideal place for theory and experiment to connect.

From the theoretical point of view, the extraction of useful predictions from QCD for spin-parity exotic states is no simpler than for any other form of hadronic matter. The complexities of low-energy QCD have necessitated the development of new theoretical technologies. Chief among these is lattice QCD.

S	L	J	P	C	PDG
0	0	0	$-$	$+$	η,η'
1	0	1	$-$	$-$	ω, ϕ
0	1	1	$+$	$-$	h_1
1	1	0	$+$	$+$	f_0
		1			f_1
		2			f_2
0	2	2	$-$	$+$	η_2, η_2'
1	2	1	$-$	$-$	ω, ϕ
		2			ω_2, ϕ_2
		3			ω_3, ϕ_3
$\vdots$			$\vdots$		$\vdots$

$I = 0$ mesons

S	L	J	P	C	PDG
0	0	0	$-$	$+$	π
1	0	1	$-$	$-$	ρ
0	1	1	$+$	$-$	b_1
1	1	0	$+$	$+$	a_0
		1			a_1
		2			a_2
0	2	2	$-$	$+$	π_2
1	2	1	$-$	$-$	ρ
		2			ρ_2
		3			ρ_3
$\vdots$			$\vdots$		$\vdots$

$I = 1$ mesons

Table 1.1: Summary of the spin, parity and C-parity combinations permitted by the quark model for isospin $I = 0$ and $I = 1$ mesons. The Particle Data Group (PDG, [17]) nomenclature for each spin-parity combination is also included. In practice, when labeled a state according to the PDG scheme, the mass of the state is included in parentheses, like $a_2(1320)$, to differentiate between radial or other excitations. Also, a connection in name between the spin-parity of the state and the way it acts under improper transformations is often made. $J^P = 0^+$ states are called *scalars*, $J^P = 0^-$ states are called *pseudoscalars*, $J^P = 1^-$ are called *vectors*, and $J^P = 1^+$ are called *axial vectors*.

Lattice QCD provides approximate solutions to the QCD Lagrangian by evaluating the quantum-mechanical action over a discrete set of spacetime points rather than over the continuum. Employing a discrete spacetime introduces a natural momentum cutoff on the order of the reciprocal of the lattice spacing, allowing the theory to be regularized. Quarks and antiquarks are allowed to exist at any vertex (or *site*) on the lattice, while the links between the lattice sites represent gluons. In practice these calculations are carried out on clusters of computers, with unphysically large values for the quark masses and the lattice spacings. As the lattice spacing approaches continuum and the quark masses approach their physical values, the computational complexity rises enormously. Thus, lattice theorists must strike a compromise between results which have physical meaning and getting results in a manageable amount of time. Often, several calculations are done for a given action definition and set of operators, each calculation with its own set of quark masses and lattice spacing, such that after all are complete, one can extrapolate the results down to the real-world values. Such extrapolations are risky because the behavior of QCD on the lattice close to the physical mass of the quarks is unknown, so results from the lattice are usually interpreted for the existence and relative positions of states in the mass spectrum, rather than absolute masses.

Calculations on the lattice indicate that QCD harbors a rich spectrum of spin-parity exotics. Limiting ourselves to the light-quark sector, the lattice indicates that the lightest exotic-J^{PC} state is the 1^{-+}, with various calculations placing the mass from 1.7 to 2.1 GeV [18], [19], [20], [21], [22], the results of which are summarized in Figure 1.3. The most comprehensive of these calculations is the one undertaken by the Hadron Spectrum Collaboration, where they have obtained predictions for the for the full isovector meson spectrum [23]. Their calculations used volumes of $N = 16$ and $N = 20$, where N is the number of cells in the lattice. Both used the same lattice spacing of $a = 0.12$ fm, along with three flavors of quark, corresponding to u, d, and s, configured for four different mass settings. The spectra are summarized in Figure 1.2. In all configurations, including that shown in Figure 1.2, the lowest-lying exotic has $J^{PC} = 1^{-+}$; although Ref. [23] provides no extrapolation to the physical pion mass, the position of the 1^{-+} relative to other well-known states reproduced in the spectrum seems to indicate a mass between 1.5 and 2 GeV.

Given the complexity of calculations in the hadronic regime, it is often useful to try and build a more intuitive picture that still retains the salient features of QCD. One such picture models the effect of the gluonic field by confining quarks and antiquarks to live within a fixed volume. This so-called "bag model" was originally introduced by Alan Chodos and collaborators in 1974 [25]. With the suitable tuning of four model parameters, it described the experimentally-observed non-exotic meson spectrum with more precision than the conventional quark model of Gell-Mann and Zweig [26]. Furthermore, the bag model allows for a transparent introduction of gluonic and multiquark degrees of freedom. Robert Jaffe *et al* showed that the bag model produces a rich spectrum of glueballs and multiquark states with exotic and non-exotic quantum numbers, all with masses in the 1 to 2 GeV range [27]. Similarly, in the gluonic hybrid sector, work by Ted Barnes, Frank Close, and Françoise de Viron, and independently by Michael Chanowitz and Stephen Sharpe, found that the bag model predicts four gluonic hybrid nonets with $J^{PC} = 0^{-+}, 1^{--}, 1^{-+}$ and 2^{-+}, all with masses on the 1 to 2 GeV range as well [28], [29]. Of particular interest to the present analysis is the 1^{-+} prediction, since it is a spin-parity exotic. Chanowitz and Sharpe

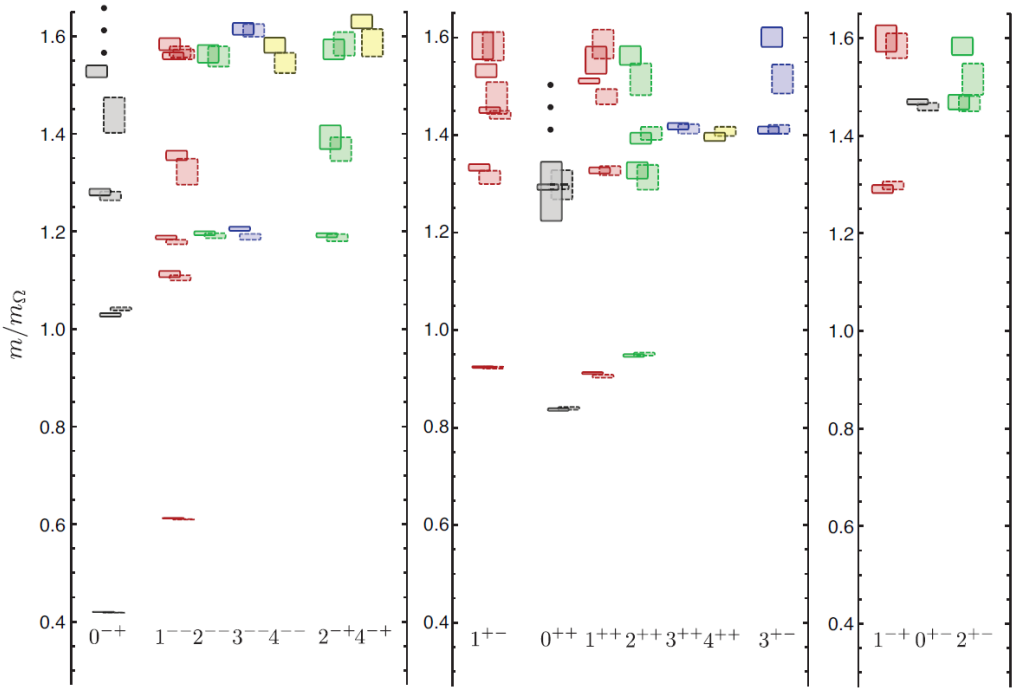

Figure 1.2: The full spectrum of predicted isovector states from Ref. [23], from the calculation where the quark masses are set such that the mass of the pion is 743 MeV. Boxes indicate the existence of bound states for the given J^{PC} column, and the height of the box indicates the uncertainty in the calculation. Boxes with solid (dashed) borders indicate calculations from a volume of 16^3 (20^3) cells. Colors correspond to spin. Due to the non-physical u and d quark masses used in the calculation, the y-axis is normalized to the mass of the Ω baryon. The three columns represent $L = 0$ mesons (left), $L = 1$ mesons (center), and exotic J^{PC} mesons (right); note the low-lying 1^{-+} state, and the degenerate 0^{+-} and 2^{+-} states a few hundred MeV above.

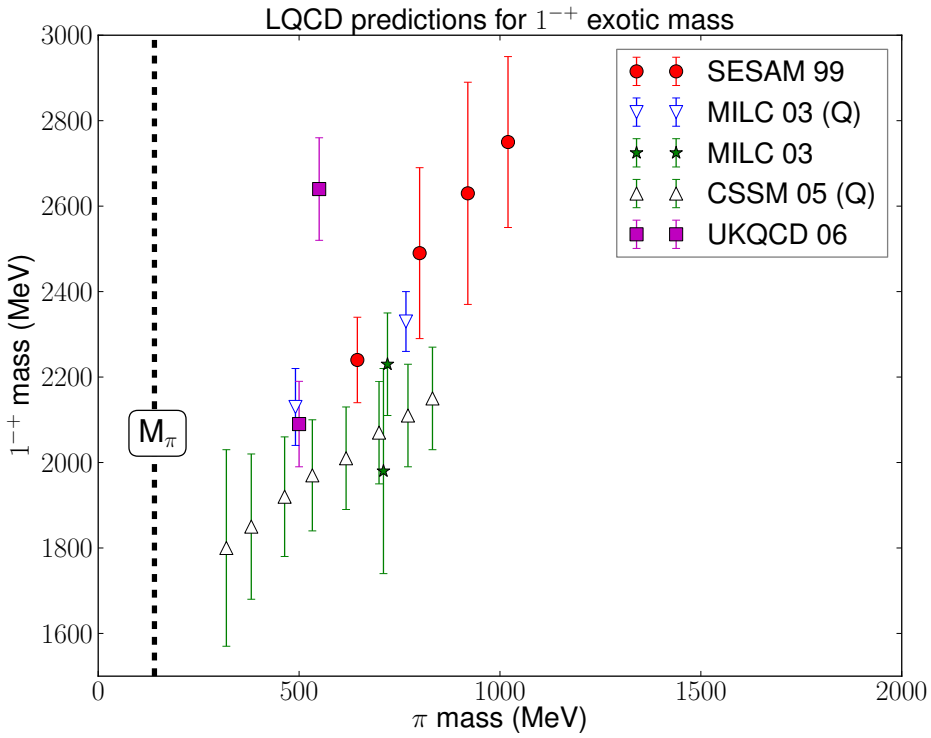

Figure 1.3: Comparison of lattice calculations for the 1^{-+} mass as a function of the pion mass used. Open symbols represent the quenched approximation. The trends are clearly linear and point toward a 1^{-+} exotic between 1 and 2 GeV; however, it is probably unwise to assume a linear extrapolation all the way to the mass of the physical pion. (Figure reproduced from [24] with permission from the author.)

predicted a degenerate 1^{-+} nonet from 1.4 to 1.6 GeV, depending on the parametrization of the gluonic constituent, while Barnes, Close, and de Viron found their 1^{-+} nonet to be at 1.4 GeV as well.

Another useful model is the flux-tube model developed by Nathan Isgur and Jack Paton [30]. In the flux-tube model, rather than enforcing confinement by means of a fixed volume, the gluonic field is assumed to be confined to a narrow "flux-tube" of constant energy density which ties the quark and antiquark together. Then this flux tube is permitted to vibrate, and its vibrational modes augment the observable quantum numbers of the overall system. Following this through, Isgur and Paton reproduced the known quark-model meson spectrum when the flux tube is left in its ground state. Elevating the flux tube to its first excited state, they find eight new meson nonets, degenerate in mass at 1.9 GeV. Of these eight, three nonets have combinations of quark, antiquark, and flux-tube angular momentum which yield exotic J^{PC}; they are 0^{+-}, 2^{+-}, and 1^{-+}. While the lattice calculations of [23] predict a several-hundred-MeV separation between the 1^{-+} and the $[0,2]^{+-}$, lattice predictions for the 1^{-+} states seem to be consistent with the flux-tube model. It is somewhat remarkable that both of these models, essentially unchanged since their introduction, have remained competitive with lattice results for some thirty years.

In experiment, we can examine a hadronic decay channel and calculate a list of possible J^{PC} combinations based on conservation of parity and C-parity among the final state particles. We can then examine the angular distributions in our data via partial-wave analysis (PWA), which allows us determine the contributions from different J^{PC} states. Experimental searches for exotic mesons have had the most success investigating the 1^{-+} spin-parity exotic. Most models and lattice calculations agree it to be the lightest exotic candidate and its quantum numbers identify it as manifestly non-$q\bar{q}$, so it makes a tantalizing target for experimental study. Indeed, several experiments have made observations of 1^{-+} states, but the results were not without controversy. For the most part, the experiments summarized below use PWA to derive their conclusions. Specifically, they employ PWA in the *helicity formalism* using the *reflectivity basis*, as does the analysis presented here. Both are discussed at length in Chapter 4. For the purposes of the results below, in the reflectivity basis, each partial wave carries a reflectivity eigenvalue ϵ and a spin projection M as well as the standard J, P, and C. The formatting convention of $J^{PC}M^{\epsilon}$ will be used throughout the rest of this document.

The first claim for a 1^{-+} exotic came in 1988, from $\pi^- p \to \pi^0\eta n$ data taken during the GAMS experiment at CERN [31]. PWA fit results showed that the $2^{++}1^+$, $2^{++}0^+$ (both corresponding to the $a_2(1320)$), and $1^{-+}0^-$ (corresponding to a new $J^{PC} = 1^{-+}$ exotic) partial waves were required to describe the data. The new 1^{-+} state was found to be centered at 1400 MeV. These results were later thrown into dispute when one of the GAMS collaborators later pointed out [32] that their fit did not take into account mathematical ambiguities arising from a spinless two-particle system, which in fact allow for up to eight different and equally valid solutions to the fit.

Then in 1993, the VES collaboration published results of a fit to a sample of data in the $\pi^- N \to \eta\pi^- N$ and $\pi^- N \to \eta'\pi^- N$ channels [33]. Their results showed a small, broad enhancement in the $1^{-+}1^+$ wave, which corresponds to a $J^{PC} = 1^{-+}$ wave in the natural parity exchange channel. The GAMS result, being in the $1^{-+}0^-$ wave, was an unnatural parity exchange interaction. Correspondingly, the VES collaboration chose not to claim

their results as observation of an exotic meson.

Later in 1993, a collaboration at KEK published results from a fit to a sample of $\pi^- p \to \eta\pi^- p$ data [34]. They too observed an enhancement in the 1400 MeV mass region in the $1^{-+}1^+$ wave. However, enhancements due to production of a Breit-Wigner resonance go through a 180° change in phase across the pole mass; this is discussed further in Section 4.4. The result in Ref. [34] did not observe any phase motion relative to the $2^{++}1^+$, associated with the $a_2(1320)$ resonance. Thus the KEK group thus also did not claim a 1^{-+} resonance.

Then in 1997, the E852 collaboration at Brookhaven published the results of a fit to a data sample of $\pi^- p \to \eta\pi^- p$ [35], claiming the discovery of a 1^{-+} exotic at 1400 MeV . Their fits (including all eight ambiguous solutions, as GAMS did not) demonstrated the existence of a broad enhancement from 1200 to 1600 MeV in the P_+ partial wave, in addition to the dominant $a_2(1320)$. The relative phase motion between the a_2 and the 1^{-+} wave, now known as the $\pi_1(1400)$, could not be described by an a_2 decay in isolation.

However, even though this claim was confirmed shortly after by the Crystal Barrel collaboration [36], the E852 $\pi_1(1400)$ claim was also not without controversy. Calculations using the flux-tube model [37] have placed the mass of the lightest 1^{-+} exotic at a minimum of 1800 MeV, uncomfortably far from the observed mass of the $\pi_1(1400)$. There have been several alternative explanations of the sightings of the $\pi_1(1400)$, including final-state interactions masquerading as a resonance [38] (much like the σ meson providing the intermediate-range attraction of the nucleon-nucleon potential), as well as the Deck effect [39]. The true identity of the $\pi_1(1400)$ remains unclear.

The E852 collaboration also published results of a fit to a sample of events in the $\pi^- p \to \pi^-\pi^-\pi^+ p$ channel. Their results found the expected $a_1(1260)$, $a_2(1320)$, and $\pi_2(1670)$ in the $\rho(770)\pi$ and $f_2(1270)\pi$ decay channels. In addition, they also found evidence of a new $J^{PC} = 1^{-+}$ state at 1.6 GeV in the $\rho(770)\pi$ decay mode [40]. The $1^{-+}1^+$, $1^{-+}1^-$, and $1^{-+}0^-$ partial waves showed enhancements in the 1.1 to 1.4 GeV and 1.6 to 1.7 GeV mass regions. The $1^{-+}1^+$ wave also showed rapid phase motion in the 1.5 GeV to 1.7 GeV region relative to all other natural parity-exchange waves, and based on these observations, the E852 collaboration claimed discovery of a new 1^{-+} exotic at 1600 MeV, the $\pi_1(1600)$. E852 was unable to make any claim on the enhancement in the 1.1 to 1.4 GeV mass region, due to leakage effects from the $a_1(1260)$.

As the $\pi_1(1400)$ has had a rather controversial history, so too has the $\pi_1(1600)$. After the publication of the analysis in Ref. [40], some members of the E852 collaboration, mostly from Indiana University, left the collaboration in dispute over the interpretation of the first $\pi^- p \to \pi^+\pi^-\pi^- p$ results. The IU-E852 collaboration, as they came to be known, published results of a partial-wave analysis of a larger 3π dataset that challenges the earlier $\pi_1(1600)$ claims [41]. Using a larger set of partial waves (42 waves in Ref. [41] versus 27 in Ref. [40]), the analysis in Ref. [41] shows that amplitude of the previously-seen exotic signal identified as the $\pi_1(1600)$ disappears in both reaction channels, which the IU group attributes to leakage from the non-exotic $\pi_2(1670)$ and $a_4(2040)$. Specifically, they found the addition of the 2^{-+} waves decaying through $\rho\pi$ in an F-wave were particularly important in that their addition caused the intensity of the 1^{-+} to be substantially reduced. However, the 1^{-+} phase motion observed in Ref. [41] is consistent with the findings in the original E852 analysis.

Recently, the E852 $\pi_1(1600)$ sighting in the 3π system was confirmed by the COMPASS experiment at CERN. Analyzing a sample of 400K $\pi^- \mathrm{Pb}^{208} \to \pi^+\pi^-\pi^-(\mathrm{Pb}^{208})$ events, they found that the $1^{-+}1^+$ partial wave was needed to describe their data [42]. The intensity observed was at the level of 2% of the total observed intensity, consistent with the findings in Ref. [40]. They also observed resonant phase motion for the 1^{-+} relative to the nonexotic $a_1(1260)$ and $\pi_2(1670)$, again consistent with Ref. [40].

Furthermore, the $\pi_1(1600)$ has been observed in three other decay modes in E852 data: $\eta'\pi$ [43], $f_1(1285)\pi$ [44], and $b_1(1285)\pi$ [45]. The most interesting of these results is that the dominant feature of the $\eta'\pi$ mass spectrum is a peak at 1600 MeV, identified in [43] as due to the 1^{-+}. The sightings in $b_1\pi$ and $f_1\pi$ are consistent with the preferred decay modes of the flux-tube model hybrids, while the $\eta'\pi$ mode was predicted for bag model hybrids. Also important to note is that Ref. [44] and [45] claim existence of a third 1^{-+} candidate, the $\pi_1(2000)$, based on their mass-dependent analysis.

However, with the exception of the $\pi_1(1600)$ decaying to $\eta'\pi$, all of the 1^{-+} candidates make small contributions to the overall observed intensities. It is possible that alternative production processes might provide an environment where exotics could be produced more copiously. Specifically, in the case of gluonic hybrids, both the bag model and the flux-tube model reported a preference for a 1^{-+} hybrid to combinations of P- and a S-wave mesons. Following the arguments of Frank Close, Philip Page, and Jozef Dudek, if one imagines reversing the diagram, a situation in which a beam of $L = 1$ mesons such as the b_1 or a_1 would be ideal to produce a 1^{-+} hybrid through pion exchange. Even the hybrid production strength for a beam of $L = 0$ vector mesons such as the ρ and ω could be significant if an exchanged off-shell ρ, π, or ω harbors some nontrivial gluonic structure [46], or if the selection rules preferring $(L = 0)(L = 1)$ decays are broken [47], [48]. Conversely, no calculation predicts a strong hybrid coupling to identical $L = 0$ mesons, and thus the production of hybrids via pion beams must be suppressed. However, vector meson dominance [49] suggests that a real photon beam is mostly composed of slightly off-shell ρ and ω mesons, and thus the photoproduction of hybrids should be enhanced relative to pion production. Indeed ordinary and hybrid mesons could be photoproduced in equal amounts [47], rather than at the 1% level seen in Refs. [40], [42]. Also, calculations on the lattice show strong couplings for radiative decays for hybrid charmonium [50], an effect which, again considered in reverse, bodes well for the photoproduction of light-quark hybrids.

Motivated by these arguments, some initial studies into 1^{-+} production in photoproduction have already been published. Completed in 2001, Jefferson Lab experiment E99-005 employed a circularly polarized 5.7 GeV tagged photon beam on a hydrogen target. A sample of 83,000 $\gamma p \to \pi^+\pi^+\pi^-n$ events were collected after tight forward-angle and low-t cuts and subjected to a PWA. The results showed no clear evidence for the $\pi_1(1600)$ [51]. A number of possibilities exist:

- the theoretical arguments put forth in Refs. [47], [46], [52], and [53] that hybrids should be produced on an equal footing with ordinary mesons are wrong,
- the $\pi_1(1600)$ may not be a gluonic hybrid but perhaps a tetraquark,
- the $\pi_1(1600)$ was produced at a level similar to pion production observations, and the analysis in Ref. [51] was not sensitive enough to observe it.

In the interest of improving statistical yields in this channel and others of interest, the HyCLAS experiment was proposed and approved in 2004 as the main experiment of the CLAS g12 rungroup.

1.3 The Rest of This Document

We seek to further investigate the photoproduction of the $\pi_1(1600)$ meson, using data from the CLAS g12 running period. We have acquired a sample of about 6M $\gamma p \to \pi^+\pi^+\pi^- n$ events using the CEBAF Large Acceptance Spectrometer, described in detail in Chapter 2. From these 6M events, we select approximately 500K to subject to a PWA in search of the $\pi_1(1600)$. These statistics allow us to make an observation of the $\pi_1(1600)$ if it is produced at levels comparable to those seen in Refs. [40] and [42]. Selection of the exclusive $\gamma p \to \pi^+\pi^+\pi^- n$ and PWA event samples, along with features of the data are described in Chapter 3. Details of the generation of Monte Carlo events for our PWA are detailed at the end of Chapter 3. Partial-wave analysis formulas used within this document are summarized in Chapter 4. Finally, fit results from our PWA and our conclusions drawn therefrom are described in Chapter 5.

CHAPTER 2

EXPERIMENTAL APPARATUS

The analysis described in this document was performed on data produced with an electron beam from the Continuous Electron Beam Accelerator Facility (CEBAF) and recorded with the CEBAF Large Acceptance Spectrometer (CLAS), both located at the Thomas Jefferson National Accelerator Facility (Jefferson Lab). CEBAF is an accelerator providing a continuous-wave electron beam of up to 6 GeV in energy and 200 μA in current to three experimental halls, A, B and C. CLAS, housed in Hall-B, is a system of detectors optimized for the detection of final states with multiple charged particles across a broad range of angles. The data underlying this analysis are selected from the g12 dataset, which was taken with the Hall B photon tagger converting a 5.71 GeV electron beam from CEBAF to a bremsstrahlung photon beam incident on a 40 cm liquid-hydrogen target. These data were taken in the name of a diverse collection of experimental proposals including meson spectroscopy, baryon spectroscopy, and in-medium modification measurements. These experiments and their principal investigators, students, and interested parties make up the g12 *rungroup*.

2.1 CEBAF Accelerator

CEBAF is the electron accelerator located at the Thomas Jefferson National Accelerator Facility (JLab) in Newport News, Virginia. CEBAF was designed and built during the 1980s with the aim of providing the particle physics community with a tool to explore QCD in the confinement regime. Design requirements dictated that CEBAF be able to provide high quality, continuous-wave polarized electron beam on the scale of a few GeV, at currents of up to 200 μA, and to deliver this beam to multiple experimental halls simultaneously. The most cost-effective solution turned out to be a novel one: the use of superconducting radio-frequency (SRF) cavities to provide the acceleration gradient. Accelerators before CEBAF used copper cavities to provide the acceleration gradient, but due to resistive heating, such cavities had low duty factors and were expensive to operate. CEBAF's design and budget requirements would have pushed copper cavity technology to its limits in complexity and beam quality. SRF technology was under rapid development in the 1980s and promised a solution that allowed for inexpensive production of a high-quality electron beam as well as a straightforward path to future upgrades. Thus CEBAF became the world's first large-scale implementation of SRF cavity technology. An example of a cavity used at CEBAF is shown

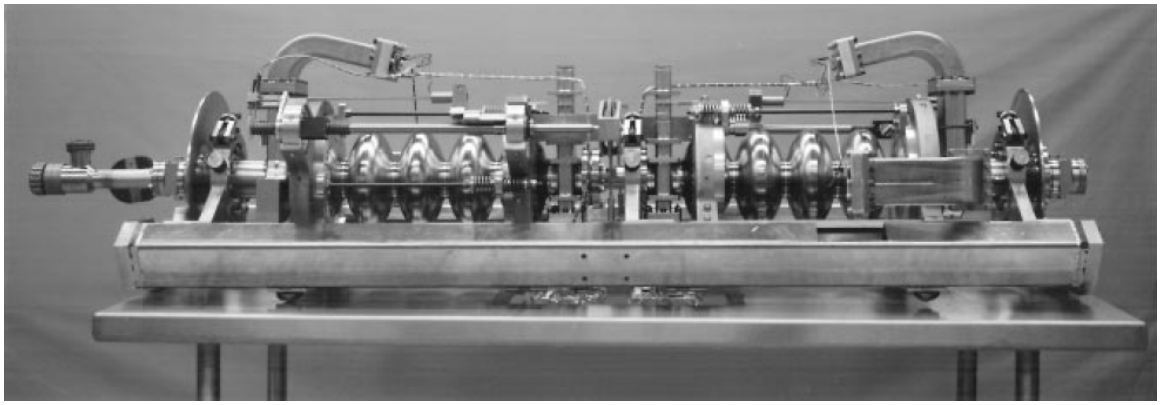

Figure 2.1: A photograph of a typical cavity used at CEBAF, made up of two superconducting niobium klystrons. A positive potential is applied across each cavity in turn as an electron bunch passes through, providing a constant acceleration gradient. This alternating of potentials down each linac amounts to a standing electromagnetic wave at radio frequencies within the cavity; the superconducting walls of the cavity ensure that almost all of the energy of the standing EM wave goes into the electrons passing through. (Image source: [54]).

in Figure 2.1.

CEBAF's final shape, diagrammed in Figure 2.2 and shown from the air in Figure 2.3, consists of two linear accelerators (linacs) connected by recirculation arcs at each end, in a racetrack shape. Electrons are first produced in the injector by a laser incident on a photocathode sample and are boosted to 67 MeV by the injector linac. Then within CEBAF proper, electron bunches are grouped into bunches about 90 μm in length and separated by 667 picoseconds in time. After a trip through a linac, electrons pass through different sets of bending magnets according to their momentum. These electron bunches acquire roughly 1200 MeV of kinetic energy with each lap around the track, traveling up to five times around before being delivered to experimental halls. The beam switchyard delivers successive electron bunches in turn to each experimental hall, resulting in beam bunches every 2.004 ns in any given experimental hall. The experimental halls themselves are at the south end of the CEBAF site. Halls A and C provide equipment for precision measurements at well-defined kinematic points, and are often occupied by groups with their own customized experiment-specific detector packages. Hall B is the smallest of these three and houses the CEBAF Large Acceptance Spectrometer (CLAS), the detector used in the present analysis.

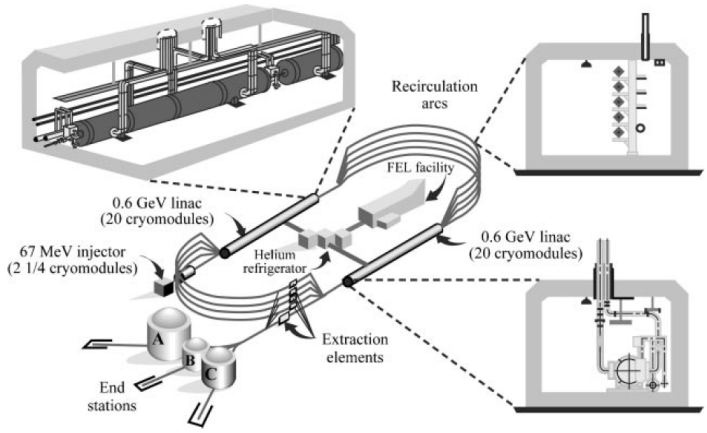

Figure 2.2: The components of CEBAF (Image source: [54]).

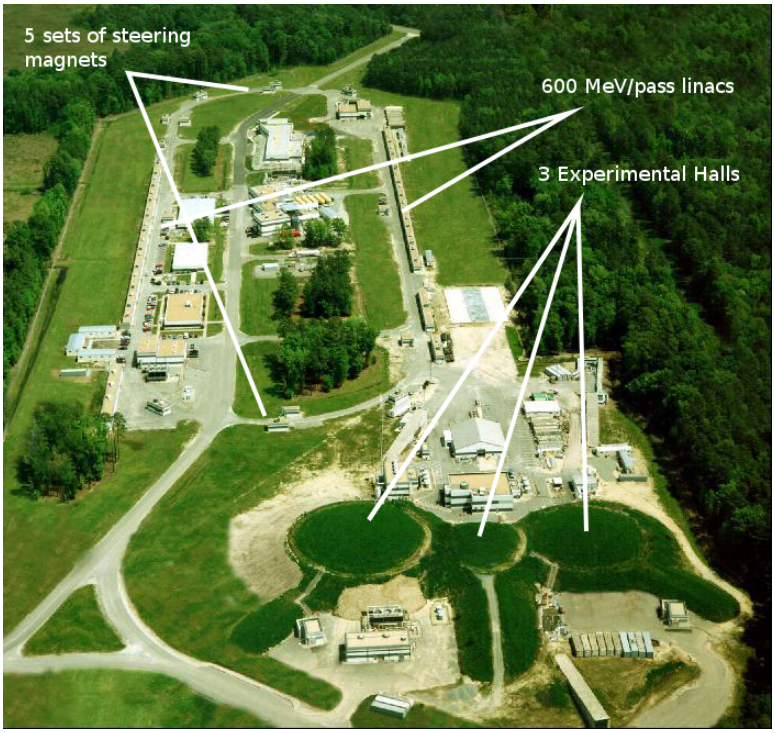

Figure 2.3: An aerial photograph of CEBAF (Image source: [54], with labels added by the author).

2.2 Hall B Photon Tagger

In addition to the electron beam supplied by CEBAF, Hall B also has a photon tagging system ("tagger", shown in Figure 2.4) for producing a real photon beam. The Hall B tagger operates on the bremsstrahlung principle. A thin target called the *radiator*, typically made of gold or copper, is anchored in the path of the electron beam. Electrons passing through the Coulomb fields of nuclei in the radiator are decelerated and emit photons corresponding to this deceleration. A negligible amount of momentum is transferred to a nucleus during a bremsstrahlung process, so one can write:

$$E_\gamma = E_e^i - E_e^f \tag{2.1}$$

where E_γ is the energy of the bremsstrahlung photon, E_e^i is the energy of the electron from CEBAF, and E_e^f is the energy of the electron after scattering through the radiator. Thin radiators help ensure that a single electron is correlated with a single photon. In order to measure the energy of the scattered electron, a magnetic spectrometer is used.

The tagger's magnetic spectrometer consists of a uniform-field dipole magnet capable of producing fields of up to 1.75 T. This dipole bends the scattered electron onto a focal plane, covered by two arrays of scintillation detectors, as shown in Figure 2.5. The first layer of scintillators are used to determine the energy of the scattered electron, and are thus called *E-counters*. There are 384 overlapping E-counters in the Hall B tagger and their role is solely to register hits from electrons passing through the spectrometer. Knowledge of the location of a struck E-counter in the focal plane is sufficient to determine the energy of the scattered electron. If one accounts for the overlapping of adjacent counters, this results in 768 possible measurements for the energy of the scattered electron, equivalent to a $\Delta E_\gamma / E_\gamma$ of about 10^{-3}. Below the E-counters is another array of scintillators, 61 in number, for measuring timing information about the arrival of electrons refracted through the tagger spectrometer. The information provided by these *t-counters*, combined with timing information from CEBAF, is crucial for CLAS users. After an interaction in CLAS, one can combine the t-counter timing with times from tracks in CLAS to deduce the particular photon that caused the interaction.

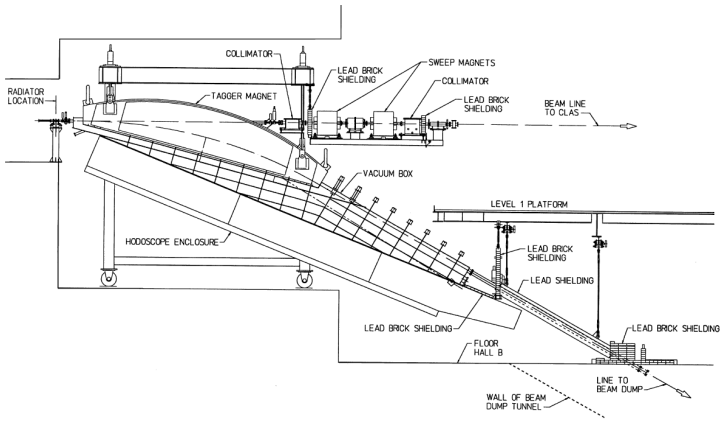

Figure 2.4: An engineering drawing of the photon tagger in Hall B. (Image source: [55]).

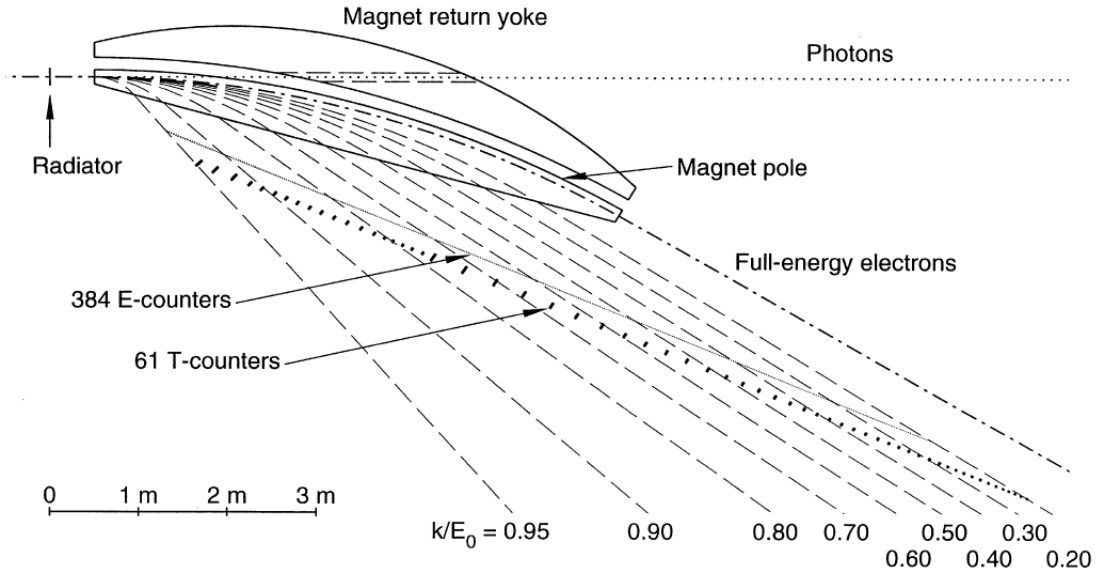

Figure 2.5: A diagram of the Hall B photon tagger in profile, showing the scintillator arrays mounted in the focal plane of the magnetic spectrometer. Electrons scattered through the radiator are bent by a dipole magnet into the scintillators; the energy of the scattered electron can be deduced by which E-counter registers a hit, and the t-counters provide a timing measurement for later correlation with tracks in CLAS (Image source: [54]).

Figure 2.6: A drawing of the target cell used during the g12 run.

2.3 Experimental Target

The target cell used during the g12 run, shown in Figure 2.2, was cylindrical in shape, 40 cm in length and 4 cm in diameter. Built at Jefferson Lab by staff engineers, the cell walls and substructure are aluminum, and the windows through which the beam passes are made from Kapton due its resistance to radiation and temperature extremes. It was commissioned by the CLAS g11 rungroup, and it has been used by several other CLAS rungroups, including the eg3a, g8b, and g13b. For g12 running, this target was placed 90 cm upstream of the geometrical center of CLAS to reduce the angle subtended by the forward hole in CLAS.

2.4 The CLAS spectrometer

CLAS is a multi-particle spectrometer situated in Jefferson Lab's Experimental Hall B. It is roughly spherical in shape, divided azimuthally along the beamline into six sectors, as shown in Figure 2.7. Each sector is a completely independent detector package and consists of:

- **A start counter for event timing:** the start counter (ST) is made of 24 scintillator paddles, six for each sector, surrounding the `g12` target cell, described in detail in Section 2.4.1.

- **A magnet for bending charged particles:** the main CLAS magnet, known as the CLAS torus because of the toroidal field it produces, is made of 6 lobes, spaced every 60°. Under normal operation, the toroidal field bends positively-charged particles away from the beamline and negatively-charged particles back into the beamline. It is described in detail in Section 2.4.2.

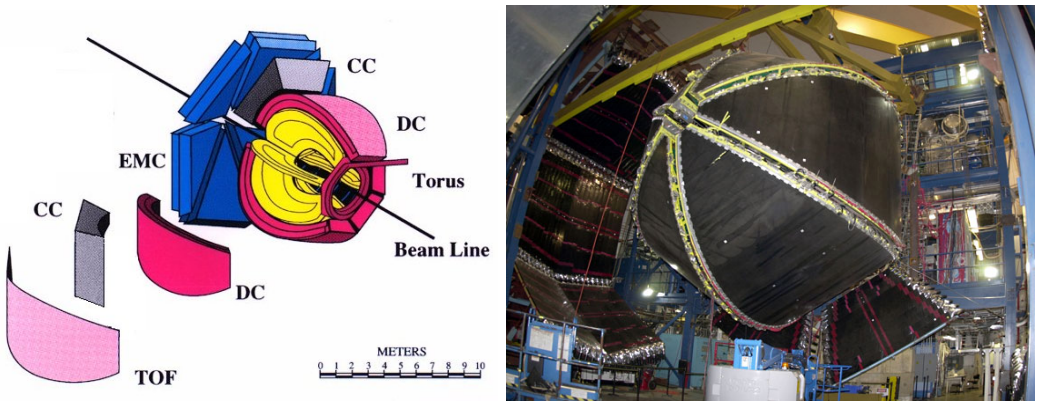

Figure 2.7: A cartoon showing the composition of the CLAS detector system (left); a photo of CLAS with the time-of-flight (TOF) withdrawn for service (right).

- **Three sets of drift chambers for charged particle tracking and momentum measurement:** the drift chambers (DC), as mentioned above, measure the trajectory of a charged particle entering, traversing, and exiting the toroidal field. They are described in Section 2.4.2 as well.

- **A time-of-flight wall for event timing:** the time-of-flight detector (TOF) consists of 342 scintillator paddles placed in six arrays of 57, one for each sector. It is described in Section 2.4.3.

- **A Čerenkov counter for particle identification:** the CLAS Čerenkov counter (CC) assists in differentiating between pions and electrons; details are found in Section 2.4.4.

- **An electromagnetic calorimeter for energy measurements:** the electromagnetic calorimeter (EC) records showers due to photons, leptons and neutrons entering its volume. It is summarized in Section 2.4.5.

Theses systems combined account for over 40,000 channels of electronics to be recorded by the data acquisition system (Section 2.5) for each trigger. After event recording, converting these vast arrays of detector digitizations to four-vectors and other useful physics quantities proceeds via specialized software and large-scale batch computing (Section 2.6). Once offline reconstruction is complete, event selection and data analysis can begin.

2.4.1 Start Counter

The first detector encountered by particles leaving the g12 target is the start counter (ST), shown in Figure 2.8. The start counter is a hexagonal array of 24 scintillator paddles, four to a side, which surround the target azimuthally. The downstream ends of the scintillators are bent toward the beamline and narrowed to converge into a six-sided cone, covering the front end of the target. Light output is collected in phototubes attached to

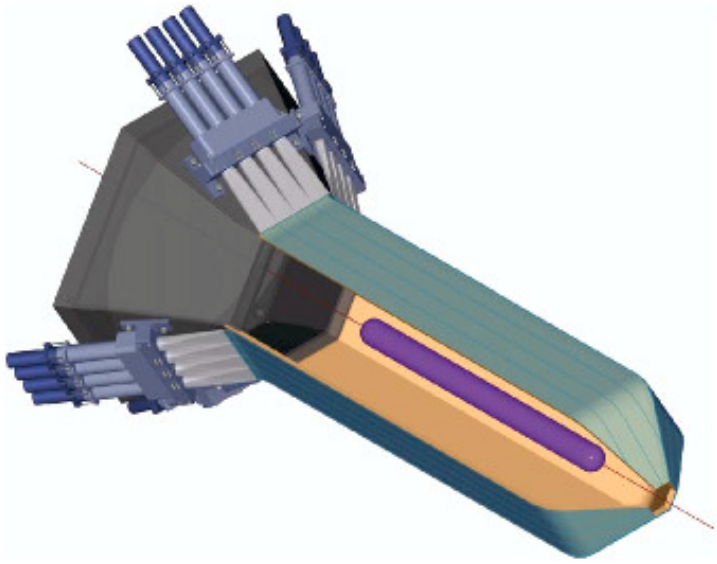

Figure 2.8: A drawing of the CLAS start counter. (Image source [56])

the upstream end. Pulses from the phototubes are read out with both TDC and ADC electronics, although typically only timing information is used in reconstruction.

Once in event reconstruction, the timing information from the start counter can be used to associate hits in the photon tagger with tracks in CLAS proper. Most tracks registering a hit in the ST will also register a hit later in the time-of-flight (TOF), and combined with the path length through the drift chambers, times from the ST and TOF can be used to derive a velocity. The track can then be propagated back from the ST to the event vertex, and scaling the time back accordingly, one can determine the time at which the event took place. Since one of these measurements can be made for each track, high-multiplicity events ($N_{tracks} > 2$) provide especially good handles on the time the tracks say the event started. Using a suitable average of these times, one can then examine the list of hits in the tagger for the event, and select the photon which arrives at the event vertex at the time suggested by the track-averaged event start time.

Additionally, the segmentation of the ST enables users to set up elaborate triggering schemes. Experiments can record only events with n tracks, using n coincidences of the ST and TOF. Specific sectors can be included or excluded, and logic from the ST can be combined with logic from the tagger t-counters to record events with photon energies in a given range. A summary of the g12 trigger can be found in Section 2.5.

2.4.2 Drift Chambers and Torus Magnet

The core of CLAS is its drift chamber system (DC), made up of eighteen detector assemblies working in conjunction with a superconducting magnet producing an approximately toroidal field (colloquially known as the "torus"). The torus and the DC together define the spherical, axially segmented shape of CLAS, shown in Figure 2.9.

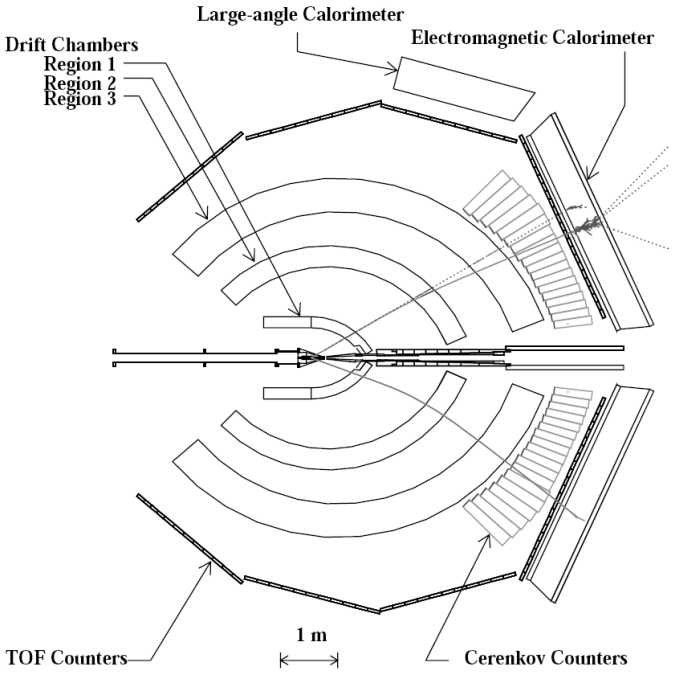

Figure 2.9: A diagram of the CLAS drift chambers.

The CLAS torus is made of six nonferrous superconducting coils, mounted radially around the beamline, as shown in Figure 2.10. At its nominal operating current of 3861 A, it produces an approximately toroidal field of 2.5 T. Tracks entering this field are bent only in polar angle, and thus charged tracks rarely travel between sectors. This simplifies the tracking algorithms and allows for optimizations in chamber design. However, there is some cost in acceptance, as negatively-charged tracks are bent back towards the beamline during normal operation and thus can be lost through the forward hole of CLAS.

A single sector of CLAS contains three sets of drift chambers, Regions 1, 2, and 3 (R1, R2, and R3). The R1 drift chambers are the smallest of the three, situated close to the target, beneath the lobes of the torus and out of its magnetic field. Region 2 (R2) is interleaved with the torus coils, in an area of high magnetic field to maximize track curvature for momentum measurements. Region 3 (R3) is the largest in size and lies outside of the torus field, at the largest radius of the three regions. All chambers are strung with 20-μm diameter gold-plated tungsten sense wires and 140-μm diameter gold-plated aluminum field wires. The field wires are interspersed with the sense wires arranged to form a hexagonal drift cell with the sense wire in the middle, giving the chambers good position measurements at a wide variety of track angles. Multiple layers of hexagonal cells are grouped into *superlayers*, with each successive layer shifted by a half-cell width to achieve a honeycomb configuration good for resolving left-right ambiguity. Each complete drift chamber has two such superlayers. The superlayer closest in radius to the target is oriented axially with respect to the magnetic field, while the outer superlayer is rotated at

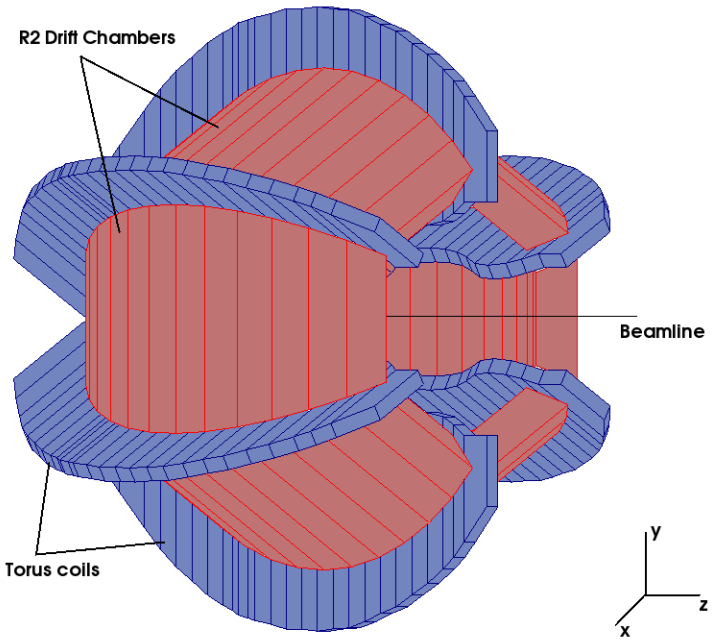

Figure 2.10: A drawing of the CLAS torus and R2 drift chambers, rendered in GEANT geometry.

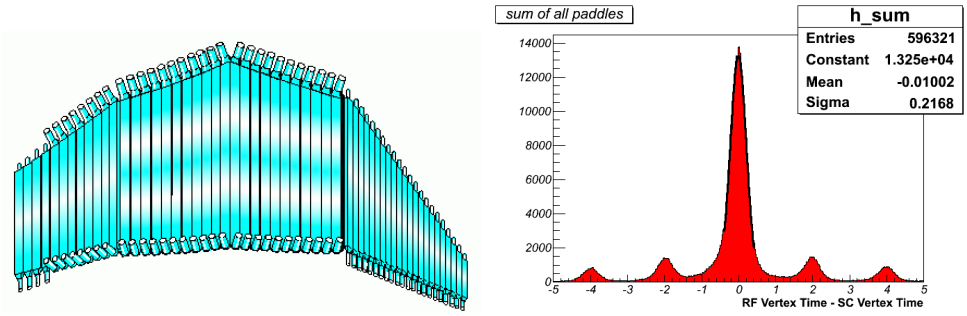

Figure 2.11: A drawing of a single sector of the CLAS time-of-flight (TOF) (left); the final g12 TOF timing resolution for pions (right). The secondary peaks at multiples of 2 ns are due to photons from different electron beam bunches.

a stereo angle of 6° to resolve track azimuth.

Details of the design and construction of the CLAS drift chamber can be found in [57] and [58].

2.4.3 Time-of-Flight

The CLAS time-of-flight (TOF) system provides precise timing for charged tracks, used primarily in particle identification. Due to its fast response time, it is commonly used in conjunction with the start counter (Section 2.4.1) to help define trigger criteria for event recording. Following the six-sector design of CLAS, the TOF has six sets of 57 scintillator paddles, mounted just outside the Čerenkov counter at a distance of about 5m from the target. Within a single sector, the 57 TOF elements are divided into three groups based on the range in polar angle for which they are responsible, with the forward angles primarily optimized for time resolution, and the larger angles optimized primarily for cost. The first 23 paddles, responsible for particles with polar angles on the range 8.6° to 45.9°, are 15 cm in width and instrumented with 2in photomultiplier tubes. Paddles 24 through 53, covering polar angles on the range of 45.9° to 131.4°, are 22 cm in width and instrumented with 3in photomultipliers. The last four paddles, operating over the range of 134.2° to 141.0°, are again 15 cm in width and instrumented with 2in photomultipliers. All paddles are of 5.08 cm-thick Bicron BC-408 scintillating plastic and have phototubes mounted on both ends. Output from the photomultipliers is passed through leading-edge discriminators before readout by both TDC and ADC components. The ADC information from the TOF is primarily used for calibration purposes, but it is also possible to perform rudimentary particle identification by examining the energy deposited by tracks passing through the TOF. This technique is most often useful to analyses with kaons in the final state, as the TOF system is unable to reliably discriminate between kaons and pions at momenta above 1.5 GeV.

Calibration of the TOF, like the rest of the components of CLAS, involves several steps. For photon runs like g12, the procedure is as follows:

1. **Counter status**: identify and eliminate dead channels.

2. **ADC pedestals**: record values of each ADC channel when no tracks are passing through the TOF.

3. **TDC linearization constants**: using fits to pulser data, determine the conversion function from TDC channels to nanoseconds.

4. **Time-walk corrections**: correct for the instrumental shift in times created by pulses of varying height passing through a leading-edge discriminator. This is typically done by fits to data taken with a laser illuminating each phototube in sync with a pulser so that the timing response over a wide range of ADC values can be probed. However, by the time the g12 run was commissioned, the CLAS TOF laser system had largely fallen into disrepair. Many alternatives were tested, and the system that gave the best timing resolution for g12 was to perform the time-walk calibration on channels with the appropriate laser data, and to use constants from prior runs for channels where no such data existed.

5. **Left-right delay constants**: determine corrections required for the differences in timing between photomultipliers at each end of the same paddle.

6. **Attenuation length**: determine and record for each paddle the average length over which the scintillation light is attenuated by half,

7. **Minimum-ionizing particle pulse heights**: for each paddle, determine and record the ADC channel number for minimum-ionizing particles.

8. **Effective velocity**: for each paddle, determine the effective velocity of light, which can vary as the plastic ages and becomes less transparent.

9. **Paddle-to-paddle offsets**: correct for shifts in the relative timing between paddles due to cable lengths or other factors.

More information on the design and construction of the TOF can be found in [59].

2.4.4 Čerenkov Counter

For lepton-pion separation during particle identification, the CLAS Čerenkov counter (CC) is a crucial component. In line with the segmented design of CLAS, the CC is made up of six identical modules. From its position mounted just outside of the R3 drift chambers (shown in Figure 2.12), the CC can detect leptons with polar angles from 8° to 45°. Within a single CC module are eighteen light-collection fixtures, with each fixture accounting for a small range of polar angle. A single fixture is made of two pairs of mirrors arranged in opposing fashion along the long axis of the CC module. Leptons traveling through the CC leave a trail of Čerenkov light traveling onto the elliptical outer-surface mirrors, which focus the light back across the body of the module onto the hyperbolic inner-surface mirror. The inner-surface mirrors then reflect the Čerenkov light into photomultiplier tubes mounted along the long edges of the CC module. The mirrors themselves are constructed from Kevlar-wrapped structural foam with a polished Lexan-backed aluminum reflective surface. During experimental running, the CC is filled with perfluorobutane (C_4F_{10}) gas,

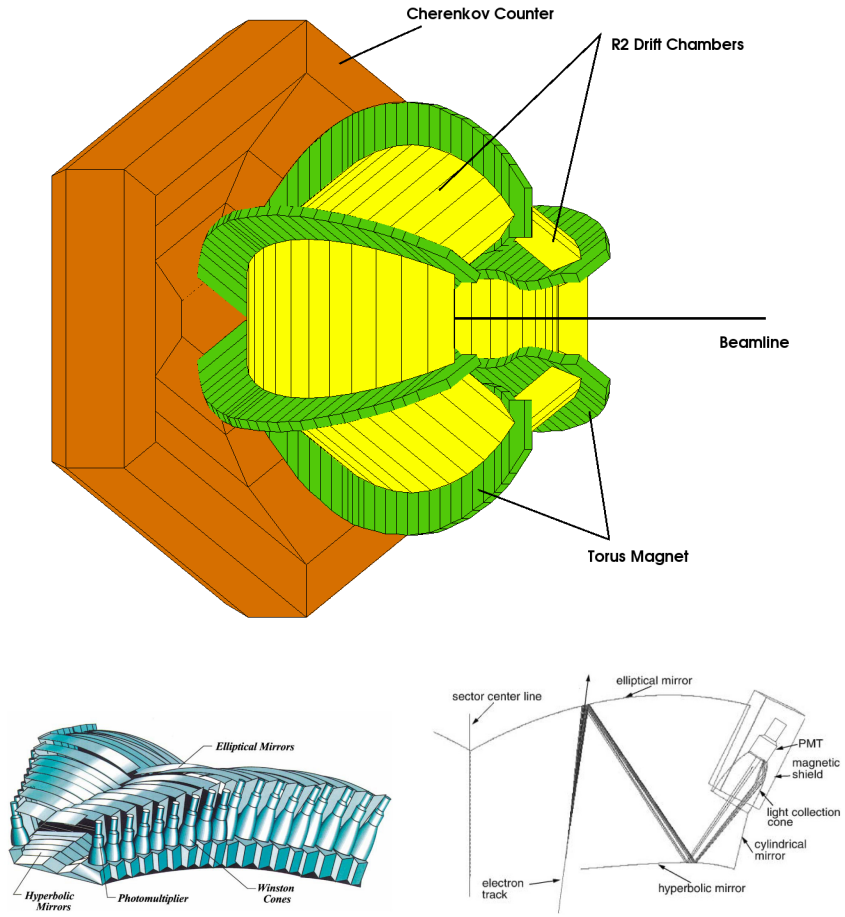

Figure 2.12: **Top:** A drawing of the CLAS Čerenkov counter, rendered in GEANT geometry with the R2 drift chambers and the CLAS torus to give a sense of scale and position. **Left:** Detail of the design of a single CC sector. Winston cones are devices that funnel light down into the phototube for more efficient collection (Image source: [60]). **Right:** Detail of the internals of a single CC mirror pair. The electron moves up the page. (Image source: [60])

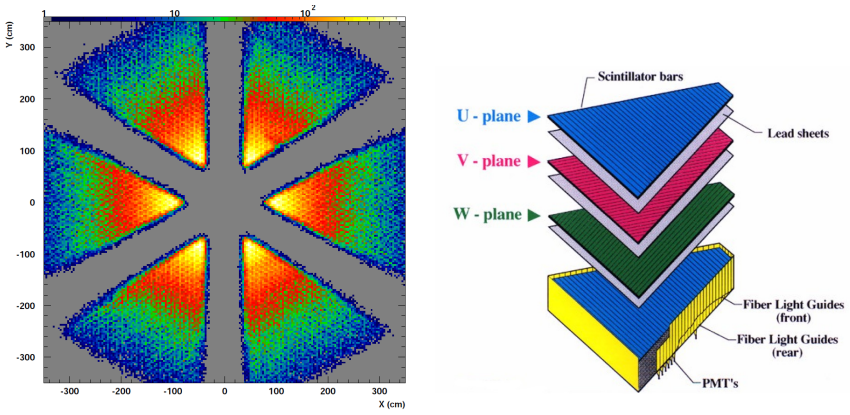

Figure 2.13: **Left:** A plot of electron occupancies in the EC looking downstream along the beamline. Warm colors indicate high occupancies. **Right:** A diagram of the u, v, and w geometry of a single sector of the EC. (Both images from [61])

which has an index of refraction of 1.00153. Light hadrons, such as pions, are not traveling greater than the speed of light in perfluorobutane, and thus do not emit any Čerenkov light, allowing separation between pions and leptons. This translates to the an upper limit for lepton-pion separation of 2.5 GeV.

This separation is especially crucial for CLAS experiments using electron beams, as the CC (in conjunction with the electromagnetic calorimeter) is necessary to detect the scattered beam electron. Also, the CC has a rapid response time so it is often used in coincidence with the electromagnetic calorimeter (EC) for trigger configurations. g12 employed an `EC*CC` trigger to record data for studying of the interference of ρ and ω mesons in their e^+e^- decay modes.

More information on the design and construction of the CC can be found in [60].

2.4.5 Electromagnetic Calorimeter

For total energy measurements independent of particle identification and momentum, CLAS is equipped with an electromagnetic calorimeter (EC). The calorimeter is essential for experiments using CLAS with electron beam, as it is used in conjunction with the Čerenkov counter (CC) to detect scattered beam electrons. The EC is also useful for reconstructing high-energy neutrals, such as photons from radiative decays or neutrons. Also like the CC, the EC has a fast response time that is useful for deriving trigger configurations. g12 employed two trigger configurations which used the EC, detailed in Section 2.5.

The EC, as shown in Figure 2.13 is a sampling calorimeter made of six panels, triangular in cross-section and arranged radially in a manner conforming to the CLAS hexagonal geometry. Each sector of the EC is made of 39 layers of plastic scintillator, interspersed with lead sheets. A scintillator layer is made up of 36 individual strips, 10 mm in thickness, with each successive layer rotated by 120° to be parallel to one side of the detector volume. These successive rotations create a u-v-w geometry suitable for making position measurements. Each layer of scintillator is lined with a 2.2 mm sheet of lead. In the innermost fifteen layers,

five complete u-v-w logical layers exist; light output from strips radially stacked with the same u, v or w orientation are fed into a single phototube via a bundle of optical fibers. For example: the light output from strip 1 of the innermost layer, which has orientation u, is routed into the same phototube as the strip 1 of the fourth, seventh, tenth, and thirteenth layers, which all have orientation u as well. This makes for $36 \times 3 = 108$ phototubes for the first fifteen layers, termed the *inner* stack. The same prescription is followed for the last 24 layers and they are collectively termed the *outer* stack. In total the EC is made up of 8424 individual strips of scintillator and is instrumented by 1296 phototubes. Each sector weighs some 17 tons.

More information on the design, construction, and performance of the EC can be found in [61].

2.5 Data Acquisition and Experimental Trigger

Particle signatures in the detector subsystems of CLAS are recorded to disk by a complex suite of electronics, known as the data acquisition (DAQ) system. The CLAS DAQ system monitors and records data from all of the individual detector elements making up CLAS, including the drift chamber sense wires, and the photomultipliers of the ST, CC, TOF, and EC, some 40K channels in total. Data is recorded in an *event-based* format, where time is divided up into finite intervals, and at the end of each interval the signals present in each detector element are written out to disk.

The presence of a signal is determined by a hardware element known as a *discriminator*, which monitors a single sense wire or phototube. The discriminator compares all signals it receives to a preset voltage threshold, and only signals exceeding the threshold are allowed to continue to the digitizing electronics downstream. Signals exceeding the discriminator threshold are considered to originate from physics interactions and are digitized by two types of hardware. Time-to-digital converters (TDCs) simply report the time at which a signal arrives. Analog-to-digital converters (ADCs) report a number corresponding to the integral of the signal. In practice, these electronic components are typically manufactured on boards capable of handling a few dozen inputs at a time. The boards are then installed into rack-mounted crates which provide power and databus services to ten or more boards at a time. Each crate assembles the digitizations from its boards and writes them to a single output stream. Software processes running on servers then communicates with each crate via broadband network connections and assembles their datastreams into an event-based data format which is then written to a disk array. Another software process monitors the disk array and moves data to long-term storage on tape silos as the disk array is filled.

To read out only events of interest from the DAQ system, we define one or more *triggers*. The trigger definition is a list of signals from various detectors we require for an event to be written out to disk. The DAQ system monitors the state of CLAS over finite intervals of time, and thus in order to make a decision about whether an event meets the trigger requirements, the signals used in the trigger definition must be available as quickly as possible. During the g12 run, the interval or *gate* for a trigger coincidence was 100 ns. All subsystems of CLAS except for the drift chambers can acquire signals in a few nanoseconds, and thus we had the freedom to define triggers using the ST, TOF, EC, and CC, as well

as the Hall-B tagger. However it is possible to use measurements from the DC in a trigger decision if a slower, second-level (L2) trigger is implemented. In this configuration, events passing the first-level (L1) trigger are passed on to the L2 trigger, which is typically a software routine rather than a pure hardware system like the L1 trigger. The software routine does coarse track reconstruction on the drift chamber hits, just to confirm that the L1 coincidence was actually caused by particles traveling through CLAS and not just an accidental coincidence of random noise.

The g12 run was the first CLAS rungroup to employ a field-programmable gate array (FPGA) as the trigger supervisor, allowing the most complex L1 trigger configuration of any CLAS experiment to date. Twelve independent trigger definitions were in place at any one time during running, and the definitions themselves could be easily changed during running. The primary or *production* trigger was designed to record meson spectroscopy events. In general the production trigger consisted of two-track events with a high-energy photon, or a three-track event with any beam energy. These were implemented as coincidences between the ST, TOF, and a logic unit providing an `OR` between the first 19 paddles of the tagger, called the master-`OR` A (MORA). Various combinations of these elements typically made up six of the available slots in the supervisor; the rest were dedicated triggers for the other aspects of the g12 experimental program. Tables summarizing all of the different g12 trigger configurations are found in Ref. [62].

Events satisfying any of the trigger definitions during the g12 run were recorded by the DAQ system at a rate of 8KHz, the highest of any CLAS experiment to date. 26B events were written to tape, corresponding to 68 pb^{-1} of luminosity. Data were collected in *runs*, nominally of 50M events each, but in the event of poor beam quality, DAQ system failures, or other mishaps runs were ended prematurely. These truncated runs were discarded if they contained fewer than 1M events, or if the run-halting failure corrupted the data contained therein. In total, 622 runs remain after the removal of these corrupted runs. The raw data taken during those 622 runs occupies 121 terabytes of disk space on the Jefferson Lab mass storage system.

2.6 Event Reconstruction

Event reconstruction is done independently in each sector and begins in the drift chambers with *hit-based tracking*. Hit-based tracking requires just the positions of wires registering a hit in a given sector, suitably corrected by drift-chamber alignment calibrations. Following the drift-chamber geometry described in Section 2.4.2, adjacent hits in each superlayer are grouped into clusters, and then these clusters are linked in each region to produce track segments. These track segments are then linked again across the three regions to produce a full hit-based track. The sign and magnitude of the curvature of the track as it passes through the R2 drift chamber gives the charge $\pm e$ and magnitude of the momentum of the track, respectively.

These hit-based tracks constitute first approximations. Often, noise hits or whole clusters can be found which are not associated with physical tracks. We can remove these by extrapolating the hit-based track to the appropriate time-of-flight panel, and searching for hits in panels the hit-based track passes through. If a hit is found, we can use its time mea-

surement to set an absolute upper limit to the times of the drift-chamber hits associated with the track. This is the beginning of what is called *time-based tracking*. After a TOF hit is associated with a given hit-based track, the drift-chamber hits associated with the track are checked one at a time, where they are required to be in increasing time order as the track moves outward. Hits or clusters not fitting this requirement are removed, and once the list of hits has been processed, the track is re-fit using the remaining hits. This process is repeated up to two more times to further refine momentum measurements, as well as the measurement of the event vertex, determined by the distance of closest approach of the track to the beamline.

Once the time-based tracking algorithm has distilled a satisfactory set of hits and assigned an optimal set of tracking parameters, this track is extrapolated to the rest of the components of CLAS. The start counter, Čerenkov counter, and electromagnetic calorimeter are all investigated for hits in the locations where the track intersects their active volumes. Should these hits be present, they are added to the description of the track.

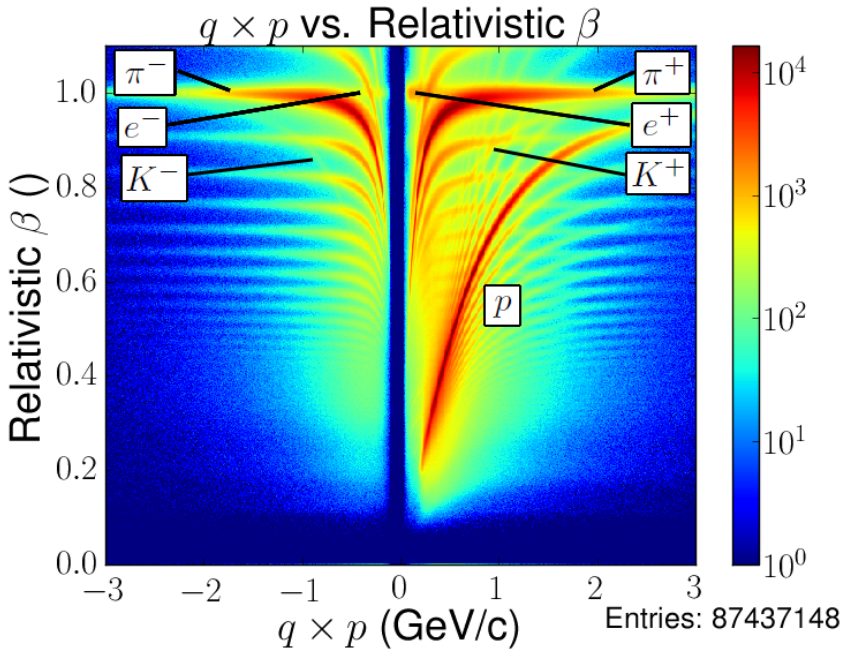

Figure 2.14: Track β versus track momentum for all tracks in run 56855. This plot is a graphical representation of how particle ID assignments are made in CLAS reconstruction.

The final reconstruction algorithm attempts to assign a well-known state to the track based on its observed charge, momentum, and timing information. This is done using the

TOF mass, calculated according to:

$$m = \frac{cp^2}{\beta^2}$$
$$\beta = \frac{t' - t}{cl}$$

where the following definitions are used:

- c is the speed of light,
- p is the track momentum as measured by the drift chambers,
- t' is the time of the TOF hit associated with the track,
- t is the time the track left the event vertex, as reported by the start counter or the tagger,
- and l is the length of the track from the event vertex to the struck TOF paddle.

Thresholds for particle identifications are then defined for the calculated value of m,

$$\text{Particle ID} = \begin{cases} \pi & \text{if } m < 0.3 \text{ GeV} \\ K & \text{if } 0.35 < m < 0.65 \text{ GeV} \\ p & \text{if } 0.8 < m < 1.2 \text{ GeV} \\ d & \text{if } 1.75 < m < 2.2 \text{ GeV} \end{cases}$$

Particles falling into the regions between these cuts are classified as unknown, and are typically the result of a failure in time-based tracking. These failures can occur when the photon causing the event is not recorded in the tagger and another is chosen in its place, or if a single TOF paddle sustains two consecutive hits with different times. More discussion of the photon selection algorithm for the g12 $\gamma p \to \pi^+\pi^+\pi^- n$ dataset is found in Section 3.1.1.

The algorithms described above are coded in software libraries of C and FORTRAN routines. For the reconstruction of the g12 dataset, these libraries were linked against the standard CLAS reconstruction executable `a1c`. The reconstruction of the full 121 TB g12 dataset was carried out using the batch computing resources of Jefferson Lab over the period spanning August to December 2009. A week-by-week history of the processing is outlined Figure 2.15.

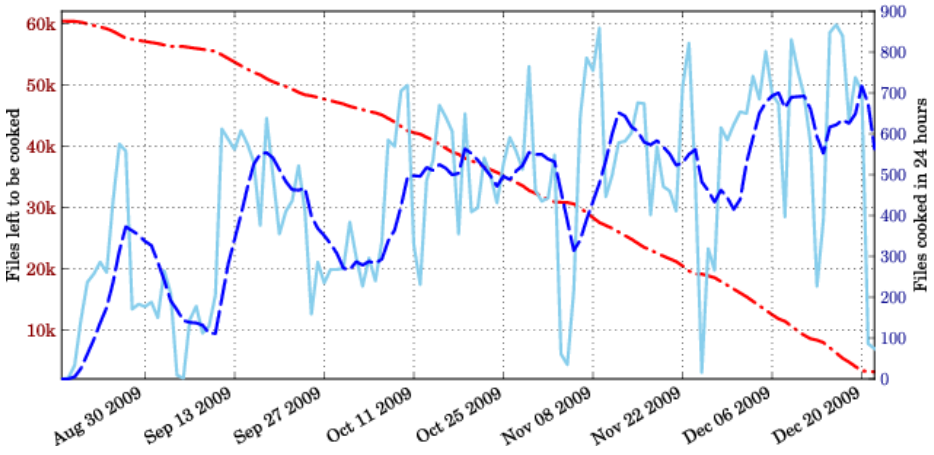

Figure 2.15: Progress over time of the event reconstruction of the full g12 dataset. (Image source: [62]).

CHAPTER 3

EVENT SELECTION AND FEATURES OF THE DATA

Event selection in any physics analysis is a compromise between the removal of *background* events and the preservation of *signal* events. Ideally, one finds a set of conditions such that all of the events of interest are kept, while the rest are thrown out. In practice of course, almost any selection will throw out some portion of the signal events along with the targeted background events. Ideally, each selection increases the ratio of signal events to background events, but at the cost of larger *statistical* uncertainties because the sample size has been reduced. Reducing the purity of the sample can also introduce *systematic* uncertainties into the analysis, depending on the physics of the events polluting the sample. Thus the scientific goals of a given analysis determine the point of balance between sample size and sample purity.

This analysis is a search for the spin-parity exotic $\pi_1(1600)$ in $\gamma p \to \pi^+\pi^+\pi^- n$. As many of the states that decay to 3π are broad and overlapping, we must use partial-wave analysis (PWA) to disentangle contributions of individual J^{PC} combinations. Thus our event selection should be a set of physically-justifiable criteria that yield a set of $\gamma p \to \pi^+\pi^+\pi^- n$ events that result in stable, reproducible, and meaningful PWA results. Additionally, we must preserve the statistical integrity of our analysis, as we are searching for a signal that is most likely very small.

The first task is to select events consistent with exclusive production of three pions and a neutron. Our method, outlined in Section 3.1, leaves selection of exclusive $\gamma p \to \pi^+\pi^+\pi^- n$ events as the last stage so that we can use the presence of the backgrounds beneath the neutron in the missing-mass spectrum to measure how well we eliminate *incidental* background in our final sample. Incidental background consists of events that are not actually well-measured $\gamma p \to \pi^+\pi^+\pi^- n$ events but have been reconstructed as such due to inefficiencies of the detector or the reconstruction algorithms. After we have isolated a sample of good-quality $\gamma p \to \pi^+\pi^+\pi^- n$ events, we then address the *physics background* present in our data. Physics background consists of well-reconstructed $\gamma p \to \pi^+\pi^+\pi^- n$ events that do not correspond to the production of a meson resonance decaying to three pions. Physics background present in our event sample threatens the validity of the PWA; its reduction is discussed in Section 3.2.

3.1 Exclusive $\gamma p \to \pi^+\pi^+\pi^-n$ Event Selection

We begin our exclusive $\gamma p \to \pi^+\pi^+\pi^-n$ event selection by examining the full g12 dataset. As discussed in Section 2.5, g12 took 622 "good" runs, nominally with 50M events in each. All told, these 622 runs contain 24.8B events. From these 24.8B events, we select events with two positively-charged pions, one negatively-charged pion, and no other charged tracks. The charge of a track is determined by the sign of its curvature through the toroidal magnetic field of CLAS; for g12, positively-charged tracks bend upwards, while negatively charged tracks bend down back into the beamline. Identifying these tracks as pions, rather than kaons, requires a measurement of the time-of-flight, so that the track's flight time can be compared to its momentum and a hypothesis about its mass can be made, as described in Section 2.6. However, to get the correct measurement for the flight-time of the track, we must examine each photon measured by the tagger during the trigger interval and select the one that actually produced the tracks.

3.1.1 Photon Selection

Depending on the photon beam intensity during the experiment, anywhere from one to over a hundred photons can be measured by the tagger during the time span of the event trigger. To determine the *trigger photon*, or the photon that interacted with the target to produce the tracks we measure, we use the CLAS start counter, described in Section 2.4.1. Charged tracks leaving the target travel a distance of a few centimeters before striking the scintillating paddles of the start counter. The start counter's instrumentation records the time and energy deposited each time it is hit. The reconstructed drift-chamber track can then be extrapolated both inward and outward to determine which start-counter and time-of-flight paddles were hit. The track is propagated even further inward to the point of closest approach with the beamline, which gives an estimate of the *track vertex*, or the location within the target where the track originated. Using the time difference between the time-of-flight and the start-counter along with the path-length along the track between the two, a speed for the track can be calculated. Using this speed and the distance along the track between its point-of-origin in the target and its point-of-contact with the start counter, we can calculate a time, which can be subtracted from the time the track hit the start counter to deduce the time the track was produced. This algorithm, when repeated for each track in an event with n tracks, will give n estimates for the time at which the event started. These guesses are then averaged together.

Armed with the average *start counter vertex time*, as the above quantity is called, one can then examine each of the photons measured by the tagger for the event. The tagger, as described in Section 2.2, measures the remaining energy and the time of entrance of electrons scattered through the bremsstrahlung radiator. Knowing the time a scattered electron arrives in the tagger, the distance from the radiator through the tagger magnet to the focal plane, and the distance between the radiator and the center of the target, one can deduce the time the bremsstrahlung photon arrived at the center of the target. Incorporating a small correction from the target center to the event vertex, one can find the time the photon arrived at the vertex. Then, for each hit recorded in the tagger for a given event, the time propagated to the vertex can be compared with the averaged time the tracks left the event vertex, and the hit with the best agreement is then selected as the

trigger photon.

Caveats exist to this algorithm. First, as mentioned in Section 2.1, CEBAF delivers electrons in bunches separated by 2.004 ns to each experimental hall, and thus photons from the Hall-B tagger arrive at the same interval. Increasing the current in the accelerator increases the number of electrons in each pulse, but not the frequency at which they arrive. g12 ran at beam currents of 60-65 nanoamperes (nA), which corresponds to a photon flux of about 5×10^8 γ/s, or about 50 photons measured by the tagger per event. Thus there is a significant possibility that a single beam pulse will produce multiple bremsstrahlung photons. As these 2.004 ns intervals represent the most accurate time intervals available to event reconstruction, there is no way to distinguish from a timing perspective between two photons whose times both agree with the event timing to a level better than 2.004 ns. Selecting at random between the two candidates is the fairest method. Selecting the photon that provides the missing mass in best agreement with that of the neutron is also possible, but understanding the sources of background introduced by such an algorithm would be nontrivial. Given that events with low-energy trigger photons (less than 4.4 GeV) will be culled from our sample (see Section 3.2.1), it is wasteful to choose a photon at random if one photon will satisfy our criteria and the other will not, so we choose the high-energy photon. If neither photon makes the beam energy cut, we still choose the higher-energy of the two, although it will later be lost no matter what choice is made.

By examining a sample of g12 data under typical running conditions, we can quantify how often these special cases in photon selection happen:

- Percentage of events with two photons produced by the same electron beam bunch: **82%**
- Percentage of events with two high-energy photons (above 4.4 GeV) produced by the same electron beam bunch: **8.2%**
- Percentage of events where two photons are in the beam pulse causing the event: **8.2%**
- Percentage of events where two high-energy photons (above 4.4 GeV) are in the beam pulse causing the event: **0.38%**

The only case where our decision-making remains ambiguous is in the last case, where we have two high-energy photons which are also the best-timed photons in the event. This outcome happens in less than 1% of events, and when it does, we select between the two photons at random.

It is also possible to record an event for which there is no in-time photon to cause the event. An electron can be scattered through the radiator and produce a bremsstrahlung photon, but not register a hit in the tagger. That photon can then go on to interact in the target and produce tracks which satisfy the trigger. Our algorithm will still select the photon closest in time, but it will generally be off-time by at least 2.004 ns. This can lead to incorrect values of missing mass, particles measured to be going at superluminal velocities, or both. Superluminal tracks can be removed by cuts on track β, as detailed in Section 3.1.5. Some events with incorrect values of missing mass can be removed by the cut on the neutron, described in Section 3.1.6, but those with missing mass close to the

neutron's nominal value will remain in the sample. These events then become a source of background to the PWA. The effects of these events can be deduced by studying the sidebands of the neutron, and such a study is described in Appendix C.1.

Finally, it is possible that two different interactions could occur in one 100 ns interval which collectively satisfy the trigger, skewing the average start-counter vertex time. It is also likely that two such interactions will take place at different vertices; thus vertex reconstruction will be compromised as well. We can estimate the rate at which such events occur. g12 took data with a photon flux in the neighborhood of $5 \times 10^8 \gamma/s$, which equates to 50 photons per 100 ns interval. The total photoproduction cross-section at 1.5 GeV is 0.151×10^{-27} cm^2; combined with 3×10^{25} protons in the g12 target, this gives a total interaction probability of 3.5×10^{-4}. Using the binomial distribution, the probability of having any two of fifty photons cause interactions is approximately one in ten thousand—a small effect.

3.1.2 Particle Identification and Kinematic Corrections

With the correct photon selected, the event start time is set to be the time that that photon arrives at the event vertex. Then a flight time for each track can be found by taking the difference between each track's time-of-flight measurement and the event start time. Then using the path length along the track from the event vertex to the each track's struck time-of-flight paddle, a speed can be derived. Comparing the speed of each track to its momentum measured by the drift chambers, an estimate of the mass of the particle causing the track can be obtained, as detailed in Section 2.6 and illustrated in Figure 2.14. This procedure is implemented in the standard CLAS reconstruction program `a1c`, so we merely require events where this procedure has found all three charged tracks to be pions. Also implemented in `a1c` are corrections to the incident photon energy due to gravitational sagging of the focal plane of the tagger, an effect first discovered and documented by We leave the identification of the neutron to a selection in the missing mass, described in Section 3.1.6.

Once the tracks have been identified as pions, their momenta are corrected for energy lost through passage through the experimental target. Our vertex cuts ensure that our tracks originate within the target volume, and thus they must exit the target in order to be measured by CLAS. Such passage reduces the momenta of the tracks by an amount proportional to the distance traveled through the target volume; we assume that the angles of track production are unchanged by interaction with the target material. The standard CLAS software package known as `eloss` calculates corrections for a given particle, produced at a given vertex with a given path-length through the volume. All events in the sample under analysis have had their pion momenta corrected in this fashion.

The energy of the beam photon was corrected during event reconstruction for the gravitational sagging of the focal plane of the CLAS tagger, first discovered and documented by the g1c rungroup and later updated by the g8b rungroup [63], [64]. These corrections don't account for all of the possible factors that could cause slight inaccuracies in the beam photon energy. Likewise, corrections for energy lost in the target cannot account for similar inaccuracies in charged track momenta. Thus it is a common practice for each CLAS rungroup to derive their own set of corrections to the incident beam energy and charged

track momenta. Such corrections for the g12 rungroup were still in development at the completion of this analysis, and thus are not included here. However, we expect no change in our conclusions from these corrections, as they amount to small adjustments of the overall kinematics, and should serve only to sharpen the results we report here.

3.1.3 Signal to Background Ratio

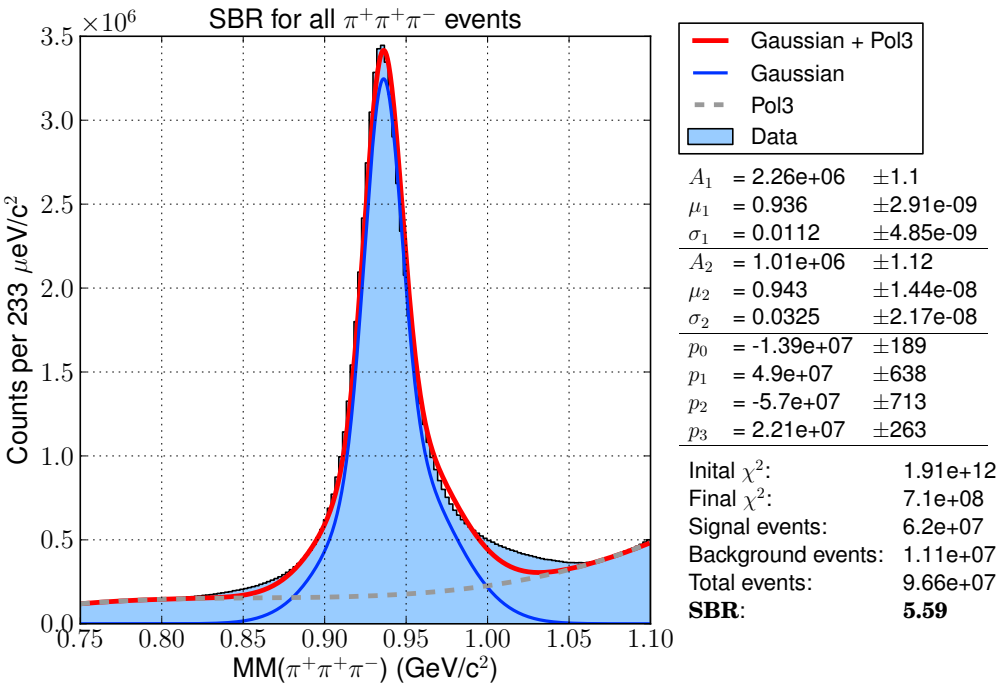

Figure 3.1: The $\gamma p \to \pi^+\pi^+\pi^- n$ missing-mass spectrum before any timing cuts are applied.

The *signal to background ratio* (SBR) is the quantity which we will use to justify the following selections. We are interested in obtaining a large and pure sample of exclusive $\gamma p \to \pi^+\pi^+\pi^- n$ events; we identify the neutron via *missing mass*, a technique described in Section 3.1.6. The missing mass spectrum for these events, shown in Figure 3.1, consists of a peak containing real neutrons sitting atop a continuous distribution of background events. We will eventually select the peak in the region of the neutron mass, but we would like to reduce the background beneath as much as possible to minimize the amount of incidental background in our PWA sample. Thus we define the SBR for this analysis to be the ratio of the number of events in the peak in the neutron mass region to the number of events beneath the peak.

In order to determine these quantities, we perform a fit. The model we use to describe the missing-mass spectrum is a sum of two Gaussian distributions sitting atop a third-order

polynomial background,

$$F_S(m) = A_1 \exp\left[(\frac{m-\mu_1}{\sigma_1})^2\right] + A_2 \exp\left[(\frac{m-\mu_2}{\sigma_2})^2\right] \tag{3.1}$$

$$F_{BG}(m) = p_0 + p_1 m + p_2 m^2 + p_3 m^3 \tag{3.2}$$

$$F(m) = F_S(m) + F_{BG}(m) \tag{3.3}$$

The function $F(m)$ is the one minimized. A sum of two Gaussians is used because g12 encountered run-dependent shifts in the measured mass of the neutron, and these shifts broaden the missing-mass spectrum in such a way that a single Gaussian is no longer an adequate description of the peak. These shifts are described further in Section 3.1.6.

Once the minimization has been performed, as illustrated in the Figure 3.1, we can derive the number of signal events N_S and background events N_{BG} as

$$N_S = \int_{-\infty}^{\infty} F_S(m)dm \tag{3.4}$$

$$N_{BG} = \int_{m_1}^{m_2} F_{BG}(m)dm \tag{3.5}$$

$$\tag{3.6}$$

where m_1 and m_2 represent the limits used later in Section 3.1.6 to select the neutron in missing mass. Then the SBR is simply $\frac{N_S}{N_{BG}}$. Once we've eliminated events we are not interested in, such as events originating outside the experimental target and those with unphysical values of the Mandelstam variable t, we can apply further selections to reduce background beneath the neutron. This background reduction will manifest itself as a higher SBR after the selection is performed. We will also examine the SBR for events *failing* the selection to make sure we are not discarding good-quality events.

3.1.4 Event Vertex and Physical Event Selections

In addition to the double interactions described in Section 3.1.1, event vertices can be badly reconstructed for other reasons. Changes in configuration or equipment failures can cause the beam to veer off-target, producing tracks off the target walls and its support structures. For consistency we restrict our analysis to events that actually originated from the liquid hydrogen contained in the target. As noted in Section 2.3, the g12 target is 40 cm in length, 4 cm in diameter, and was centered 90 cm upstream of the geometric center of CLAS during running. Also important to consider is our tracking resolution; for g12, the vertex resolution is 5 mm in the radial direction and 6 mm in the z direction.

Thus, we require:

- all events have the z position of their common reconstructed vertex on the range $(-110, -70)$ cm,
- all events have their distance $r = \sqrt{x^2 + y^2}$ from the central axis of the target less than 2.5 cm.

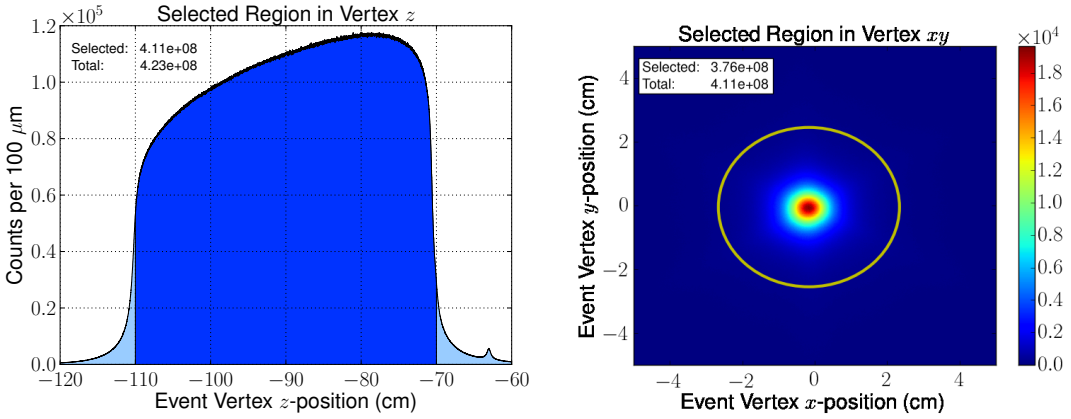

Figure 3.2: The vertex z (**left**) and $x-y$ (**right**) distributions of $\pi^+\pi^+\pi^-$ events. The darkened region is the accepted region in vertex z; events within the yellow circle in vertex $x-y$ are accepted.

We also make a cut to remove events with values of Mandelstam t greater than zero; these events are poorly reconstructed, most likely due to the interaction photon being unmeasured by the tagger.

The consequences of these cuts on vertex-z and vertex-r are shown in Figure 3.2.

3.1.5 Track Timing Selections

As described in Section 3.1.1, we sometimes record events for which the wrong photon is selected. This yields an incorrect value for the event start time, which can lead to measurements of superluminal speeds for tracks in the event. The quantity $\beta = \frac{v}{c}$ is the quantity of interest, where v is the speed of the track and c is the speed of light. We seek to remove events with unphysical values of β, choosing our threshold to incorporate the timing resolution of CLAS.

Many selections on track timing were attempted. The conditions we found to be optimal are as follows:

- $\beta_{\text{TOF}}(\pi_1^+) < 1.04$,
- $\beta_{\text{TOF}}(\pi_2^+) < 1.04$,
- $\delta\beta < 0.03$, where $\delta\beta = |\beta_{\text{TOF}}(\pi_2^+) - \beta_{p/m}(\pi_2^+)|$.

where

- π_1^+ (π_2^+) is the fast (slow) π^+,
- β_{TOF} is the value of β derived solely from time-of-flight measurements,
- and $\beta_{p/m}$ is the value of β derived from the track momentum and the mass hypothesis given to the particle.

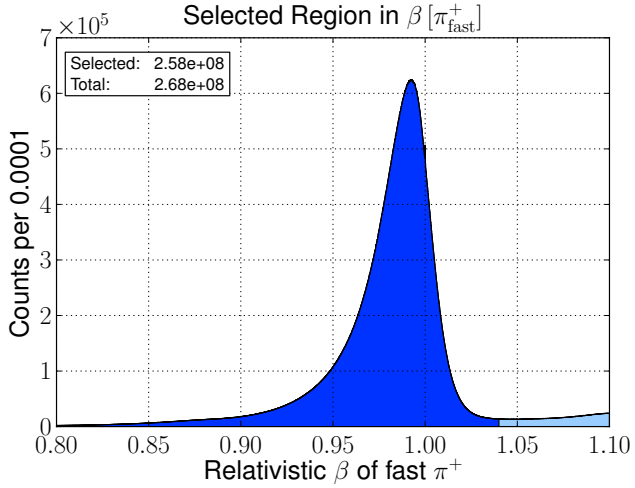

Figure 3.3: The fast π^+ β distribution for all events; the selected region is the darker area.

We accept events with values of β slightly larger than one to allow for the effects of timing resolution; the numerical value 1.04 was chosen by visual inspection of the β distributions. The selected regions for the β cuts are shown in Figures 3.3 and 3.5, with the SBR for events passing and failing these cuts shown in Figures 3.4 and 3.6. The numerical value for the $\delta\beta$ cut was obtained by performing a Gaussian fit around the peak and taking approximately 3σ about the mean; the selected region is shown in Figure 3.7, and the SBR for events passing and failing this cut is shown in Figure 3.8. Events which fail these cuts are typically events where the wrong photon has been selected as the trigger photon. For the plain $\beta_{\rm TOF}$ cuts, superluminal tracks are mostly just tracks that were produced by a photon arriving earlier than the trigger photon, giving them the appearance of arriving at the time-of-flight wall unphysically early. The $\delta\beta$ cut is equivalent to requiring the mass calculated by time-of-flight and momentum of a given track to be close to the physical mass of its hypothesis.

3.1.6 Neutron Selection

As CLAS does not have equipment for efficient neutron reconstruction, we rely on the *missing mass technique* to identify the neutron. The measured quantities in our events are the four-momenta of the three charged tracks (π^+, π^+, and π^-) as well as the energy of the beam photon. Using these quantities and considering our target to be a stationary proton, we can define the following four-vectors (in the (E, p_x, p_y, p_z) convention):

- $p^\mu_\gamma = (E_\gamma, 0, 0, E_\gamma)$ is the four-momentum of the beam photon as measured by the tagger,
- $p^\mu_p = (M_p, 0, 0, 0)$ is the four-momentum of the target proton,

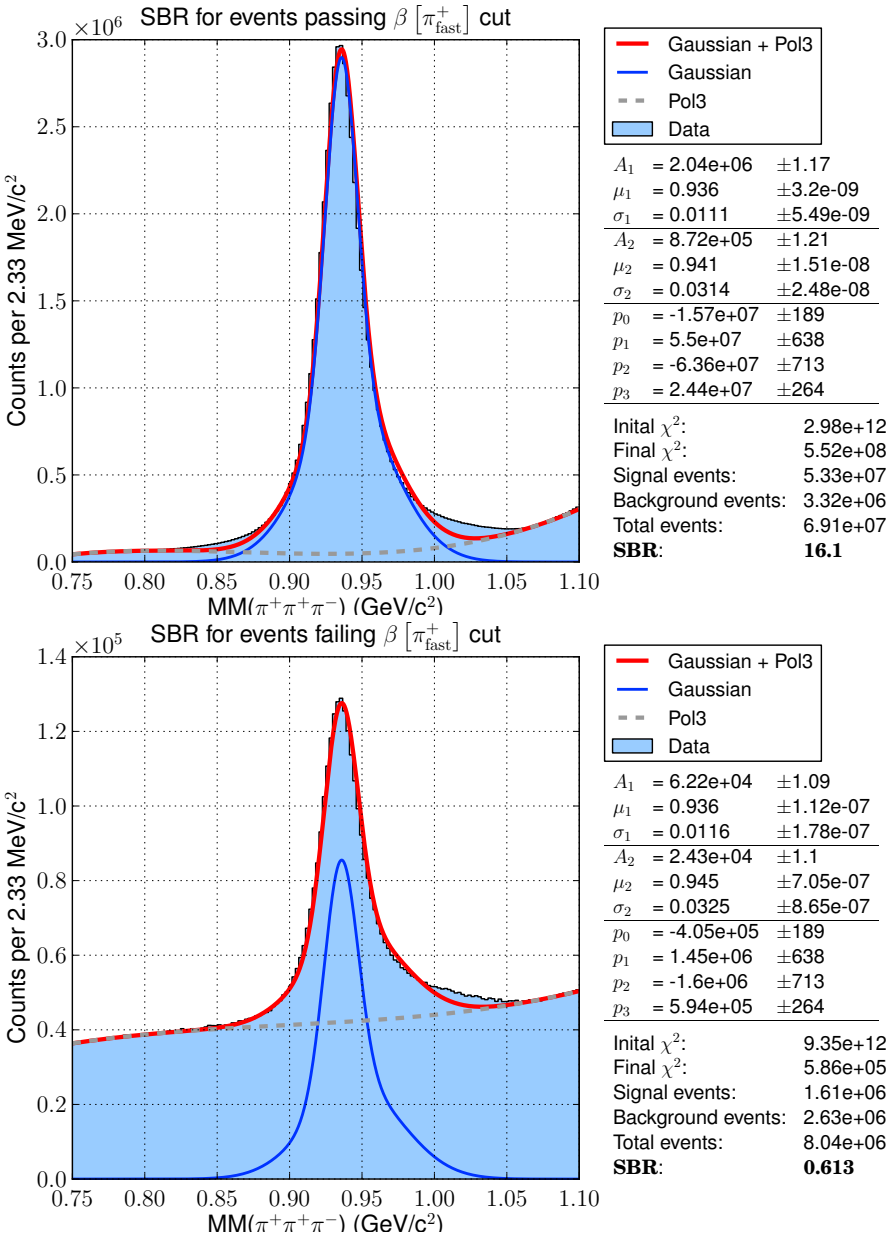

Figure 3.4: **Top:** The SBR measurement for events where the fast π^+ is required to have a physical value β. **Bottom:** SBR measurement for events failing the above cut.

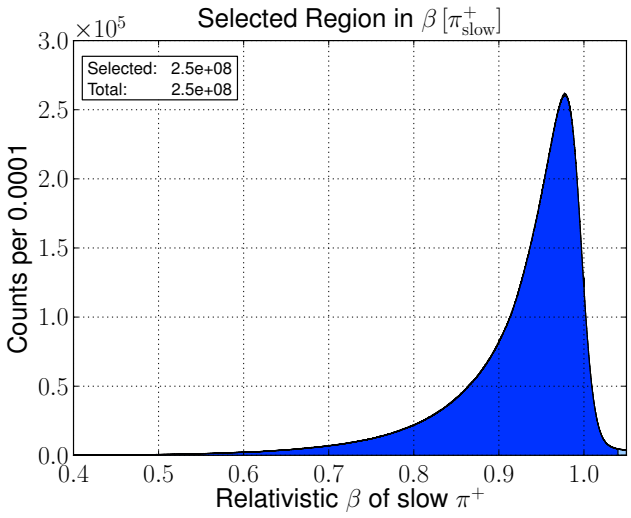

Figure 3.5: The slow π^+ β distribution for all events; only a small fraction of events are removed by this cut (the lighter region above 1.04).

- $p^\mu\left[\pi_1^+\right]$ is the four-momentum of the *fast* π^+,
- $p^\mu\left[\pi_2^+\right]$ is the four-momentum of the *slow* π^+,
- and $p^\mu\left[\pi^-\right]$ is the four-momentum of the π^-.

Using these definitions and the conservation of four-momentum, we can derive a four-momentum of the neutron p_n^μ as:

$$p_n^\mu = p_\gamma^\mu + p_p^\mu - p^\mu\left[\pi_1^+\right] - p^\mu\left[\pi_2^+\right] - p^\mu\left[\pi^-\right] \tag{3.7}$$

The squared mass of the neutron is then just the square of p_n^μ.

The numerical value of the selection we make must take into account the width of the neutron after all timing and vertex cuts have been applied. The neutron is a stable particle on the scale of the strong interaction, and thus its distribution ought to be a δ-function at 939 MeV. However the energy resolution of the tagger and the momentum resolution of the drift chambers each make a contribution to the neutron's non-zero width.

In addition, the measured value of the neutron mass is not constant over the duration of the g12 running period, as shown in Figure 3.9. The effect of the `eloss` correction, described in Section 3.1.2, is obvious, as the correct allocates more momenta to the measured tracks, leaving less available to the missing particle. The corrected mass is systematically low, indicating an underestimation of the photon beam energy of a few MeV. However, this inaccuracy in the neutron mass will not negatively affect our results, as the PWA procedure depends only on the pion momenta.

The resulting missing-mass spectrum after timing and vertex cuts is fit with the model in Equation 3.3, and the results are shown in Figure 3.9. We would like to subject a large sample of events to our PWA, as this will increase our sensitivity to weakly-produced states, which we expect the $\pi_1(1600)$ to be. Also, as we discuss in Section 5.3.9, the incidental background events around and beneath the neutron do not seriously threaten the validity of our fit results. The dual-Gaussian fit to the neutron peak in the missing mass spectrum

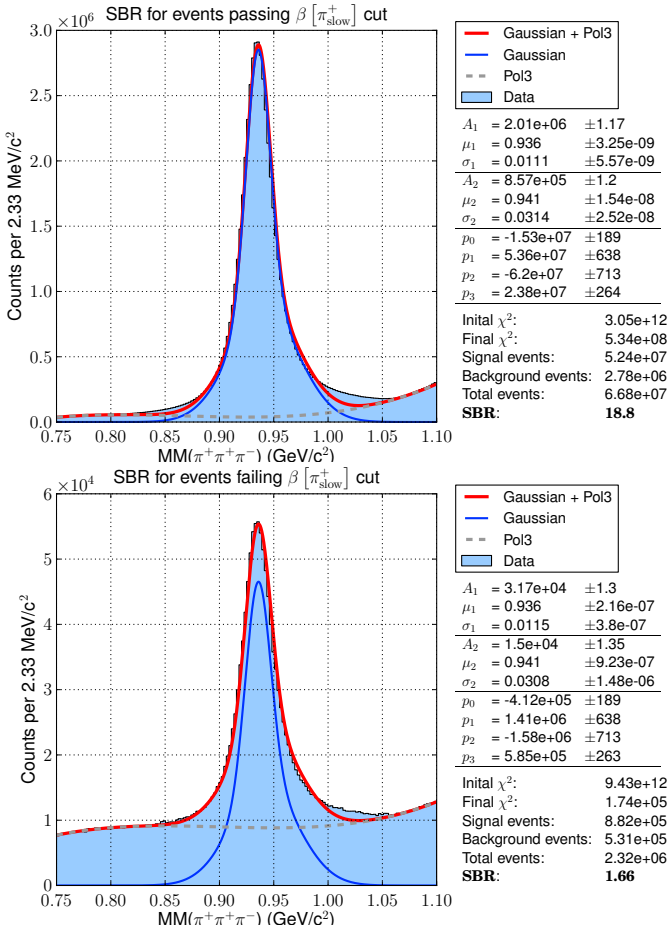

Figure 3.6: **Top:** The SBR measurement for events where the slow π^+ is required to have a physical value β. **Bottom:** SBR measurement for events failing the above cut.

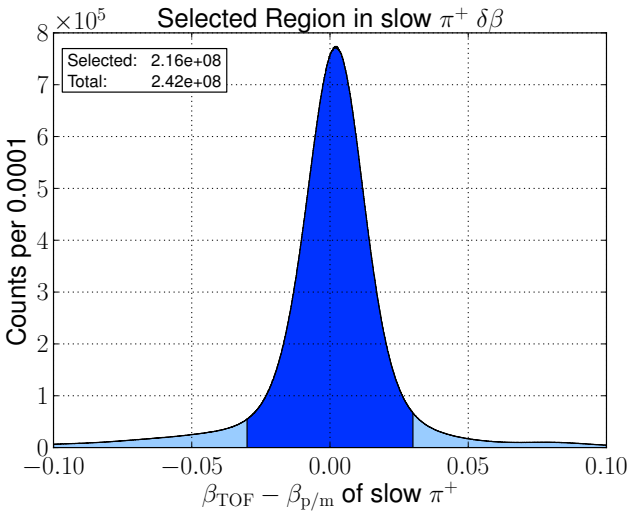

Figure 3.7: The $\delta\beta$ distribution for the slow π^+; the selected region is darkened.

shown in Figure 3.9 yields values of 11.1 and 31.6 MeV for the two σ parameters in the fit. Taking the mean of these two, weighted by the amplitude A_1 and A_2 of their respective Gaussians, we obtain a value for $\bar{\sigma}$ of 17.3 MeV. Taking an interval of about seven $\bar{\sigma}$ about the weighted mean of μ_1 and μ_2, $\bar{\mu} = 937.5$ MeV, we select events with missing mass on the range (820, 1060) MeV.

Event counts before and after the selections detailed in Sections 3.1.4 and 3.1.5, as well as the missing mass cut described in this Section, are tabulated in Table 3.1.

3.1.7 Features of the Exclusive $\gamma p \to \pi^+\pi^+\pi^- n$ Sample

Now with a purified sample of exclusive $\gamma p \to \pi^+\pi^+\pi^- n$ events, we can examine some quantities of interest to get a feel for the production processes at work. The most important distribution to examine is the invariant mass of $\pi^+\pi^+\pi^-$, as it is the spectrum which we will eventually be decomposing into partial waves. It is shown in Figure 3.10. The most prominent feature is the peak at 1.3 GeV; we will show in the following sections that this corresponds to the production of the $a_2(1320)$ meson. Also visible is a slight shoulder closer to 1.6 GeV, which we will show corresponds to $\pi_2(1670)$ production.

These features sit atop a large background, much of it due to excitations of the nucleon. s-channel processes could produce a baryon state which decays sequentially to $\pi^+\pi^+\pi^- n$. Also, $N\pi$ and $N\pi\pi$ resonances produced via t-channel processes are possible as well.

Starting with the $n\pi\pi$ states, as shown in Figures 3.11, 3.12, and 3.13, we can immediately see several features. In the $n\pi_1^+\pi^-$ mass (Figure 3.11), where π_1^+ is the fast π^+, a small peak is visible at about 1.7 GeV, and a shoulder at about 2.4 GeV. Examining the accompanying two-dimensional plots in Figure 3.14, one can see a definite correlation between the peak at 1.7 GeV and the production of a Δ^-, suggesting that the state at 1.7 GeV has a substantial decay through $\Delta(1232)\pi$. The $\pi_1^+\pi^-$ invariant mass, when plotted against the $n\pi_1^+\pi^-$ invariant mass, as in Figure 3.16, shows little evidence for a correlation of the peak

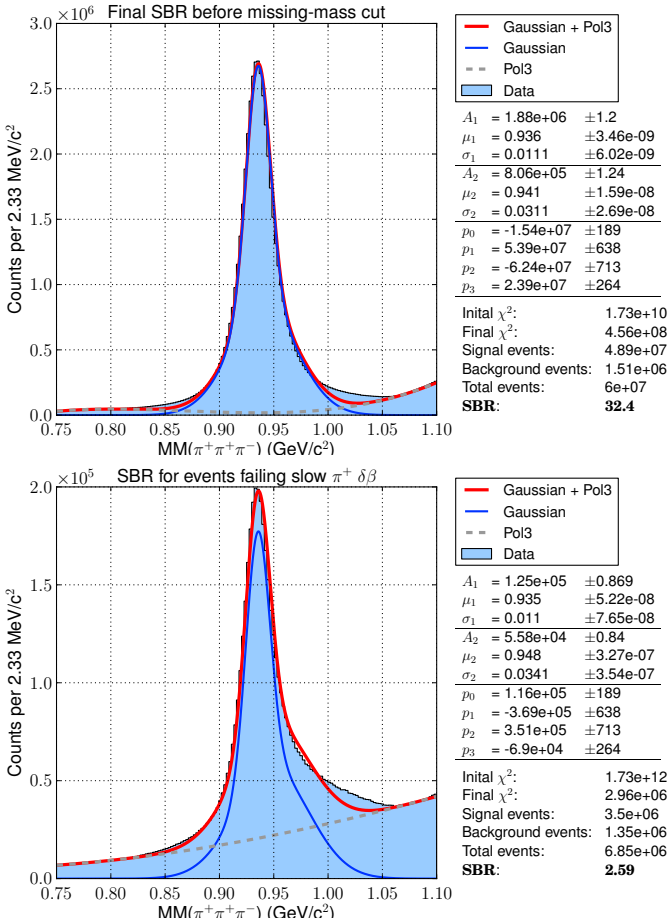

Figure 3.8: **Top:** The SBR measurement for events with good agreement between the two methods of measuring β. This measurement is the final signal-to-background ratio before we select the neutron in missing mass. **Bottom:** SBR measurement for events failing the above cut.

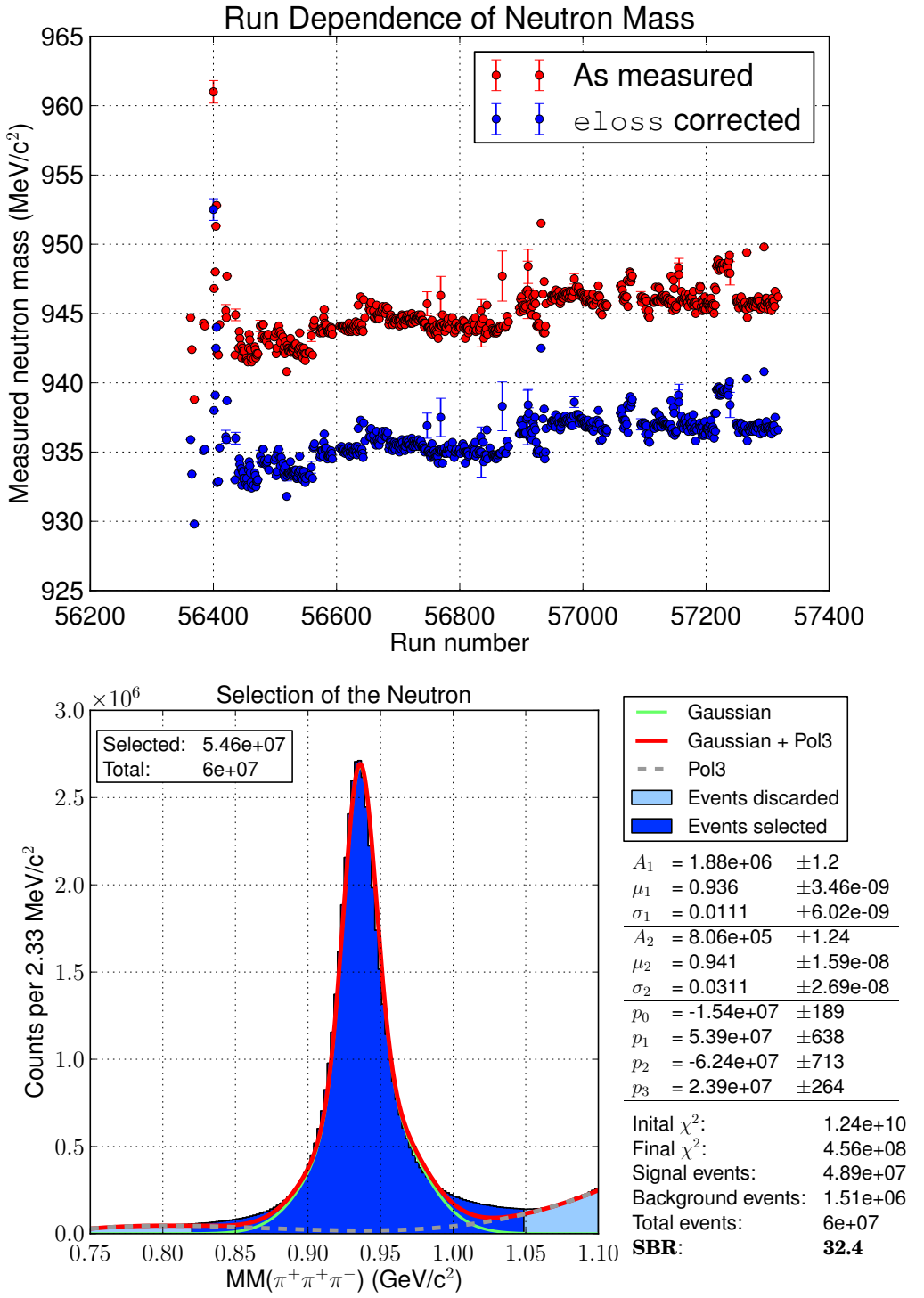

Figure 3.9: **Top**, an illustration of the neutron's run-dependent mass. The mass was determined by fits of a single Gaussian plus a third-order polynomial background, and the mean of the Gaussian along with the error in its determination according to the fit are plotted. **Bottom**, the selection of the neutron via missing mass.

Description	**Interval**	**Events In**	**Events Selected**
Vertex within z-extent of target	$-110 < z < -70$ cm	423,391,193	410,834,658
Vertex within target radius	$r < 2.5$ mm	410,834,658	318,534,046
t less than 0	$t < 0$ GeV^2	318,534,046	294,175,780
Physical fast π^+ β	$0 < \beta < 1.04$	294,175,780	258,818,984
Physical slow π^+ β	$0 < \beta < 1.04$	258,818,984	249,856,422
Small slow π^+ $\delta\beta$	$\lvert\beta_{TOF} - \beta_{p/m}\rvert < 0.03$	249,856,422	216,150,344
Missing mass consistent with neutron	$0.82 <$ MM < 1.06 GeV	216,150,344	55,335,182

Table 3.1: Table with the event counts before and after each of the cuts used to select our exclusive $\gamma p \to \pi^+\pi^+\pi^- n$ event sample.

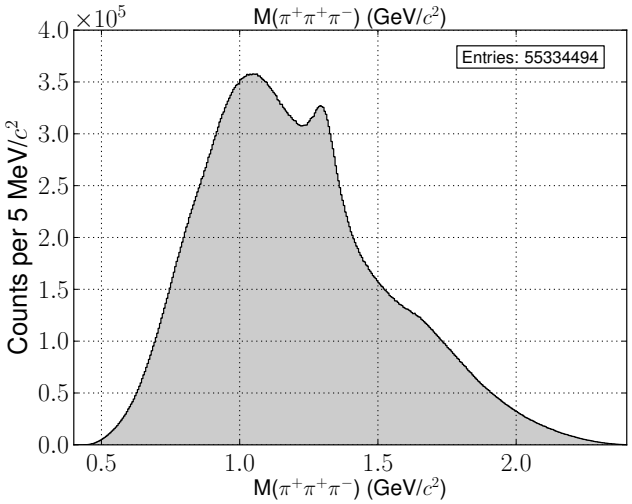

Figure 3.10: The $\pi^+\pi^+\pi^-$ invariant mass spectrum for exclusive $\gamma p \to \pi^+\pi^+\pi^- n$ events.

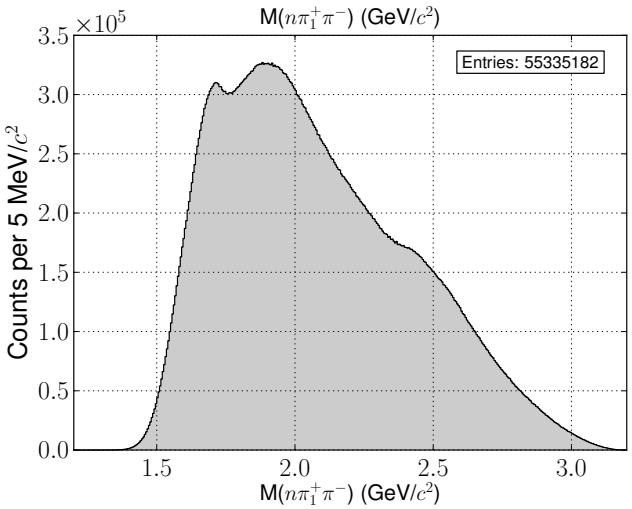

Figure 3.11: The $n\pi_1^+\pi^-$ invariant mass spectrum for exclusive $\gamma p \to \pi^+\pi^+\pi^-n$ events, where π_1^+ is the faster of the two π^+.

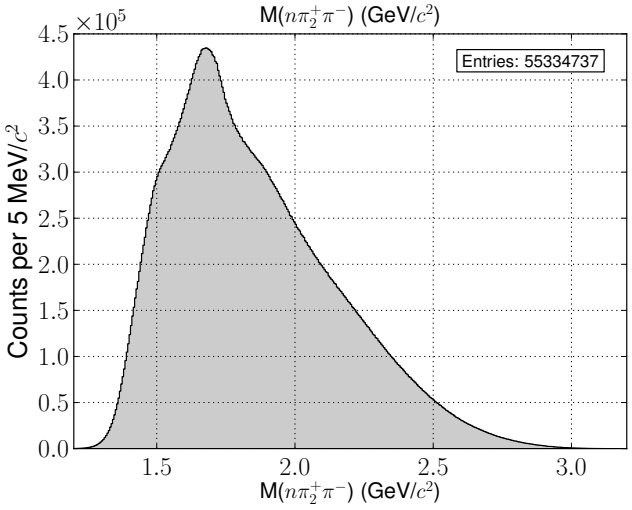

Figure 3.12: The $n\pi_2^+\pi^-$ invariant mass spectrum for exclusive $\gamma p \to \pi^+\pi^+\pi^-n$ events, where π_2^+ is the slower of the two π^+.

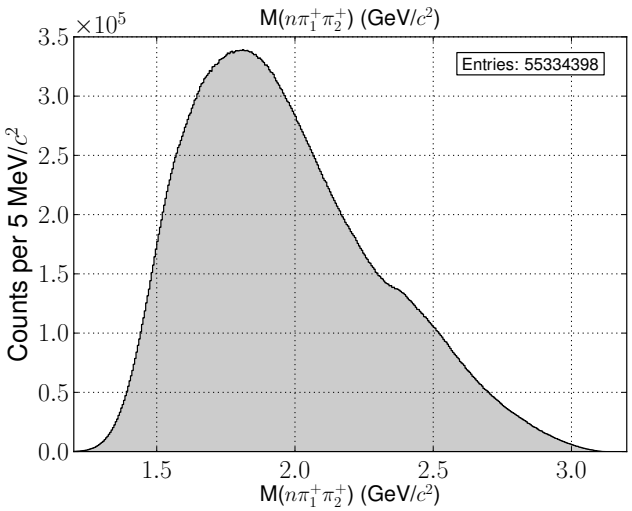

Figure 3.13: The $n\pi^+\pi^+$ invariant mass spectrum for exclusive $\gamma p \to \pi^+\pi^+\pi^- n$ events.

at 1.7 GeV with production of the ρ meson at 0.77 GeV.

Switching to the $n\pi_2^+\pi^-$ system (shown in Figure 3.12), where π_2^+ is the slow π^+, the peak at 1.7 GeV becomes the most prominent feature, and the shoulder at 2.4 GeV disappears. The $n\pi$ correlations in Figure 3.15 show plenty of ground-state Δ production, but most of it away from the 1.7 GeV region in $n\pi_2^+\pi^-$. When plotted against the $\pi_2^+\pi^-$ invariant mass (Figure 3.17), there is again little evidence for $n\rho$ decays.

Finally, in the $n\pi^+\pi^+$ distribution in Figure 3.13, we see an inflection close to 2.4 GeV, similar to what we seen in the $n\pi_1^+\pi^-$ invariant mass. This could be due to the well-known $\Delta(2420)$ $H_3, 11$ resonance.

Turning now to the single-pion baryon decays, the invariant mass spectrum of $n\pi_1^+$ is shown in Figure 3.19 along with its correlations versus the invariant mass of $\pi_2^+\pi^-$; visible are a peak at 1.5 GeV, and a shoulder at 1.7 GeV. Examining the $\pi_2^+\pi^-$ combination recoiling off of the $n\pi_1^+$ system, we see some evidence for the ρ meson produced simultaneously with the $n\pi^+$ enhancement at 1.5 GeV. Also visible at 500 MeV along the y-axis are features consistent with the presence of a small fraction of $\gamma p \to \Sigma^+ K_S$ events in our sample. These are well-reconstructed $\gamma p \to \pi^+\pi^+\pi^- n$ events, as the $\Sigma(1189)$ decays via $n\pi$ and the K_S decays to $\pi^+\pi^-$. The $n\pi_2^+$ distribution in Figure 3.20 has a prominent peak at 1.2 GeV, made up of both the $\Delta(1232)$ and the $\Sigma(1189)$, along with points of inflection at 1.5 and 1.7 GeV, possibly corresponding to features similarly located in the $n\pi_1^+$ invariant mass. The peak at 1.2 GeV is strongly correlated with both the $\rho(770)$ and the K_S in the complementary $\pi_1^+\pi^-$ system. The $n\pi^-$ distribution in Figure 3.18 is dominated by the Δ^-, already shown to be a likely isobar for $n\pi\pi$ states discussed above. As no isospin-2 mesons are known, the correlation of the $n\pi^-$ with the $\pi^+\pi^+$ combination shows no structure.

In summary, in terms of excited baryon production, we see evidence for resonance production in at least two mass regimes, around 1.5 GeV as well as 1.7 GeV. We also see a shoulder at 2.4 GeV in two $n\pi\pi$ invariant mass distributions which cannot be explained in

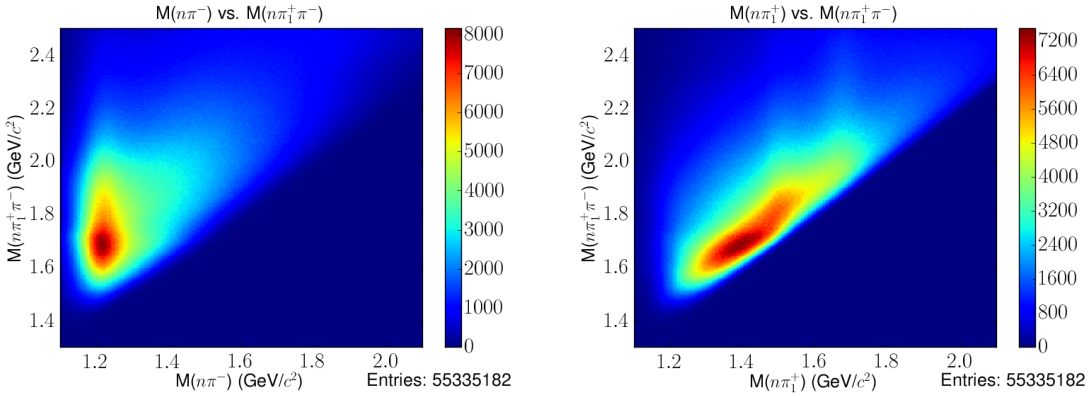

Figure 3.14: **Left**, the correlations between the $n\pi^-$ invariant mass and the $n\pi_1^+\pi^-$ invariant mass, where π_1^+ is the fast π^+. **Right**, the correlations between the $n\pi_1^+$ invariant mass and the $n\pi_1^+\pi^-$ invariant mass.

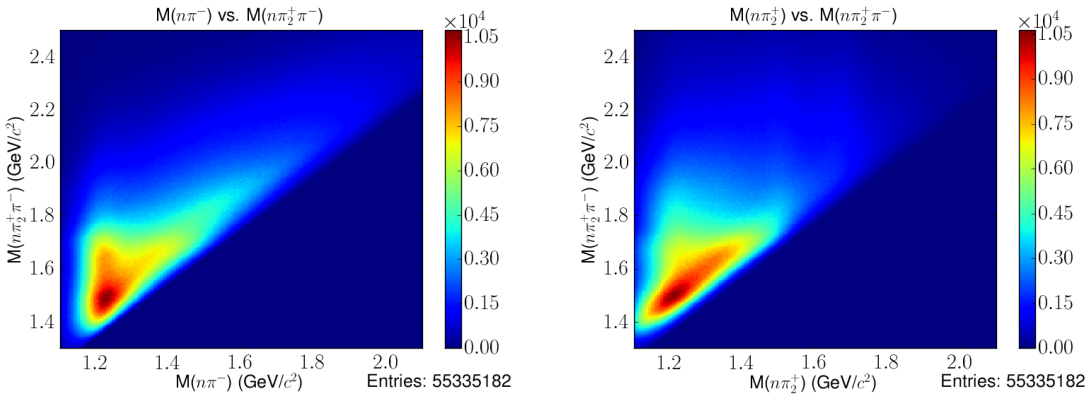

Figure 3.15: **Left**, the correlations between the $n\pi^-$ invariant mass and the $n\pi_2^+\pi^-$ invariant mass, where π_2^+ is the slow π^+. **Right**, the correlations between the $n\pi_2^+$ invariant mass and the $n\pi_2^+\pi^-$ invariant mass.

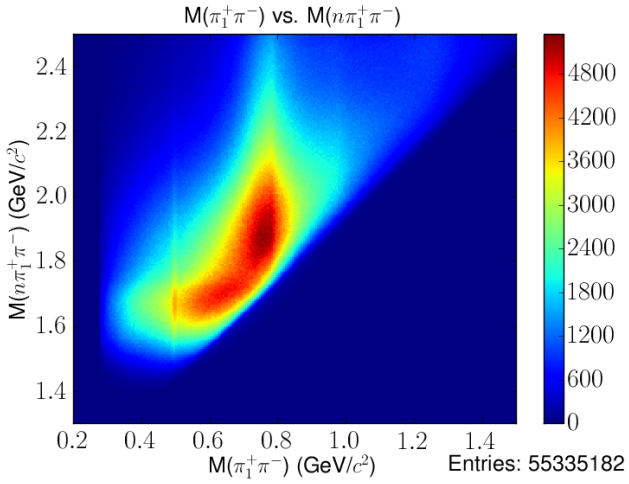

Figure 3.16: The correlations between the $\pi_1^+\pi^-$ invariant mass and the $n\pi_1^+\pi^-$ invariant mass, where π_1^+ is the fast π^+.

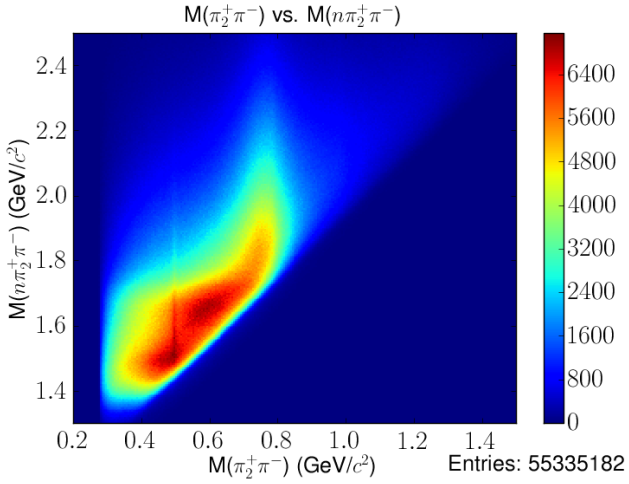

Figure 3.17: The correlations between the $\pi_2^+\pi^-$ invariant mass and the $n\pi_2^+\pi^-$ invariant mass, where π_2^+ is the slow π^+. The narrow stripe at 05 GeV is due to K_S production from $\gamma p \to \Sigma^+ K^0$ events.

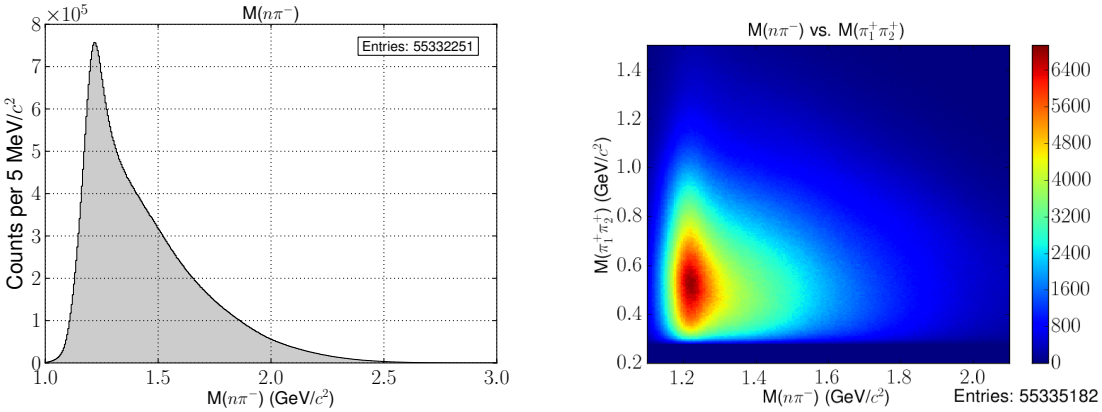

Figure 3.18: **Left**, the $n\pi^-$ invariant mass spectrum for exclusive $\gamma p \to \pi^+\pi^+\pi^-n$ events, showing a clear peak for the $\Delta(1232)$. **Right**, the correlations between the $n\pi^-$ system and the $\pi^+\pi^+$ system.

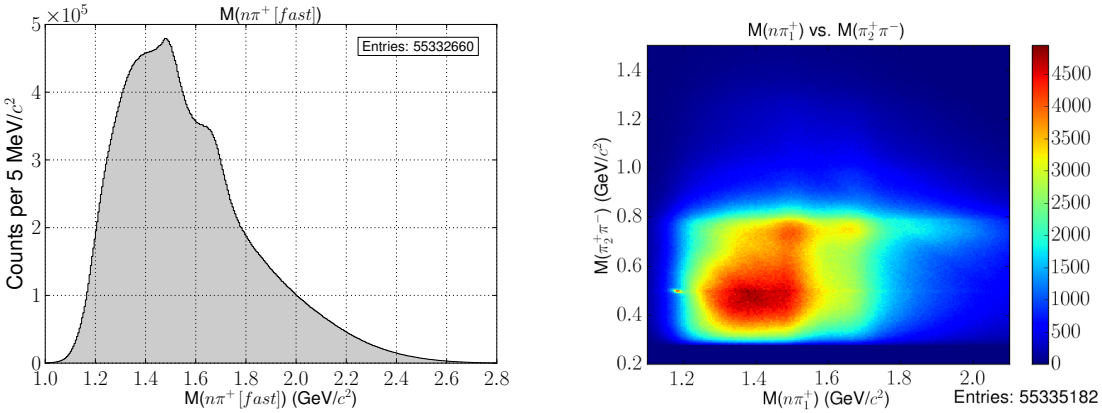

Figure 3.19: **Left**, the $n\pi_1^+$ invariant mass spectrum for exclusive $\gamma p \to \pi^+\pi^+\pi^-n$ events, where π_1^+ is the faster of the two π^+. **Right**, the correlations between the $n\pi_1^+$ system and the $\pi_2^+\pi^-$ system. The tiny enhancement just below 1.2 GeV in $n\pi_1^+$ invariant mass is due to $\gamma p \to \Sigma^+ K^0$ events.

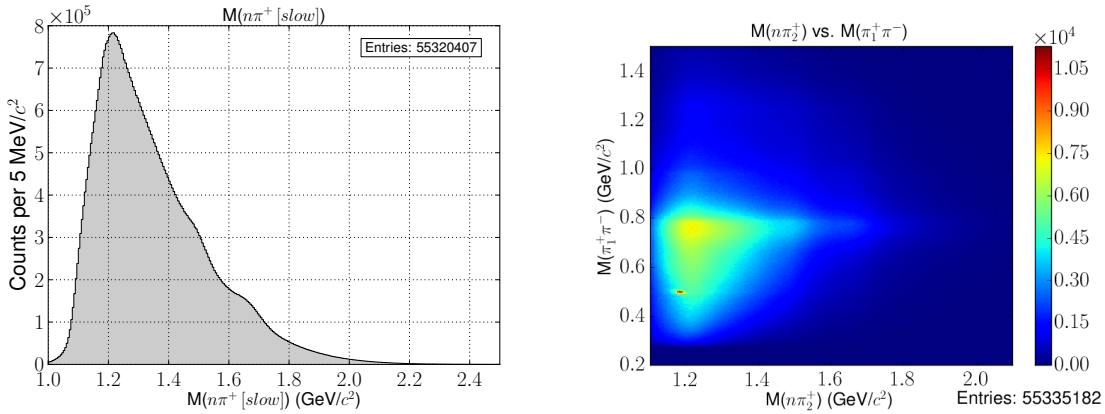

Figure 3.20: **Left**, the $n\pi_2^+$ invariant mass spectrum for exclusive $\gamma p \to \pi^+\pi^+\pi^-n$ events, where π_2^+ is the slower of the two π^+. **Right**, the correlations between the $n\pi_2^+$ system and the $\pi_2^+\pi^-$ system. The tiny enhancement just below 1.2 GeV in $n\pi_2^+$ invariant mass is due to $\gamma p \to \Sigma^+ K^0$ events.

terms of known baryon resonances. Known states decaying to $N\pi$ around 1.5 GeV include the $N(1520)$ D_{13} and $N(1535)$ S_{11}; both are probably present in comparable numbers, as their branching fractions to $N\pi$ are similar. At 1.7 GeV, the known baryon spectrum is a bit more crowded. The lack of evidence for ρ production in correlation with the state at 1.7 GeV makes the $\Delta(1700)$ D_{33} unlikely to be present. As for excitations of the nucleon, six known states are close by in mass, namely the $N(1650)$ S_{11}, $N(1675)$ D_{15}, $N(1680)F_{15}$, $N(1700)D_{13}$, $N(1710)$ P_{11}, and $N(1720)P_{13}$. The S_{11} prefers to decay to $N\pi$, so it cannot alone explain the significant peak at 1.7 GeV. The D_{15} is a good candidate, as it has significant branching fractions to $N\pi$ and $\Delta\pi$. A combination of F_{15} and D_{13} could result in the distributions we see, as the F_{15} decays primarily via $N\pi$, and the D_{13} primarily to $\Delta\pi$. Finally, the P_{11} and P_{13} are outside candidates; the P_{11} has at best has a combined $\Delta\pi$-$N\pi$ branching fraction of 0.6, and the P_{13} primarily decays to $N\rho$, which we see little evidence for.

Of course, to definitively determine the identities of these features, we need to perform a PWA. We are interested in performing a PWA on these data, or at least a subset of it; however, we are interested in the meson states. This copious production of various $n\pi$ and $n\pi\pi$ resonances demands that we either incorporate these states into our PWA, or apply selections to remove them. For the purposes of our analysis, we find it most expedient to refine our sample to exclude the conditions under which these $n\pi$ and $n\pi\pi$ states are produced. This allows us to employ a simpler, better-understood PWA which can be directly compared to the pion production results motivating our search. Thus the next section will be dedicated to the discussion of our selection criteria for the reduction of baryon background.

3.2 Reduction of Baryon Background

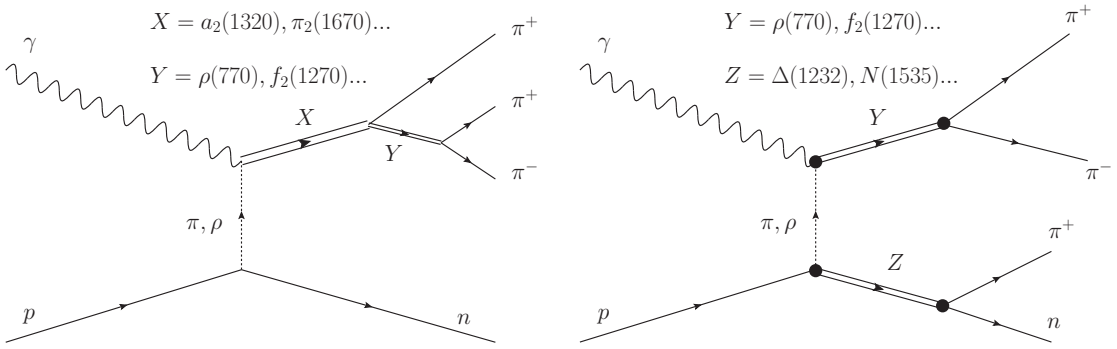

Figure 3.21: Two processes which exist in our exclusive $\gamma p \to \pi^+\pi^+\pi^-n$ event sample. On the left, the three pions come from the decay of a meson resonance. On the right, one π^+ resonates with the nucleon while the other π^+ resonates with the π^- in a ρ meson.

As discussed in Chapter 2, CLAS was designed primarily as a tool for baryon spectroscopy. Thus, its acceptance is optimized for the wide-angle decays of s-channel baryon resonances, rather than the forward-angle decays of t-channel meson resonances. The configuration of CLAS for the g12 run was optimized in some ways to improve angular acceptance for events at forward angles, mostly through the upstream placement of the target (as mentioned in Section 2.3), but a significant proportion of baryon background remains in our exclusive $\gamma p \to \pi^+\pi^+\pi^-n$ sample. These are events where the three-pion system is produced through alternate mechanisms, shown in Figure 3.21.

$$\gamma p \to B^{**}\pi \to B^{*}\pi\pi \to n\pi^+\pi^+\pi^- \tag{3.8}$$

$$\gamma p \to B^{*}\rho \to n\pi^+\pi^+\pi^- \tag{3.9}$$

where B^{**} and B^{*} in this context simply represent excited states of the nucleon or of the Δ baryon. These events are troublesome because they introduce correlations into the angular distributions that we use to perform our PWA. If our PWA interprets such events as originating from a meson decaying to three pions, our fit results will be corrupted to the degree that the baryon background competes with our mesonic events of interest.

The $n\pi$ and $n\pi\pi$ invariant masses, shown previously in Section 3.1.7, demonstrate the presence of these events in our sample. They indeed exist in significant numbers, which leaves us with two alternatives in our approach. The first alternative is to attempt to reduce the proportion of these events in our sample by studying the production mechanisms and kinematics of the baryon background, and isolate one or more quantities that we can cut on to remove these events from our sample. The second is to attempt to account for baryon resonance production alongside the meson production by adding amplitudes for baryon resonance production to our set of possible partial waves. The former is the simpler of the two paths; ideally it results in a pure meson sample which we can treat in the

helicity formalism with relatively small wavesets. But, our cuts may introduce systematic dependencies into the remaining events which affect the reliability of our results. Including baryon resonance production in the PWA gives a complete description of the exclusive $\gamma p \to \pi^+\pi^+\pi^- n$ sample, the statistical power is improved, and there is no risk of systematic dependencies from event selection. However, using the helicity formalism to describe the baryon decays would be difficult at best, as the rest frames for calculating decay amplitudes would not be well-defined between the different production processes. We could abandon the helicity formalism for another spin formalism, but we would lose our ability to directly compare with past results in pion production. Also, except for perhaps the a_2, the baryon states would likely dominate over the meson states, and the reliability of measuring what we expect to be a small signal in such an environment would be suspect. Furthermore, large wavesets would be required to describe all meson and baryon processes present, further inhibiting the stability and reproducibility of our results, and thus contributing to a different source of systematic errors. Taking all of this into account, we choose to proceed with a reduction of the baryon background by introduction of additional kinematic constraints on our data sample. The $n\pi$ and $n\pi\pi$ invariant mass distributions will inform us of the efficacy of any cuts we perform, and we can pin down any systematic errors introduced by examining the change in our fit results as these cuts are varied.

Thus in this Section, we discuss several conditions in addition to the criteria of Section 3.1 that we have found reduce the proportion of resonant baryon events in our sample while maintaining control over systematic uncertainties.

3.2.1 Incident Photon Energy

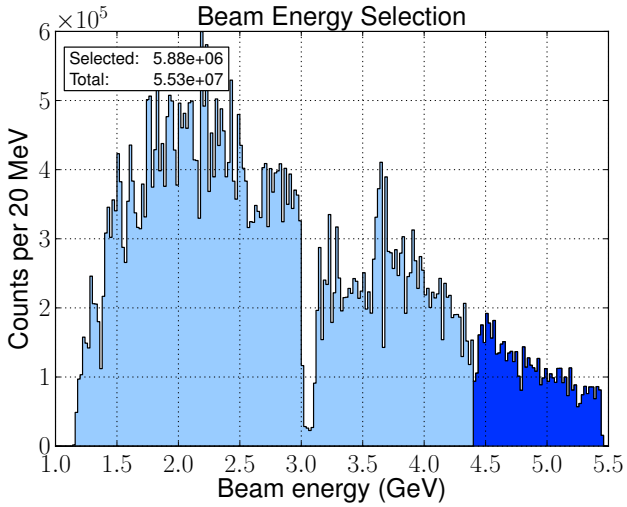

Figure 3.22: The beam energy spectrum for exclusive $\gamma p \to \pi^+\pi^+\pi^- n$ events, with the selected region highlighted (dark blue). The notch at 3 GeV is due to a tagger t-counter with a malfunctioning phototube that was not accounted for in the reconstruction.

The first cut we employ to reduce our baryon background is the enforcement of a minimum energy for the trigger photon. Requiring high-energy photons enhances the population of events with 3π invariant masses in the region of 1 to 2 GeV while simultaneously taking us to an energy regime where any s-channel processes are safely suppressed.

The actual value of the selection is taken from our experimental configuration. The design of the Hall B tagger, wherein the first 19 t-counters are of a different geometry than the remaining 42, introduces a natural separation point between the high- and low-energy parts of the tagger's focal plane. In fact, the trigger configurations described in Section 2.5 include the first 19 counters of the tagger as part of the trigger logic to boost our yields of events with high-energy photons. For the configuration of CEBAF during the g12 run, t-counter 19 measured electrons producing 4.4 GeV bremsstrahlung photons, so we require that the trigger photon for each event in our sample have an energy greater than 4.4 GeV. This translates to a minimum of $\sqrt{s}$ of approximately 3 GeV, comfortably above the regime of s-channel baryon production.

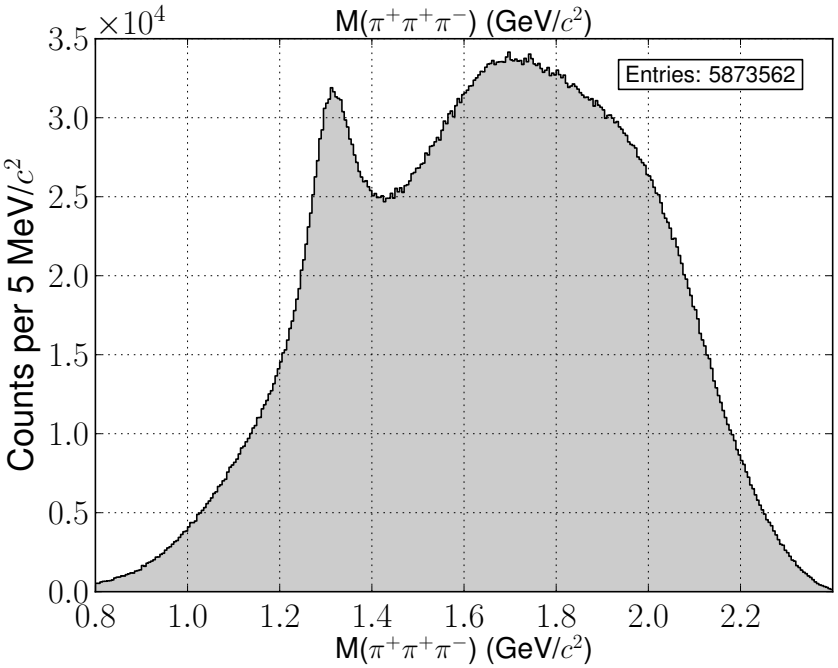

Figure 3.23: The $\pi^+\pi^+\pi^-$ invariant mass distribution for events with beam photon energy above 4.4 GeV.

The 3π invariant mass after this cut is shown in Figure 3.23. The peak at 1.3 GeV is more prominent, while events with 3π mass less than 1.3 GeV have been largely removed. The shoulder at 1.6 GeV in Figure 3.10 has been replaced with a large and broad peak, now closer to 1.7 GeV. We will show evidence in Section 3.3 indicating that the peak at 1.3 is the $a_2(1320)$, and the shoulder at 1.7 GeV has as a major component the $\pi_2(1670)$.

To determine the number of baryon background events still present in the spectrum of

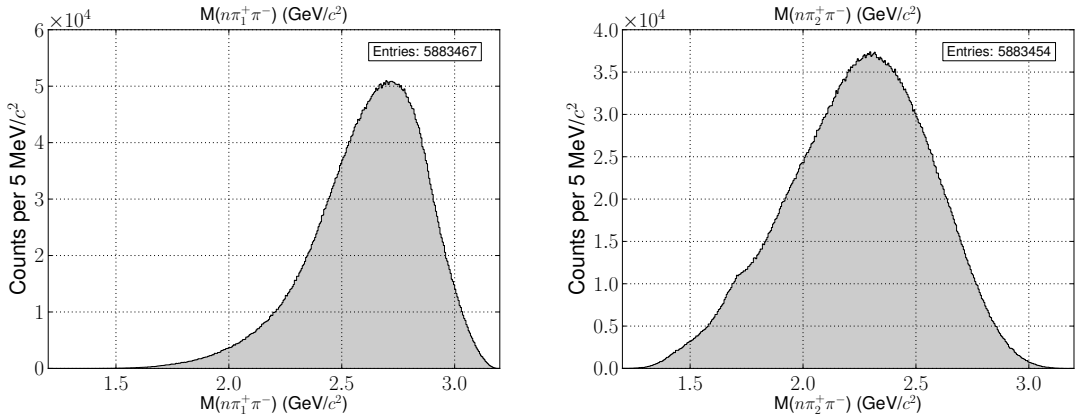

Figure 3.24: The $n\pi_1^+\pi^-$ (**left**) and $n\pi_2^+\pi^-$ (**right**) invariant mass distributions for events with beam photon energy above 4.4 GeV.

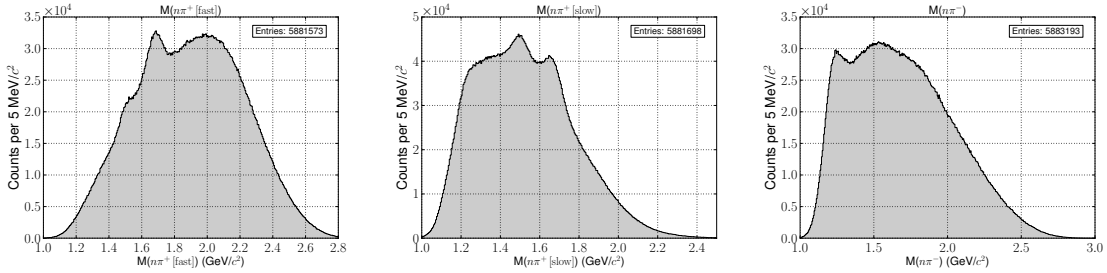

Figure 3.25: The $n\pi_1^+$ (**left**), $n\pi_2^+$ (**center**), and $n\pi^-$ (**right**) invariant mass distributions for events with beam photon energy above 4.4 GeV.

Figure 3.23, we re-examine the $n\pi$ and $n\pi\pi$ invariant masses after the cut. The peaks in the $n\pi\pi$ invariant masses, shown in Figure 3.24, have largely been eliminated. As for the $n\pi$ invariant masses, shown in Figure 3.25, the Δ^- peak has been substantially reduced in the $n\pi^-$ spectrum, consistent with elimination of the $N\pi\pi$ states decaying via $\Delta\pi$. The $n\pi^+$ spectra still show troublesome peaks at 1.5 and 1.7 GeV. Examining their correlations with their complementary $\pi^+\pi^-$ combinations in Figure 3.26, one can see definite evidence of $B^*\rho$ and $B^*f_2(1270)$ production remaining in the event sample; however, most of the Σ^+K_S events have been removed. Looking at their correlations to the 3π invariant mass, as shown in Figure 3.27, one can clearly see the tendency of the peaks in the $n\pi$ mass spectrum to populate the 1.6-2.0 GeV region of the 3π mass spectrum.

Thus, while a cut in beam energy all but eliminated background contributions from $N\pi\pi$ resonances, a significant contribution from $B^*\rho$ and $B^*f_2(1270)$ remains.

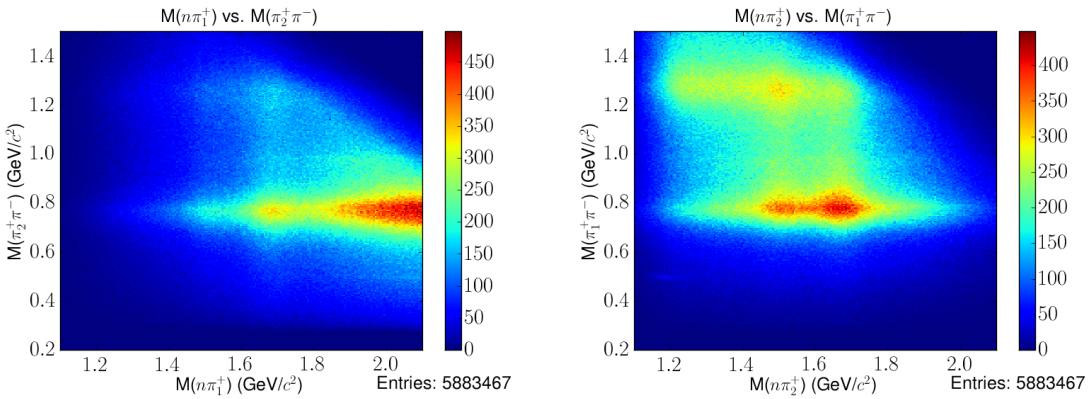

Figure 3.26: The $n\pi_1^+$ correlations with the $\pi_2^+\pi^-$ (**left**), and the $n\pi_2^+$ correlations with the $\pi_1^+\pi^-$ (**right**), all for events with beam photon energy above 4.4 GeV.

3.2.2 Kinematic Cuts

In order to attack these single-pion baryon decays, we will use two kinematic cuts. The first depends on the momentum transfer between the beam and the recoiling nucleon, quantified by the Mandelstam variable t. The Mandelstam variables s, t, and u are defined as:

$$s = (p_\gamma^\mu + p_p^\mu)^2 = (p_X^\mu + p_n^\mu)^2 \tag{3.10}$$

$$t = (p_\gamma^\mu - p_X^\mu)^2 = (p_p^\mu - p_n^\mu)^2 \tag{3.11}$$

$$u = (p_\gamma^\mu - p_n^\mu)^2 = (p_p^\mu - p_X^\mu)^2 \tag{3.12}$$

where

- p_γ^μ is the 4-momentum of the beam photon,
- p_p^μ is the 4-momentum of the target proton,
- p_X^μ is the 4-momentum of X, the 3π resonance,
- and p_n^μ is the 4-momentum of the neutron.

t quantifies the exchanged momentum between the beam and the recoiling nucleon. Meson resonance production occurs primarily when the beam photon interacts not directly with the nucleon, but rather with the cloud of virtual mesons surrounding it. Such a process transfers very little momentum to the nucleon. Additionally, the more momentum transferred to the nucleon, the greater the chance that some of that transferred momentum will go into the excitation of the nucleon. Thus we want to limit our event sample to events in which most of the beam momentum remains with the 3π system.

Before we make this cut, it is important to examine the exponential *slope* of the t distribution, as it can give insight into the particular production mechanisms at work. The

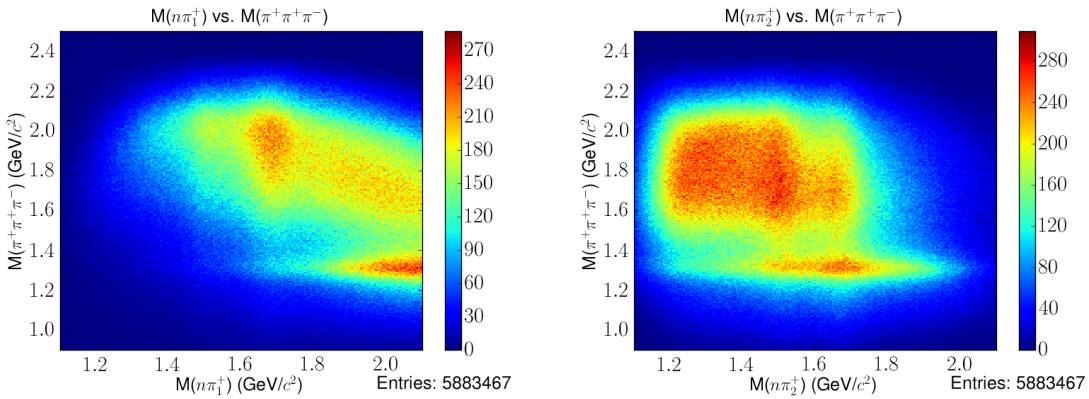

Figure 3.27: The $n\pi_1^+$ (**left**) and $n\pi_2^+$ (**right**) correlations with the $\pi^+\pi^+\pi^-$ invariant mass, all for events with beam photon energy above 4.4 GeV.

slope of the t-distribution in the neighborhood of the $a_2(1320)$, as shown in Figure 3.30, is consistent with production via π exchange. Studying the t-distribution for the higher-mass region, also shown in Figure 3.30, near the mass of the $\pi_2(1670)$, one sees that the slope is much gentler, indicative of the large proportion of baryon background events still in our sample after the beam energy cut.

In place of the Mandelstam variable t we use t', defined as:

$$t' = t - t_0 \tag{3.13}$$

$$t_0 = \left[\frac{m_n^2 - m_X^2 - m_p^2}{2\sqrt{s}}\right]^2 - (p_\gamma^{CM} - p_X^{CM})^2 \tag{3.14}$$

$|t_0|$ defines the *minimum momentum transfer required* to produce a resonance of mass m_X with momentum in the overall center-of-mass frame p_X^{CM}, given the center-of-mass photon momentum p_γ^{CM} and target and recoil nucleon masses m_p and m_n. The plots in Figure 3.28 illustrate this effect; in the t versus m_X distribution, one can see the upward trend in t as we go to higher masses. Applying a selection on plain t amounts to a sliding mass cut, where higher 3π masses are increasingly suppressed. We want to retain those higher-mass events, as the $\pi_1(1600)$ occupies the upper half of our mass range.

Examining the $n\pi^+$ invariant masses shown in Figure 3.29, one can see the bands corresponding to the excited nucleon resonances at 1.5 and 1.7 GeV. Their strength seems to increase as the values in t' approach 0, but a significant proportion of these events can still be eliminated by a cut in low-$|t'|$. Furthermore, examining the three-pion invariant mass versus t' in Figure 3.28, one can see that most events are at low-$|t'|$ anyway, especially those due to $a_2(1320)$ production.

To determine the effectiveness of limiting t' in reducing our background, we examine the $n\pi$ invariant mass distributions over a range of cuts in t'. The result, shown in Figure 3.31, is that at no value of t' are the peaks at 1.5 and 1.7 GeV completely gone, even at the lowest value, which approaches the limit of our experimental acceptance. Thus we cannot

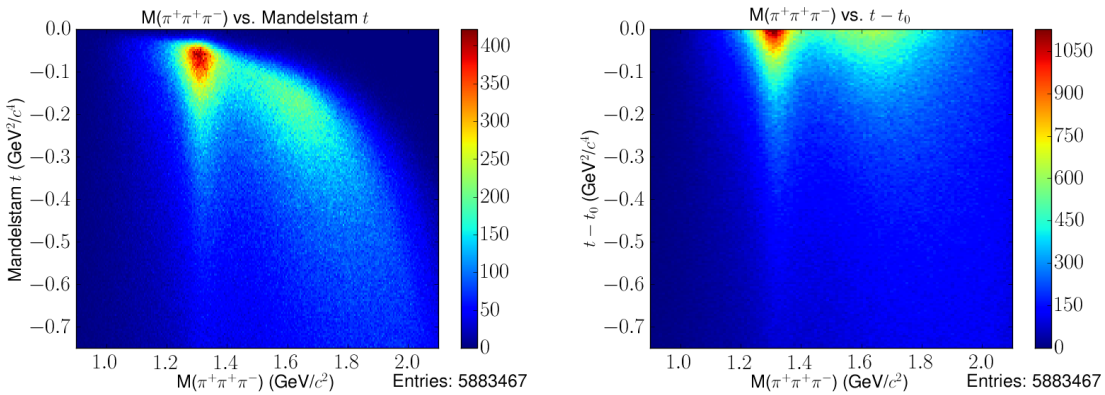

Figure 3.28: **Left:** Mandelstam t plotted against the 3π invariant mass, showing the upturn at 1.5 GeV and above due to the limitations imposed by t_0. **Right**, Mandelstam t normalized to t_0 (t') plotted against the 3π invariant mass—the upturn is corrected to be flat.

achieve a complete reduction in baryon background from t' alone. Indeed, one can imagine a process whereby an excited baryon is produced essentially at rest, recoiling off a di-pion state such as the ρ or f_2. However, a slow-moving excited baryon decaying through single-pion emission will likely do so over a broad range of polar angle in the lab frame. Our peripherally-produced 3π resonances deliver more-or-less equal boosts to all three pions, making them more likely to populate the forward angles. Constraining our sample to low momentum transfer, we have enhanced the probability that the fast pion is associated with a meson resonance, either 2π or 3π. Then if we cull events with the slow π^+ at a large polar angle in the laboratory frame, we are primarily removing baryon events, and thus we could achieve a considerable reduction in our background. The distributions of the polar angle θ_{lab} for π_1^+ and π_2^+ versus their associated $n\pi$ invariant mass are shown in Figure 3.34. For the fast $n\pi$ combination, most of the events are at low angles anyway, but the tails of the $N(1500)$ and $N(1700)$ distributions still protrude out to large angles. However, the cut in t' precludes an additional cut in $\theta_{lab}\left[\pi_1^+\right]$ by reducing such large-angle fast-π events to a negligible level, as shown in Figure 3.33. For the slow $n\pi$ combination in Figure 3.34, many events still reside at low angles, but a larger proportion extend out to the wider angles. The a_2, however, is produced exclusively at small angles, as shown in Figure 3.37.

Thus, we elect to combine our cut in t' with a cut in the laboratory polar angle of the slow π^+, $\theta_{lab}\left[\pi_2^+\right]$. For both cuts, we choose relatively tight values to get the best possible background reduction; we can loosen them later to study the systematic effects such cuts may introduce into the PWA. From the choices of cuts in t' shown in Figure 3.31, we choose $|t'| < 0.1$ GeV^2, with the selected region shown in Figure 3.38. Applying this cut to our sample, we can then look at the $n\pi$ masses after various values of cuts in $\theta_{lab}\left[\pi_2^+\right]$, shown in Figure 3.35. From these we select $\theta_{lab}\left[\pi_2^+\right] < 25°$, with the selected region shown in Figure 3.38.

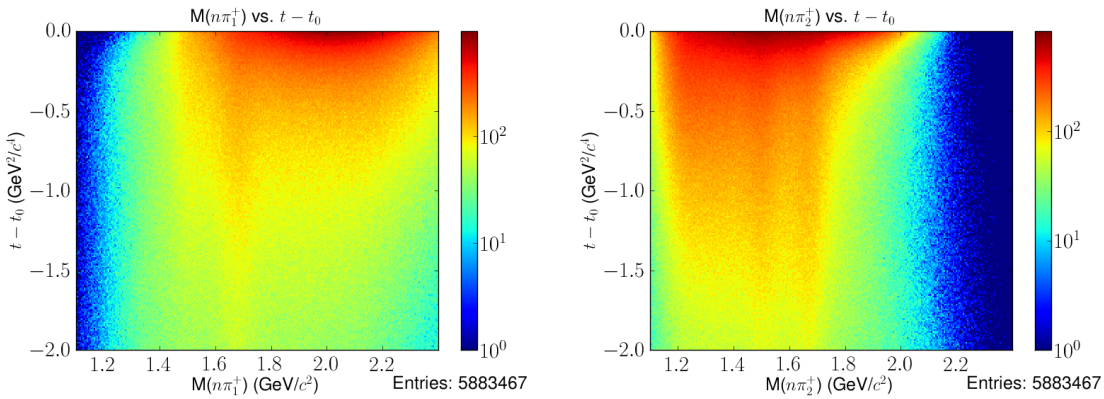

Figure 3.29: Invariant mass of the $n\pi_1^+$ system (**left**) and $n\pi_2^+$ system (**right**) versus the normalized momentum exchange t'. Vertical stripes are visible in the 1.5 and 1.7 GeV regions.

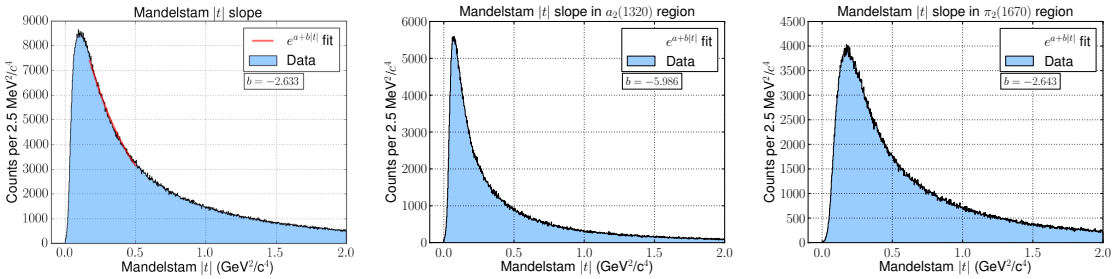

Figure 3.30: Exponential fits to the t distribution over the full 3π mass range (**left**), in the region of the $a_2(1320)$ (**center**), and in the region of the $\pi_2(1670)$ (**right**). These distributions have the cut in laboratory polar angle applied, but no cut in t'. The values for $|b|$ are 2.633, 5.986, and 2.643, respectively.

With the cuts in t' and $\theta_{lab}\left[\pi_2^+\right]$ finalized, the complete set of criteria used to isolate the sample of events from the g12 dataset which we will use in our PWA are tabulated in Table 3.2.

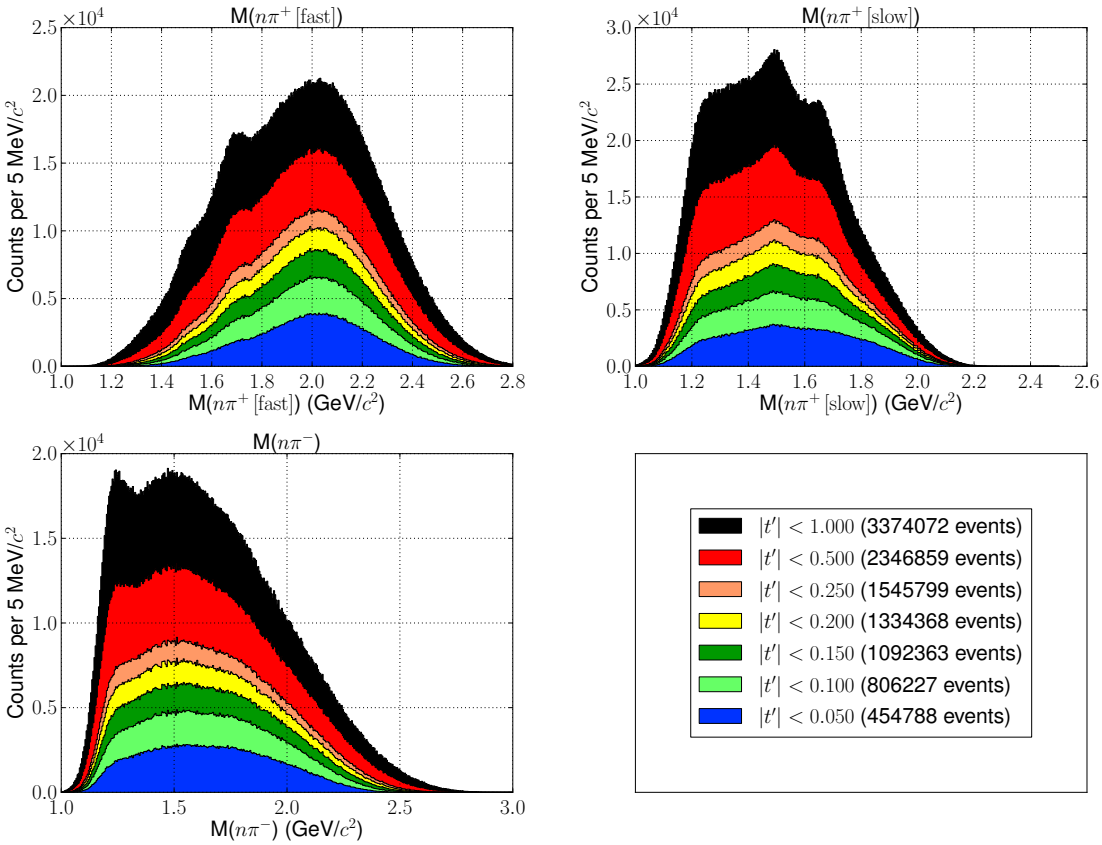

Figure 3.31: Invariant masses of $n\pi_1^+$ (**top left**), $n\pi_2^+$ (**top right**), and $n\pi^-$ (**bottom left**) after various cuts in t'. The final event sample uses the cut shown in light green ($|t'| < 0.05$ GeV^2, second from the front) to ensure the maximal reduction in baryon background possible without getting too close to the limits of our experimental acceptance.

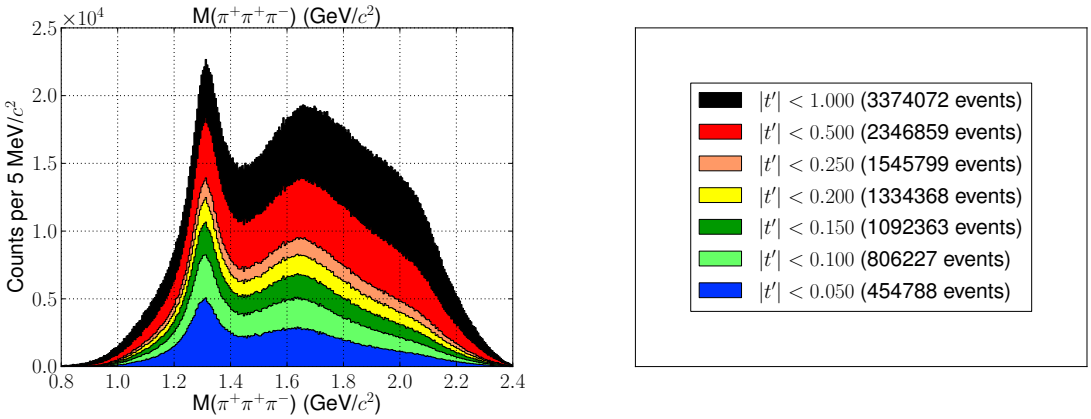

Figure 3.32: Invariant mass of $\pi^+\pi^+\pi^-$ after various cuts in t'. The final event sample uses the t' cut shown in light green (second distribution from the front).

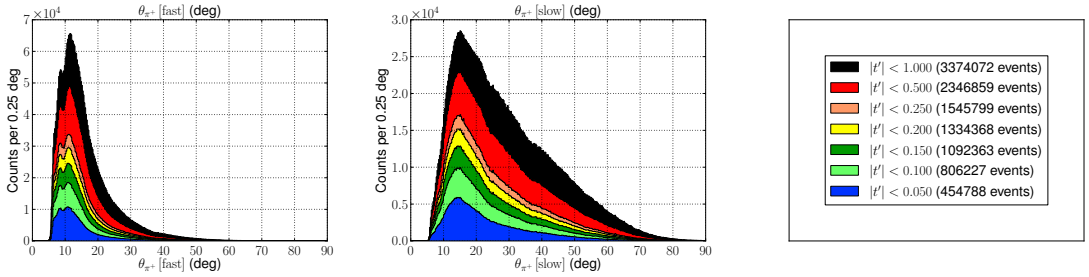

Figure 3.33: Distributions of the polar angle in the laboratory frame for the fast **left** and slow **center** pions as a function of several different cuts in t'. The final event sample uses the t' cut shown in light green (second distribution from the front).

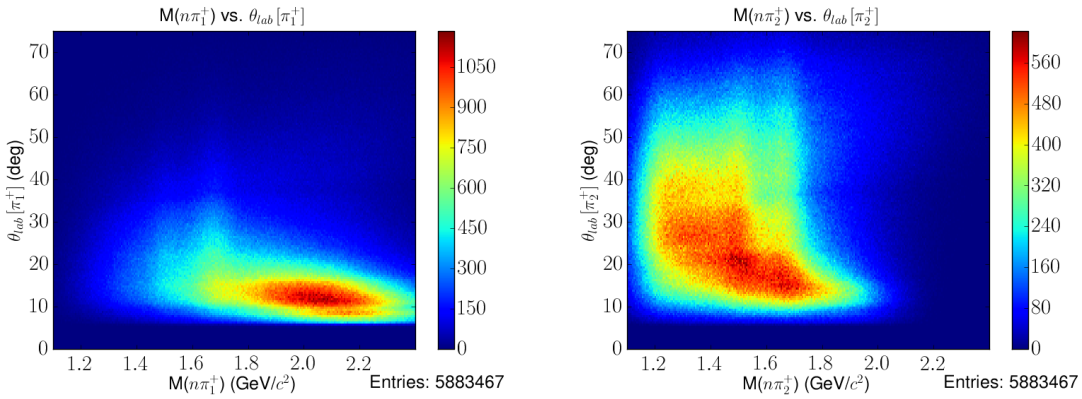

Figure 3.34: Invariant mass of $n\pi^+$ versus the polar angle in the laboratory frame of the associated π^+. The fast $n\pi$ combination is shown on the left, and the slow $n\pi$ combination is on the right.

Description	**Interval**	**Events In**	**Events Selected**
Vertex within z-extent of target	$-110 < z < -70$ cm	423,391,193	410,834,658
Vertex within target radius	$r < 2.5$ cm	410,834,658	318,534,046
t less than 0	$t < 0$ GeV^2	318,534,046	294,175,780
Physical fast π^+ β	$0 < \beta < 1.04$	294,175,780	258,818,984
Physical slow π^+ β	$0 < \beta < 1.04$	258,818,984	249,856,422
Small slow π^+ $\delta\beta$	$\lvert\beta_{TOF} - \beta_{p/m}\rvert < 0.03$	249,856,422	216,150,344
Missing mass consistent with neutron	$0.82 <$ MM < 1.06 GeV	216,150,344	55,335,182
High energy beam photon	$E_\gamma > 4.4$ GeV	55,335,182	5,883,467
Low momentum transfer	$\lvert t'\rvert < 0.01$ GeV^2	5,883,467	806,245
Small polar angle for slow π^+	$\theta_{lab}\left[\pi_2^+\right] < 25°$	806,245	510,500

Table 3.2: Table with the event counts before and after each of the cuts used to select our final sample of $\gamma p \to \pi^+\pi^+\pi^- n$ events for PWA.

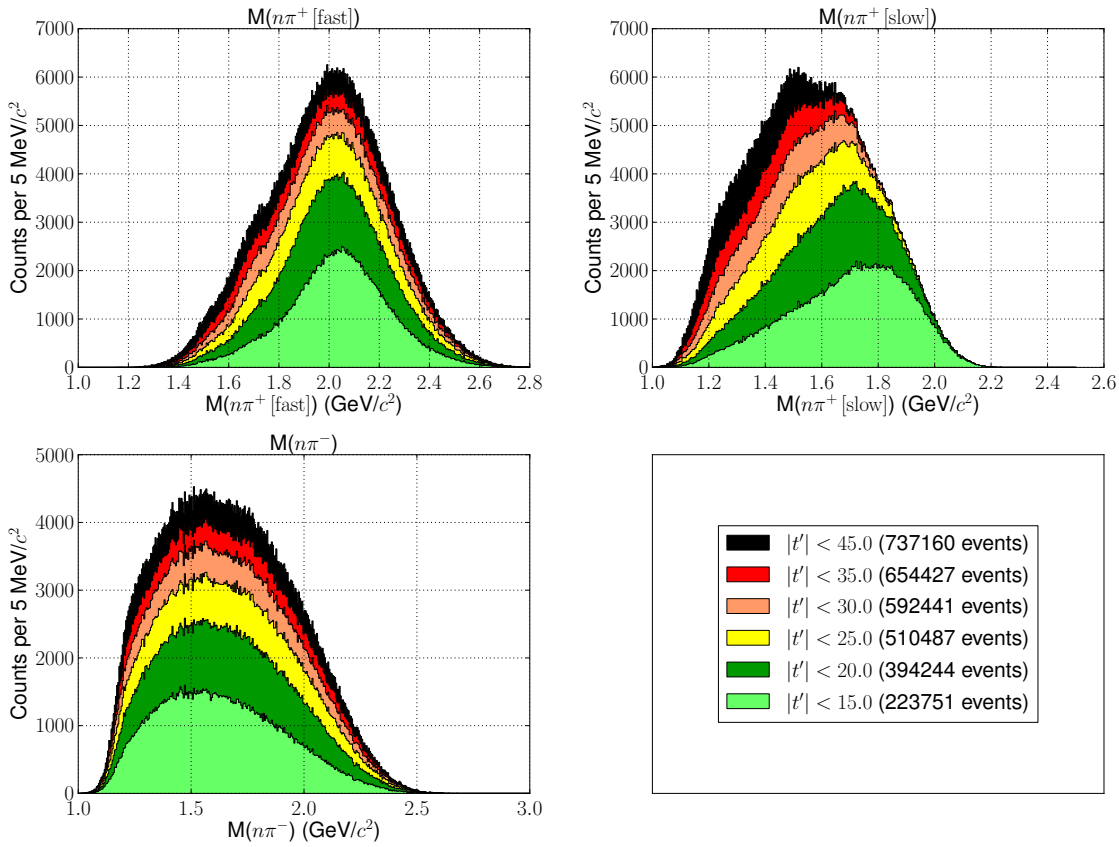

Figure 3.35: Invariant masses of $n\pi_1^+$ (**top left**), $n\pi_2^+$ (**top right**), and $n\pi^-$ (**bottom left**) after various cuts in $\theta_{lab}\left[\pi_2^+\right]$. The final event sample uses the cut shown in yellow ($\theta_{lab}\left[\pi_2^+\right] < 25°$, third from the front) to provide the best possible background reduction without compromising our acceptance.

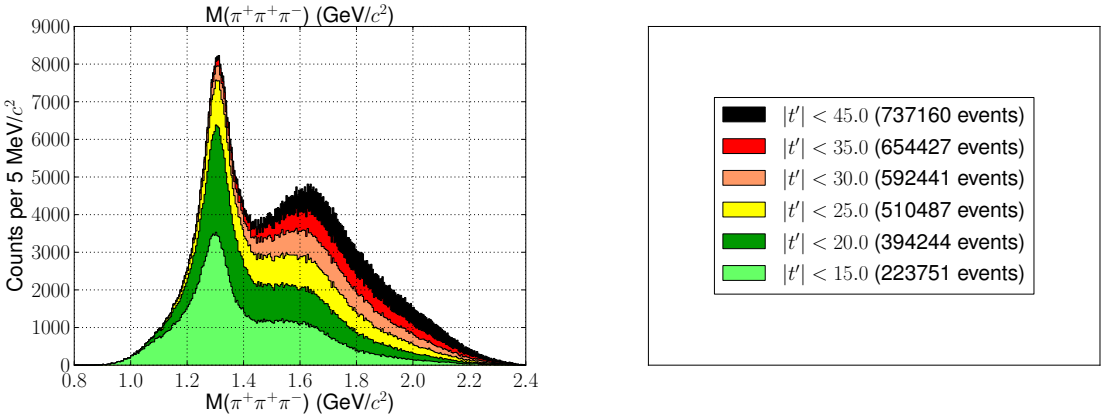

Figure 3.36: Invariant mass of $\pi^+\pi^+\pi^-$ after various cuts in $\theta_{lab}\left[\pi_2^+\right]$. The final event sample uses the The final event sample uses the cut shown in yellow ($\theta_{lab}\left[\pi_2^+\right] < 25°$, third from the front).

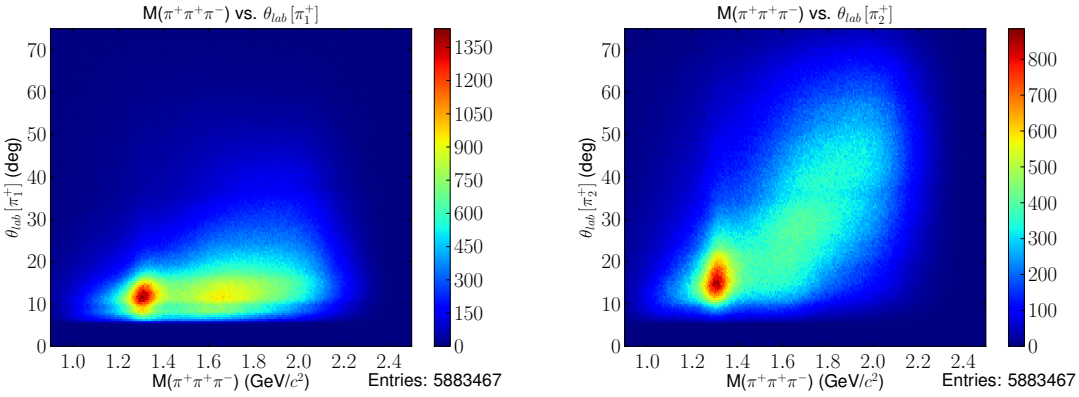

Figure 3.37: 3π invariant mass versus the polar angle in the laboratory frame of the fast π^+ (**left**) and the slow π^+ (**right**).

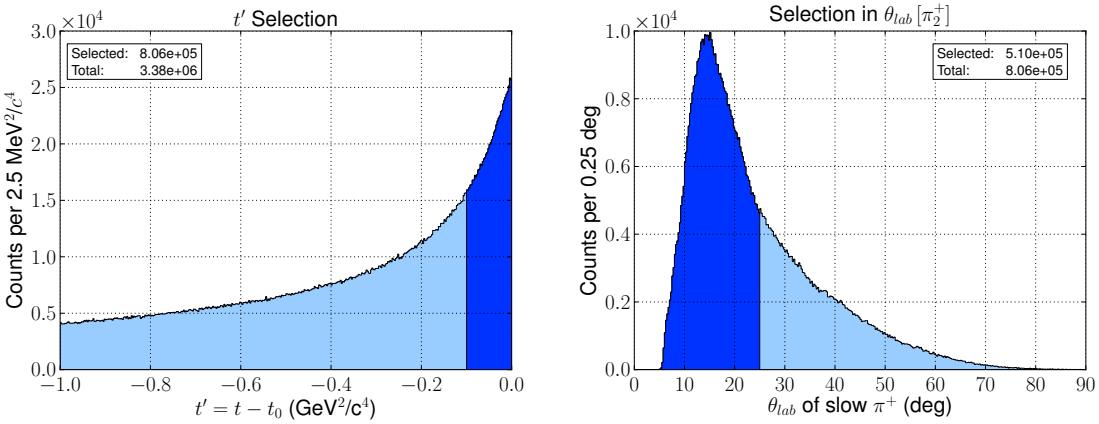

Figure 3.38: The darkened regions in t' (**left**) and $\theta_{lab}\left[\pi_2^+\right]$ (**right**) represent events which are used in the partial wave analysis.

3.3 Features of the Final $\gamma p \to \pi^+\pi^+\pi^- n$ Sample

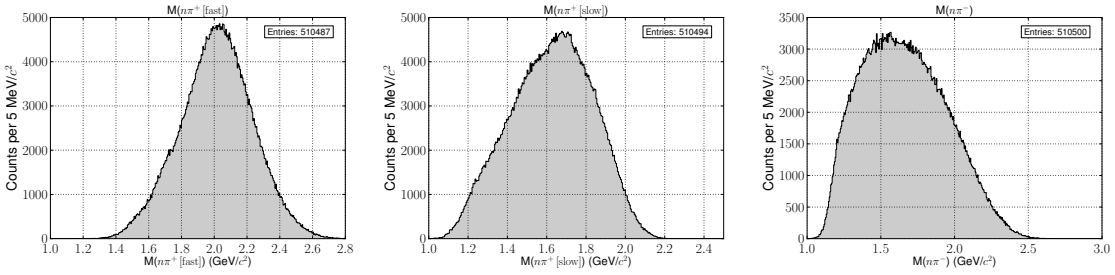

Figure 3.39: The invariant masses $n\pi_1^+$ (**left**), $n\pi_2^+$ (**center**), and $n\pi^-$ (**right**), after the application of the low-$|t'|$ cut. Note that the peaks at 1.5 GeV are substantially reduced.

After the application of the low-$|t'|$ cut, we are left with the $n\pi$ invariant mass distributions shown in Figure 3.39. Some hints of the baryon resonances at 1.5 and 1.7 GeV still remain, but they have been reduced to a level where the mesonic degrees of freedom are expressed in a dominant fashion.

With this enriched sample of mesonic $\gamma p \to \pi^+\pi^+\pi^- n$ events, we can examine in detail some of the structures we see in the 3π invariant mass distribution, shown in Figure 3.40. Two peaks are visible, one at 1.3 GeV and another just above 1.6 GeV. Selecting each of these regions in turn, we can examine the Dalitz plot, where we look at the squared invariant mass of one $\pi^+\pi^-$ combination versus the complementary combination. These are shown in Figure 3.41. In the 1.3 GeV region, shown in the top plots of Figure 3.41, we can see strong evidence for the production of the $\rho(770)$, consistent with production of the $a_2(1320)$ meson, which primarily decays via $\rho\pi$. In the 1.6 GeV region, shown in the bottom plot of Figure 3.41, we can see strong evidence for the production of the $f_2(1270)$ isobar, as well as some evidence of $\rho(770)$ production as well. The $f_2(1270)\pi$ channel is the primary decay channel of the $\pi_2(1670)$ meson, which also decays about 30% of the time to $\rho\pi$. The presence of $\rho\pi$ in this region of 3π mass could also be due to production of the $\pi_1(1600)$ exotic, but we must refer to Chapter 5 for the final word. The one-dimensional $\pi\pi$ invariant masses can be seen in Figure 3.42.

Our PWA is built upon the angular distributions in the rest frame of the three-pion resonance, as well as the as those in the rest frames of the two $\pi^+\pi^-$ combinations. In the rest frame of the 3π resonance, we define the axes according to the Gottfried-Jackson convention; for the di-pion rest frames, we use the helicity convention. Both are described in detail in Appendix A. The angular distributions in these frames are shown in Figure 3.43. The forward and backward regions of the Gottfried-Jackson θ are populated by the fast and slow di-pion combinations, respectively. In the helicity frame, the distributions in $\cos\theta$ are quite different between the fast and slow isobar combinations, although this is mostly an artifact of acceptance. Also heavily sculpted by acceptance are the azimuthal angles in the helicity frame. More details on our acceptance follow in the next Section.

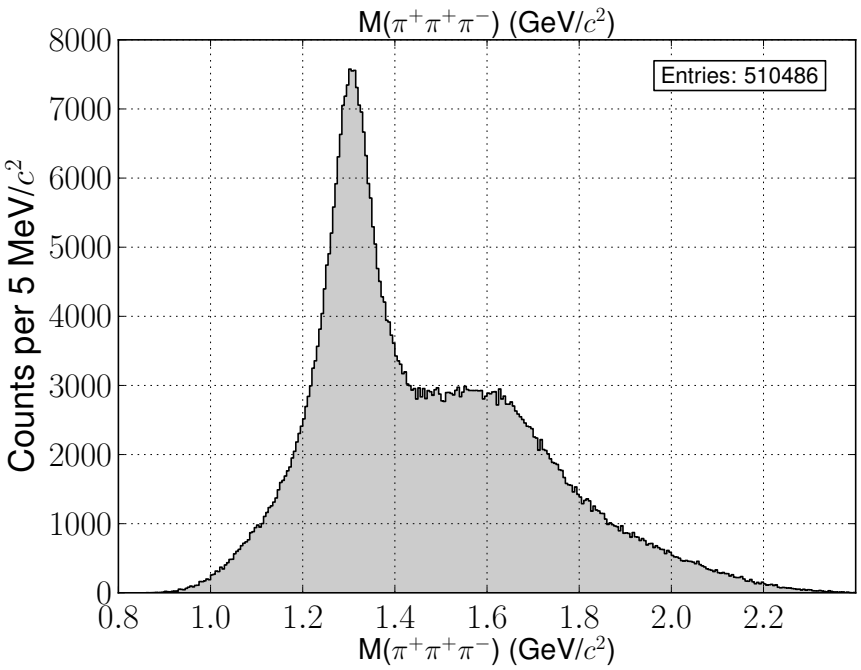

Figure 3.40: The invariant 3π mass distribution for the final sample of events used in the PWA.

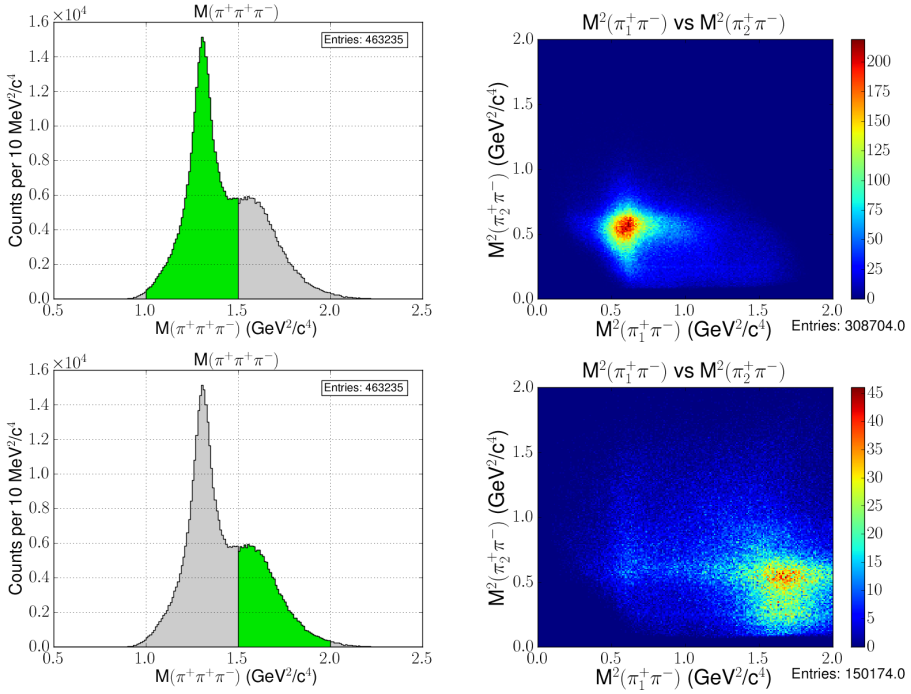

Figure 3.41: Dalitz distributions for the $a_2(1320)$ (**top**) and $\pi_2(1670)$ (**bottom**) regions of the 3π invariant mass. The selected regions in 3π mass in the left column are darkened.

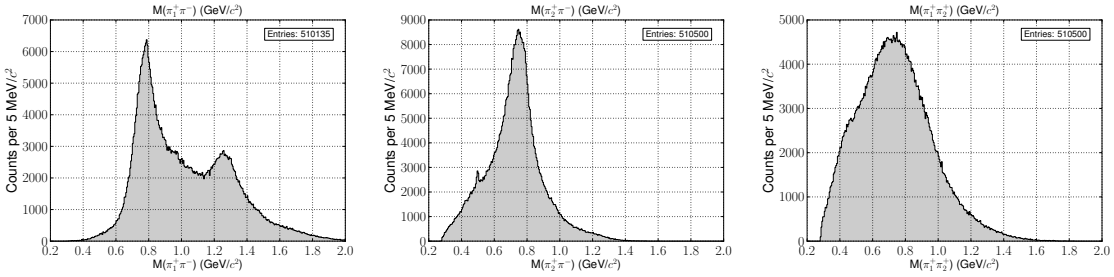

Figure 3.42: $\pi\pi$ mass distributions for the final event sample. Peaks due to $\rho(770)$ and $f_2(1270)$ isobars are visible in the $\pi_1^+\pi^-$ invariant mass (**left**), while ρ production dominates the $\pi_2^+\pi^-$ spectrum (**center**) above a small peak corresponding to the K_S. The $\pi^+\pi^+$ spectrum (**right**) is largely featureless, apart from a slight inflection at 0.5 GeV.

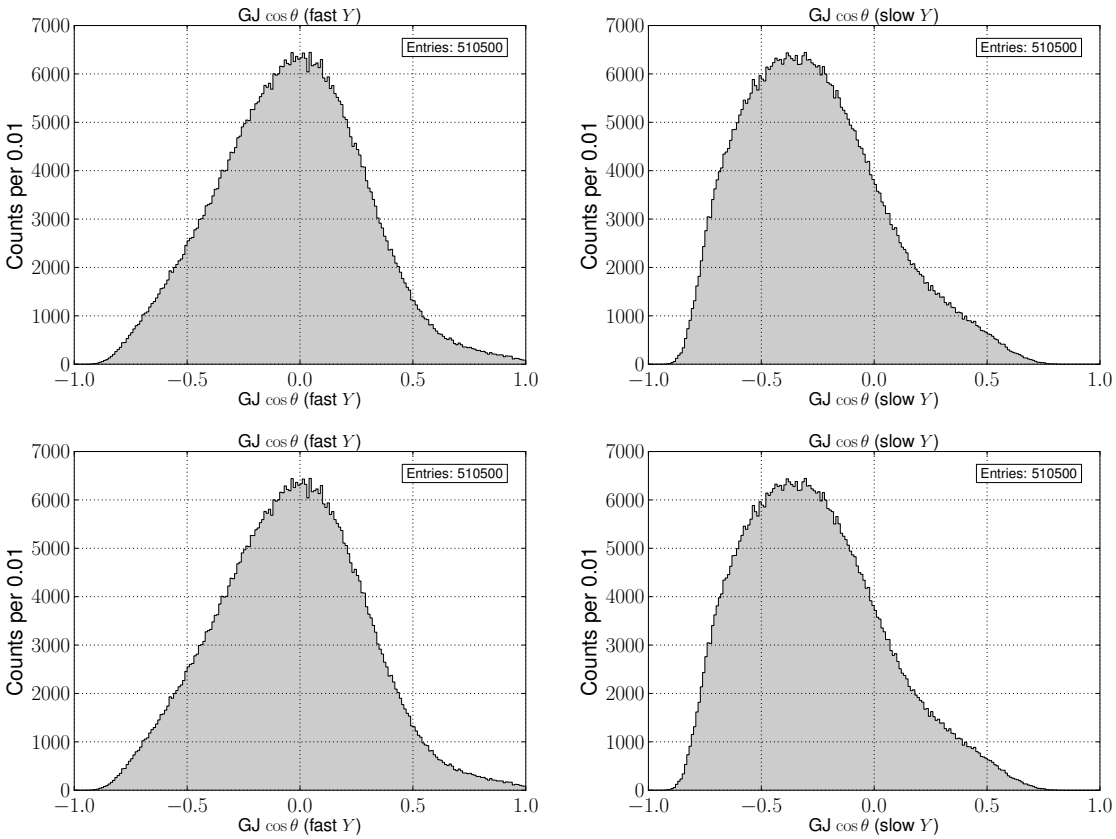

Figure 3.43: The polar angle (**top left**) and azimuth (**top right**) of the two $\pi^+\pi^-$ combinations (called Y in the figures) in the Gottfried-Jackson frame; the polar angle (**bottom left**) and azimuth (**bottom right**) of the π^+ in the helicity frame.

3.4 Detector Acceptance and Normalization

We now turn to the procedure we employ to determine the acceptance of CLAS, necessary to ensure our likelihood function is properly normalized. In order to have confidence in the results of our PWA, we must have a thorough understanding of how much of our observed intensity distribution is due to physics, and how much is due to the ability of CLAS to see events in a given kinematical region. Ideally we would like to know how CLAS colors data generated with no physics whatsoever, with all configurations of τ equally populated. In other words, to use the language of Section 4.1, we are interested in the CLAS response to events uniform in three-body *phase space*.

3.4.1 Monte-Carlo Event Generation

Our study of acceptance of CLAS begins by generating a sample of $\gamma p \to \pi^+\pi^+\pi^- n$ events, sampling randomly and uniformly the phase space available to a three-pion decay at CEBAF energies. We will call these generated events the *raw monte-carlo*. Once these events have been pushed through the CLAS detector simulation and reconstructed, those successfully reconstructed as $\gamma p \to \pi^+\pi^+\pi^- n$ events will be known as *accepted* monte-carlo.

We perform our PWA fits in narrow slices of 3π mass; thus we will also bin our raw and accepted monte-carlo in the same bins of 3π mass to preserve the mass independence of our results. However, as varying bin size is an important systematic check on fit results, it behooves us to generate monte-carlo in very narrow bins, narrower than the smallest practical bin size for our real data, so that we can then normalize fits in a variety of bin sizes simply by merging bins of monte-carlo. In this spirit we choose to generate our raw monte-carlo in 5 MeV bins in 3π mass.

Also, the raw monte-carlo sample must be large enough to ensure no region of phase space is by chance overlooked. Furthermore, by generating a large monte-carlo dataset, we can minimize its contribution to the total statistical uncertainties of our fit results. Plus, modern batch computing environments can cheaply produce large quantities of monte-carlo data in relatively short times. A common rule is to have on hand a factor of ten greater accepted monte-carlo events than data events in each bin; thus we generated sufficient raw monte-carlo in each 5 MeV bin to meet this criterion.

Our experimental data also has an exponential distribution in Mandelstam t with a characteristic slope b, as shown in Figure 3.30. In the ideal case, we would like to generate our monte-carlo with a t-slope that exactly reproduces what we see in the data. However, the t-slope we measure in data is determined by the physical processes taking place, and varies by quite a bit when measured in different regions of the 3π mass spectrum. We could possibly generate monte-carlo with a different t-slope in each bin of 3π mass to mock up these dynamics; however, doing so results in an unrealistic, non-smooth experimental acceptance. Additionally, as CLAS has poor acceptance for events with very low $|t|$, a set of events generated with a given t-slope will be reconstructed with a different t-slope. To account for this effect, several samples of raw monte-carlo events generated with different t-slopes were passed through the CLAS software simulation and reconstruction chain, and the t distribution of the output events measured. The result is shown in Figure 3.44. Using the parameters determined from Figure 3.44, the raw monte-carlo was generated with a t-slope $b = 4.37$, as shown in Figure 3.45, to try and reproduce the experimentally-measured t-slope

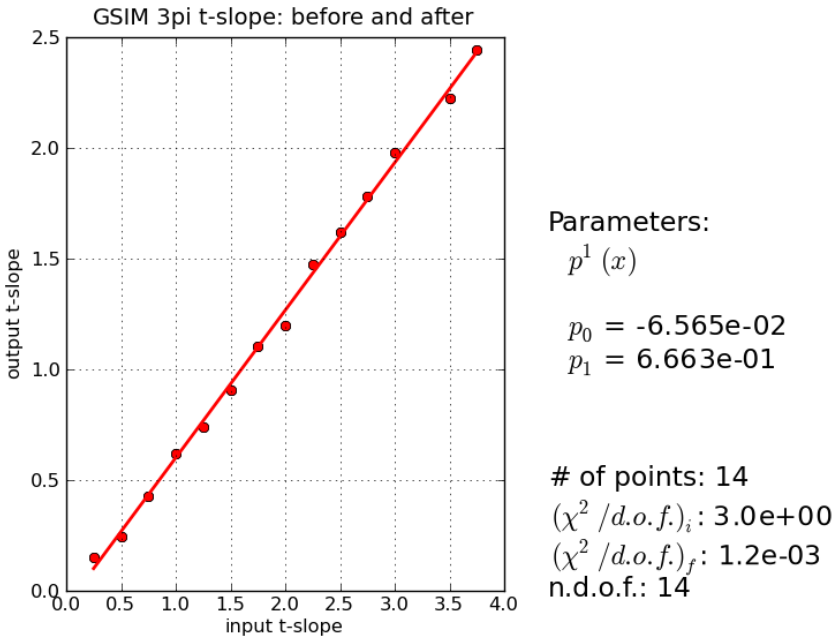

Figure 3.44: The effect of CLAS acceptance on t-slope. CLAS tends to lessen the steepness of the t-slope in an approximately linear fashion; these points are fit with a line and the parameters used to generate monte-carlo with a t-slope that will be, after acceptance, consistent with the real data.

of 2.633. The photon beam energy for events was generated according to a bremsstrahlung distribution of photon energies from 4.4 to 5.45 GeV.

All told, about 400M events of raw monte-carlo were generated. The uniformity of these events in 3π phase space can be seen in the Dalitz plot in Figure 3.46, and the uniformity in the physics angles can be seen in Figure 3.47.

Decay amplitudes are calculated for the raw monte-carlo events in the same fashion as the real data events, described in Section 4.2. These amplitudes are then used as input to the normalization integral calculation as described in Section 4.3, with the output of that procedure known as the *raw normalization integral*. The raw normalization integral is not used during the minimization, but it is necessary for producing acceptance-corrected intensity distributions, as described in Section 4.4.

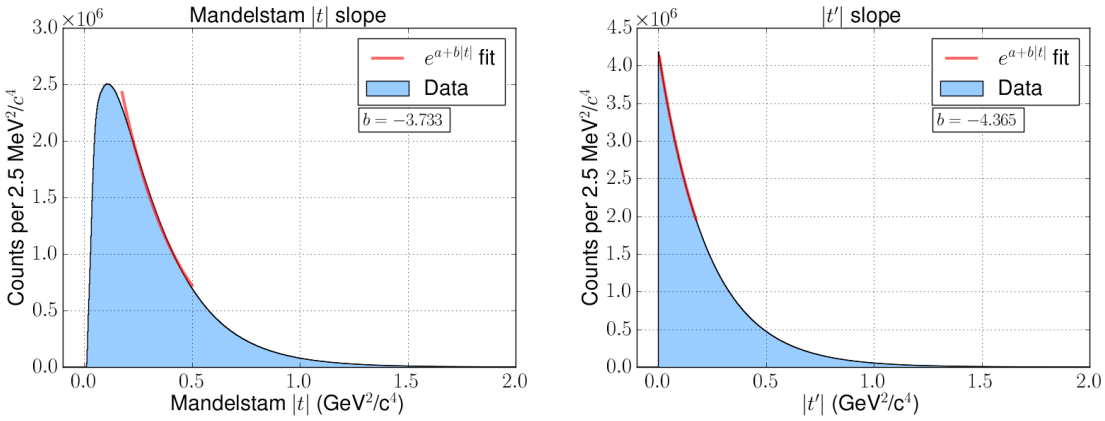

Figure 3.45: The $|t|$ (**left**) and $|t'|$ (**right**) distribution of the raw monte-carlo. The slope in $|t|$ is modified by the available phase space, but this is corrected for in $|t'|$, so the slope in $|t'|$ is the one that matches the input value of 4.37.

3.4.2 Modeling the CLAS Detector Response

The response of CLAS to our raw monte-carlo events is modeled by the program `GSIM`, which is based on the CERN `GEANT3` libraries [65]. Given a set of input events, it swims the constituent tracks though the various volumes which mimic the geometry of CLAS. Hits are produced in the "detectors", represented by so-called *active volumes*, and are written out as mock detector digitizations similar to what the real-world CLAS would have reported if the same events occurred in Nature. After a set of events is processed by `GSIM`, a second program, `gpp`, compares each digitization to a map of the state of CLAS during the g12 run period. If `GSIM` records a hit in a detector element that was nonfunctional during the g12 run, that hit is removed. Should a particle interact with a functional detector element in `GSIM`, the value measured by the element is smeared according to that element's resolution during the g12 run period. After passing through `gpp`, the smeared events are then fed into `a1c`, the event reconstruction program described in Section 2.6. The reconstructed events, now known as accepted monte-carlo, are then subjected to the same event selections

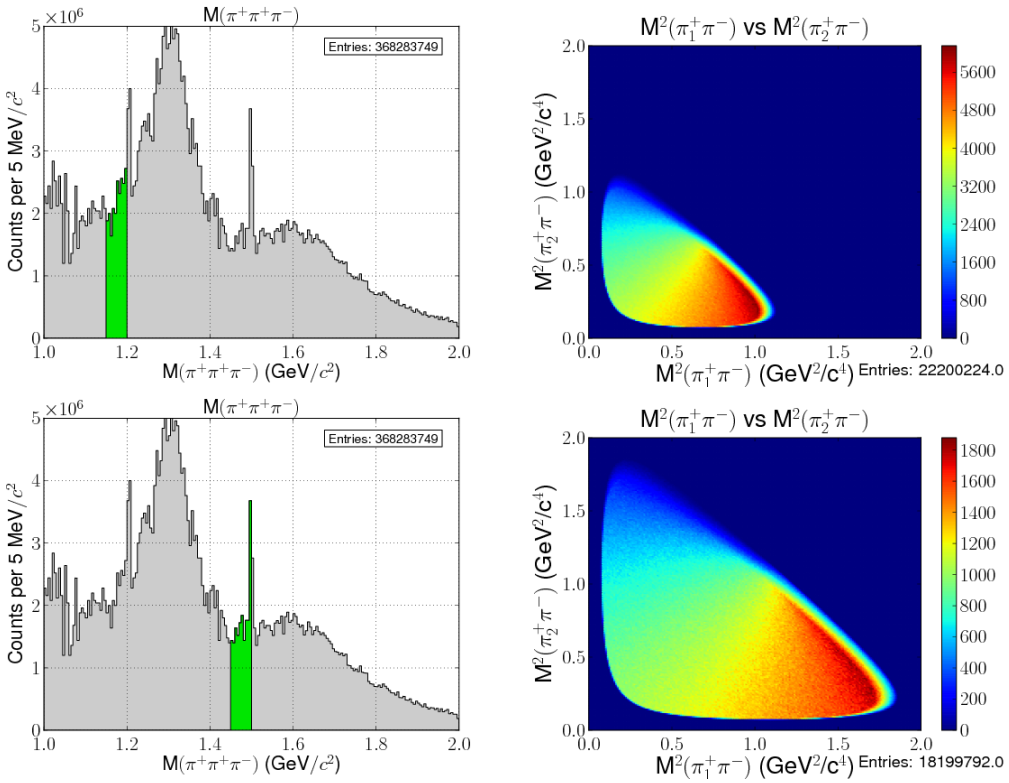

Figure 3.46: The Dalitz plot for the raw monte-carlo in two regions of 3π mass; the plot is symmetrically enhanced and depleted along the x and y axes, respectively, because we sort the π^+ by their velocity. The shape of the 3π mass spectrum is ragged because we generate our monte-carlo independently in 5 MeV bins in proportion to the amount of real data present in a given bin.

described in Sections 3.1 and 3.2.

Examining the fraction of accepted events as a function of 3π invariant mass, shown in Figure 3.48, we see that we have rather low acceptance at the low end of the 3π mass spectrum, but the acceptance varies smoothly over the whole range. The Dalitz plot of the accepted monte-carlo, as well as distributions of the physics angles, are shown in Figures 3.50 and 3.51. While our acceptance varies smoothly in the Gottfried-Jackson frame, the helicity angles show structure that will cause us some problems during our fit. We will discuss this more in Chapter 5.

Decay amplitudes are also generated for the accepted monte-carlo in each bin of 3π mass; these amplitudes are used as input into the calculation of the *accepted normalization integral*, described in Section 4.3. The accepted normalization integral is necessary in the definition of the likelihood function to ensure a valid probability distribution; without it, the likelihood function would have no minimum.

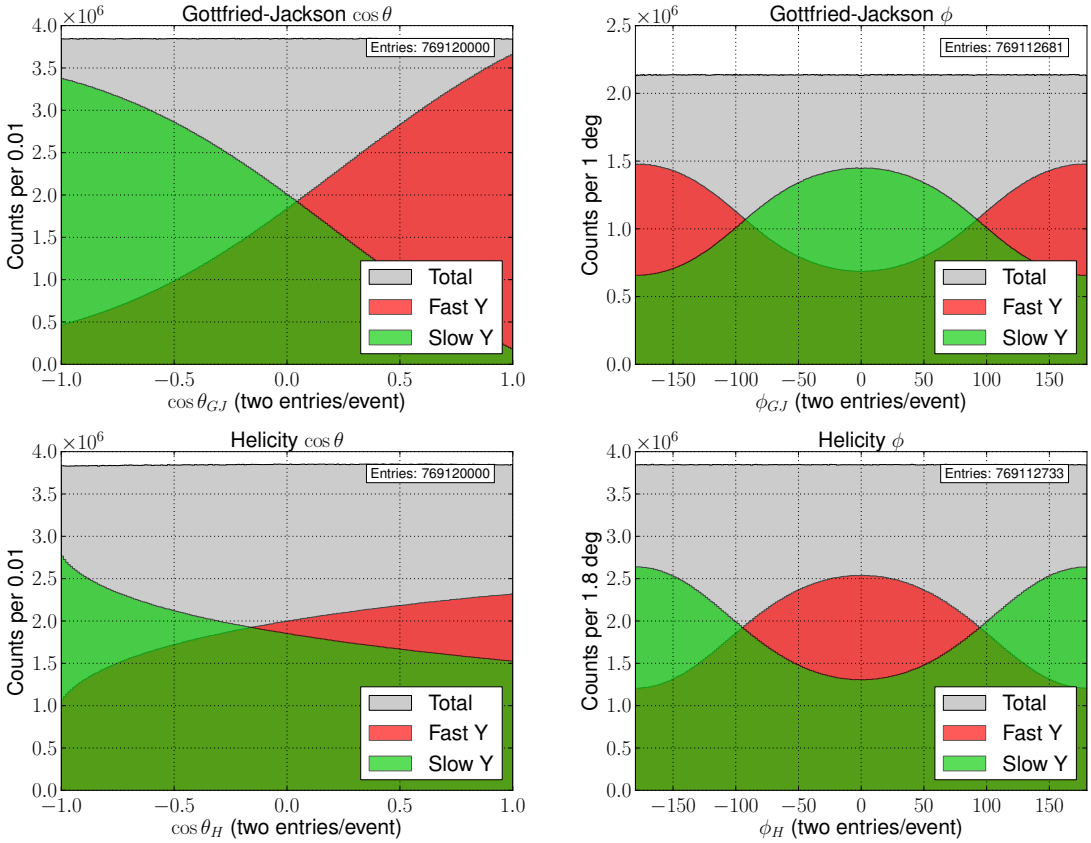

Figure 3.47: Physics angles for the raw monte-carlo. **Top left** is $\cos\theta$ of the isobar in the Gottfried-Jackson (GJ) frame (as defined in Appendix A). **Top right** is the ϕ distribution in the GJ frame. **Bottom left** and **bottom right** are $\cos\theta$ and ϕ of the π^+, respectively, measured in the helicity frame for both combinations of $\pi^+\pi^-$. Note the uniformity in all distributions.

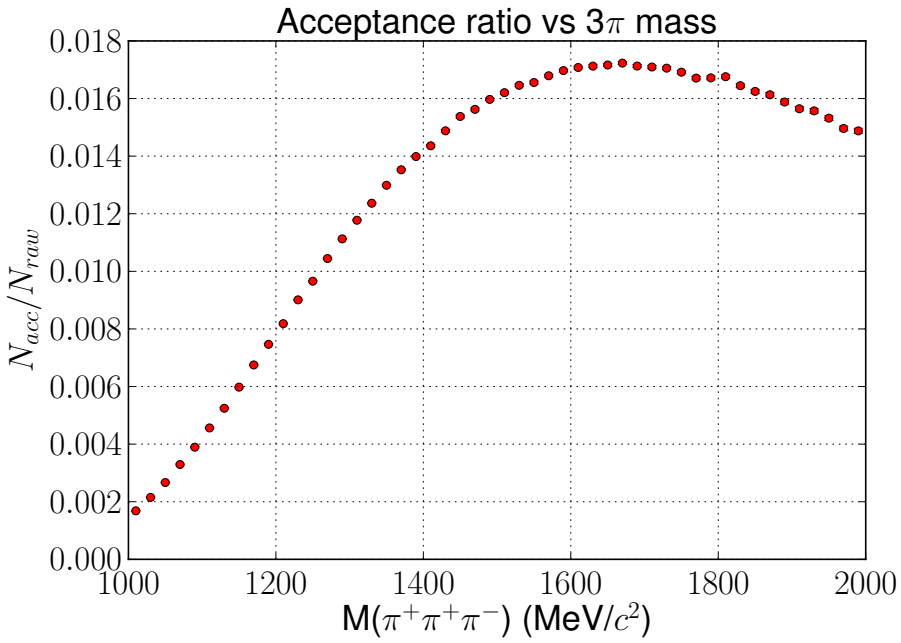

Figure 3.48: The shape of CLAS acceptance for $\gamma p \to \pi^+\pi^+\pi^- n$ events (subject to all the cuts of Sections 3.1 and 3.2) as a function of 3π mass.

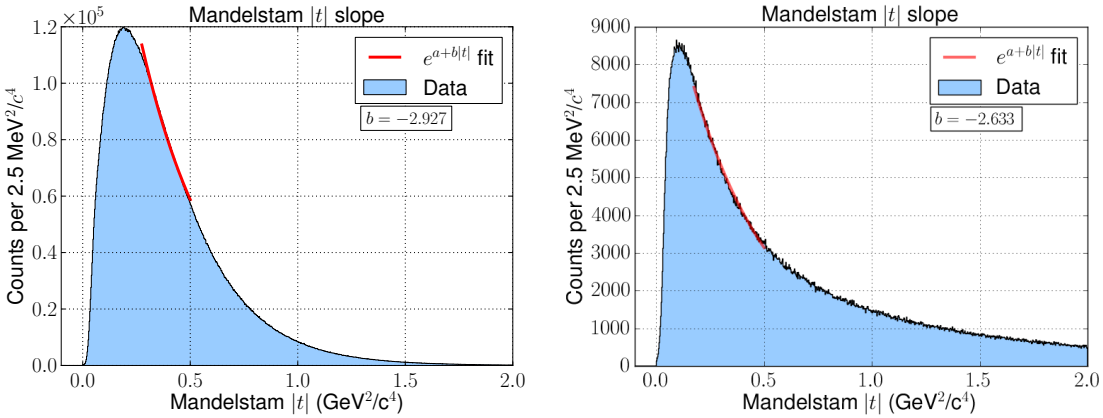

Figure 3.49: The t distribution of the accepted monte-carlo (**left**) and the experimental data (**right**); the measured t-slopes are in approximate agreement.

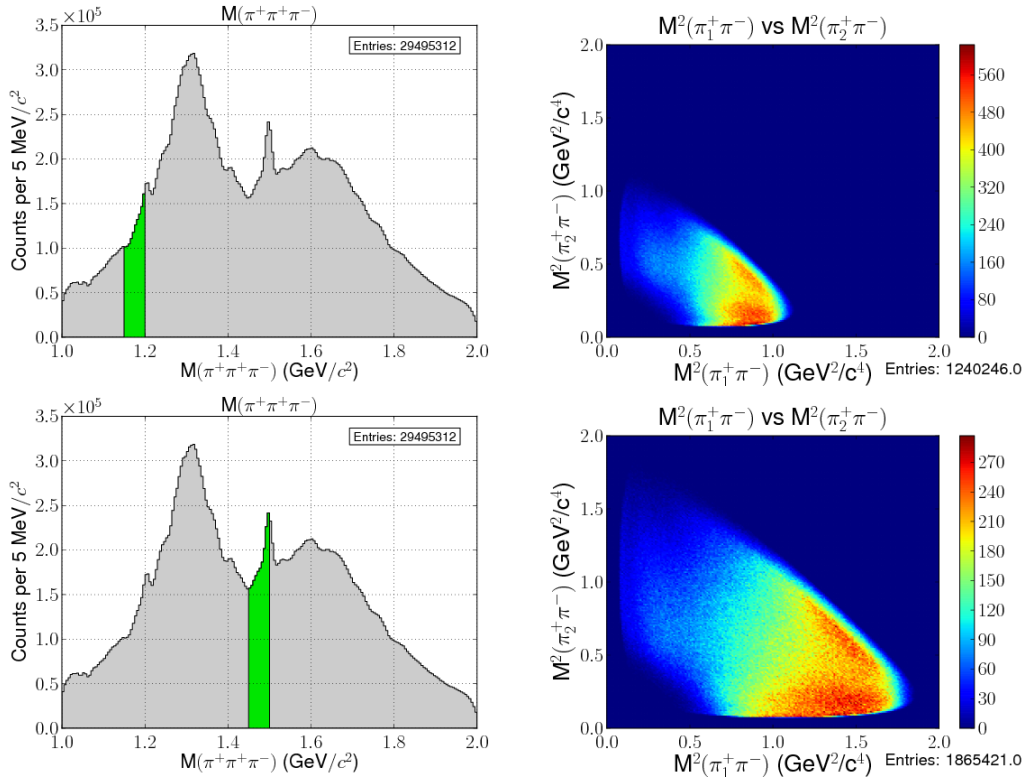

Figure 3.50: The Dalitz plots for the accepted monte-carlo as a function of two selections in 3π mass. The 3π mass distribution is ragged because events are generated in 5 MeV bins of 3π mass according to the statistics of the data in those same bins.

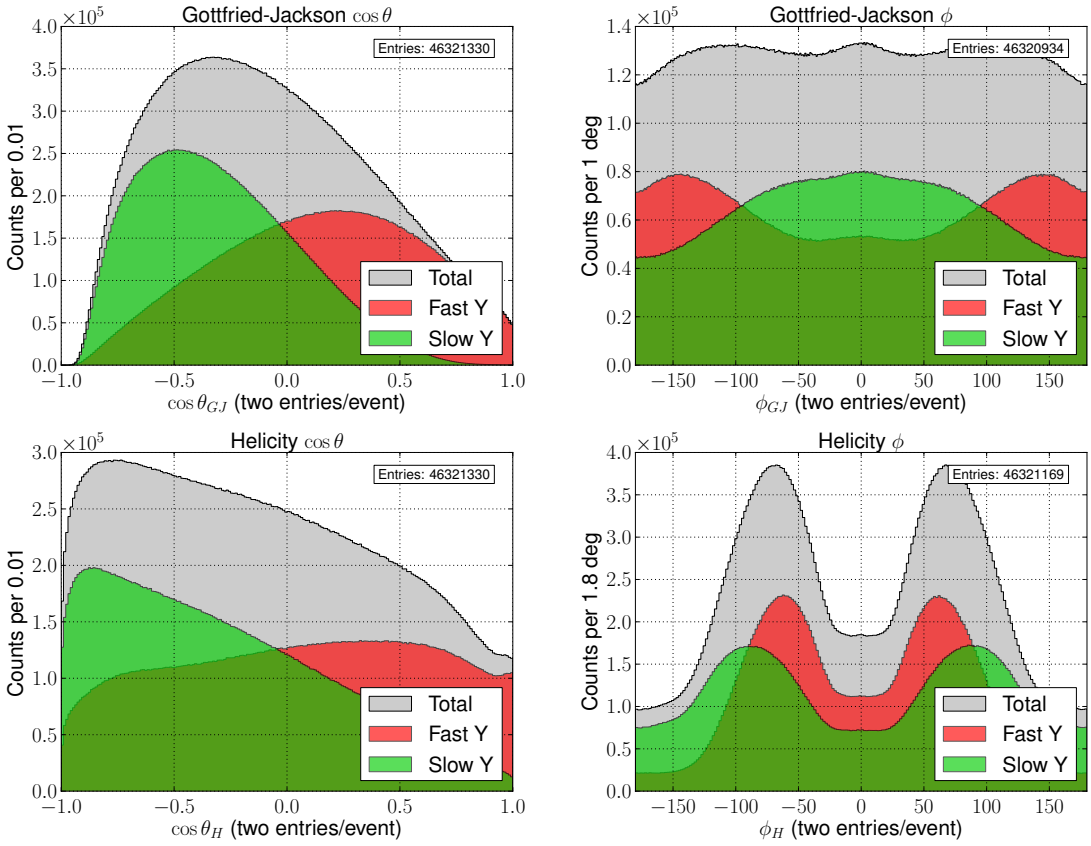

Figure 3.51: Physics angles for the accepted monte-carlo. **Top left** is $\cos\theta$ of the isobar in the Gottfried-Jackson (GJ) frame (as defined in Appendix A). **Top right** is the ϕ distribution in the GJ frame. **Bottom left** and **bottom right** are $\cos\theta$ and ϕ of the π^+, respectively, measured in the helicity frame for both combinations of $\pi^+\pi^-$.

3.5 Summary

From 24B triggers collected by the g12 rungroup, we selected 55M exclusive $\gamma p \rightarrow \pi^+\pi^+\pi^- n$ events. 5.9M of these were produced by a beam photon above 4.4 GeV in energy, and 510K pass our kinematic cuts. 494K of these 510K reside in the 1 to 2 GeV region of 3π invariant mass. We have generated about 400M raw monte-carlo events and successfully reconstructed 33M of them after passage through `GSIM`. Of those 33M, about 4.5M pass the cuts applied to the real data. With all of these datasets in place, we are now ready to perform our PWA. We start in Chapter 4 with a description of the formalism on which our PWA is based.

CHAPTER 4

PARTIAL-WAVE ANALYSIS FORMALISM

Partial-wave analysis is a tool for determining the contribution of various spin-parity states to an observed intensity distribution. In this chapter, we describe the theoretical framework used to decompose our sample of $\gamma p \to \pi^+\pi^+\pi^-n$ events into its constituent spin-parity or J^{PC} contributions.

4.1 Introduction

The usual quantity of interest in any scattering experiment is the *cross-section*. The cross-section is a measure invented by Rutherford when he reported the results from his gold-foil scattering experiments. Since he was interested in determining the spacial extent of the positive charge of the atomic nucleus, the cross-sectional area of the scattering center was a natural quantity to derive theoretically and then measure.

The cross-section survives today as the primary interface between theory and experiment, although it no longer characterizes the size of the particles involved in the interaction under study. Instead, it is used primarily to describe the strength of a particular production process; that is, processes with large cross-sections happen more often than those with small cross-sections. Since we are interested in determining the production strengths of exotic mesons, the cross-section seems a natural place to begin our discussion.

We write down the total cross-section σ in a familiar form,

$$\sigma(\gamma p \to \pi^+\pi^+\pi^-n) = \frac{n}{n_\gamma l_t \rho_t N_A} \tag{4.1}$$

where n is the number of observed $\gamma p \to \pi^+\pi^+\pi^-n$ events, n_γ is the total number of photons on target, l_t is the length of the target, ρ_t is its mass density, and N_A is Avogadro's number. However, this just tells us the overall cross-section for a $\gamma p \to \pi^+\pi^+\pi^-n$ event to occur at all combinations of angles and momenta. A more useful measure is the cross-section normalized to a unit of all the possible combinations of angles and momenta for a given reaction—a unit of *phase space*. For elastic two-body scattering from a central potential, phase space can be described by just the scattering angle θ, and thus the unit cross-section $d\sigma$ can be normalized to the unit scattering angle $d\theta$. The quantity $d\sigma/d\theta$ is known as the *differential cross-section*. For $\gamma p \to \pi^+\pi^+\pi^-n$ events, extracting the normalization for $d\sigma$ is more complex, because we have four particles in the final state.

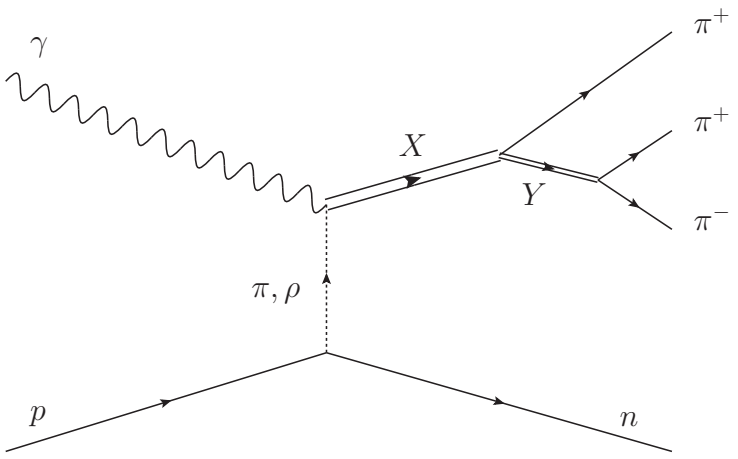

Figure 4.1: A diagram of the isobar model interpretation of a $\gamma p \to \pi^+\pi^+\pi^-$ decay. The impinging photon exchanges a charged π or ρ with the proton, leaving it as a neutron, and produces a resonance X. X then decays first by emission of a π^+, leaving it in the state Y, called the isobar. The isobar then decays to $\pi^+\pi^-$. Common hypotheses for X and Y are listed.

We begin by describing our $\gamma p \to \pi^+\pi^+\pi^- n$ decay as shown in Figure 4.1. We assume the decay $X \to \pi^+\pi^+\pi^-$ is well-described by the *isobar model* [66]; that is, it follows the form:

$$X \to Y\pi_b^+ \to \pi^+\pi^-\pi_b^+ \tag{4.2}$$

where the di-pion resonance Y is known as the *isobar*, and π_b^+ is known as the *bachelor* π. Note that in practice, there is no way to distinguish between the two π^+, so we symmetrize our amplitude calculation across them. With sequential decays like these, we typically begin analysis of a given event in the overall center-of-mass (CM) frame. In the center-of-mass frame, we regard X as the produced particle, so the situation reduces to two-body scattering, and we count a factor of $d\theta$ towards our phase-space element. Next, we boost into the rest frame of X and consider the two-body decay $X \to Y\pi^+$. This is a one-to-two body process, and thus we count factors of $d\Omega_X = (d\theta_X, d\phi_X)$, p_Y, and dm_X toward our total phase-space element, where p_Y is the momentum of the isobar Y in the X rest frame, and m_X is the mass of X. Finally, we boost once more to the rest frame of Y, where we encounter another one-to-two process. We insert factors of p_{π^+}, $d\Omega_Y = (d\theta_Y, d\phi_Y)$, and dm_Y into our phase space element, where p_{π^+} is the momentum of the π^- in the Y rest frame, and m_Y is the mass of Y. We also use particular orientations of axes in the X and Y rest frames; they are described in detail in Appendix A.

Now we have arrived at the expression suggested in Ref. [67] for the three-body phase space element:

$$d\rho \propto d\theta(p_Y\ d\Omega_X\ dm_X)(p_{\pi^+}\ d\Omega_Y\ dm_Y) \tag{4.3}$$

where $d\rho$ is the name for our unit of phase space. It is helpful to rewrite $d\rho$ so that it

depends on the Lorentz-invariant Mandelstam variable t rather than θ. t can be defined as:

$$t = (p^{\mu}_{\gamma} - p^{\mu}_{\mathrm{X}})^2 \tag{4.4}$$

$$= t_0 - 4|p_{\gamma}||p_X|\sin^2(\frac{\theta}{2}) \tag{4.5}$$

where t_0 is the familiar quantity from Section 3.2, albeit written in the equivalent form

$$|t|_{min} = m_X^2 - 2E_{\gamma}E_X + 2E_{\gamma}|p_X|. \tag{4.6}$$

With these definitions, the differential cross-section for a two-to-four process such as $\gamma p \to \pi^+\pi^+\pi^-n$ has the following form:

$$\frac{d\sigma}{dt\; dm_X\; d\tau} \propto |\mathcal{M}|^2 p_Y p_{\pi^+}, \tag{4.7}$$

where

$$|\mathcal{M}|^2 = \mathcal{I}(\tau), \tag{4.8}$$

and we have followed the convention of Ref. [67] by lumping together all of the variables needed to describe the $X \to Y\pi^+ \to \pi^+\pi^-\pi^+$ decay into a single label, τ. Five quantities are needed to fully specify the decay of the X: the angles Ω_X of p_Y in the X rest frame, the angles Ω_Y of p_{π^+} in the Y rest frame, and the mass of the isobar m_Y. In the Lorentz-invariant transition amplitude $\mathcal{M}$ we have found our connection between the observed intensity distribution we want to decompose and the differential cross-section which is the traditional meeting point for theory and experiment. We can now move forward and describe the procedure for the expansion of $\mathcal{I}(\tau)$ in a series of partial waves.

To begin, we write $\mathcal{M}$ in terms of the transition operator $\hat{T}$,

$$\mathcal{M} = \langle \pi^+\pi^+\pi^-n|\,\hat{T}\,|\gamma\; p\rangle\,. \tag{4.9}$$

We should mention here that in this analysis, we assume that the baryon arm of Figure 4.1 couples to the production of X only through the exchange or lack of exchange of one unit of angular momentum, neglecting higher-spin exchanges. Thus, in the following discussion, we will address only the production and decay of the 3π resonance X, leaving a detailed discussion of the baryon arm for Section 4.3.

Since we are interested in extracting the I^GJ^{PC} contributions to $\mathcal{I}(\tau)$, we choose a basis in which isospin, angular momentum, parity, and G-parity are all good quantum numbers. In the same fashion as the variable τ, we amalgamate all of the quantum numbers used to identify a given basis state into a single label α, with the understanding that later in this discussion, some of the components of α will be labeled separately for clarity. We can insert a complete set of states $\sum_{\alpha} |\alpha\rangle\langle\alpha|$ into Eq. 4.9,

$$\mathcal{M} = \sum_{\alpha} \langle \pi^+\pi^+\pi^-n|\,\hat{T}\,|\alpha\rangle\,\langle\alpha|\gamma p\rangle, \tag{4.10}$$

where α is a conglomerate of all the quantum numbers needed to specify a mesonic state and its subsequent decay:

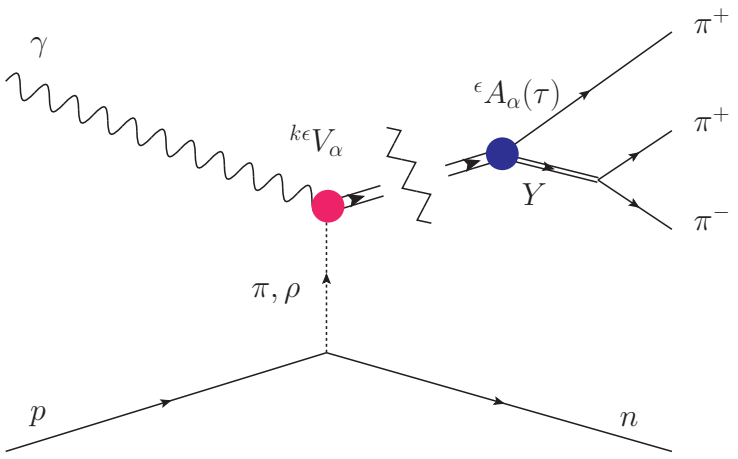

Figure 4.2: An illustration of the factorization performed within the isobar model. The diagram of Figure 4.1 is split into an amplitude $^{\epsilon k}V_\alpha$ describing the production of X and an amplitude $^{\epsilon}A_\alpha(\tau)$ describing the decay of X into three pions.

- the total spin J of X,
- the intrinsic parity P of X,
- the spin z-projection M of X,
- the spin s of the isobar Y,
- the intrinsic parity P_{Y} of Y,
- the mass m_Y of Y,
- the orbital angular momentum l between Y and the bachelor π^+.

The basis of choice for the states $|\alpha\rangle$ is the *reflectivity* basis, which is described in detail in Section 4.2.

The next step in the expansion is founded again on the isobar model description of our reaction. The production of X and its sequential decay allows us to assume that the transition operator $\hat{T}$ can be represented by the product of two operators: one for the production of the state X, and the other for the decay of X into $\pi^+\pi^+\pi^-$, as shown in Figure 4.2. It should be noted that this factorization precludes the description of any Deck-effect processes which is a nonresonant explanation for the $\pi_1(1400)$ observations, as well as any processes where the baryon interacts more substantially with the meson arm than an exchange of spin.

In any case, applying this to Eq. 4.10, we find

$$\mathcal{M} = \sum_{\alpha,\beta} \langle \pi^+\pi^+\pi^- n | \hat{T} | Y_\beta \pi^+ n \rangle \langle Y_\beta \pi^+ n | \hat{T} | X_\alpha n \rangle \langle X_\alpha n | \hat{T} | \gamma p \rangle \tag{4.11}$$

where we introduce β as a conglomerate for all the parameters required to identify the isobar Y. This factorization allows us to isolate the quantity of interest: the production amplitudes $\langle X_\alpha n|\,\hat{T}\,|\gamma p\rangle$, or simply V_α for brevity. The decay amplitudes $\langle \pi^+\pi^+\pi^- n|\,\hat{T}\,|Y_\beta \pi^+ n\rangle$ and $\langle Y_\beta \pi^+ n|\,\hat{T}\,|X_\alpha n\rangle$, combined as $A_\alpha(\tau)$ for brevity, can be calculated by a procedure detailed in Section 4.2. Since we are considering only decays via the strong force, parity and C-parity (or more generally, G-parity) must be conserved, and combined with conservation of angular momentum we can generate a list of possible configurations of α where a resonance X can decay to $\pi^+\pi^+\pi^-$.

To be exact, the expansion in Eq. 4.11 requires an infinite set of basis states to completely describe $\mathcal{M}$. Practically this is impossible, so we truncate the number of states in the basis at some value of J, taking comfort in the lack of previously-observed high-spin states in our m_X region of interest. Then, we iterate over the events in our data sample, and for each event τ_i, we calculate the overlap of τ_i with each pure state α, and obtain an amplitude. For the production amplitudes V_α, we parametrize them as complex numbers, but generally speaking they are functions of t and m_X. To justify our parametrization, we perform our partial-wave analysis in bins of m_X with the assumption that the production amplitude is constant over the bin width. We can bin in t as well to accommodate the t-dependence of V_α. With the production amplitudes parametrized as complex parameters, we use a software minimization routine to find the optimal (most probable) and minimal (in terms of number of states) mix of α configurations that describe our data. The specifics of this procedure are described in the following sections.

4.2 Decay Amplitudes

We have now expanded our intensity distribution $\mathcal{I}(\tau)$ in the following way:

$$\mathcal{I}(\tau) = \sum_\alpha |V_\alpha|^2 |A_\alpha(\tau)|^2, \tag{4.12}$$

where $A_\alpha(\tau)$ represent complex $X \to \pi^+\pi^+\pi^-$ decay amplitudes that can be calculated, V_α represent production amplitudes that are parametrized as complex numbers, to be determined by a fit to our data sample, and α contains the spin, parity, C-parity, angular momentum in the $Y\pi_b^+$ system and spin-parity of the Y of a particular state permitted to decay to $\pi^+\pi^+\pi^-$. In this section, we describe the procedure for the calculation of $A_\alpha(\tau)$.

In the helicity formalism, we calculate the overall amplitude for a particular $X \to Y\pi^+ \to \pi^+\pi^-\pi^+$ decay in a frame-by-frame, decay-by-decay fashion. The general form for a decay amplitude in an isobar model process must contain functions to describe the angular distributions of quantum-mechanical objects with spin, as well as some description for the mass-dependence of the isobar. We put this into effect by factoring $A_\alpha(\tau)$ into $A_\alpha(\Omega_X, \Omega_Y)$ for the angular portion, and then $A_\alpha(m_Y)$ for the isobar mass-dependence, such that

$$A_\alpha(\tau) \equiv A_\alpha(\Omega_X, \Omega_Y) A_\alpha(m_Y). \tag{4.13}$$

We'll look first at the form for $A_\alpha(\Omega_X, \Omega_Y)$.

The angular dependence of the decay amplitude can be described by the eigenfunctions of the quantum-mechanical rigid rotor Hamiltonian: the Wigner-D- and d-functions. They

are defined as

$$D^J_{M'M}(\alpha,\beta,\gamma) = e^{-im'\alpha} d^J_{M'M}(\beta) e^{-im\gamma}, \tag{4.14}$$

with

$$\begin{aligned} d^J_{M'M}(\beta) &= [(J+M')!(J-M')!(J+M)!(J-M)!]^{1/2} \\ &\times \textstyle\sum_S \frac{(-1)^{M'-M+S}}{(J+M-S)!S!(M'-M+S)!(J-M'-S)!} \\ &\times \left(\cos\tfrac{\beta}{2}\right)^{2J+M-M'-2S} \left(\sin\tfrac{\beta}{2}\right)^{M'-M+2S}. \end{aligned} \tag{4.15}$$

The symbols J and M represent the spin and spin-z projection, respectively. Ref. [67] gives the following form for $A_\alpha(\Omega_X,\Omega_Y)$ in terms of $D^{J*}_{M'M}(\alpha,\beta,\gamma)$,

$$A_\alpha(\Omega_X,\Omega_Y) = \tilde{l}\tilde{s} \sum_\lambda D^{J*}_{M_X\lambda}(\phi_X,\theta_X,\phi_Y) d^J_{\lambda 0}(\theta_Y) C(l0s\lambda|J\lambda) \tag{4.16}$$

where s and λ are the spin and helicity of the isobar, $C(j_1m_1j_2m_2|JM)$ is the relevant Clebsch-Gordan coefficient, and

$$\tilde{J} = \sqrt{2J+1} \tag{4.17}$$

$$\tilde{s} = \sqrt{2s+1}, \tag{4.18}$$

and the sum is over λ because Y is an internal propagator.

For the mass dependence of the isobar decay $A_\alpha(m_Y)$, Ref. [67] again guides us:

$$A_\alpha(m_Y) = F_l(p_X) F_s(p_{\pi^+}) \psi(m), \tag{4.19}$$

where $\psi(m)$ is a fully-relativistic Breit-Wigner distribution,

$$\psi(m) = \frac{m_0\Gamma_0}{m_0^2 - m^2 - im_0\Gamma_Y(m)}, \tag{4.20}$$

where

$$\Gamma_Y(m) = \Gamma_0 \frac{m_0}{m} \frac{p}{p_0} \frac{F_s^2(q)}{F_s^2(q_0)}, \tag{4.21}$$

where q and q_0 represent the center-of-mass breakup momentum for a resonance of mass m and m_0, respectively. The functions $F_l(p)$ are Blatt-Weisskopf angular momentum barrier factors [68].

So, combining $A_\alpha(\Omega_X,\Omega_Y)$ and $A_\alpha(m_Y)$, the form of the decay amplitude $A_\alpha(\tau)$ becomes:

$$A_\alpha(\tau) = \tilde{l}\tilde{s} \sum_\lambda D^{J*}_{M\lambda}(\phi_X,\theta_X,\phi_Y) d^J_{\lambda 0}(\theta_Y) C(l0s\lambda|J\lambda) F_l(p_Y) F_s(p_{\pi^+}) \psi(m) \tag{4.22}$$

However, to use Eq. 4.22 as it stands would not allow us to determine the parity of the observed states, because pure helicity states are not eigenfunctions of helicity.

To further understand this, consider the following: the CLAS g12 run acquired data with a unpolarized photon beam; in other words the photon, as a $J^P = 1^-$ particle, was equally likely to have spin z-projection $M_\gamma = \pm 1$ (since the photon is massless, $M_\gamma = 0$ is

forbidden). Furthermore, as the Gottfried-Jackson frame defines the z-axis to be along the direction of the photon beam, M_γ is called the *helicity* of the photon. Helicity is conserved by the strong force, and thus we expect the spin z-projection of the X, M, to have access to ± 1, unless of course the X is spinless. $M = 0$ is not forbidden as it is in M_γ, because the exchange of a spin-1 particle between the photon and the initial-state proton allows access to this configuration. But imagine applying the parity operator $\hat{P}$ to a pure helicity state with momentum p, spin J, intrinsic parity P, and helicity M, denoted as $|pJPM\rangle$. The parity operation negates both position and momentum vectors while having no effect on angular momenta, as they are a product of position and momentum vectors. Assuming the X is traveling in the positive z direction, parity will invert the direction of travel but leave the angular momentum unchanged. This means when we measure the helicity again by taking the projection of the spin along $\hat{p}_\mathrm{X}$, it will now be -1, since it's still pointing in the original direction of travel. Mathematically, we find

$$\hat{P}\,|pJPM\rangle = P\,|-pJP-M\rangle\,; \tag{4.23}$$

thus pure helicity states are not eigenstates of parity. This is a serious concern because we are trying to find contributions to our intensity distribution of states which *are* eigenstates of parity. To restore parity as a good quantum number, we must perform a change of basis.

A basis that restores parity can be built from a simple linear combinations of helicity states. The correct construction of these states, as detailed in Ref. [69], involves the introduction of the reflectivity operator $\hat{\epsilon}$, defined as:

$$\hat{\epsilon} = \hat{P}e^{-i\pi J_y}, \tag{4.24}$$

where $\hat{P}$ is parity operator and $e^{-i\pi J_y}$ represents a 180° rotation through the x-z plane, which is the same as the production plane in the rotated rest frames in which we do these calculations. One can then define eigenstates $|\epsilon JPM\rangle$ of $\hat{\epsilon}$ as:

$$|\epsilon JPM\rangle = \left[|JPM\rangle + \epsilon P(-1)^{J-M}\,|JP-M\rangle\right]\Theta(M) \tag{4.25}$$

where $\Theta(M)$ is simply

$$\Theta(M) = \begin{cases} \frac{1}{\sqrt{2}} & \text{if } M > 0 \\ \frac{1}{2} & \text{if } M = 0 \\ 0 & \text{if } M < 0 \end{cases} \tag{4.26}$$

The eigenvalues of ϵ are ± 1. Additionally, as ϵ appears in both sides of Eq. 4.25 we have a choice in defining which combinations are $\epsilon = +1$ and which are $\epsilon = -1$. We adopt the convention of choosing $\epsilon = \eta$, where η is the *naturality* of the exchange, defined as:

$$\eta = P(-1)^J \tag{4.27}$$

where P and J in this context are the spin and parity of the exchange particle. Thus by examining the strengths of waves by their reflectivities, we immediately learn about

the process by which these states were produced. As a further example, constructing a reflectivity eigenstate for a decay of the $J^{PC} = 1^{++}$ $a_1(1260)$ in the $|\epsilon JPM\rangle = |1111\rangle$ state:

$$|1111\rangle = \frac{1}{\sqrt{2}} \left[|111\rangle + \epsilon P (-1)^{J-M} |11-1\rangle \right] \tag{4.28}$$

$$|1111\rangle = \frac{1}{\sqrt{2}} \left[|111\rangle + |11-1\rangle \right] \tag{4.29}$$

In addition, states of differing reflectivity do not interfere, as they are in separate blocks of the now block-diagonal spin-density matrix. We can then re-label our decay amplitudes $A_\alpha(\tau)$ as:

$$A_\alpha(\tau) \equiv {}^{\epsilon}A_\alpha(\tau) \tag{4.30}$$

where ϵ is now the sole index by which states can interfere and α now contains the remainder of the quantum numbers required to completely identify the state.

With Eq. 4.25, we can rewrite the angular component $A_\alpha(\Omega_X, \Omega_Y)$ of the decay amplitude in the reflectivity basis,

$${}^{\epsilon}A_\alpha(\Omega_X, \Omega_Y) = \tilde{l}\tilde{s} \sum_\lambda \Theta(m) \left[D^{J*}_{M\lambda}(\theta_X, \phi_X, \phi_Y) + \epsilon D^{J*}_{M\lambda}(\theta_X, \phi_X, \phi_Y) \right] d^s_{\lambda 0}(\theta_Y) C(l0s\lambda|J\lambda). \tag{4.31}$$

The mass-dependence of the isobar remains the same after the change of basis, so we can write ${}^{\epsilon}A_\alpha(\tau)$ as

$${}^{\epsilon}A_\alpha(\tau) = {}^{\epsilon}A_\alpha(\Omega_X, \Omega_Y) A_\alpha(m_Y) \tag{4.32}$$

For the $\pi^+\pi^+\pi^-$ final state, total amplitude is then symmetrized with respect to the two identical π^+.

Now, finally, it is possible to insert the values of Ω_X, Ω_Y, and m_Y for each event into Eq. 4.32 to obtain a complex number which measures the agreement between the observed event τ_i and the hypothesis configuration α. With a list of the values of the amplitudes for each event and each hypothesis state $|\epsilon\alpha\rangle$, we now need to determine how much of each hypothesis is in $\mathcal{I}(\tau)$. These strengths are found in the squares of the production amplitudes, which we now label ${}^{\epsilon k}V_\alpha$, and we discover these strengths using the extended maximum likelihood method.

4.3 Production Amplitudes and the Extended Maximum Likelihood Method

Our treatment of the decay amplitudes has brought us to the reflectivity basis, and now our expansion of the intensity distribution $\mathcal{I}(\tau)$ has the following form:

$$\mathcal{I}(\tau) = \sum_{k\epsilon\alpha\alpha'} {}^{\epsilon k}V^*_\alpha \, {}^{\epsilon k}V_\alpha \, {}^{\epsilon}A^*_\alpha(\tau) \, {}^{\epsilon}A_\alpha(\tau) \tag{4.33}$$

where ϵ denotes the eigenvalue of reflectivity, α is the amalgamation of the rest of the quantum numbers of the state, and the new index k is indicative of the *rank* of the *spin-density matrix* ${}^{\epsilon}\rho_{\alpha\alpha'}$. The spin-density matrix and its rank are discussed in more detail

at the end of this section. We deduce the production amplitudes ${}^{\epsilon k}V_\alpha$ by parametrizing them as complex numbers. As outlined in Section 4.1, the ${}^{\epsilon k}V_\alpha$ generally are a function of m_X and t, but we study the dependence in m_X by performing our partial-wave analysis in narrow bins of m_X. The t dependence can be removed by binning in t as well. Then, with ${}^{\epsilon k}V_\alpha$ represented by complex parameters, we perform an extended maximum-likelihood fit in each m_X bin to determine the mixture of different decay states $|\epsilon\alpha\rangle$.

The maximum likelihood method is a statistical procedure which can be used to match a parametrized model to a sample of data. In this way it is similar to the familiar method of least squares, except where least-squares regression deals with *distances* between measurements and model predictions, the maximum likelihood method (MLM) deals with *probabilities*. Specifically, the central quantity of interest in an MLM analysis is the *likelihood*, or $\mathcal{L}$:

$$\mathcal{L} = \prod_i P_i(\boldsymbol{x}) \tag{4.34}$$

where P_i is the probability of the ith measurement occurring according to some model dependent on parameters contained in $\boldsymbol{x}$. One then seeks to maximize the collective probability of making the whole set of measurements.

In our case, since the intensity $\mathcal{I}(\tau)$ over our set of n events is the result of a sum of squares of quantum-mechanical states, it is already a probability distribution, apart from normalization:

$$\mathcal{L} \propto \prod_i^n \mathcal{I}(\tau_i) \tag{4.35}$$

In order to properly normalize $\mathcal{L}$, we follow the procedure described in Ref. [67].

Our data sample consists of n events. The observation of n events is itself a probabilistic occurrence, because if the experiment were run again with identical conditions, chance might lead us to yield a different number of events. Thus we should introduce a Poisson distribution as part of our definition of $\mathcal{L}$,

$$\mathcal{L} \propto \frac{\bar{n}^n}{n!} e^{-\bar{n}} \prod_i^n \mathcal{I}(\tau_i) \tag{4.36}$$

We have now moved from the maximum likelihood method to the *extended* maximum likelihood method, since the number of measurements is a statistical quantity as well as the measurements themselves.

The likelihood of observing n events given their associated values of τ is also directly dependent on the detector's ability to measure events occurring at τ. This τ-dependent ability to measure events is known as the *acceptance* of the detector, and is denoted by $\eta(\tau)$. Inserting $\eta(\tau)$ into the likelihood function, we find

$$\mathcal{L} \propto \frac{\bar{n}^n}{n!} e^{-\bar{n}} \prod_i^n \frac{\mathcal{I}(\tau_i)}{\int \mathcal{I}(\tau)\eta(\tau)d\tau} \tag{4.37}$$

The factor of $\bar{n}^n$ can be canceled by applying the definition of the expectation value,

$$\bar{n} = \int \mathcal{I}(\tau)d\tau, \tag{4.38}$$

leaving

$$\mathcal{L} \propto \frac{1}{n!} \exp\left[- \int \mathcal{I}(\tau) d\tau \right] \prod_{i}^{n} \mathcal{I}(\tau_i). \tag{4.39}$$

In the ideal case one could find an analytical form for $\eta(\tau)$ and thus get an event-by-event normalization. However, analytical forms for the acceptances of real-world detectors are hard to come by, and thus we must rely on monte-carlo methods for generating acceptance. Following the procedure of Section 3.4, we acquire a set of *raw monte-carlo* events that has been generated uniformly according to the available 3π phase space, and a set of *accepted monte-carlo* events that has survived the CLAS simulation and reconstruction process. We normalize by calculating the decay amplitudes for all raw monte-carlo events and all accepted monte-carlo events, for all states $|\epsilon\alpha\rangle$. The sums of these we define to be:

$${}^{\epsilon}\Psi^{r}_{\alpha\alpha'} = \frac{1}{n_r} \sum_{i}^{n_r} {}^{\epsilon}A_{\alpha}(\tau_i)\ {}^{\epsilon}A^{*}_{\alpha}(\tau_i) \tag{4.40}$$

$${}^{\epsilon}\Psi^{a}_{\alpha\alpha'} = \frac{1}{n_a} \sum_{i}^{n_a} {}^{\epsilon}A_{\alpha}(\tau_i)\ {}^{\epsilon}A^{*}_{\alpha}(\tau_i) \tag{4.41}$$

Normalizing the likelihood to the number of events observed and taking the logarithm of the whole expression, we find

$$\log\ \mathcal{L} = \sum_{i}^{n} \log \left[\sum_{k\epsilon\alpha\alpha'} {}^{\epsilon k}V_{\alpha}\ {}^{\epsilon k}V^{*}_{\alpha}\ {}^{\epsilon}A_{\alpha}(\tau_i)\ {}^{\epsilon}A^{*}_{\alpha}(\tau_i) \right] - n \left[\sum_{k\epsilon\alpha\alpha'} {}^{\epsilon k}V_{\alpha}\ {}^{\epsilon k}V^{*}_{\alpha}\ {}^{\epsilon}\Psi^{a}_{\alpha\alpha'} \right]. \tag{4.42}$$

Eventually we want to use optimization software to find values of ${}^{\epsilon k}V_{\alpha}$ that maximize the likelihood, so it is in this spirit that we prefer to work with $\log\ \mathcal{L}$ rather than $\mathcal{L}$ itself. The same values of ${}^{\epsilon k}V_{\alpha}$ that maximize $\mathcal{L}$ will maximize $\log\ \mathcal{L}$, but the derivatives of $\log\ \mathcal{L}$ are easier to calculate and the numerical precision is more reliable for small values of $\log\ \mathcal{L}$ (a sum of terms) than for $\mathcal{L}$ (a product of terms). Furthermore, in the optimization only terms proportional to ${}^{\epsilon k}V_{\alpha}$ will factor into the determination of the maximum; additional factors not dependent on ${}^{\epsilon k}V_{\alpha}$ can only shift the likelihood space up or down. Thus we have dropped all terms not dependent on ${}^{\epsilon k}V_{\alpha}$.

Finally, a word on the index k that has been lurking throughout this section. In Section 4.2, we mentioned that the baryon arm couples to the production of the X resonance only through the exchange or non-exchange of a single unit of angular momentum. That is, the proton in the initial state and the neutron in the final state are both spin-$\frac{1}{2}$ particles; it is possible that before the interaction, the proton has spin z-projection $M_z = +\frac{1}{2}$, and afterward, the neutron has $M_z = -\frac{1}{2}$, or vice-versa. We call such an interaction a *spin-flip* interaction. It is also possible that no such change in M_z occurs during the interaction, and we call those *spin-nonflip*. The net effect of this degree of freedom is that it adds an extra dimension to the spin-density matrix ${}^{\epsilon}\rho_{\alpha\alpha'}$. The spin-density matrix contains all of the spin information available about a given quantum system; its diagonal elements give the probabilities of various states, and its off-diagonal elements give information about the interferences between different states. It has a simple form in terms of the production

amplitudes,

$$^{\epsilon}\rho_{\alpha\alpha'} = \sum_{k} {}^{\epsilon k}V_{\alpha}\ {}^{\epsilon k}V^{*}_{\alpha} \tag{4.43}$$

The change of basis to eigenstates of reflectivity *diagonalizes* the spin-density matrix; in other words, it puts the spin-density matrix into a form where states of $\epsilon = +1$ occupy one region, and those of $\epsilon = -1$ occupy another. Thus states with differing reflectivity do not interfere. Additionally, states produced via spin-flip processes do not interfere with processes produced in spin-nonflip processes. We commonly denote the rank of the spin-density matrix via Roman numerals; thus inclusion of reflectivity and flip-nonflip in the spin-density matrix makes it of rank II. This means four non-interfering sets of production amplitudes ${}^{\epsilon k}V_{\alpha}$ will be used in the fits to describe the data. Rank considerations for the titular analysis are described in the next Chapter.

4.4 Observables

A successful bin-independent partial-wave analysis has two main quantities of interest: the event yields for a specific partial wave and the differences in the complex phase between two partial waves. Both are calculated independently in each bin and are plotted as a function of the resonance mass, to study the mass dependence of the physics at work in the analysis.

The event yield, or partial-wave intensity, is proportional to the square of the complex number that is the production amplitude. One can examine the intensity for a single partial wave in the fit basis, or for a coherent sum of many waves. These intensities should of course be normalized to the number of data events in each bin. Of course, the number of data events in each bin n_d is a function of the acceptance, so we should scale the number of observed data events by the inverse of the acceptance in that bin, or $\frac{n_r}{n_a}$. The formula is the following:

$$N = \frac{n_d n_r}{n_a} \sum_{\alpha\alpha'} V_{\alpha} V^{*}_{\alpha'}\ {}^{\epsilon}\Psi^{r}_{\alpha\alpha'} \tag{4.44}$$

where α represents a single partial wave or a enumeration of a subset of partial waves. Studying N as a function of the resonance mass can give clues to resonant behavior in a given partial wave, just like peaks in the overall resonance mass spectrum can indicate the presence of bound states. Peaks with shapes reminiscent of a Breit-Wigner amplitude are the most common indication of resonance behavior, but one cannot rely on the intensity alone to conclusively identify a partial wave as resonant or nonresonant. Interference between two states can cause dips in the intensity instead of peaks, or a resonant state can have its lineshape distorted by kinematics or its own internal dynamics. Furthermore, a false peak can appear due to *leakage* between partial waves, discussed further in Chapter 5.

We can make a more conclusive measurement by examining the phase difference $\delta\phi$ between two partial waves. Our production amplitudes are complex numbers, and the partial-wave intensity uses their magnitude. We can use the complex phase by looking for changes in the phase over a mass region of interest. Waves which are produced with a Breit-Wigner amplitude do so with a 180° rise in phase across the pole mass. As a single phase is cyclic and thus ambiguous, we need to examine a difference of phases between

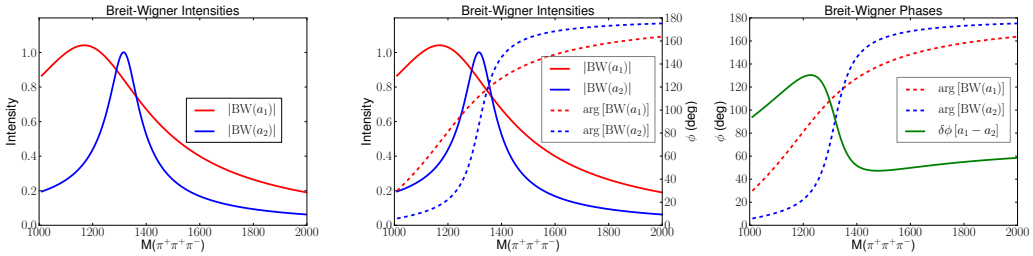

Figure 4.3: An illustration of the phase difference technique in determining resonant behavior. Two Breit-Wigner resonances with parameters of the $a_1(1260)$ (red) and $a_2(1320)$ (blue) mesons are created. The leftmost plot shows the intensity or norm of the complex Breit-Wigner amplitude for each state. In the center, the overlaid dotted curves are the complex phases of the resonances. On the right, the difference of the two dotted curves is shown in green, providing an example of the shape of resonant phase motion.

two waves to see something physically meaningful. Typically, one examines the phase of a suspicious partial wave against one that corresponds to a well-known state. If one sees only phase motion of the well-known state, then there is no evidence for resonant behavior in the suspicious wave. If the phase motion of the well-known state is abbreviated in some fashion, then the suspicious wave may be in fact resonant. This effect is illustrated using the PDG values for two known states, the $a_1(1260)$ and $a_2(1320)$, in Figure 4.3.

The phase difference is valuable because it is independent of the intensity; its uncertainties correspond only to the uncertainty of the production amplitudes, not the number of events observed or simulated. Thus one can identify very small resonant signals by their phase motion. Based on previous results, we expect the intensity for the 1^{-+} to be small; thus, the phase motion will be crucial in the identification of the $\pi_1(1600)$ in our $\gamma p \to \pi^+\pi^+\pi^- n$ sample.

4.5 Summary

We assume that our events are well-described by the isobar model. Our observed intensity distribution $\mathcal{I}(\tau)$ is decomposed into a sum of terms composed of independent production and decay amplitudes,

$$\mathcal{I}(\tau) = \sum_{k\epsilon bb'} {}^{\epsilon k}V_{\alpha}^{*}\ {}^{\epsilon k}V_{\alpha}\ {}^{\epsilon}A_{\alpha}^{*}(\tau)\ {}^{\epsilon}A_{\alpha}(\tau) \tag{4.45}$$

The decay amplitudes for each data event are calculated by taking products of Wigner-D and -d functions in the rest frame of each decay. The production amplitudes are determined by performing an extended maximum-likelihood fit to determine the optimal mix of states α. Fits are performed on data binned in m_X and t to remove the dependence of ${}^{\epsilon k}V_{\alpha}$ on those variables. The actual function maximized, including normalization and acceptance,

is

$$\log\ \mathcal{L} = \sum_{i}^{n} \log \left[\sum_{k\epsilon\alpha\alpha'} {}^{\epsilon k}V_{\alpha}\ {}^{\epsilon k}V_{\alpha}^{*}\ {}^{\epsilon}A_{\alpha}(\tau_i)\ {}^{\epsilon}A_{\alpha}(\tau_i)^{*} \right] - n \left[\sum_{k\epsilon\alpha\alpha'} {}^{\epsilon k}V_{\alpha}\ {}^{\epsilon k}V_{\alpha}^{*}\ {}^{\epsilon}\Psi_{\alpha\alpha'}^{a} \right]. \quad (4.46)$$

The specifics of this procedure, including wave sets, software tools, binning, and background parametrizations are described in the following Chapter.

CHAPTER 5

PARTIAL-WAVE ANALYSIS PROCEDURE AND FIT RESULTS

In this Chapter, the specifics of the partial-wave analysis (PWA) procedure are described in detail, followed by results from several fits whereby we have determined the major partial waves contributing to our overall intensity distribution. Secondary effects due to rank, event selection, and wave selection are also briefly discussed. Our conclusions follow in Chapter 6.

5.1 Preparation of g12 $\gamma p \to \pi^+\pi^+\pi^-n$ Event Sample

The preparation of our sample of 510K $\gamma p \to \pi^+\pi^+\pi^-n$ events begins with binning our data in the 3π invariant mass. In step with Section 4.3, we would like to parametrize the production strengths of our hypothesis states as complex numbers. In order to justify such a parametrization, we should sample the production amplitude space by performing independent analyses over many small regions of 3π mass and t.

At first glance, we would like to bin as finely as possible, because as we narrow the bins, our assumption that the 3π mass dependence of the production amplitudes is constant over the width of a bin becomes more valid. Also, binning finely allows the states we observe to assume their natural decay widths, making a mass-dependent analysis more accurate. However, the more events we have in a given bin, the more leverage the minimizer has to correctly determine the most probable mix of production amplitudes. Conversely, having too few events in a given bin will increase the chances of the minimizer finding a local minimum, either because the likelihood space is not well-sampled or because of statistical fluctuation. This can adversely affect a mass-dependent analysis by blurring the intensity distributions. Furthermore, maintaining a high event count is especially important as we increase the number of partial waves in the fit. For this analysis, we feel most comfortable maintaining a ratio of about 500 events per wave, and thus we find that binning in 3π mass bins 20 MeV in width from 1 to 2 GeV is an optimal choice. This reduces our sample size to 494K events.

Also, we will need to be cautious at the uppermost end of our 3π mass range. In addition to the minimum momentum transfer $|t_0|$ defined in Eq. 3.14, there also exists a *maximum*

momentum transfer $|t_1|$, defined as

$$t_1 = \left[\frac{m_n^2 - m_X^2 - m_p^2}{2\sqrt{s}}\right]^2 - (p_\gamma^{CM} + p_X^{CM})^2 \tag{5.1}$$

where the only change from Eq. 3.14 is that the difference between center-of-mass momenta becomes the sum. This means that for our case, there is some M_X whereby t_0 becomes *equal* to t_1 and thus we can no longer produce *any* 3π resonances. This limit is about 2.4 GeV, far enough away to confidently measure any $\pi_1(1600)$ production we find. However this effect combined with our diminishing acceptance at large 3π mass prevents us from making a claim on any states heavier than 1.8 GeV, thus ruling out a search for the $\pi_1(2000)$.

With 50 bins from 1 to 2 GeV, we keep on average 10K events in each bin, with up to 30K events in the single largest bin (1300-1320 MeV), and about 11K events in bins from 1500 to 1700 MeV. Once the events are binned in 3π mass, we iterate through the bins, calculating for every event and every allowed intermediate state its decay amplitude via the formalism of Section 4.2. This calculation is performed by the `gamp` program [70], and the resulting amplitudes are saved to disk for later input into the minimizer. The set of allowed intermediate states for a meson decaying to $\pi^+\pi^+\pi^-$ is described in Section 5.2.3.

The study of the t-dependence of the production amplitudes is complicated by the acceptance of CLAS. As we explore samples with larger values of t, we are also allowing in increasing amounts of baryon background that may obfuscate any t-dependence. Thus instead of doing multiple fits in different bins in t, we will average the t-dependence of the production amplitudes over the region of t' selected in Section 3.2.2.

5.2 Fitting Procedure

Below, we discuss the details of the minimization, including the software tools used to maximize the likelihood function, the process for selecting waves to include in a given fit, and methods to determine the stability and quality of a given fit.

5.2.1 Minimization

We would like to find the values of production amplitudes that make the dataset we observe the most probable one for a given set of intermediate states. As described in Section 4.3, the likelihood function is the tool we use to achieve this goal. The most probable dataset is the one where the likelihood function is maximized; thus we need a software routine to systematically vary the production amplitudes included in the fit until the likelihood reaches its maximal value.

For this task, we use the software package `MINUIT` [71]. `MINUIT` is designed to find parameters that will *minimize* a function, so we supply it with the negative of the logarithm of the likelihood, mostly for numerical precision reasons.

The parameters themselves are the real and imaginary components of the production amplitudes. We find that `MINUIT` converges rapidly and reliably with the production amplitudes in rectangular form, rather than a strength and phase. Also, as we have the freedom to define an overall phase, we choose to fix the imaginary component of the $2^{++}1^+$ $\rho\pi$

D-wave to be zero, as the $2^{++}1^{\epsilon}D$ waves are the most strongly represented in our data and thus are present in every fit that we perform.

Actual set-up and execution of `MINUIT` commands, as well as many other aspects of our partial-wave analysis were handled by the `ruby-pwa` software package [72].

5.2.2 Fit Quality

As we are dealing with a likelihood space of dozens of parameters, it is quite possible that `MINUIT` could find a local minimum and thus give us incorrect values for the production amplitudes. In order to ensure the correct minimum is found in every fit, several strategies are used. The first strategy, *shotgunning*, is to perform each mass-independent fit multiple (at least ten) times with randomized initial values, selecting as the correct minimum the fit with the smallest likelihood. Parallel computing allows us to expedite this process by fitting all bins simultaneously, as each minimization is completely independent.

A second strategy is to *track* across the bins in 3π. The best minimum for a *seed* bin is found by performing multiple fits with randomized initial values for the parameters, and then the adjacent bins are fit using the final parameters from the first bin as initial parameters. Then bins adjacent to the second and third bins can be fit in the same manner, and so on, until all bins have been fit using the final values of the previous bins, "fanning out" in a sense from the seed bin. This method has the added benefit of rapid convergence for subsequent bins, as the production amplitudes vary smoothly over the 3π mass range. But since each bin is dependent on its predecessor, we cannot fully parallelize the process like in the former case; bins above the peak and bins below the peak are independent and can be performed in parallel, but no more.

In terms of execution speed, both algorithms are comparable, provided sufficient CPU power is available for parallelization. For a million events across fifty bins, we find that a tracked fit with twenty partial waves with the upper and lower ranges computed independently on two cores of an AMD Opteron 6174 processor takes about an hour. Running the same fit via the shotgun method on four Opteron 6174 processors, each with twelve cores, also takes about an hour. We also find that the two strategies give results that are in good agreement; one can see this demonstrated in Figure 5.1, where the minimal likelihoods found by the two methods are compared. The results presented have been obtained via the tracking method, with the shotgunning method used to confirm that our solution is free of local minima.

Finally, while a χ^2 fit has a natural measure for goodness-of-fit, there is no universally-accepted method for determining the quality of an unbinned maximum likelihood fit. Multiple fits performed with the same model, same number of parameters, on the same data may have the values of their likelihoods compared, as in the shotgun method we employ, but comparing likelihoods between two different parameter sets gives no quantitative measure of how well the model matches the data.

However, one can get a qualitative estimate of the quality of a given waveset in describing the data by doing an analysis of a *weighted monte-carlo* dataset. After a fit is performed on real data, one takes a sample of raw phase-space monte-carlo events and calculates a weight

$$W_{i,\alpha} = V_{\alpha}^{*} V_{\alpha} A_{i,\alpha}^{*} A_{i,\alpha} \tag{5.2}$$

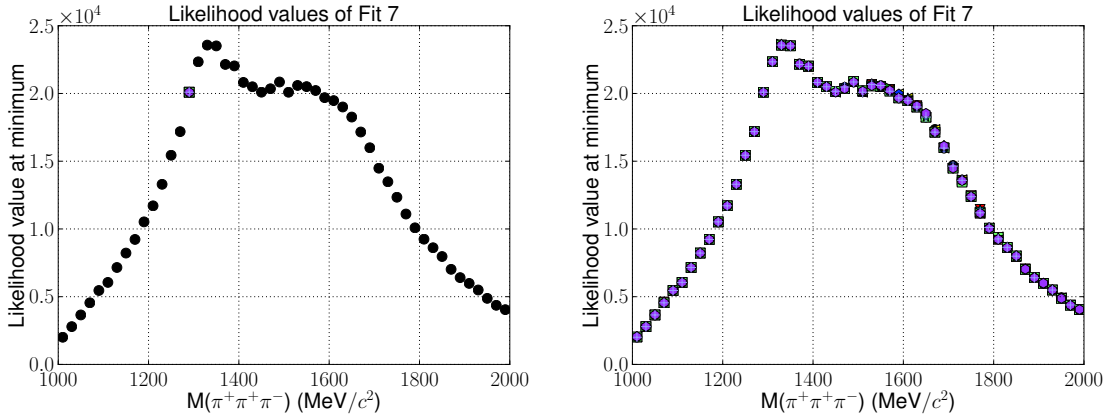

Figure 5.1: The values of the likelihood function at its minimum for each bin for the waveset in Appendix B.1. The likelihood of the tracking method is shown on the left, and the values for the shotgun method are on the right. The special point at 1280 MeV on the left is the location of the "seed" bin, where ten iterations are performed before forking off to the high- and low-mass sides.

for each wave α and each event i. Summing the weights over α, one then obtains a single number for each event quantifying the overlap of its kinematics with the measured production amplitudes. One then normalizes each weight to the maximum weight to get a number between 0 and 1 for each event. Comparing these events to a list of the raw events later accepted by GSIM, we throw out those that are not accepted. Of those remaining, we perform a random selection biased by the normalized event weights calculated previously of N monte-carlo events, where N is the number of events in the real data sample. The accepted four-vectors for these events are written out to disk. Then, in analyzing this collection of accepted monte-carlo events, we should find that the experimental distributions of our real data are reproduced by this weighted monte-carlo dataset. These distributions are often called the *predicted distributions* of the fit. If not, then we have obtained a set of production amplitudes that poorly describe our data.

Furthermore, we also use this method to test suspicious waves for *leakage*. Leakage arises when the partial-wave basis is no longer orthogonal, typically due to an incomplete understanding of the detector acceptance or the finite resolution of the detectors themselves. When the partial-wave basis is not orthogonal, events can have strong overlaps with more than one decay amplitude. We test for leakage by "zeroing out" a suspicious wave α when we generate our weighted monte-carlo dataset. Then we calculate the decay amplitudes $A_\alpha(\tau)$ for each event in our mock data, and perform a partial-wave fit including the suspicious wave. Any intensity shown by the suspicious wave in the resulting yields is due to leakage from other waves.

Given the absence of a quantitative measure of fit quality, determining the combination of partial waves which best describe the observed intensity distribution can be a complex task. The next Section discusses how this is performed in this analysis.

L	$\mathbf{f_0\pi}$	$\boldsymbol{\rho\pi}$	$\mathbf{f_2(1270)\pi}$	$\boldsymbol{\rho_3(1690)\pi}$
S	0^{-+}	1^{++}	2^{-+}	3^{++}
P	1^{++}	0^{-+}, $\boxed{1^{-+}}$, 2^{-+}	1^{++}, 2^{++}, 3^{++}	
D	2^{-+}	1^{++}, 2^{++}, 3^{++}	0^{-+}, $\boxed{1^{-+}}$, 2^{-+}, $\boxed{3^{-+}}$, 4^{-+}	
F	3^{++}	2^{-+}, $\boxed{3^{-+}}$, 4^{-+}		
G	4^{-+}	3^{++}, 4^{++}, 5^{++}		

Table 5.1: The allowed spin-parities for a $\pi^+\pi^+\pi^-$ system in the isobar model. States allowed to decay to $\sigma\pi$ and $f_0(980)\pi$ have been grouped together because the quantum numbers of the σ and f_0 are identical. Exotic J^{PC} states are boxed; the $\pi_1(1600)$ has $J^{PC} = 1^{-+}$, and has been previously observed decaying to $\rho\pi$ [40], [42]. Higher-L states for the $f_2(1270)$ and $\rho_3(1690)$ have been omitted because the mass of a parent resonance decaying through such modes would likely be greater than 2 GeV.

5.2.3 Wave Selection

In order to build up a set of partial waves capable of describing our data, we must first determine what basis we can choose from. Candidate states must conserve *all* of the symmetries of the strong interaction in their production; however for the following discussion, we will concern ourselves only with angular momentum, parity, G-parity, and isospin.

To deduce the allowed values of these quantities, we begin in the initial state with the photon ($J^P = 1^-$) and the proton ($J^P = \frac{1}{2}^+$). From the discussion of Section 4.3, we can produce a $\pi^+\pi^+\pi^-n$ final state via four different non-interfering routes, but for this analysis, the rank of the spin-density matrix is reduced to I by the dominance of pion exchange as the production mechanism. In practice, a comparison of rank II and rank I fits, discussed in detail in Appendix C.2, shows rank I to produce much cleaner results.

As the photon and the exchange particle can interact with any relative orbital angular momentum, all spins are available to be produced. Additionally, as we would like to avoid making assumptions about the production mechanism, we can enforce the rest of the symmetry requirements by working backward from the $\pi^+\pi^+\pi^-$ final state. The neutral pion has quantum numbers $J^{PC} = 0^{-+}$; as we are dealing with charged pions, we use G-parity, defined in Eq. of Section 1.2. According to that definition G-parity of the pion then negative, as is the overall G-parity of the 3π system.

Orbital angular momentum is most easily addressed in the isobar model. We associate a π^+ with the π^- in the isobar and then define an orbital angular momentum between the isobar and the bachelor π^+. The isobars themselves can be any resonance that conserves angular momentum, parity, G-parity, and isospin, both in their own $\pi^+\pi^-$ decay and in combination with the bachelor π^+.

The $\pi\pi$ system has positive G-parity, as the G-parity of the individual pions is negative.

That means that even-spin isobars must be isoscalar, while odd-spin isobars are isovectors. Furthermore, the parity P of the $\pi\pi$ system matches the orbital angular momentum in the system; even values of L have even parity, and odd values of L have odd parity. C-parity can be deduced from the G-parity constraint and follows the same prescription as P. Taking all of these criteria into account, the candidate isobars Y in order of increasing mass are:

$$Y = \sigma,\ \rho(770),\ f_0(980),\ f_2(1270),\ \rho_3(1690) \tag{5.3}$$

where the names are according to the convention described in Table 1.1. Heavier isobars will be suppressed by the lack of available phase space.

Each of the isobars Y can be combined with the bachelor π^+ and given any value of orbital angular momentum, and the values of C, P, and spin of a parent state can be deduced therefrom. A listing of possible states up to $J = 4$ decaying to $\pi^+\pi^+\pi^-$ can be found in Table 5.1. The truncation of our basis at $J = 4$ is motivated by a lack of observed states with total spin greater than 4 in the mass region from 1 to 2 GeV. Some states have also been removed because if they exist, their masses are unlikely to be less than 2 GeV; those culled include the resonances decaying to $f_2\pi$ in F- and G-wave decays, as all $\rho_3\pi$ decays with orbital angular momentum. There are 11 unique J^{PC} combinations among those listed in Table 5.1, three of them exotic. Taking into account their various decay modes gives 28 different possible states, and then considering only $M^\epsilon = 1^\pm$ waves for all states with $J > 0$ makes for 53 possible partial waves in a rank I fit.

However, most of these candidates will make an insignificant contribution to describing our data. Some should be suppressed by our production mechanism; spin-0 states, for example, should make a minimal contribution because they cannot be produced by a photon interacting via pion exchange. Also, some will form bound states, but only at masses near or greater than 2 GeV, where our sensitivity is limited, as described in Section 5.1.

Deducing the waveset which best describes our data is thus a process of trial and error, guided by our physical intuition. While mathematically speaking, our intensity distribution will be increasingly well-described by an increasingly-large basis of waves, we know physically that the intensity is due to a limited number of resonant decays plus interfering and non-interfering backgrounds. Thus we seek to identify those waves which make the most significant contributions to our overall observed intensity spectrum, and without which the data would be poorly described.

To come up with a list of hypotheses for our major contributors, we can study our intensity distribution in the context of well-known isovector states decaying to 3π. As discussed in Section 3.3, the dominant feature of the 3π invariant mass spectrum is a peak at about 1300 MeV. The Dalitz plot for events in the 1200 to 1400 MeV mass region, shown in Figure 3.41, shows strong evidence for decays to $\rho\pi$. The $a_2(1320)$ fits all of these observations well; thus we should be sure to include the 2^{++} waves decaying to $\rho\pi$.

Also prominent in the intensity distribution is the shoulder from 1500 to 1700 MeV. The Dalitz plot in Figure 3.41 shows strong evidence for an isobar around 1275 MeV in this region, consistent with the $f_2(1270)$. Some evidence for $\rho\pi$ decay is visible as well. The $\pi_2(1670)$ fits these observations, decaying predominantly to $f_2\pi$ and also significantly to $\rho\pi$. We should then include 2^{-+} waves decaying to $f_2\pi$ and $\rho\pi$. Of course, this region is also where we would expect to see the $\pi_1(1600)$, if it is produced. So we will also include 1^{-+} waves decaying to $\rho\pi$ to search for the $\pi_1(1600)$.

Finally, with all the visible features accounted for, we survey the spectrum of well-established isovector mesons 1 to 2 GeV in mass with parity and C-parity accessible to 3π. From these we find the 1^{++} waves to be a prudent inclusion, as the $a_1(1260)$ has been observed decaying to $\rho\pi$ and $f_2\pi$.

So in summary, we expect the 2^{++} and 2^{-+} to contribute heavily. The $a_1(1260)$ and $a_1(1700)$ mesons have been observed in the 1^{++} partial waves in the pion-produced 3π system, but not yet in charge-exchange photoproduction [51], [73]. It would be an interesting result if we observed any sign of the a_1, so we include waves of $J^{PC} = 1^{++}$ as well. As we are producing our $\pi^+\pi^+\pi^-n$ final state via pion exchange with unpolarized photons, we expect waves with $M^\epsilon = 1^\pm$ to be dominant and produced in equal proportions. As spin-0 waves should be suppressed by pion exchange, so too should $M = 0$ projections be suppressed. Previous experimental results in pion production lead us to expect production of the $\pi_1(1600)$ at the level of a few percent of the $a_2(1320)$.

5.3 Fit Results

This section describes in detail the results we have obtained from performing a partial-wave analysis on our sample of $\gamma p \to \pi^+\pi^+\pi^-n$ events from the CLAS g12 dataset. Hundreds of fits have been performed to determine the partial waves which make the most significant contributions to describing our data. Complete results from several of our best fits are located in Appendix B. Here, we will summarize the results pertinent to our conclusions. All intensities shown in this section are corrected for acceptance. In addition to the $J^{PC}M^\epsilon$ notation introducted in Chapter 1, we will append another label of the form $[Y\pi]_L$, where Y is the PDG state whose parameters are used for the isobar, π represents the bachelor π^+, and L is the relative orbital angular momentum between Y and π_b^+.

5.3.1 $2^{++}\,[\rho(770)\pi]_D$

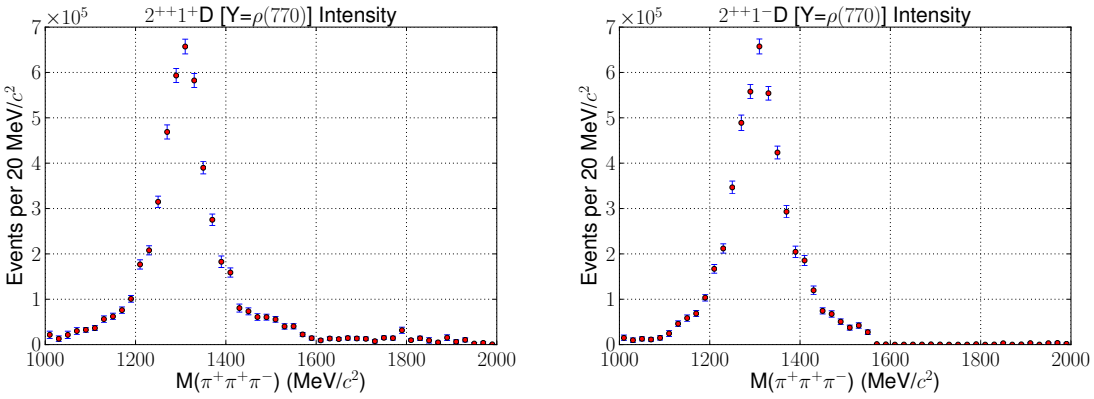

Figure 5.2: Typical 2^{++} intensity spectra; the $2^{++}1^+D$ is on the left, and the $2^{++}1^-D$ is on the right.

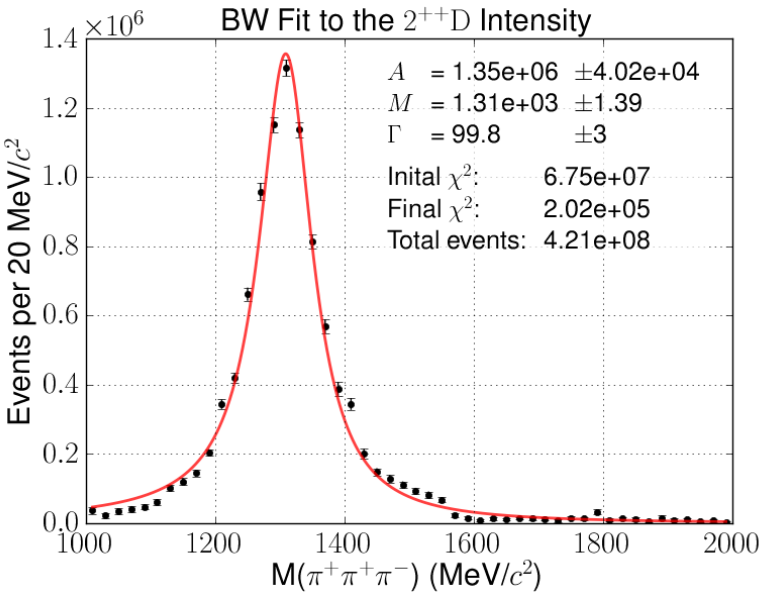

Figure 5.3: A Breit-Wigner fit of the total 2^{++} intensity, as measured by our minimal waveset.

In every fit we performed, the waves most strongly represented were the $2^{++}1^{\epsilon}\ [\rho\pi]_D$ partial waves. In line with our expectations for photoproduction via pion exchange, the dominant contribution comes from the $J^{PC}M^{\epsilon} = 2^{++}1^{\pm}$ states. The intensities for these two waves are shown in Figure 5.2. Both exhibit as their lone feature a large peak at 1.3 GeV. This peak is the dominant feature of our 3π mass spectrum, as has been the case in previous charge-exchange photoproduction analyses [51], [73]. With this peak now identified as $J^{PC} = 2^{++}$, we can conclusively say we have observed production of the $a_2(1320)$ meson. Furthermore, the similarity between the two distributions in terms of shape and scale are consistent with our expectations for the $a_2(1320)$ produced via pion exchange with unpolarized photons. Also consistent with the above production mechanism, we found the $2^{++}0^{+}\ [\rho\pi]_D$ partial wave to be consistent with zero, and the $M = 2$ waves to make a very small contribution to the total 2^{++} intensity.

Figure 5.3 shows the result of a Breit-Wigner fit to the combined 2^{++} intensity spectra, from which we extract a mass $M^{\text{stat}}_{\text{sys}}$ of $1310^{\pm 1.4}_{\pm 16}$ MeV and a width of $100^{\pm 3}_{\pm 10}$ MeV. These are consistent with the PDG values of 1318 MeV for the mass and 107 MeV for the width.

5.3.2 $1^{++}\,[\rho(770)\pi]_S$

The $1^{++}\,[\rho(770)\pi]_S$ with $M^{\epsilon} = 1^{\pm}$ are the dominant contributors of the 1^{++} class of waves. The $1^{++}0^{+}S$ wave was found to be consistent with zero in the majority of our fits. Also excluded are the waves corresponding to the P-wave decays of the $a_1(1260)$ to $\sigma\pi$ and $f_2\pi$, which were found to make an insignificant contribution to our overall intensity.

The intensities of the $1^{++}1^{\epsilon}S$ waves are shown in Figure 5.4. Both projections show

a strong enhancement close to 1.2 GeV, consistent with production of the $a_1(1260)$ meson. The symmetry in shape and scale between the two $M^\epsilon = 1^\pm$ states, along with the $M = 0$ suppression, is again consistent with our expectations regarding production via pion exchange with unpolarized photons.

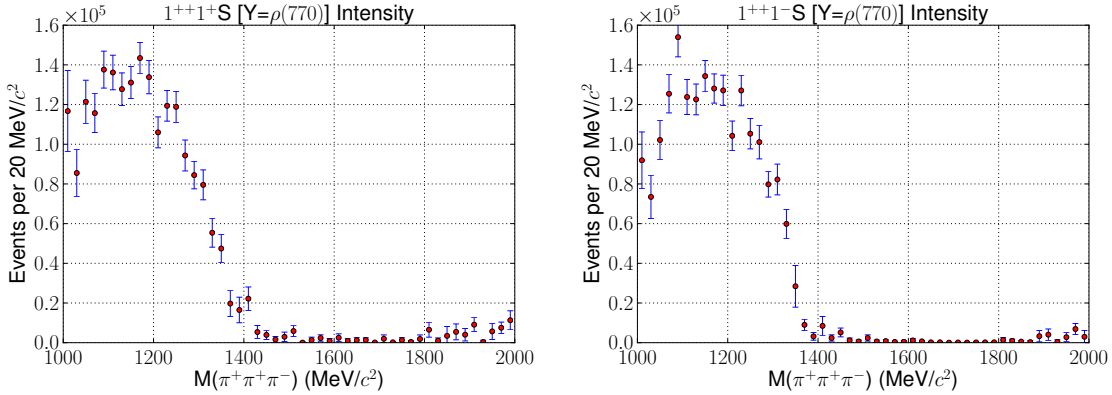

Figure 5.4: Typical intensities of the $1^{++}1^+S$ (**left**) and $1^{++}1^-S$ (**right**).

Summing these two waves and fitting the resulting distribution to a Breit-Wigner, shown in Figure 5.5, we find a mass $M^{\text{stat}}_{\text{sys}}$ of $1190^{\pm 10}_{\pm 50}$ MeV and a width of $303^{\pm 41}_{\pm 40}$ MeV. These measurements are consistent with the PDG values for the $a_1(1260)$ of 1230 ± 40 MeV in mass and 250-600 MeV in width.

The $a_1(1260)$ has never been seen in charge-exchange photoproduction, including the previous CLAS result as well as the analysis in Ref. [73]. To firmly establish a resonant 1^{++} signal, we examine its phase motion versus another well-known state; however, the phase motion of the $1^{++}S$ is sensitive to the presence of the 1^{++} D-waves. Thus we defer discussion of the motion of the $1^{++}S$ partial waves relative to the $2^{++}1^\epsilon$ $[\rho\pi]_D$ to Section 5.3.3.

5.3.3 1^{++} $[\rho(770)\pi]_D$

As we see strong evidence for resonant $a_1(1260)$ production in the 1^{++} $[\rho\pi]_S$ intensity, the 1^{++} $[\rho(770)\pi]_D$ is a logical inclusion for our analysis as well. Furthermore, the analysis in Ref. [40] observed evidence for both the $a_1(1260)$ and the $a_1(1700)$ in the $1^{++}D$ intensity. Typical intensity spectra of the $1^{++}D$ for our analysis are shown in Figure 5.6.

The $M^\epsilon = 1^\pm$ intensity spectra are rather complex, and focused on the 1.4 to 1.6 GeV mass region. No evidence for any known mesons is visible. Furthermore, in many other fits, the region from 1.4 to 1.6 GeV tended to be occupied by a number of different partial waves, none of which were found to be significant. Additionally, the $M^\epsilon = 0^+$ intensity spectrum is characterized by a single peak at 1.3 GeV. Studying the $1^{++}0^+D$ more closely, we find that it absorbs significant leakage from the 2^{++}, consistent with the peak at 1.3 GeV.

The $1^{++}D$ was found to have a significant impact on the other partial waves as well. Figure 5.7 shows the $2^{++}1^\pm$ spectra in the presence of the $1^{++}D$. The peaks in both reflectivities lose a large fraction of their intensity, and the fluctuations at high mass grow

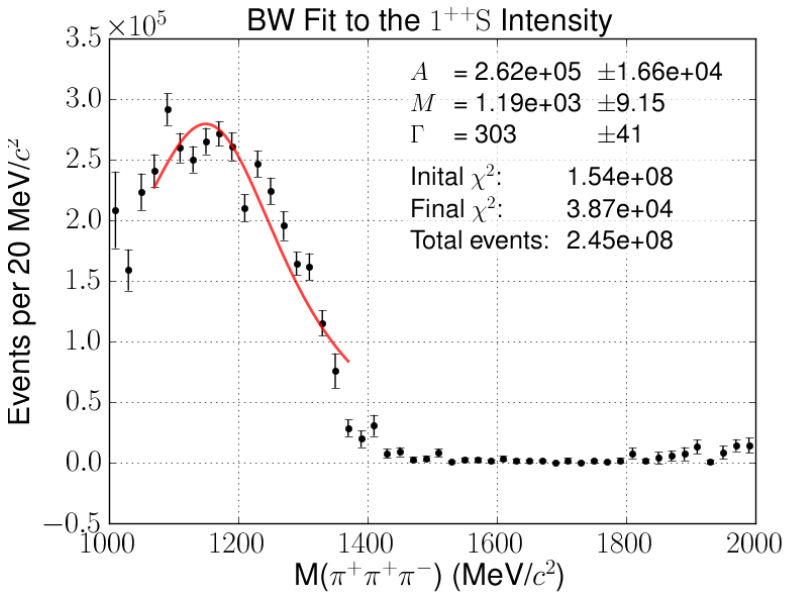

Figure 5.5: A Breit-Wigner fit of the total $1^{++}S$ intensity.

in size slightly. The $1^{++}S$ intensities, shown in Figure 5.8, look largely the same; however, the phase difference between the $1^{++}S$ and 2^{++} acquires a slope downwards close to 1.4 GeV, shown in Figure 5.9. This downward slope is consistent with $a_1(1260)$ production.

Figure 5.11 shows the phase difference between the 1^{++} and 2^{++} when the $1^{++}D$ is *not* included in the fit. We see in both the $M^\epsilon = 1^+$ and 1^- differences a slowly-varying distribution, with a minimum at about 1200 MeV. If we were seeing two resonances interfering, we would expect to see this distribution *inverted*; that is, the phase difference should first rise with the 1^{++}, then fall as the 2^{++} takes over, as the 2^{++} peaks at a larger mass than the 1^{++}. Such a result is ambiguous, because if the 1^{++} were non-resonant, we should certainly see the phase of the a_2, and we do not. This ambiguous phase motion is consistent across the majority of our fits; only by including *all three* $1^{++}D$ waves do we observe the

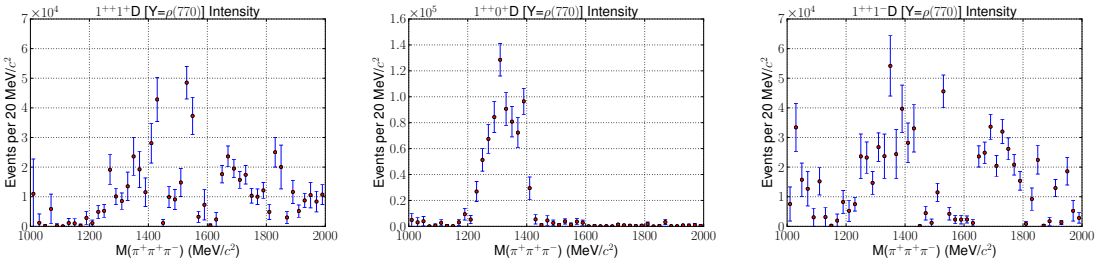

Figure 5.6: The intensities of the $1^{++}1^+D$ (**left**), $1^{++}0^+D$ (**center**), and $1^{++}1^-D$ (**right**).

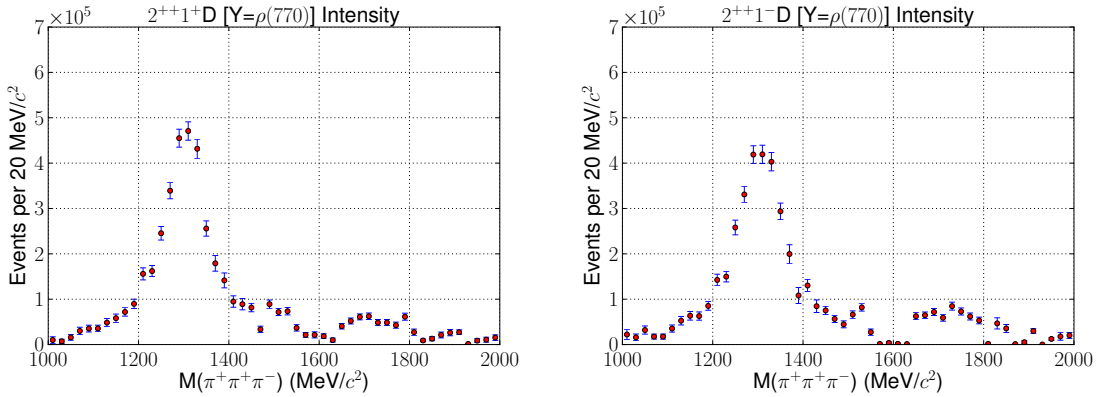

Figure 5.7: The intensities of the $2^{++}1^{+}D$ (**left**) and $2^{++}1^{-}D$ (**right**) when the $1^{++}D$ waves are included in the fit.

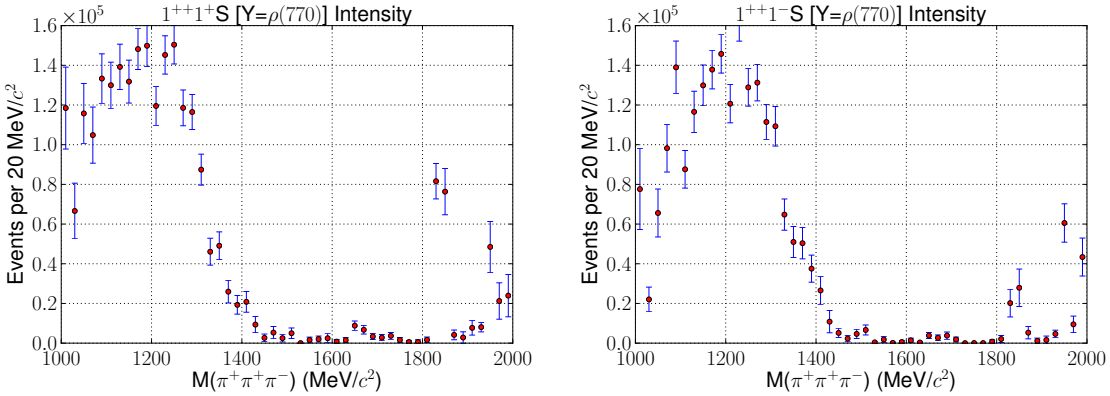

Figure 5.8: The intensities of the $1^{++}1^{+}S$ (**left**) and $1^{++}1^{-}S$ (**right**) when the $1^{++}D$ waves are included in the fit.

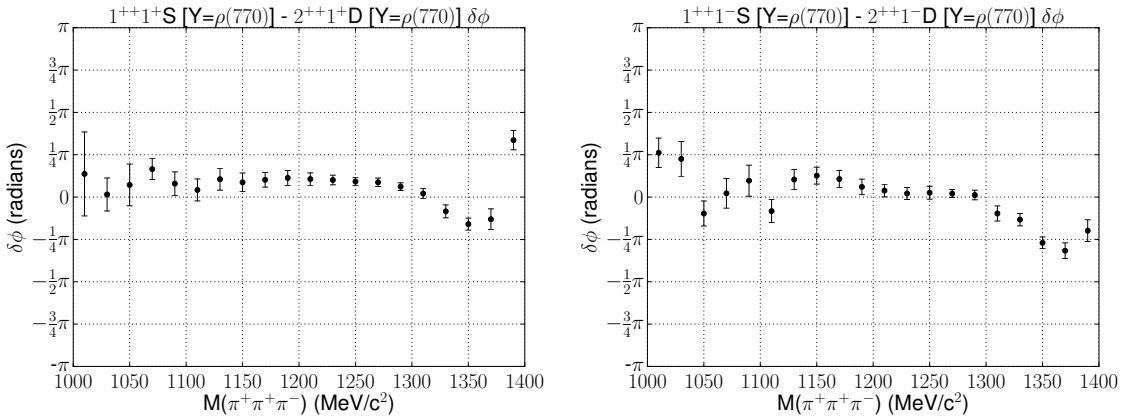

Figure 5.9: The phase difference between the $1^{++}1^{+}S$ and $2^{++}1^{+}D$ (**left**) and between the two 1^{-} waves (**right**) when the 1^{++} $[\rho\pi]_D$ decays are included.

resonant phase motion of Figure 5.9. No other combination of waves was found that could reproduce this phase motion.

We can extract the parameters of the Breit-Wigners by performing a simultaneous χ^2 fit to both intensity distributions and the phase difference. The results are shown in Figure 5.10. For the $M^{\epsilon} = 1^{+}$ combination, we obtain a mass $M^{\text{stat}}_{\text{sys}}$ of $1198^{\pm 0.1}_{\pm 40}$ MeV and a width of $275.8^{\pm 0.2}_{\pm 35}$ MeV for the 1^{++}, and $1310^{\pm 0.01}_{\pm 10}$ and $118^{\pm 0.03}_{\pm 12}$ for the mass and width of the 2^{++}. For the $M^{\epsilon} = 1^{-}$, we measured $1217^{\pm 0.1}_{\pm 40}$ and $275.8^{\pm 0.2}_{\pm 35}$ MeV as the mass and width of the 1^{++}, and $1310^{\pm 0.01}_{\pm 10}$ and $118^{\pm 0.03}_{\pm 12}$ as the mass and width of the 2^{++}. All of these numbers are consistent with values found in the PDG for the mass and width of the $a_1(1260)$ and $a_2(1320)$.

Complete results for all major waves in the presence of the $1^{++}D$ waves can be found in Appendix B.

5.3.4 $2^{-+}\,[f_2(1270)\pi]_S$

In the upper regime of the 3π mass range, we find that the dominant contributions came from the $[f_2(1270)\pi]_S$ decays of the 2^{-+}. Again, the dominant contributions are from the $M^{\epsilon} = 1^{\pm}$ projections, but we also find a non-negligible contribution from the 0^{-} wave as well. The intensity spectra are shown in Figure 5.12. All three waves share a peak at just above 1.6 GeV, consistent with the production of the $\pi_2(1670)$. Similar to the 1^{++} and 2^{++}, we see good symmetry between the $M^{\epsilon} = 1^{+}$ and 1^{-}, but the significant strength of the 0^{-} wave may point toward an additional production mechanism other than π exchange. $M = 2$ projections for the $2^{-+}S$ were also tried; they were found to be consistent with zero.

Summing the $f_2\pi$ S- and D-wave intensities of the 2^{-+} (the $[f_2\pi]_D$ is discussed in Section 5.3.6), we get the distribution shown in Figure 5.13. A fit to a Breit-Wigner yields values of 1650 ± 4 MeV for the mass, and 235 ± 12 MeV for the width. Both values are lower than those reported by the PDG; the nominal mass of the $\pi_2(1670)$ is 1672 ± 3.2 MeV, and its width 259 MeV.

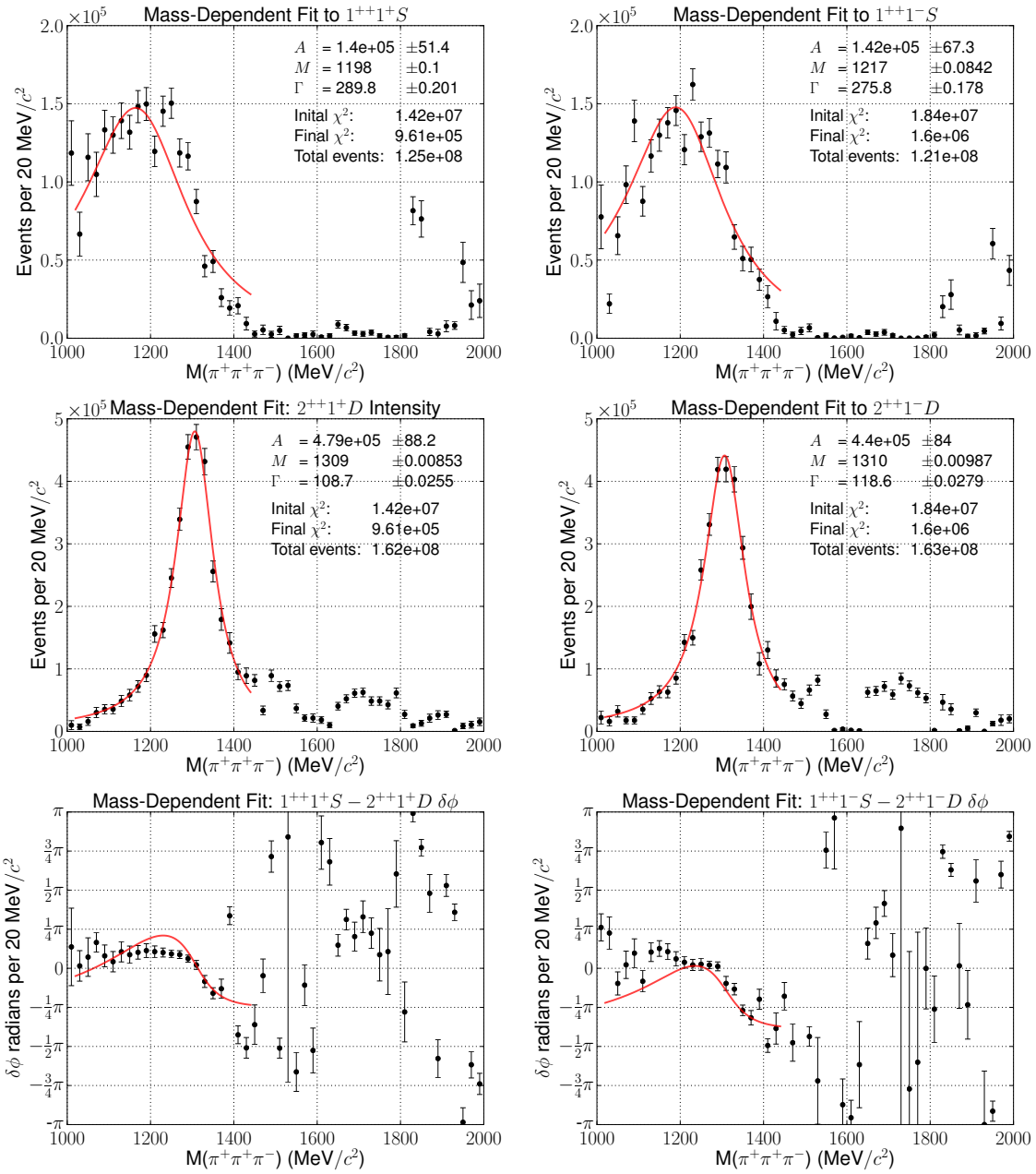

Figure 5.10: Mass-dependent fits of the $1^{++}S$ and $2^{++}D$ intensity distributions and phase motion in the presence of the $1^{++}D$ waves. The $M^\epsilon = 1^+$ combination is the left column, and the 1^- is the right column.

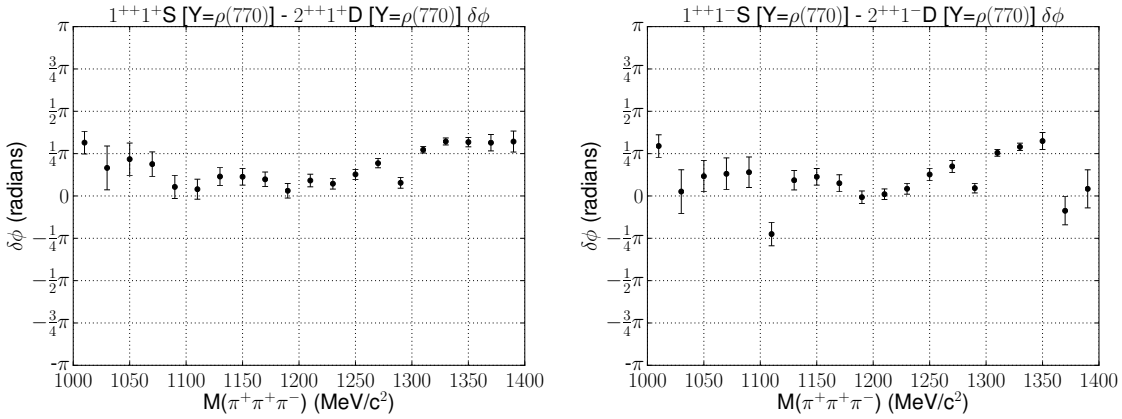

Figure 5.11: Phase differences between the $1^{++}1^{+}S$ and $2^{++}1^{+}D$ (**left**) and the $1^{++}1^{-}S$ and $2^{++}1^{-}D$ (**right**), *without* the inclusion of the 1^{++} $[\rho\pi]_D$ waves.

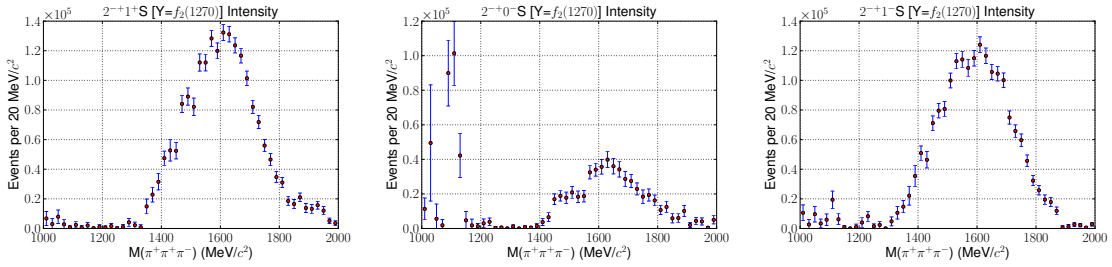

Figure 5.12: 2^{-+} S-wave intensities for the minimal waveset: $M^{\epsilon} = 1^{+}$ (**left**), 0^{-} (**middle**), and 1^{-} (**right**).

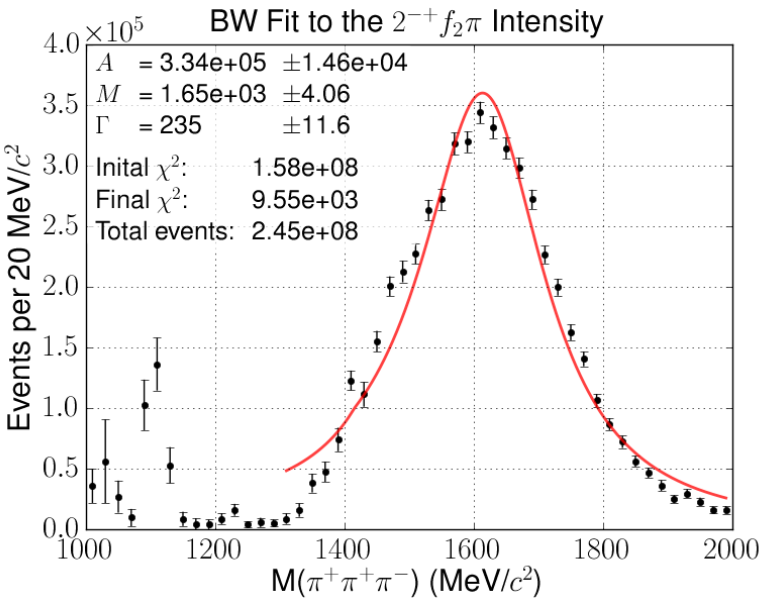

Figure 5.13: A Breit-Wigner fit of the total $2^{-+}1^{\epsilon}$ $f_2\pi$ intensity (both S and D waves).

5.3.5 $2^{-+}\,[\rho(770)\pi]_P$

Of surprisingly similar strength in the high-mass region are the $2^{-+}\,[\rho\pi]_P$ waves, shown in Figure 5.14. The $M^{\epsilon} = 0^-$ is especially strong in the example we have shown, but we find it to be highly unstable between different wavesets. The PDG branching fractions of the $\pi_2(1670)$ are 0.496 to $f_2\pi$, and just 0.31 to $\rho\pi$ [17]; furthermore, the $2^{-+}0^-S$ is produced at about a third of the level of the $2^{-+}1^{\epsilon}S$.

The $2^{-+}1^{\pm}P$ intensity spectra exhibit instabilities in the intensity at 1.4 GeV in the 1^- and slightly higher in the 1^+. These low-mass artifacts are highly sensitive to waveset composition, and in some cases they can mar the rising edge of the $2^{-+}1^{\pm}$ intensity due to genuine $\pi_2(1670) \to \rho\pi$ events. Aside from these low-mass artifacts, the distributions are quite consistent in shape and strength with $\pi_2(1670) \to [\rho\pi]_P$, and these features are consistent across many fits. The $2^{-+}P$ waves are also sensitive to the particular values of the baryon background rejection cuts; this is discussed further in Appendix C.4.6.

5.3.6 D-wave Decays of the 2^{-+}

For $L = 2$ decays of the 2^{-+}, both the $f_2\pi$ and $\sigma\pi$ decay modes were tried, but only the $[f_2\pi]_D$ decays acquired intensity in the $\pi_2(1670)$ region. The $[f_2\pi]_D$ intensity spectra, shown in Figure 5.15, show good, symmetric shapes centered just above 1.6 GeV in the $M^{\epsilon} = 1^{\pm}$ waves, consistent with $\pi_2(1670)$ photoproduction via π exchange. However, the 1^+ does carry slightly more intensity; the symmetry between reflectivities is not as exact as with the major waves.

The 0^- intensity shows a depleted rising edge followed by a more continuous falling edge. Additionally, like the $2^{-+}0^-P$, the $2^{-+}0^-\,[f_2\pi]_D$ is stronger than its corresponding

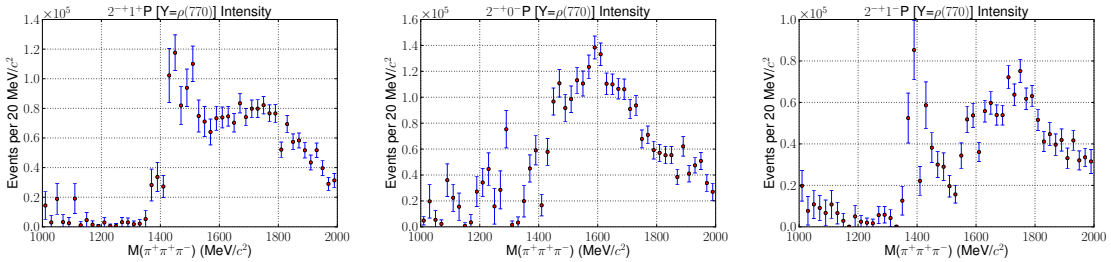

Figure 5.14: 2^{-+} $[\rho\pi]_P$ intensities for the minimal waveset: $M^\epsilon = 1^+$ (**left**), 0^- (**middle**), and 1^- (**right**).

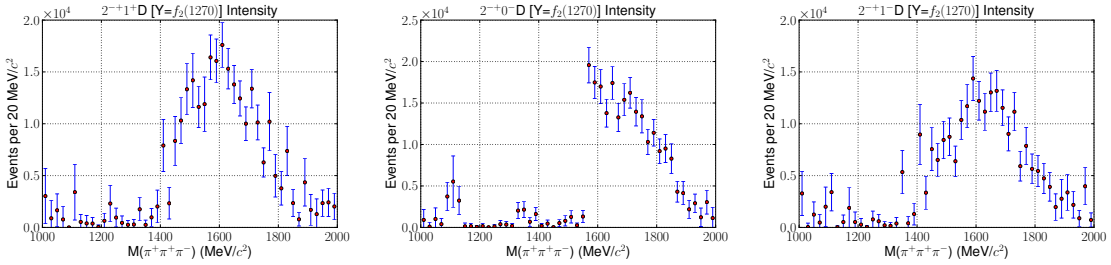

Figure 5.15: 2^{-+} $[f_2\pi]_D$-wave intensities: $M^\epsilon = 1^+$ (**left**), 0^- (**middle**), and 1^- (**right**).

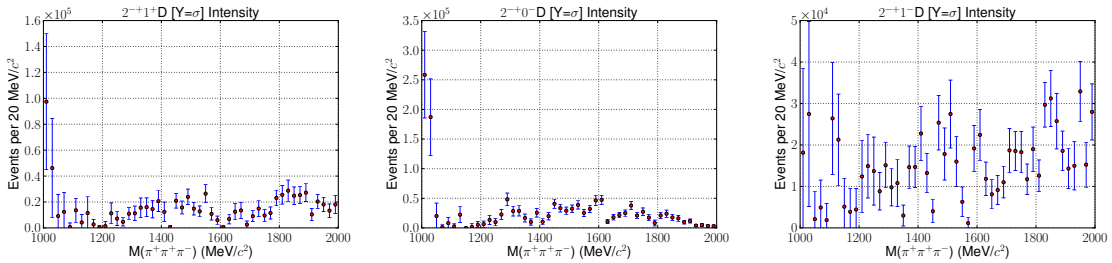

Figure 5.16: $2^{-+}\ [\sigma\pi]_D$ intensities: $M^\epsilon = 1^+$ (**left**), 0^- (**middle**), and 1^- (**right**).

$M^\epsilon = 1^\pm$ waves, which is inconsistent with what one would expect from the $2^{-+}\ [f_2\pi]_S$ intensity distributions. Also like the $2^{-+}0^-P$, the $2^{-+}0^-\ [f_2\pi]_D$ is unstable and quite sensitive to the composition of the waveset.

All of the $2^{-+}\ [f_2\pi]_D$ signals are quite small compared to the major waves, at less than 3% of the total intensity. Thus they do not make a major contribution, but they are useful to serve as a clean second reference wave to search for possible phase motion of the $\pi_1(1600)$ in the 1^{-+} partial waves. Also, the $M^\epsilon = 1^\pm$ waves illustrate our ability to cleanly extract small $f_2\pi$ signals.

The $\sigma\pi$ decay, shown in Figure 5.16, suffers from a great deal of leakage at low mass, and its presence distorts the spectra of several other partial waves. For simplicity, the σ is parametrized as a Breit-Wigner with mass and width both equal to 800 MeV. While this parametrization is an approximation to the more complicated $\pi\pi_S$ lineshape, it is sufficient to allow events with a strong $2^{-+}\ [\sigma\pi]_D$ overlap to manifest themselves in the intensities. The negligible contributions from $\sigma\pi$ decays in the resonance region precludes the study of any more sophisticated parametrizations.

5.3.7 The Exotic 1^{-+} Waves

As discussed previously, the $\pi_1(1600)$ has $J^{PC} = 1^{-+}$, and thus should manifest itself as a peak in the 1^{-+} intensity at 1.6 GeV, as well as exhibiting phase motion relative to another state, such as the 2^{-+}. The intensities of the $1^{++}S$, 2^{++}, and $2^{-+}1^\pm S$ partial waves lead us to expect the exotic to be strongly produced in the $M^\epsilon = 1^\pm$, if it is produced at all. Furthermore, the observation of $\pi_1(1600)$ decay to $\rho\pi$ in pion production leads us to expect equal production between $M^\epsilon = 1^+$ and $M^\epsilon = 1^-$. However, the observation of clean intensity in the $2^{-+}0^-S$ partial wave, most likely attributable to $\pi_2(1670)$ production, also opens the possibility for exotic production in the $1^{-+}0^-$ wave.

Typical intensity spectra for these three 1^{-+} waves are shown in Figure 5.17. Their distributions are remarkably consistent across all of our fits. In the $M^\epsilon = 1^+$, some smaller features consistent with the unknown 1.4 GeV artifacts seen in the $2^{-+}P$ spectra are present, but no evidence of resonant intensity at 1.6 GeV is visible. Both $M^\epsilon = 1^\pm$ waves exhibit a rise starting at 1.6 GeV all the way to our upper limit of 2 GeV. Above 1.6 GeV, the two reflectivities show good consistency in shape with one another, although the 1^+ is slightly stronger. The $M^\epsilon = 0^-$ wave is consistent with zero. None of these observations

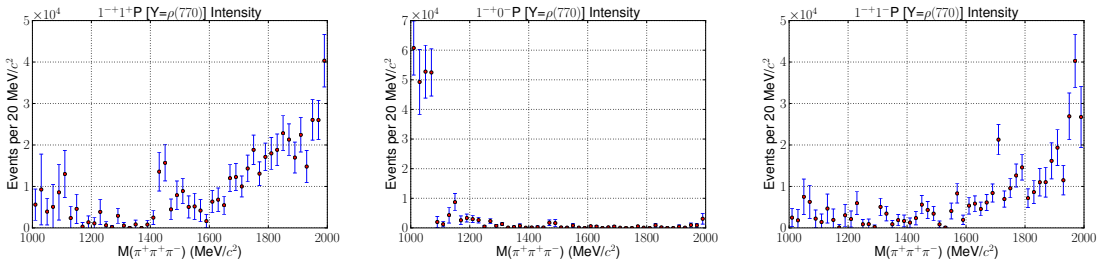

Figure 5.17: Typical intensities for the exotic waves: $1^{-+}1^{+}\mathrm{P}$ (**left**), $1^{-+}0^{-}\mathrm{P}$ (**middle**), and $1^{-+}1^{-}\mathrm{P}$ (**right**).

are consistent with $\pi_1(1600)$ production.

It is possible that a 1^{-+} resonance is produced at a much lower cross-section than the dominant resonances. In Refs. [40] and [42], the resonant nature of the 1^{-+} is established by the observation of resonant phase motion. To confirm that the 1^{-+} intensity we see in our data is non-resonant, we examine its phase difference relative to the 2^{-+} $[f_2\pi]$ S- and D-wave decays. These distributions are shown in Figure 5.18. The overall trend of the phase across all four differences is descending, indicative of a resonant 2^{-+} subtracted from a non-resonant background. This observation is inconsistent with the phase motion seen in E852; a comparison is discussed further in Chapter 6.

Additionally, the IU-E852 analysis of the 3π system [41] claims that the 1^{-+} intensity can be *constructed* by the omission of the 2^{-+} $[\rho\pi]_F$ partial waves. While we found that the $2^{-+}F$ does not make any major contribution to our intensity spectrum, we did investigate the effect of the $2^{-+}F$ on the 1^{-+} intensity. Figure 5.19 shows the resulting 1^{-+} intensity after adding the $2^{-+}0^{-}F$, $1^{+}F$, and $1^{-}F$ to our minimal waveset. The only appreciable loss of intensity is at 1.7 GeV in the $1^{-+}1^{-}$ partial wave. However, when we also add the 2^{-+} $[\sigma\pi]_D$ partial waves we see a much greater reduction in the 1^{-+} intensity. The 1^{-+} intensity in the presence of both the 2^{-+} $[\sigma\pi]_D$ and the $[\rho\pi]_F$ is shown in Figure 5.20. The 42-wave set used in Ref. [41] included an additional 2^{-+} $[\sigma\pi]_D$ wave relative to the waveset in Ref. [40], along with the additional $[\rho\pi]_F$ waves. Thus it is possible that the reduction in intensity seen in Ref. [41] may be due the $\sigma\pi$ and $[\rho\pi]_F$ decays working *in concert*, rather than the $[\rho\pi]_F$ partial waves alone.

Complete fit results including the $2^{-+}F$ waves, as well as those with both the $[\rho\pi]_F$ and $[\sigma\pi]_D$ waves, are found in Appendices B.4 and B.5.

5.3.8 Predicted Angular Distributions

The qualities of our various fits were determined with weighted monte-carlo, following the procedure outlined in Section 5.2.2. Typical measured and predicted invariant mass distributions are shown in Figures 5.21 and 5.22. The 3π and $n\pi$ masses are reproduced quite well. The di-pion masses show a few areas of slight disagreement, but overall the reproduction is good. The Gottfried-Jackson angles in Figure 5.23 also match quite well, but the angles in the helicity frame, shown in Figure 5.24 are of some concern. The distribution

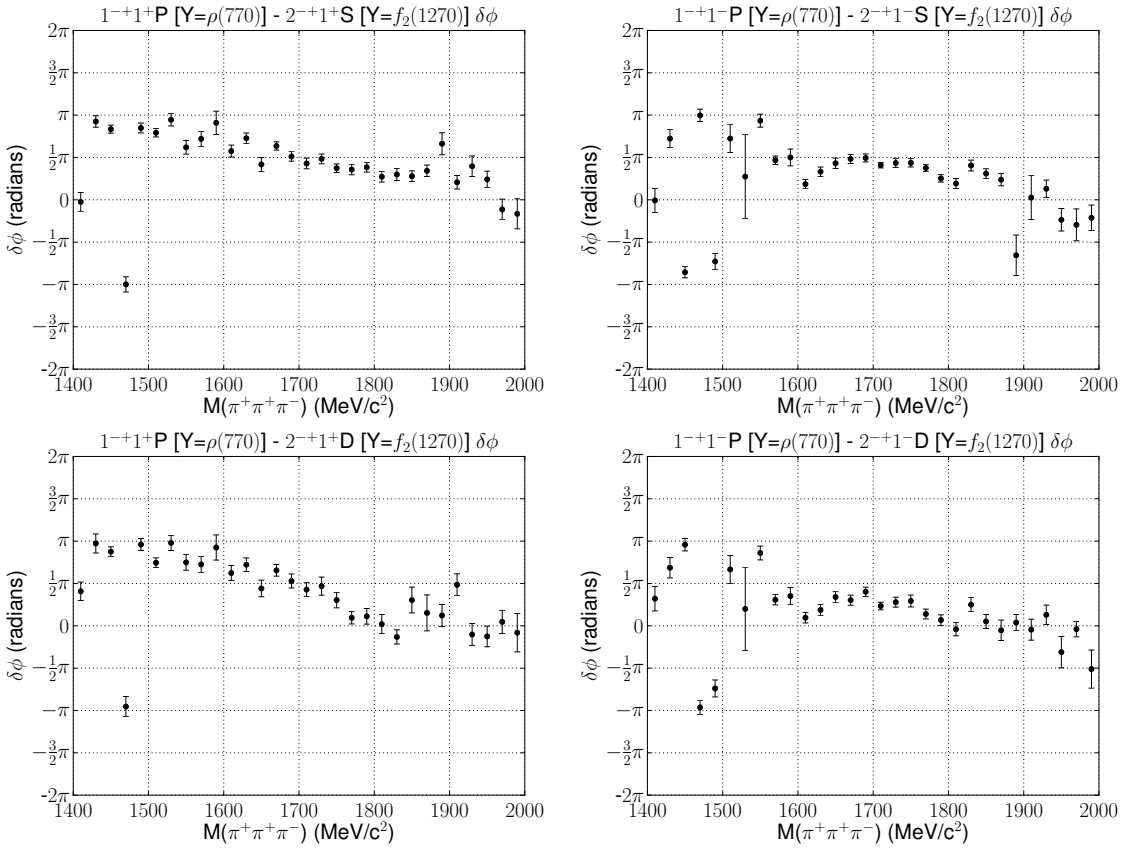

Figure 5.18: The phase motion of the $1^{-+}1^{\epsilon}$ against the $2^{-+}1^{\epsilon}$ S-wave (**top**) and D-wave (**bottom**). $M^{\epsilon} = 1^{+}$ is on the left, and 1^{-} is on the right.

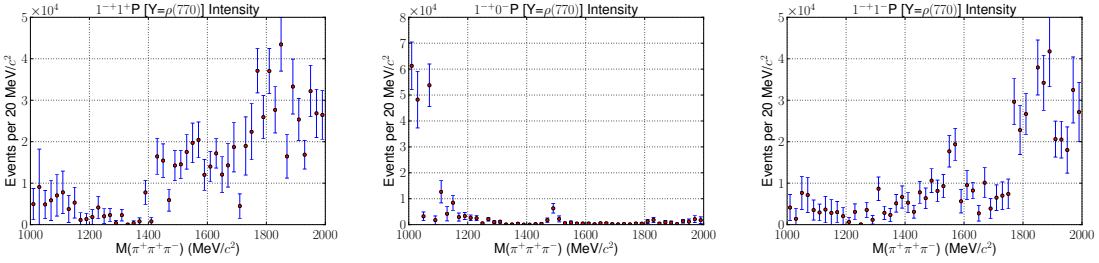

Figure 5.19: Intensity spectra for the 1^{-+} waves in the presence of the $2^{-+}F$: $1^{-+}1^{+}$P (**left**), $1^{-+}0^{-}$P (**middle**), and $1^{-+}1^{-}$P (**right**).

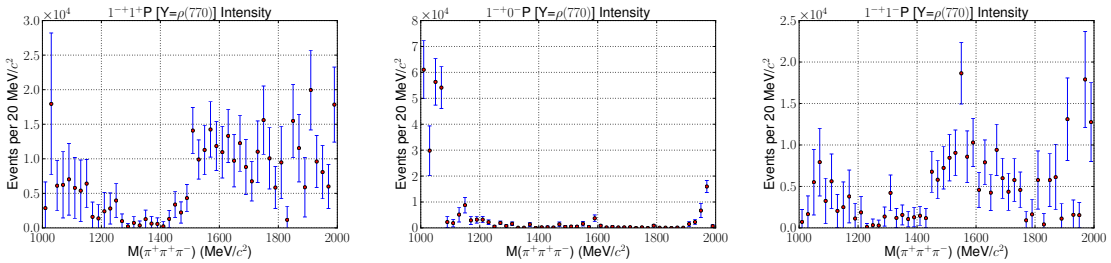

Figure 5.20: Intensity spectra for the 1^{-+} waves in the presence of the both the $2^{-+}F$ and the 2^{-+} $[\sigma\pi]_D$: $1^{-+}1^+$P (**left**), $1^{-+}0^-$P (**middle**), and $1^{-+}1^-$P (**right**).

in $\cos\theta_H$ in the rest frame of the fast $\pi^+\pi^-$ combination is poorly reproduced at the edges, and both ϕ_H distributions have the right shape but the wrong proportions. These poor descriptions are consistent across all of our partial-wave fits, indicative of a systematic effect in our analysis. We found that reproduction of both $\cos\theta_H$ and ϕ_H can be improved by removing events with ϕ_H close to 0, shown as the red region in Figure 5.24. However, no substantive change in intensity or phase distributions were seen, so we do not include this fiducial cut in our final results. Results from an example fit with this cut in place are shown in Appendix B.9.

5.3.9 Systematic Dependencies of Fit Results

On a whole, the results presented above are quite robust against changes in our analysis method. We examined the roles of rank, bin size, incidental physics background, and baryon background on our fit results.

The effect of increasing levels of baryon background is of principal importance, as it is a complication unique to our experiment. In order to study its influence on our results, we began with our nominal cuts in $|t'|$ and $\theta_{lab}\left[\pi_2^+\right]$, as described in Section 3.2. The fit results for the basis described in Appendix B.1 were compared to fits where the cut in $\theta_{lab}\left[\pi_2^+\right]$ was relaxed to 35°, 55°, and 90°. Then fits with the cut in $|t'|$ opened from its nominal value of 0.1 GeV^2 to 0.175, 0.250, 0.5, and 1 GeV^2 were performed before fitting with the $|t'|$ cut removed entirely. The only partial waves dependent on the angular cut for a clean signal are the 2^{-+} $[\rho\pi]_P$ waves. The major waves varied predictably as the cut in $|t'|$ was opened, with all acquiring increasing amounts of intensity in the upper half on the 3π mass regime. The 1^{-+} did show some fluctuations in the 1.6 GeV region as the cuts were opened but none that were found to be consistent across all values of the cuts in $|t'|$ and $\theta_{lab}\left[\pi_2^+\right]$. The isotropic background wave is found to absorb a significant amount of the baryon background, especially in the high mass region. A detailed summary of this study can be found in Appendix C.4.

The effects of incidental background (non-$[\gamma p \to \pi^+\pi^+\pi^- n]$ events) were studied by selecting events in the sidebands of the neutron. Events in both sidebands were found to have 3π invariant mass distributions similar to that of the nominal event sample. A partial-wave

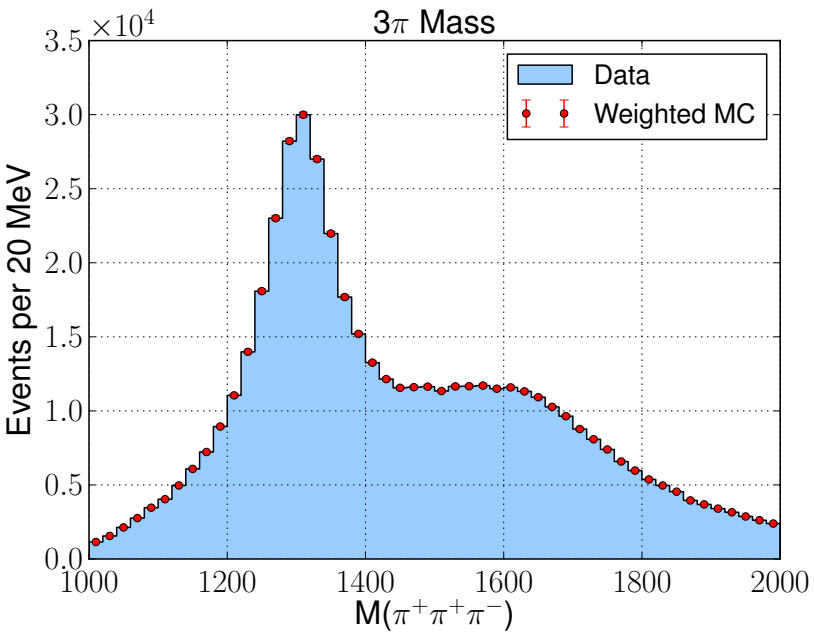

Figure 5.21: The measured (blue histograms) and predicted (points) 3π invariant mass distributions.

analysis of the high-sideband events showed the composition of the spectrum to be mostly 2^{++}, with a suppressed 2^{-+} contribution relative to the nominal sample. The isotropic background wave was peaked sharply beneath the $a_2(1320)$. Also within our nominal sample is a background contribution from $\gamma p \to K_S K^+ \Sigma^0$ events where the reconstruction has labeled the K^+ as a π^+; this contribution is enhanced in the high sideband as the missing mass is closer to the mass of the Σ. This is due to the high sideband being primarily composed of $\gamma p \to \pi^+\pi^+\pi^-\Delta^0$ events. The low sideband is composed of $\gamma p \to \pi^+\pi^+\pi^- n$ events for which the photon causing the event was not recorded in the tagger. In both cases the events still contain 3π systems which are largely due to the same resonances we measure in $\gamma p \to \pi^+\pi^+\pi^- n$. Events leaking in from the upper sideband could amplify a_2 signal slightly in our nominal event sample, as well as pushing the isotropic background wave up in the same region. Events from the lower sideband will have an incorrect energy-momentum balance, which will skew the Wigner rotations performed during the decay amplitude calculation, which could in turn contribute to leakage between partial waves. However, the number of events on the low side of the neutron is so small that any such effects will be negligible. Details of this study are presented in Appendix C.1.

Rank II fits showed significantly noisier intensity spectra; these are described further in Appendix C.2. Furthermore, our results were found to have very little dependence on bin size; fits with 10 and 40 MeV bins are described in Section C.3.

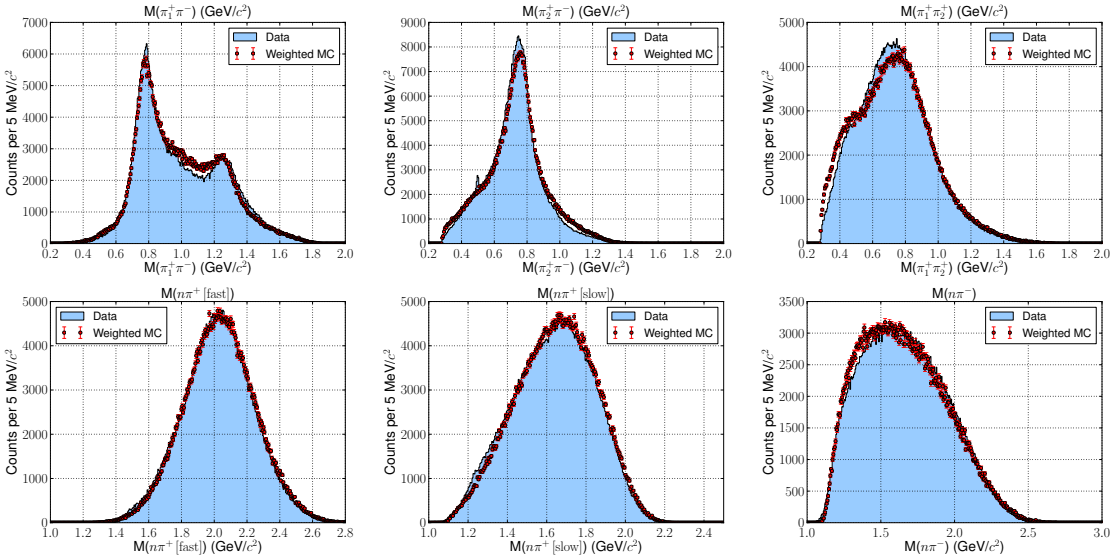

Figure 5.22: Typical measured (blue histograms) and predicted (points) invariant mass distributions: $M(\pi_1^+\pi^-)$ (top left), $M(\pi_2^+\pi^-)$ (top center), $M(\pi^+\pi^+)$ (top right), $M(n\pi_1^+)$ (bottom left), $M(n\pi_2^+)$ (bottom center), $M(n\pi^-)$ (bottom right).

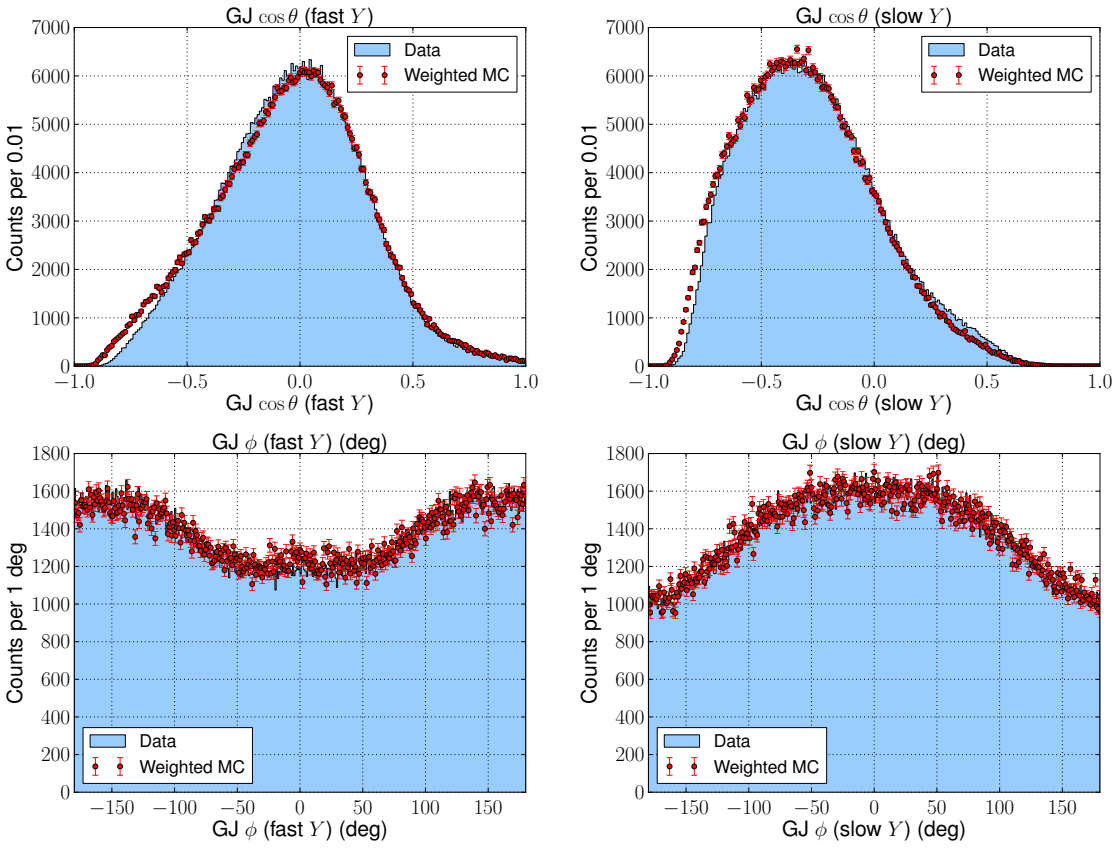

Figure 5.23: The measured (blue histograms) and predicted (points) angular distributions in the Gottfried-Jackson frame. $\cos\theta_{GJ}$ (ϕ_{GJ}) distributions are shown on top (bottom) row, with the fast (slow) $\pi^+\pi^-$ combination in the left (right) column.

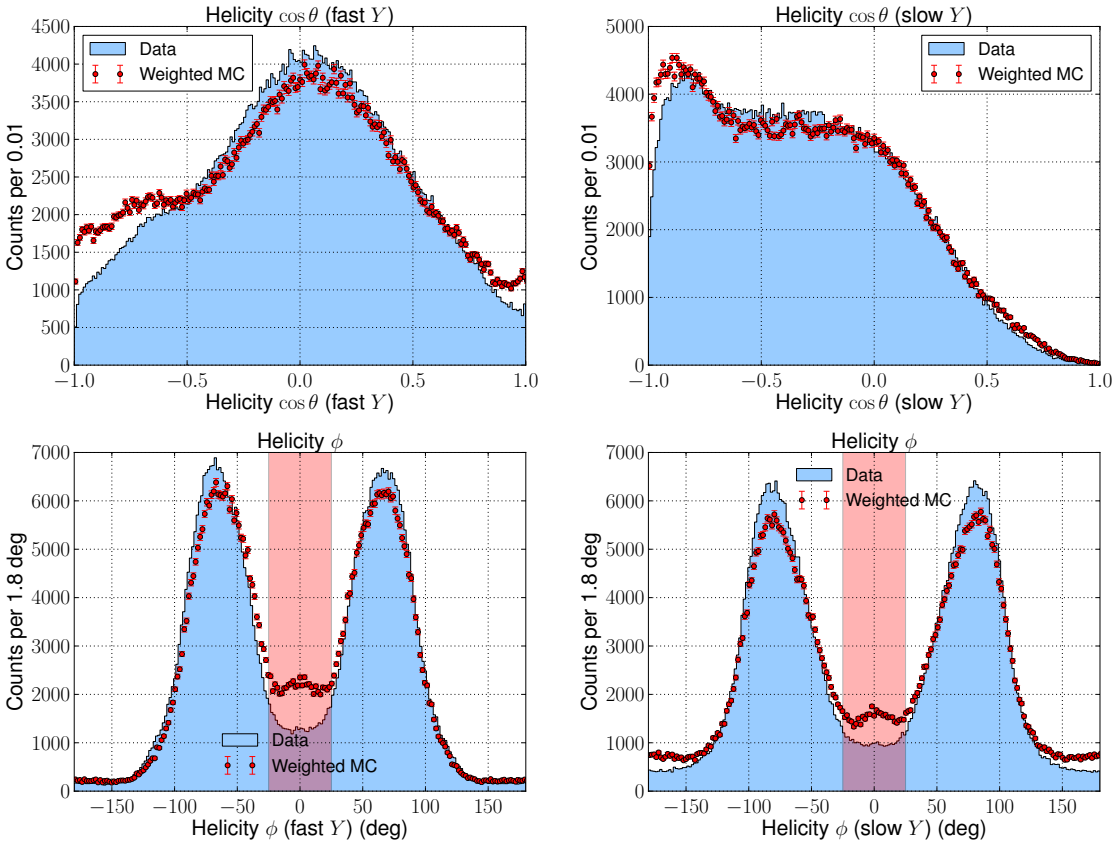

Figure 5.24: The measured (blue histograms) and predicted (points) angular distributions in the helicity frame. $\cos\theta_H$ (ϕ_H) distributions are shown on top (bottom) row, with the fast (slow) $\pi^+\pi^-$ combination in the left (right) column. Fits with the region in red removed from our data showed no substantive changes from results where it is included.

CHAPTER 6

INTERPRETATION OF RESULTS AND FUTURE WORK

We have performed a mass-independent partial-wave analysis of the reaction $\gamma p \to \pi^+\pi^+\pi^- n$. Our fit results show strong evidence in the 1^{++} $[\rho(770)\pi]_S$, 2^{++} $[\rho(770)\pi]_D$, and 2^{-+} $[f_2(1270)\pi]_{S,D}$ intensity spectra for production of the $a_1(1260)$, $a_2(1320)$, and $\pi_2(1670)$ mesons, respectively. These mesons are primarily and equally produced in the $M^\epsilon = 1^+$ and 1^- projections, a consequence of our unpolarized photon beam interacting via pion exchange. Waves with $M = 0$ were expected to be suppressed, due to the dominance of π exchange. They indeed were in the case of the 1^{++}, 1^{-+}, and 2^{++}; however, the 2^{-+} $[f_2\pi]_S$, $[\rho\pi]_P$ and $[f_2\pi]_D$ all showed significant production strength at 1.6 GeV in their $M = 0$ projections, indicating an exchange of spin in the production process or high mass background effects. Spin-0 waves were also found to be suppressed.

The observation of $1^{++}S$ intensity consistent with the $a_1(1260)$ is an important result, as the $a_1(1260)$ has never been seen in charge-exchange photoproduction. We were able to see resonant phase motion in the $1^{++}S$ versus the $a_2(1320)$, but *only* when we include all three $1^{++}D$ waves as well. Other wavesets omitting the $1^{++}D$ were found to have ambiguous phase motion between the $1^{++}S$ and the $2^{++}D$.

Some waves showed distortions in their intensity spectra which are inconsistent with t-channel meson production. Most notable among these are the 2^{-+} $[\rho\pi]_P$ waves. While showing significant intensity consistent with the $\rho\pi$ decay mode of the $\pi_2(1670)$, these waves also showed significant distortions in the low-mass region. Additionally, the angular distributions predicted by our fit results do not exactly match those of the data. This mismatch, especially in the ϕ_H distribution, is consistent across many different wavesets, but worse in the higher 3π invariant masses. The decay of the isobar is calculated in the helicity frame, and the poor reproduction of the angles there could be indicative of ambiguities in distinguishing between the $f_2\pi$ and $\rho\pi$ decays.

As the goal of this analysis was to search for the spin-parity exotic $\pi_1(1600)$, our conclusion is that we see *no evidence* in the intensity or phase motion of $\pi_1(1600)$ production in our event sample. The 1^{-+} intensity spectra consistently show no sign of a peak in the 1.6 GeV region. However, the original discovery claim for the $\pi_1(1600)$ in Ref. [40] was based not on the 1^{-+} intensity spectrum, but on the observation of resonant 1^{-+} phase motion versus the 2^{-+}. Our phase differences of the 1^{-+} versus the 2^{-+} S- and D-wave amplitudes consistently show a decreasing trend, consistent with a resonant 2^{-+} subtracted

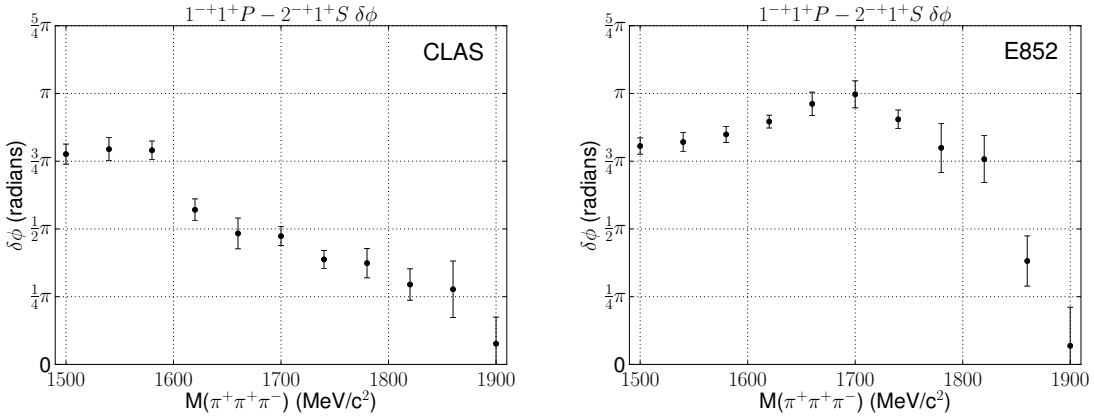

Figure 6.1: Comparison of the $1^{-+}1^+ - 2^{-+}1^+$ phase difference for our result (**left**) and the original discovery result [40] (**right**). The CLAS result is from our 40-MeV-bin fit so that the two may be directly compared.

from a *non-resonant* 1^{-+}. These phase differences drive our conclusion of no $\pi_1(1600)$ production in our $\gamma p \to \pi^+\pi^+\pi^- n$ event sample. Figure 6.1 shows a direct comparison of a $1^{-+} - 2^{-+}$ phase difference between this analysis and that in Ref [40].

As discussed in Chapter 1, E852 [40] and COMPASS [42] have published analyses of 3π data which show evidence of $\pi_1(1600)$ production in both the intensity and phase. However, the 3π system analyzed in those results was produced via $\pi^- p \to \pi^+\pi^-\pi^- p$, a neutral-exchange process. Indeed, all observations of the $\pi_1(1600)$ have been via neutral-exchange processes. But the $\gamma p \to \pi^+\pi^+\pi^- n$ process involves the exchange of a charged particle. Thus, it could be possible that the $\pi_1(1600)$ is suppressed in reactions where charge is exchanged. At the energies of E852 and COMPASS, diffractive processes are dominated by Pomeron exchange, which in some models [74], [75], [76] can be associated with a tensor glueball state. If the $\pi_1(1600)$ is understood to be a glue-rich state, then its production via a glue-rich exchange makes sense.

Another possibility is that previous $\pi_1(1600)$ observations in pion production are the consequence of an incomplete understanding of the parametrization of the σ isobars prevalent in the 0^{-+} waves. This could perhaps result in unaccounted-for leakage between the 0^{-+} and 1^{-+}, giving rise to a false $\pi_1(1600)$ signal. The $0^{-+} \to \sigma\pi$ intensities reported in [40] are complex, showing a three-peaked structure across the 1 to 2 GeV mass range. Furthermore, the text notes that the 0^{-+} intensity is quite sensitive to the σ parametrization below 1.5 GeV. The COMPASS result makes no mention of these concerns. Such sensitivity means that the models used are insufficient to describe the physics at work, and thus some unaccounted-for dynamical effects could be giving rise to the $\pi_1(1600)$ signal.

From a theoretical standpoint, the expectations espoused in [47], [50] that photoproduction might see enhanced levels of hybrid production are called into question, if the $\pi_1(1600)$ is indeed a gluonic hybrid. As noted earlier, calculations of the flux-tube model [37] put the lightest 1^{-+} state between 1.8 and 1.9 GeV, a bit far from the $\pi_1(1600)$. These numbers are more consistent with the $\pi_1(2000)$, observed in E852 in $f_1\pi$ [44] and $b_1\pi$ [45] in

mass-dependent analyses. Indeed, the rising intensity of the 1^{-+} as it approaches 2 GeV certainly doesn't rule out a $\pi_1(2000)$ coupling strongly to the photon, and such an observation would satisfy both the claim of enhanced production as well as the flux-tube model mass prediction. This would leave the internal dynamics of the $\pi_1(1600)$ in limbo, however, unless it could be shown to be a multiquark state. By the same token, the predictions of Ref. [37] find a 400 MeV split between the first and second 1^{-+} states, consistent with the $\pi_1(1600)$ and $\pi_1(2000)$ taken together.

In any case, we feel that the most likely explanation is that the $\pi_1(1600)$ is most strongly produced via Pomeron exchange, and that its absence in our data is due to the exchange of a charged particle. Unfortunately, if the Pomeron is truly a state with quantum numbers of the vacuum, we cannot test this claim directly on currently-available photoproduction data. While a copious amount of $\gamma p \to \pi^+\pi^-\pi^0 p$ data exists within the g12 dataset, that process cannot proceed via tensor exchange, as it is forbidden by G-parity. Nevertheless, a comparison between neutral and charged exchanges in photoproduced 3π will be an important test of these conclusions. Additionally, the 3π channel can be studied with g12 data in processes with a recoiling Δ, as alluded to in Section 5.3.9; however, if the $\pi_1(1600)$ is suppressed in pion exchange, as our results indicate, we expect results of such an analysis to be negative as well.

Light exotics are being explored in other production mechanisms as well. The BES-III collaboration, located at the Beijing Electron-Positron Collider in Beijing, China, is currently exploring the light meson spectrum in J/ψ and ψ' decays produced at threshold via e^+e^- annihilation. BES-III plans to collect 10B J/ψ decays and 3B ψ' decays by 2014; as the J/ψ and ψ' are both $c\bar{c}$ mesons, they have a broad array of decay channels which can be probed for light exotic mesons. The PANDA experiment, located at the Facility for Antiproton and Ion Research (FAIR) at Gesellschaft für Schwerionenforschung in Darmstadt, Germany, will study the spectrum of light mesons in $p\bar{p}$ annihilation. They expect first beam in 2018.

In terms of photoproduction however, on April 14th, 2009, ground was broken at Jefferson Lab for the construction of a new experimental hall, Hall D. Hall D will house the GlueX experiment, whose express purpose is to discover and map out the light exotic spectrum. Using a linearly-polarized 9 GeV photon beam and a spectrometer designed for partial-wave analysis, GlueX will run at a peak intensity of 10^8 photons/s for several years, starting in 2015. Promising channels which are impractical for observation with CLAS, such as $b_1\pi$, $f_1\pi$, and $\eta'\pi$, will certainly be studied in GlueX data and should prove more fruitful in terms of pinning down the production and properties of the $\pi_1(1600)$. Of course the $\gamma p \to \pi^+\pi^+\pi^- n$ channel will be studied at GlueX as well, and measurements made there will certainly preclude those reported here. We look forward to it; such is the march of science.

APPENDIX A

REFERENCE FRAMES

When calculating the decay amplitudes for a meson resonance X to go to $\pi^+\pi^+\pi^-$, we do so via the isobar model. The isobar model builds up an N-body decay by a sequence of $N-1$ two-body decays. In our case, there are two decays; one of the X into an isobar Y and a single π^+, called the *bachelor* π, and then the decay of Y itself to $\pi^+\pi^-$. The amplitudes for these decays are calculated in the respective rest frames of the X and Y.

For the rest frame of the X, we define the axes according to the Gottfried-Jackson convention. The z-axis is chosen to lie along the beam direction in the X rest frame. $\hat{y}_{GJ}$ is defined as $\hat{p}_\gamma \times \hat{p}_n$, the normal to the production plane. $\hat{x}_{GJ}$ is then obtained by enforcing a right-handed coordinate system via $\hat{y}_{GJ} \times \hat{z}_{GJ}$. With these definitions, θ_{GJ} is defined as the angle between $\vec{p}_Y$ and $\hat{z}_{GJ}$, and ϕ_{GJ} is defined as the angle between $\hat{x}_{GJ}$ and the projection of $\vec{p}_Y$ into the $X-Y$ plane.

For the axes in the Y rest frame, we use the helicity convention. The helicity convention defines $\hat{z}_H$ as $\hat{p}_Y$ before the boost into the Y rest frame. After the boost is complete, $\hat{y}_H$ is defined as $\hat{z}_H \times \hat{p}_\gamma$, and then $\hat{x}_H$ can be obtained by again enforcing a right-handed coordinate system with $\hat{y}_H \times \hat{z}_H$. θ_H and ϕ_H are again defined as in any spherical coordinate system as the declination from and rotation about $\hat{z}_H$ of the $\hat{p}\,[\pi^+]$.

These definitions are illustrated in Figure A.1.

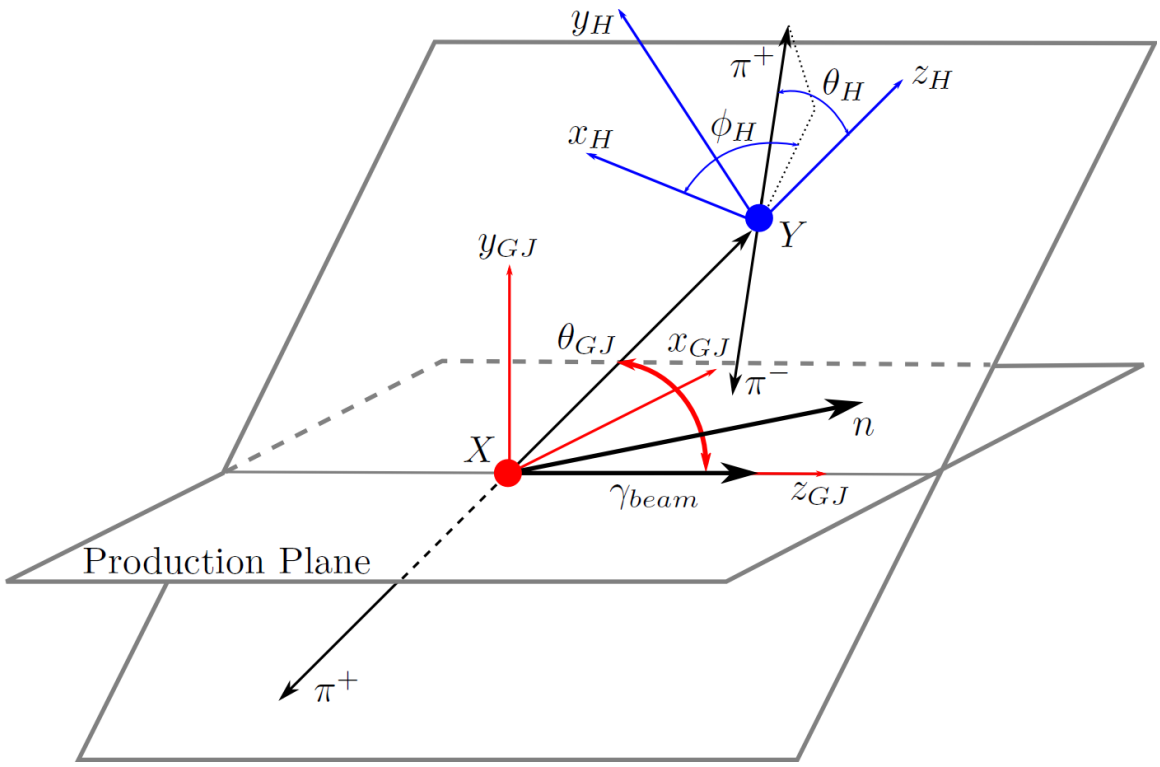

Figure A.1: The definitions of the Gottfried-Jackson (red) and helicity (blue) reference frames used in the calculation of decay amplitudes.

APPENDIX B

EXTENDED FIT RESULTS

In this Appendix, the complete set of intensity spectra are shown for several fits, the results of which were used in the discussion in Section 5.3. All spectra are corrected for intensity unless otherwise noted.

B.1 Minimal Basis

J^{PC}	M^{ϵ}	L	Y	Number of waves
1^{++}	$1^{\pm}$	S	$\rho(770)$	2
1^{-+}	$0^{-}, 1^{\pm}$	P	$\rho(770)$	3
2^{++}	$1^{\pm}$	D	$\rho(770)$	2
2^{-+}	$0^{-}, 1^{\pm}$	S, P, D	$f_2(1270)$, $\rho(770)$	9
isotropic background wave				

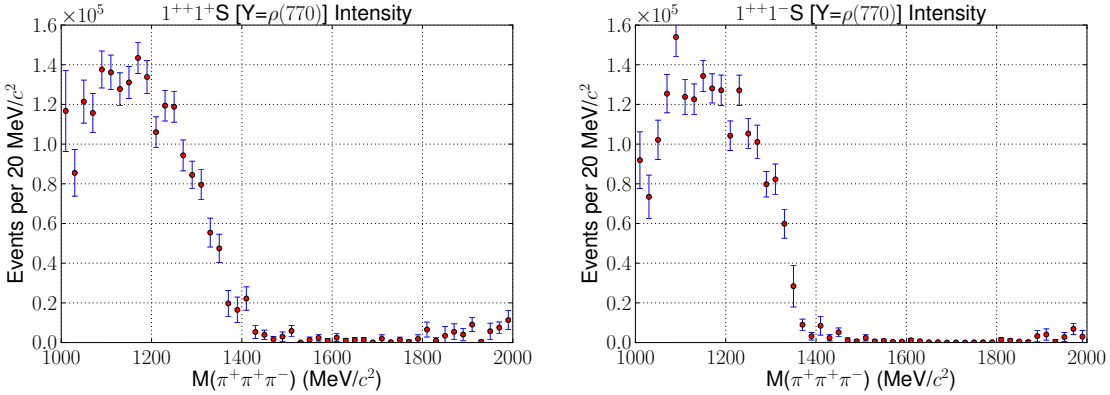

Figure B.1: $1^{++}S$ intensity: $1^{++}1^+S$ (**left**) and $1^{++}1^-S$ (**right**) for the minimal-basis fit.

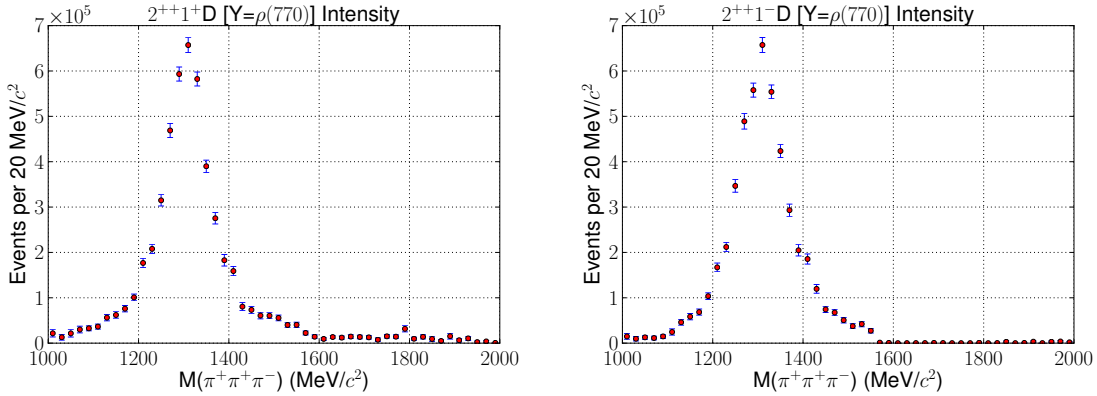

Figure B.2: $2^{++}D$ intensity: $2^{++}1^+D$ (**left**) and $2^{++}1^-D$ (**right**) for the minimal-basis fit.

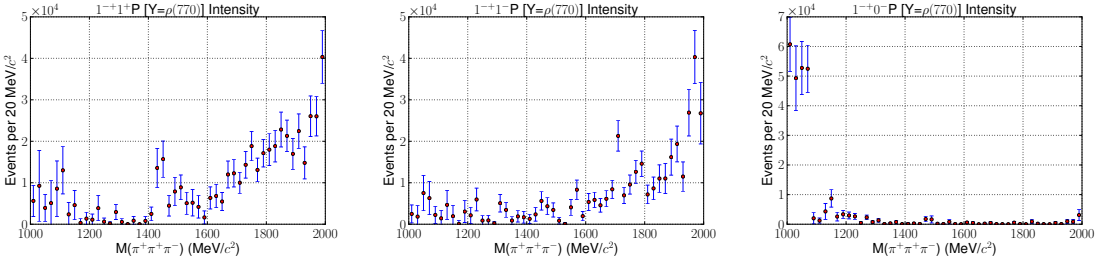

Figure B.3: 1^{-+} intensity spectra: $1^{-+}1^+P$ (**left**), $1^{-+}1^-P$ (**center**), and $1^{-+}0^-P$ (**right**) for the minimal-basis fit.

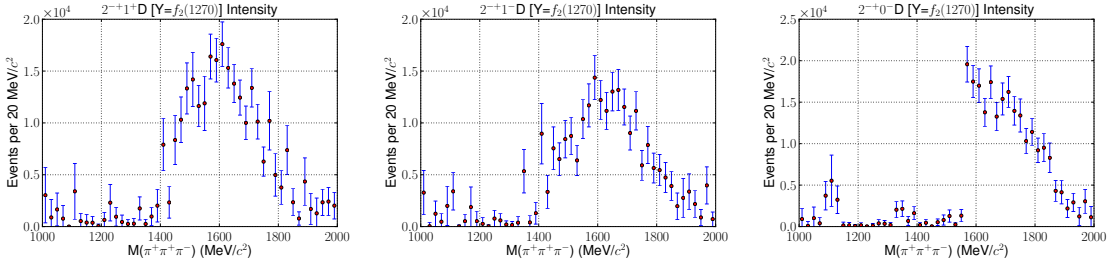

Figure B.4: 2^{-+} $[f_2(1270)\pi]_D$ intensity spectra: $2^{-+}1^+D$ (**left**), $2^{-+}1^-D$ (**center**), and $2^{-+}0^-D$ (**right**) for the minimal-basis fit.

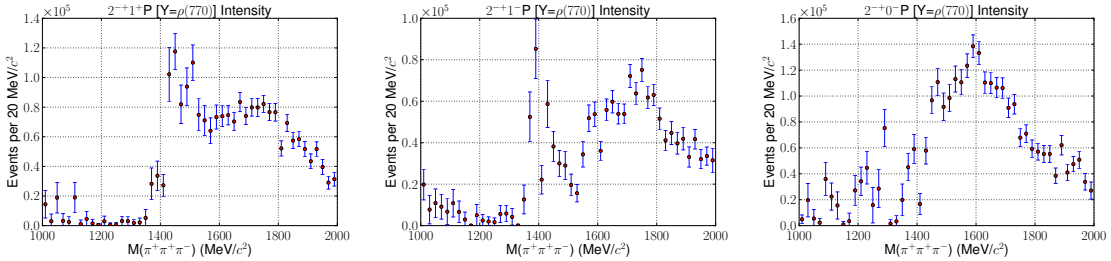

Figure B.5: 2^{-+} $[\rho\pi]_P$ intensity spectra: $2^{-+}1^+P$ (**left**), $2^{-+}1^-P$ (**center**), and $2^{-+}0^-P$ (**right**) for the minimal-basis fit.

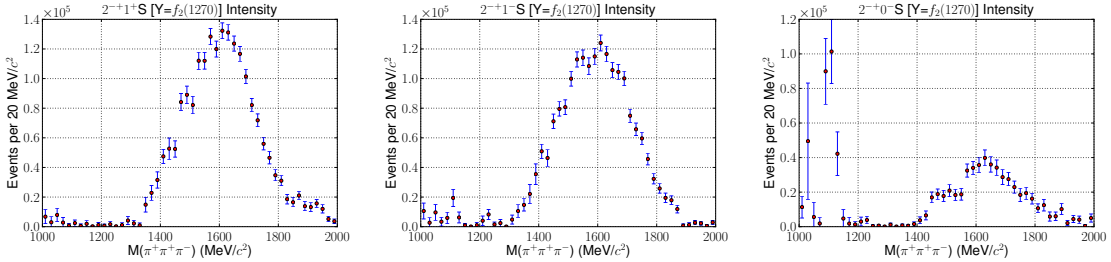

Figure B.6: 2^{-+} $[f_2(1270)\pi]_S$ intensity spectra: $2^{-+}1^+S$ (**left**), $2^{-+}1^-S$ (**center**), and $2^{-+}0^-S$ (**right**) for the minimal-basis fit.

B.2 Minimal Basis plus $1^{++}D$

J^{PC}	M^{ϵ}	L	Y	Number of waves
1^{++}	$1^{\pm}$	S	$\rho(770)$	2
1^{++}	$0^{+}, 1^{\pm}$	D	$\rho(770)$	3
1^{-+}	$0^{-}, 1^{\pm}$	P	$\rho(770)$	3
2^{++}	$1^{\pm}$	D	$\rho(770)$	2
2^{-+}	$0^{-}, 1^{\pm}$	S, P, D	$f_2(1270)$, $\rho(770)$	9
isotropic background wave				

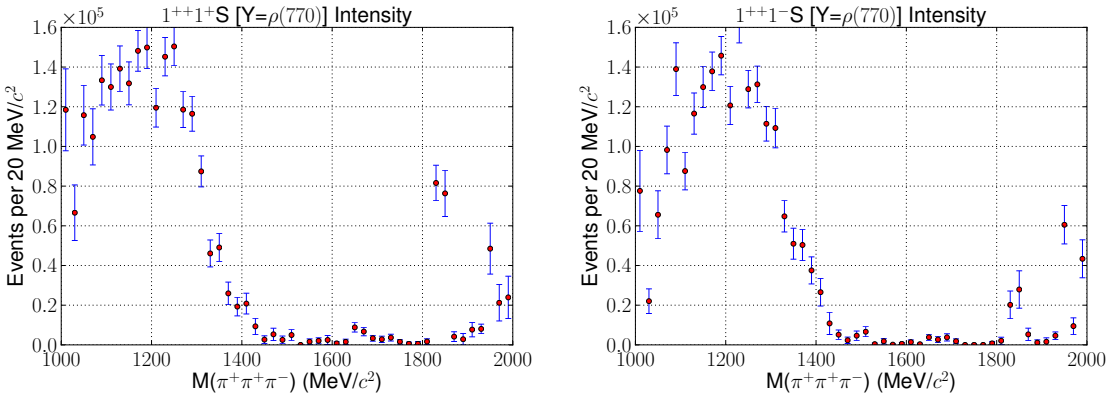

Figure B.7: $1^{++}S$ intensity in the presence of the $1^{++}D$ waves: $1^{++}1^{+}S$ (**left**) and $1^{++}1^{-}S$ (**right**) for the minimal basis plus the $1^{++}\,[\rho\pi]_D$ waves.

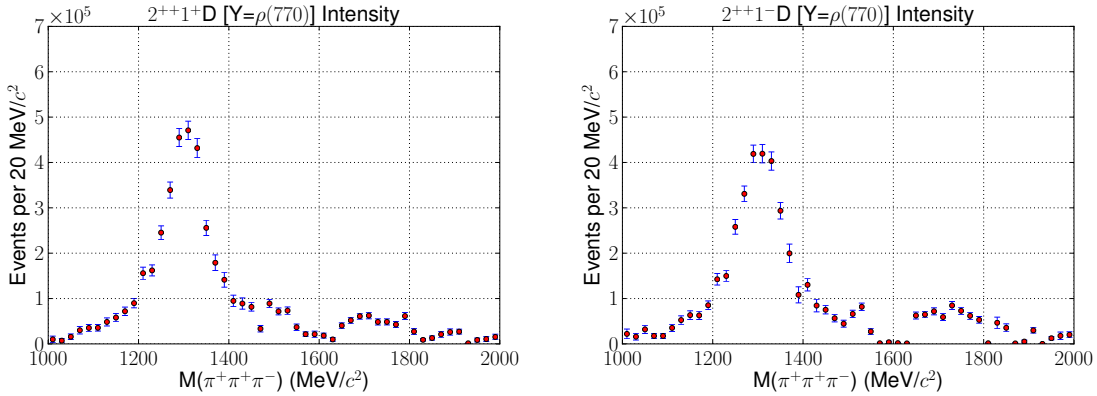

Figure B.8: $2^{++}D$ intensity in the presence of the $1^{++}D$ waves: $2^{++}1^{+}D$ (**left**) and $2^{++}1^{-}D$ (**right**) for the minimal basis plus the $1^{++}\left[\rho\pi\right]_D$ waves.

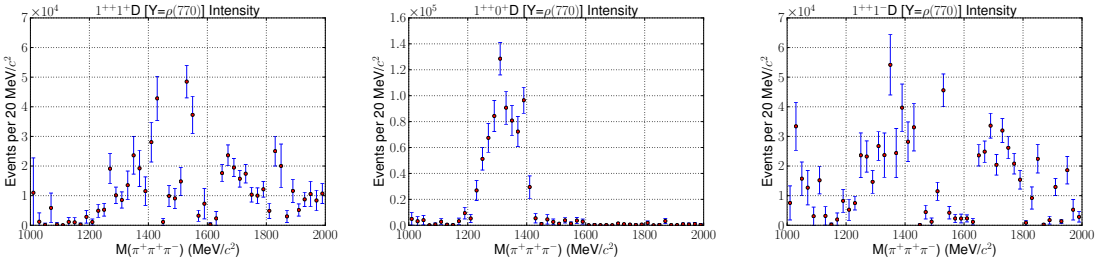

Figure B.9: $1^{++}D$ intensity when combined with our minimal waveset: $1^{++}1^{+}D$ (**left**), $1^{++}0^{+}D$ (**center**), and $1^{++}1^{-}D$ (**right**) for the minimal basis plus the $1^{++}\left[\rho\pi\right]_D$ waves.

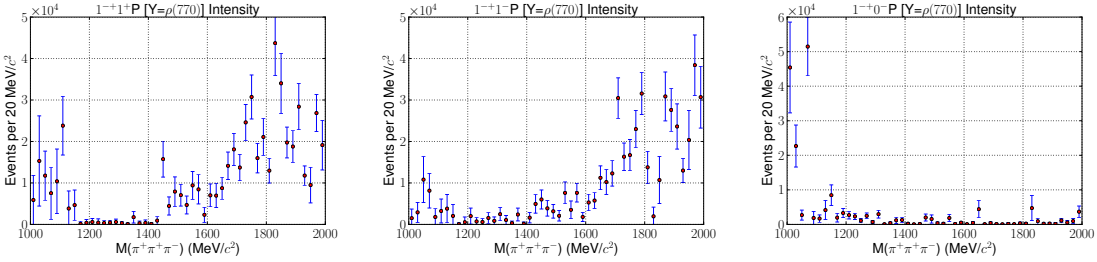

Figure B.10: 1^{-+} intensity spectra in the presence of the $1^{++}D$ waves: $1^{-+}1^{+}P$ (**left**), $1^{-+}1^{-}P$ (**center**), and $1^{-+}0^{-}P$ (**right**) for the minimal basis plus the $1^{++}\left[\rho\pi\right]_D$ waves.

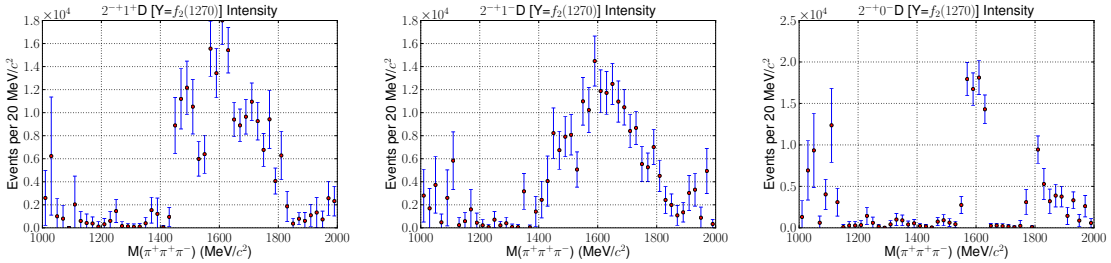

Figure B.11: $2^{-+}\ [f_2(1270)\pi]_D$ intensity spectra in the presence of the $1^{++}D$ waves: $2^{-+}1^+D$ (**left**), $2^{-+}1^-D$ (**center**), and $2^{-+}0^-D$ (**right**) for the minimal basis plus the $1^{++}\,[\rho\pi]_D$ waves.

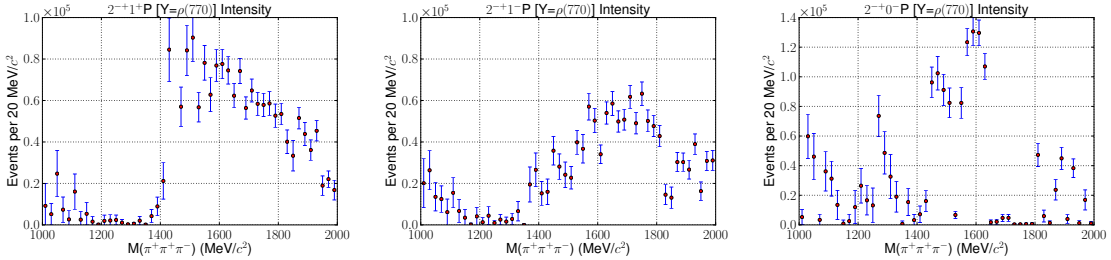

Figure B.12: $2^{-+}\ [\rho\pi]_P$ intensity spectra in the presence of the $1^{++}D$ waves: $2^{-+}1^+P$ (**left**), $2^{-+}1^-P$ (**center**), and $2^{-+}0^-P$ (**right**) for the minimal basis plus the $1^{++}\,[\rho\pi]_D$ waves.

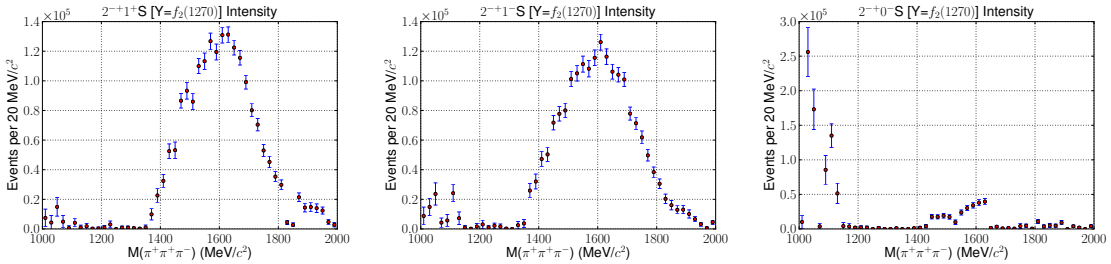

Figure B.13: $2^{-+}\ [f_2(1270)\pi]_S$ intensity spectra in the presence of the $1^{++}D$ waves: $2^{-+}1^+S$ (**left**), $2^{-+}1^-S$ (**center**), and $2^{-+}0^-S$ (**right**) for the minimal basis plus the $1^{++}\,[\rho\pi]_D$ waves.

B.3 Minimal Basis Plus 0^{-+}

J^{PC}	M^{ϵ}	L	Y	Number of waves
0^{-+}	0^{-}	S, P	$\rho(770), \sigma, f_0(980)$	3
1^{++}	$1^{\pm}$	S	$\rho(770)$	2
1^{-+}	$0^{-}, 1^{\pm}$	P	$\rho(770)$	3
2^{++}	$1^{\pm}$	D	$\rho(770)$	2
2^{-+}	$0^{-}, 1^{\pm}$	S, P, D	$f_2(1270)$, $\rho(770)$	9
isotropic background wave				

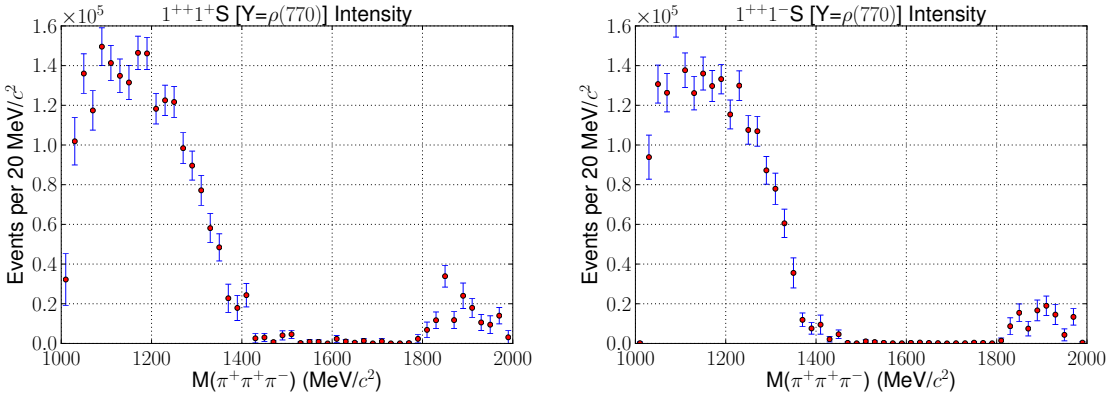

Figure B.14: $1^{++}S$ intensity in the presence of the 0^{-+} waves: $1^{++}1^{+}S$ (**left**) and $1^{++}1^{-}S$ (**right**) for the minimal basis plus the 0^{-+} waves.

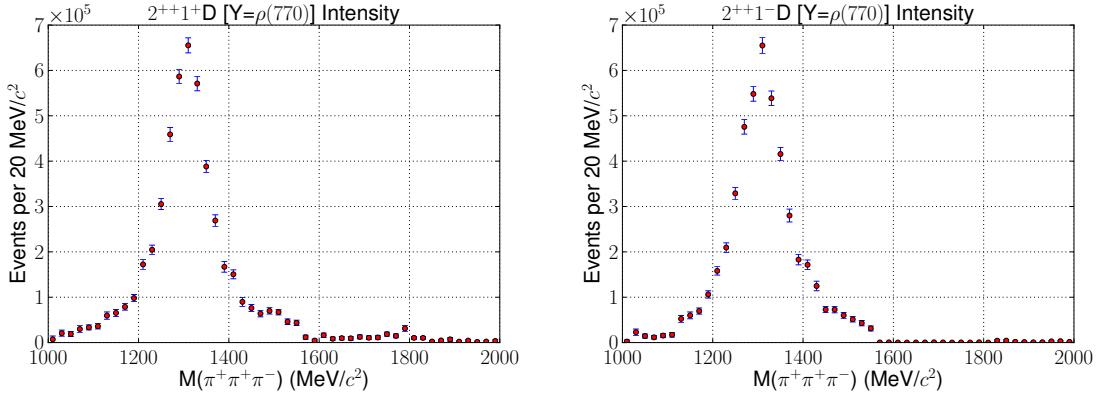

Figure B.15: $2^{++}D$ intensity in the presence of the 0^{-+} waves: $2^{++}1^{+}D$ (**left**) and $2^{++}1^{-}D$ (**right**) for the minimal basis plus the 0^{-+} waves.

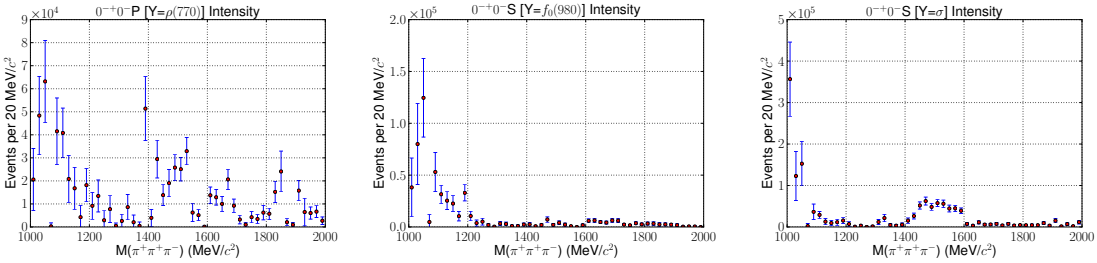

Figure B.16: 0^{-+} intensity in addition to the minimal basis: $[\rho\pi]_P$ (**left**), $[f_0(980)\pi]_S$ (**center**), and $[\sigma\pi]_S$ (**right**) for the minimal basis plus the 0^{-+} waves.

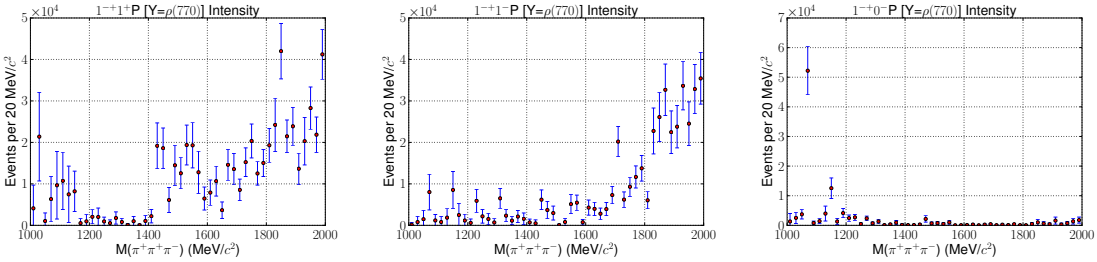

Figure B.17: 1^{-+} intensity spectra in the presence of the 0^{-+} waves: $1^{-+}1^{+}P$ (**left**), $1^{-+}1^{-}P$ (**center**), and $1^{-+}0^{-}P$ (**right**) for the minimal basis plus the 0^{-+} waves.

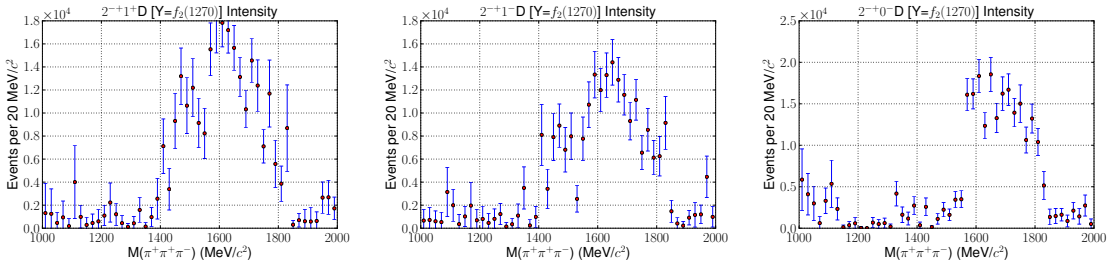

Figure B.18: 2^{-+} $[f_2(1270)\pi]_D$ intensity spectra in the presence of the 0^{-+} waves: $2^{-+}1^{+}D$ (**left**), $2^{-+}1^{-}D$ (**center**), and $2^{-+}0^{-}D$ (**right**) for the minimal basis plus the 0^{-+} waves.

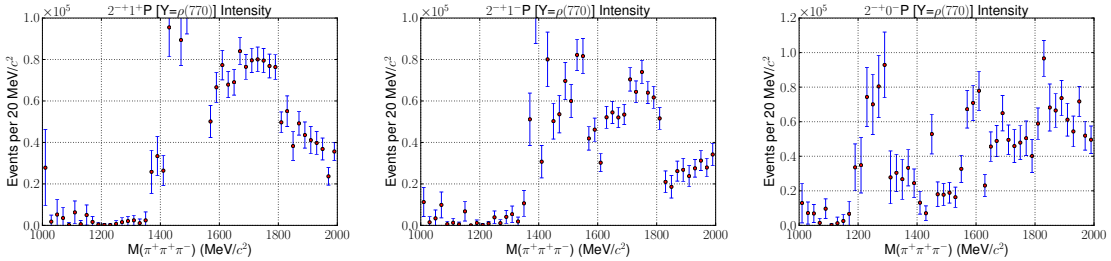

Figure B.19: 2^{-+} $[\rho\pi]_P$ intensity spectra in the presence of the 0^{-+} waves: $2^{-+}1^{+}P$ (**left**), $2^{-+}1^{-}P$ (**center**), and $2^{-+}0^{-}P$ (**right**) for the minimal basis plus the 0^{-+} waves.

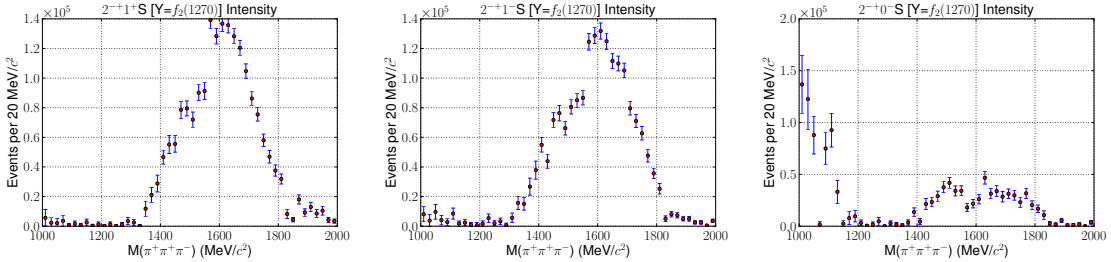

Figure B.20: 2^{-+} $[f_2(1270)\pi]_S$ intensity spectra in the presence of the 0^{-+} waves: $2^{-+}1^{+}S$ (**left**), $2^{-+}1^{-}S$ (**center**), and $2^{-+}0^{-}S$ (**right**) for the minimal basis plus the 0^{-+} waves.

B.4 Minimal Basis Plus $2^{-+}F$

J^{PC}	M^{ϵ}	L	Y	Number of waves
1^{++}	$1^{\pm}$	S	$\rho(770)$	2
1^{-+}	$0^{-}, 1^{\pm}$	P	$\rho(770)$	3
2^{++}	$1^{\pm}$	D	$\rho(770)$	2
2^{-+}	$0^{-}, 1^{\pm}$	S, P, D, F	$f_2(1270)$, $\rho(770)$	12
isotropic background wave				

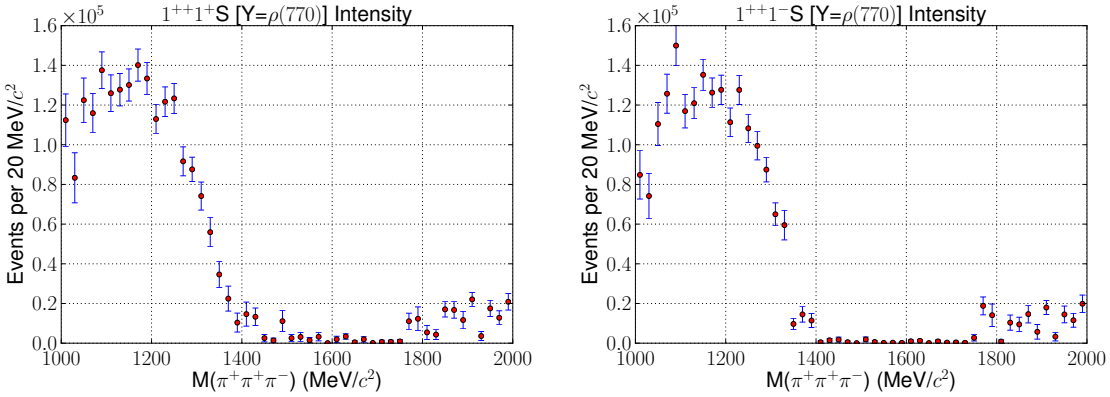

Figure B.21: $1^{++}S$ intensity in the presence of the $2^{-+}F$ waves: $1^{++}1^{+}S$ (**left**) and $1^{++}1^{-}S$ (**right**) for the minimal basis plus the $2^{-+}\,[\rho\pi]_F$ waves.

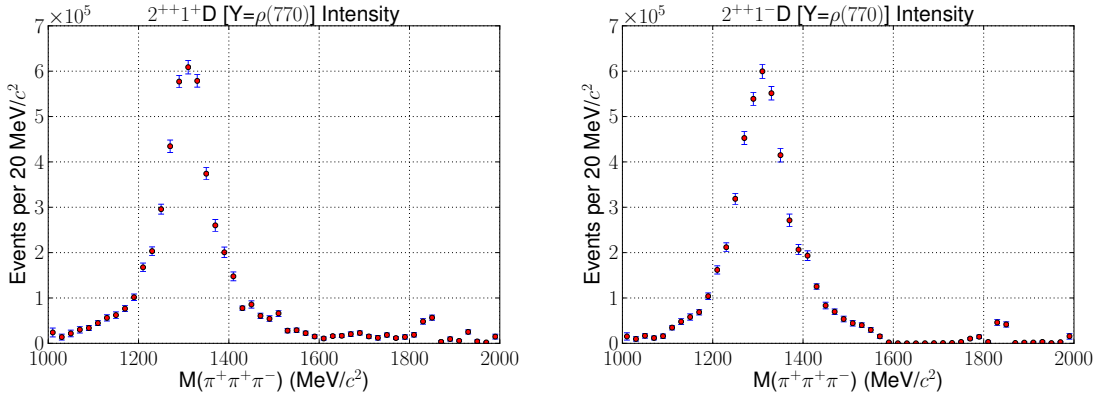

Figure B.22: $2^{++}D$ intensity in the presence of the $2^{-+}F$ waves: $2^{++}1^+D$ (**left**) and $2^{++}1^-D$ (**right**) for the minimal basis plus the $2^{-+}\left[\rho\pi\right]_F$ waves.

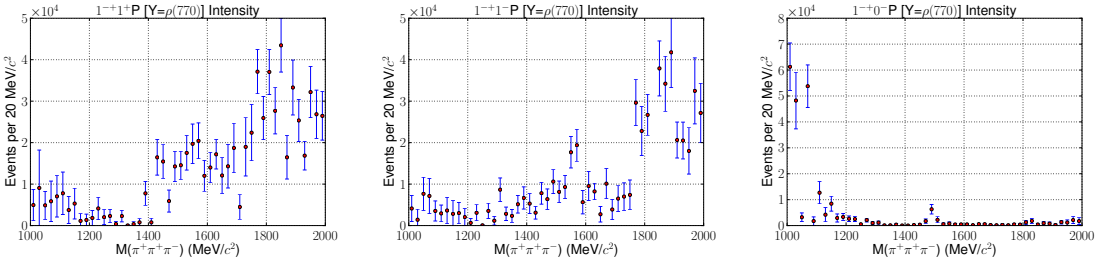

Figure B.23: 1^{-+} intensity spectra in the presence of the $2^{-+}F$ waves: $1^{-+}1^+P$ (**left**), $1^{-+}1^-P$ (**center**), and $1^{-+}0^-P$ (**right**) for the minimal basis plus the $2^{-+}\left[\rho\pi\right]_F$ waves.

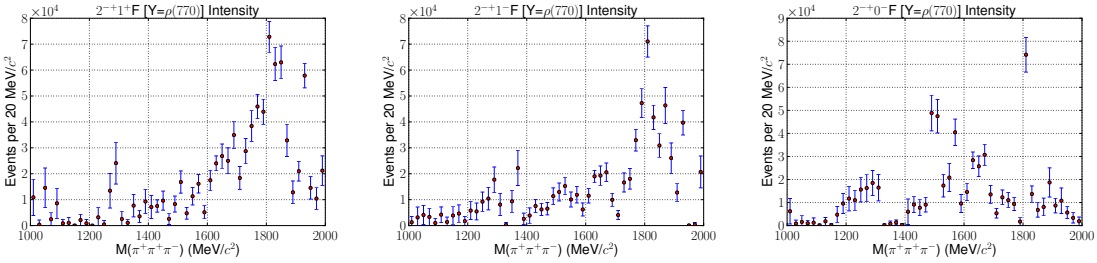

Figure B.24: $2^{-+}\left[\rho\pi\right]_F$ intensity in addition to the minimal basis: $2^{-+}1^+F$ (**left**), $2^{-+}1^-F$ (**center**), and $2^{-+}0^-F$ (**right**) for the minimal basis plus the $2^{-+}\left[\rho\pi\right]_F$ waves.

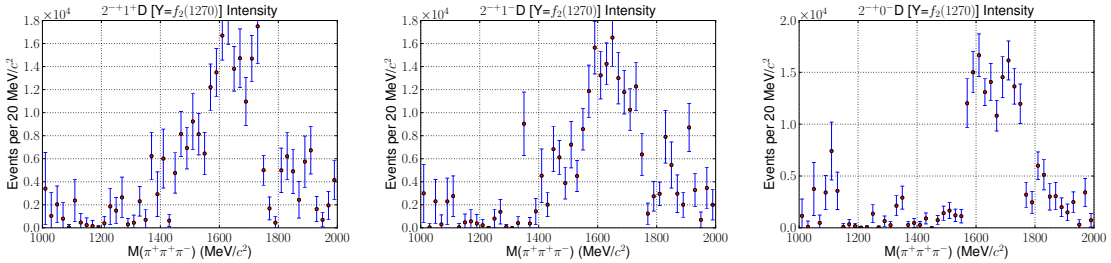

Figure B.25: 2^{-+} $[f_2(1270)\pi]_D$ intensity spectra in the presence of the $2^{-+}F$ waves: $2^{-+}1^+D$ (**left**), $2^{-+}1^-D$ (**center**), and $2^{-+}0^-D$ (**right**) for the minimal basis plus the 2^{-+} $[\rho\pi]_F$ waves.

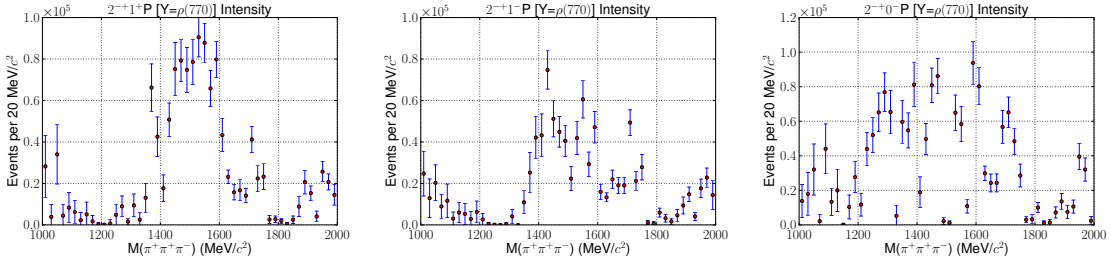

Figure B.26: 2^{-+} $[\rho\pi]_P$ intensity spectra in the presence of the $2^{-+}F$ waves: $2^{-+}1^+P$ (**left**), $2^{-+}1^-P$ (**center**), and $2^{-+}0^-P$ (**right**) for the minimal basis plus the 2^{-+} $[\rho\pi]_F$ waves.

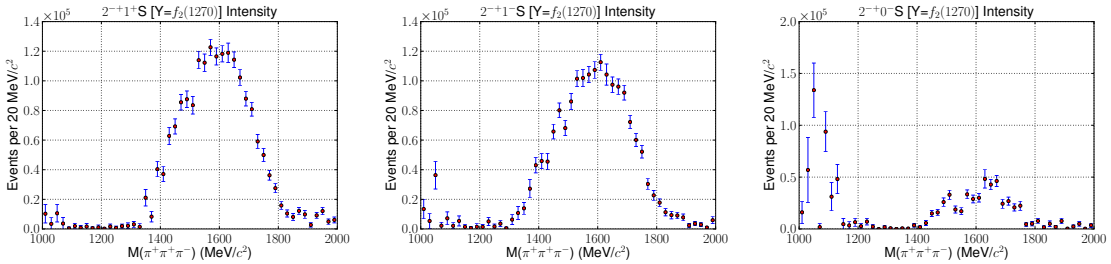

Figure B.27: 2^{-+} $[f_2(1270)\pi]_S$ intensity spectra in the presence of the $2^{-+}F$ waves: $2^{-+}1^+S$ (**left**), $2^{-+}1^-S$ (**center**), and $2^{-+}0^-S$ (**right**) for the minimal basis plus the 2^{-+} $[\rho\pi]_F$ waves.

B.5 Minimal Basis Plus $2^{-+}F$ and $2^{-+}\ [\sigma\pi]_D$

J^{PC}	M^{ϵ}	L	Y	Number of waves
1^{++}	$1^{\pm}$	S	$\rho(770)$	2
1^{-+}	$0^{-}, 1^{\pm}$	P	$\rho(770)$	3
2^{++}	$1^{\pm}$	D	$\rho(770)$	2
2^{-+}	$0^{-}, 1^{\pm}$	S, P, D, F	$f_2(1270)$, $\rho(770)$, σ	12
isotropic background wave				

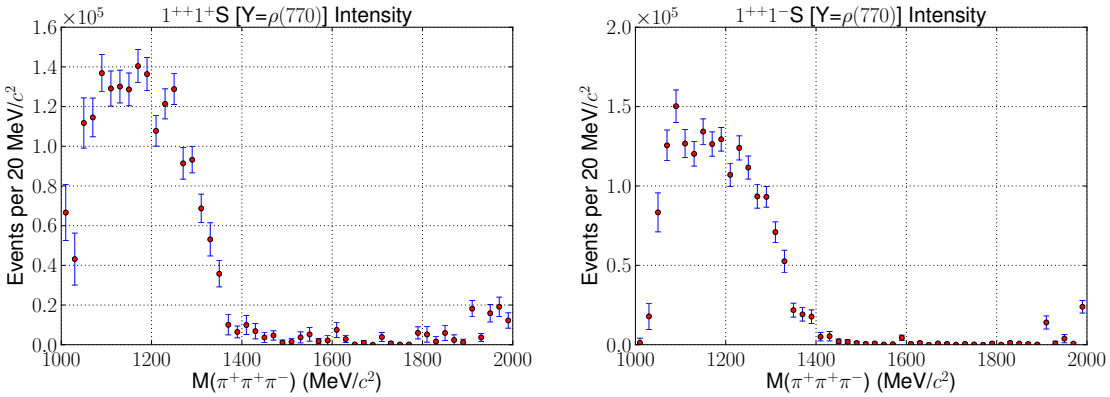

Figure B.28: $1^{++}S$ intensity in the presence of the $2^{-+}F$ and $2^{-+}\ [\sigma\pi]_D$ waves: $1^{++}1^{+}S$ (**left**) and $1^{++}1^{-}S$ (**right**) for the minimal basis plus the $2^{-+}\ [\rho\pi]_F$ and $2^{-+}\ [\sigma\pi]_D$ waves.

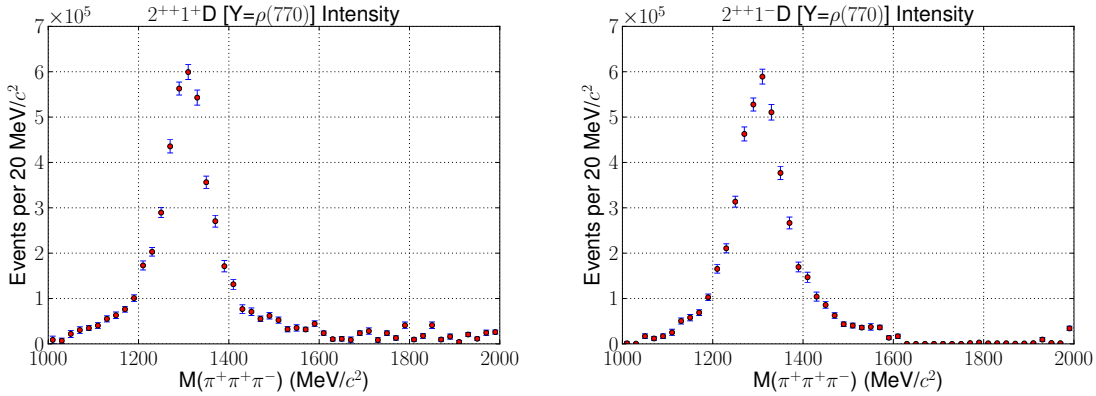

Figure B.29: $2^{++}D$ intensity in the presence of the $2^{-+}F$ and $2^{-+}\,[\sigma\pi]_D$ waves: $2^{++}1^+D$ (**left**) and $2^{++}1^-D$ (**right**) for the minimal basis plus the $2^{-+}\,[\rho\pi]_F$ and $2^{-+}\,[\sigma\pi]_D$ waves.

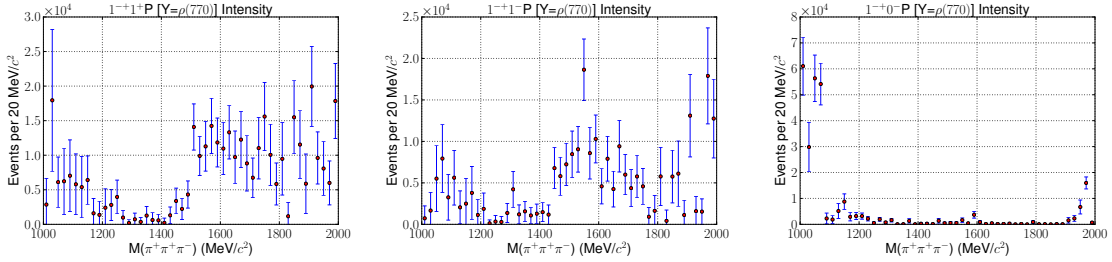

Figure B.30: 1^{-+} intensity spectra in the presence of the $2^{-+}F$ and $2^{-+}\,[\sigma\pi]_D$ waves: $1^{-+}1^+P$ (**left**), $1^{-+}1^-P$ (**center**), and $1^{-+}0^-P$ (**right**) for the minimal basis plus the $2^{-+}\,[\rho\pi]_F$ and $2^{-+}\,[\sigma\pi]_D$ waves.

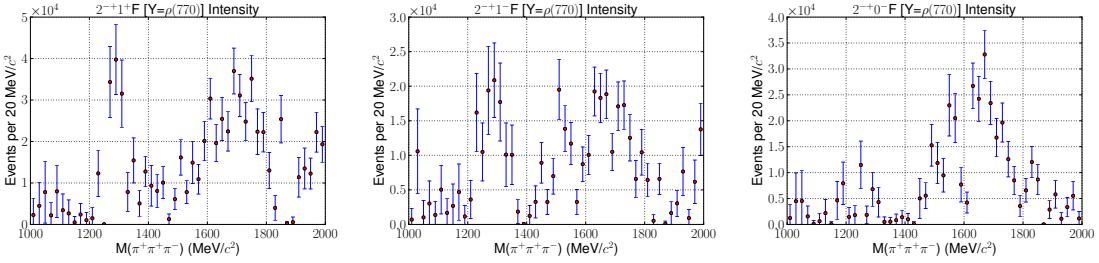

Figure B.31: $2^{-+}\,[\rho\pi]_F$ intensity in addition to the minimal basis: $2^{-+}1^+F$ (**left**), $2^{-+}1^-F$ (**center**), and $2^{-+}0^-F$ (**right**) for the minimal basis plus the $2^{-+}\,[\rho\pi]_F$ and $2^{-+}\,[\sigma\pi]_D$ waves.

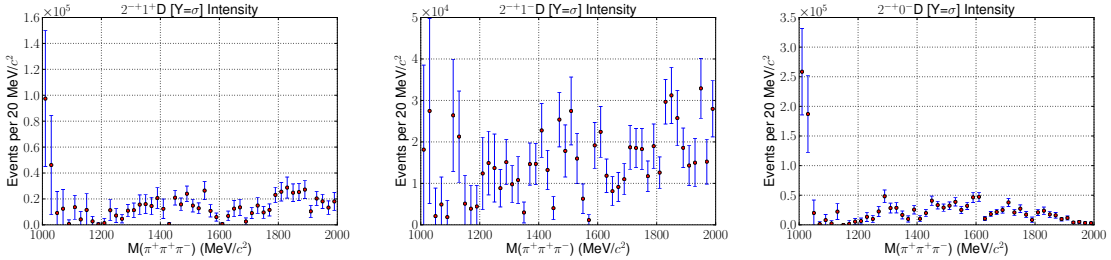

Figure B.32: 2^{-+} $[\sigma\pi]_D$ intensity in addition to the minimal basis: $2^{-+}1^{+}$ $[\sigma\pi]_D$ (**left**), $2^{-+}1^{-}$ $[\sigma\pi]_D$ (**center**), and $2^{-+}0^{-}$ $[\sigma\pi]_D$ (**right**) for the minimal basis plus the 2^{-+} $[\rho\pi]_F$ and 2^{-+} $[\sigma\pi]_D$ waves.

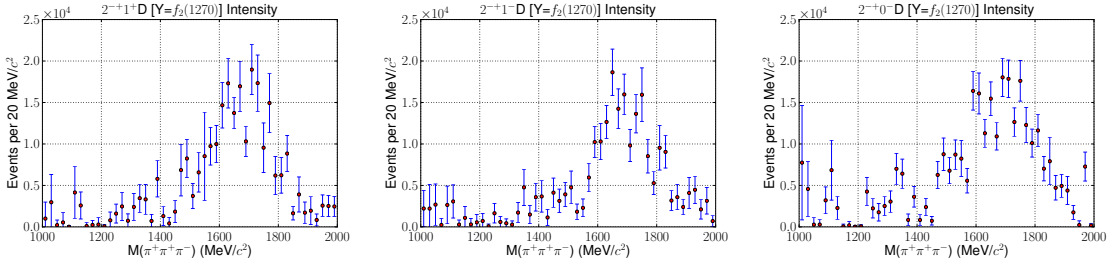

Figure B.33: 2^{-+} $[f_2(1270)\pi]_D$ intensity spectra in the presence of the $2^{-+}F$ and 2^{-+} $[\sigma\pi]_D$ waves: $2^{-+}1^{+}D$ (**left**), $2^{-+}1^{-}D$ (**center**), and $2^{-+}0^{-}D$ (**right**) for the minimal basis plus the 2^{-+} $[\rho\pi]_F$ and 2^{-+} $[\sigma\pi]_D$ waves.

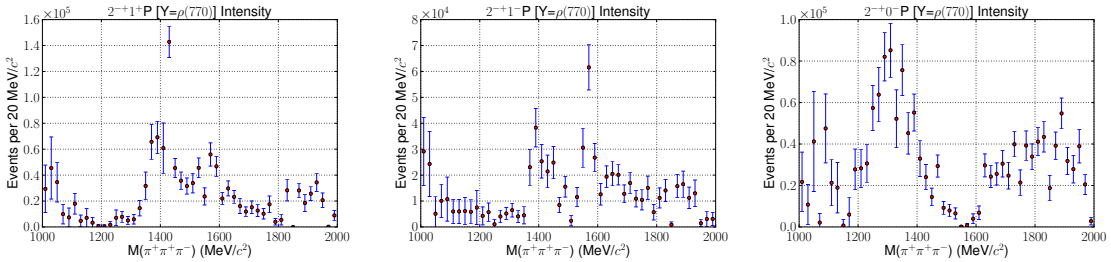

Figure B.34: 2^{-+} $[\rho\pi]_P$ intensity spectra in the presence of the $2^{-+}F$ and 2^{-+} $[\sigma\pi]_D$ waves: $2^{-+}1^{+}P$ (**left**), $2^{-+}1^{-}P$ (**center**), and $2^{-+}0^{-}P$ (**right**) for the minimal basis plus the 2^{-+} $[\rho\pi]_F$ and 2^{-+} $[\sigma\pi]_D$ waves.

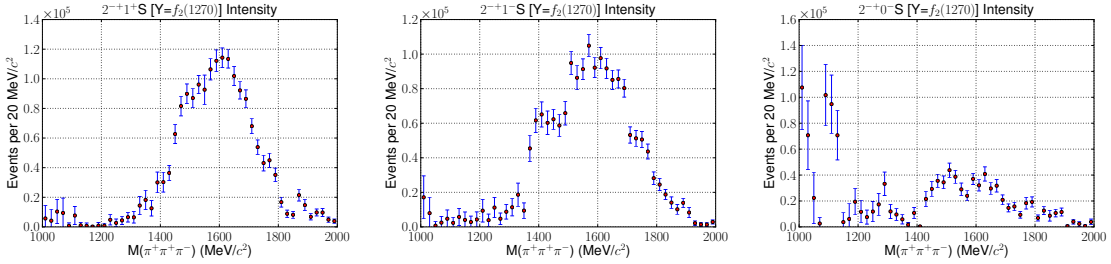

Figure B.35: $2^{-+}\,[f_2(1270)\pi]_S$ intensity spectra in the presence of the $2^{-+}F$ and $2^{-+}\,[\sigma\pi]_D$ waves: $2^{-+}1^+S$ (**left**), $2^{-+}1^-S$ (**center**), and $2^{-+}0^-S$ (**right**) for the minimal basis plus the $2^{-+}\,[\rho\pi]_F$ and $2^{-+}\,[\sigma\pi]_D$ waves.

B.6 Upper Sideband of the Neutron

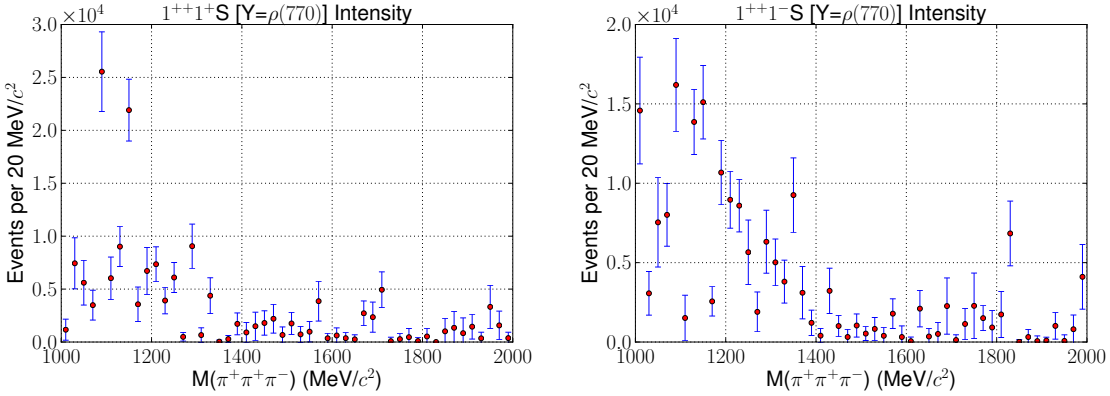

Figure B.36: 1^{++} acceptance-corrected yields for Fit 8: $1^{++}1^{+}S$ (**left**) and $1^{++}1^{-}S$ (**right**) for data selected from the upper sideband of the neutron.

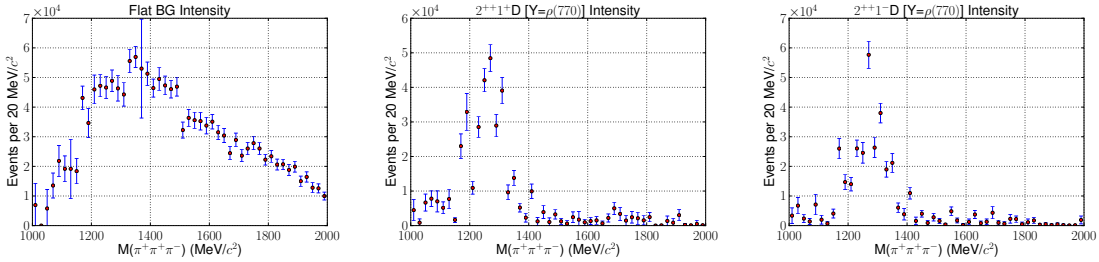

Figure B.37: Isotropic background (**left**) and 2^{++} acceptance-corrected yields for Fit 8: $2^{++}1^{+}D$ (**center**) and $2^{++}1^{-}D$ (**right**) for data selected from the upper sideband of the neutron.

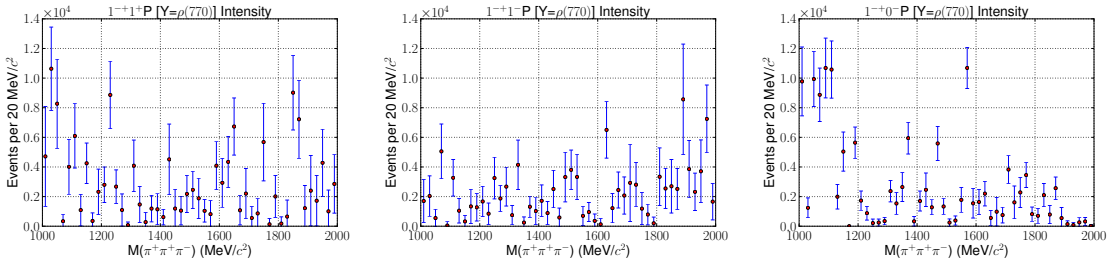

Figure B.38: 1^{-+} acceptance-corrected yields for Fit 8: $1^{-+}1^{+}P$ (**left**), $1^{-+}1^{-}P$ (**center**), and $1^{-+}0^{-}P$ (**right**) for data selected from the upper sideband of the neutron.

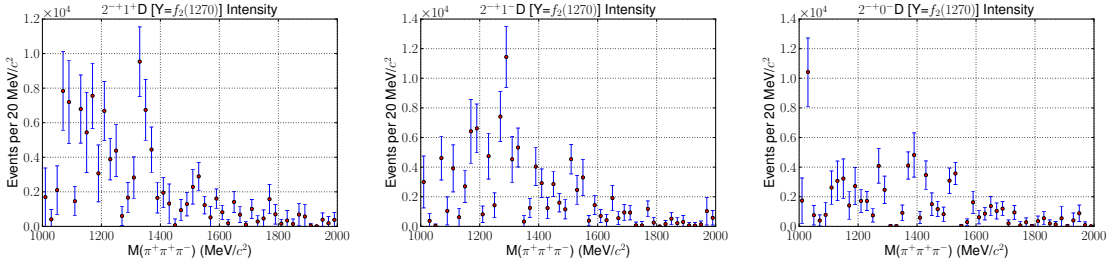

Figure B.39: 2^{-+} $[f_2(1270)\pi]_D$ acceptance-corrected yields for Fit 8: $2^{-+}1^{+}$ $[f_2\pi]_D$ (**left**), $2^{-+}1^{-}$ $[f_2\pi]_D$ (**center**), and $2^{-+}0^{-}$ $[f_2\pi]_D$ (**right**) for data selected from the upper sideband of the neutron.

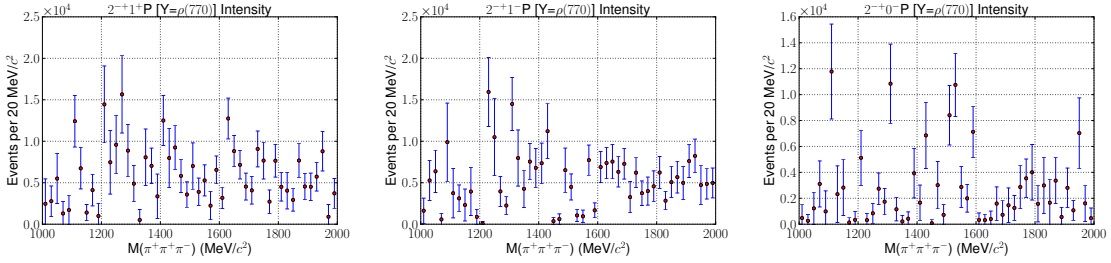

Figure B.40: 2^{-+} $[\rho\pi]_P$ acceptance-corrected yields for Fit 8: $2^{-+}1^{+}P$ (**left**), $2^{-+}1^{-}P$ (**center**), and $2^{-+}0^{-}P$ (**right**) for data selected from the upper sideband of the neutron.

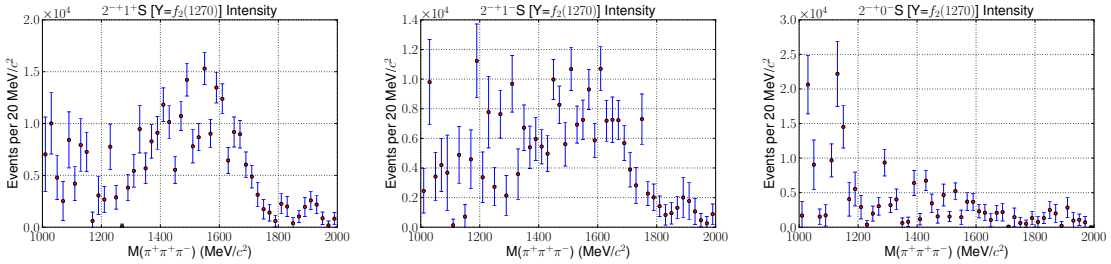

Figure B.41: 2^{-+} $[f_2(1270)\pi]_S$ acceptance-corrected yields for Fit 8: $2^{-+}1^+S$ (**left**), $2^{-+}1^-S$ (**center**), and $2^{-+}0^-S$ (**right**) for data selected from the upper sideband of the neutron.

B.7 40 MeV Bins in 3π Mass

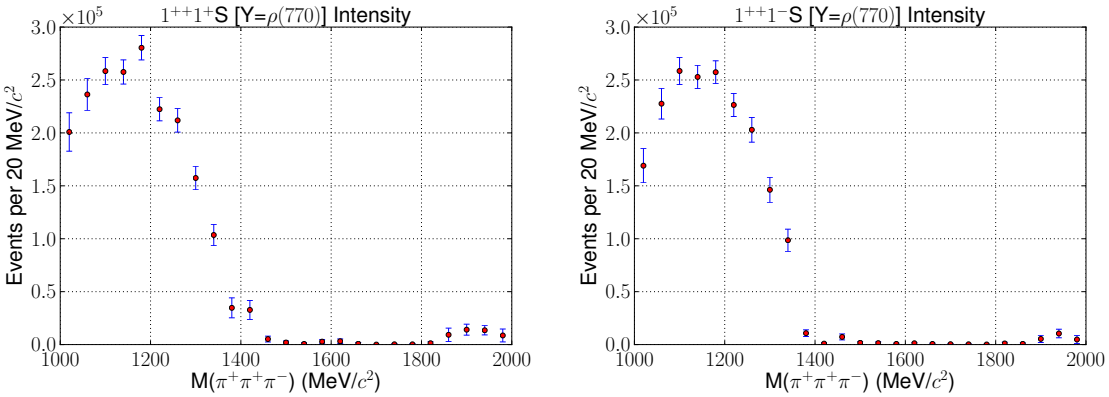

Figure B.42: 1^{++} acceptance-corrected yields for Fit 10: $1^{++}1^{+}S$ (**left**) and $1^{++}1^{-}S$ (**right**) for data selected from the upper sideband of the neutron.

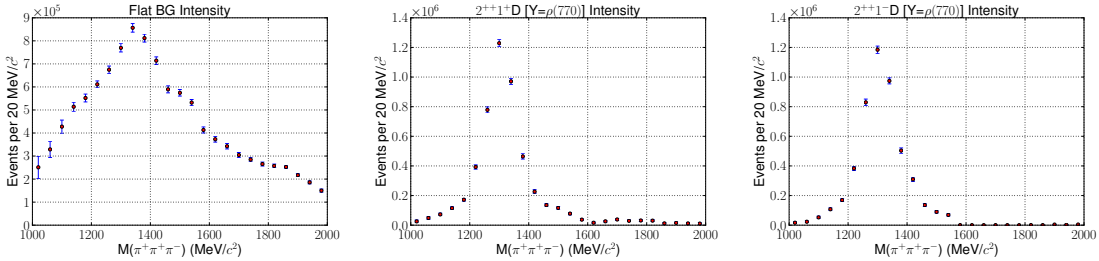

Figure B.43: Isotropic background (**left**) and 2^{++} acceptance-corrected yields for Fit 10: $2^{++}1^{+}D$ (**center**) and $2^{++}1^{-}D$ (**right**) for data selected from the upper sideband of the neutron.

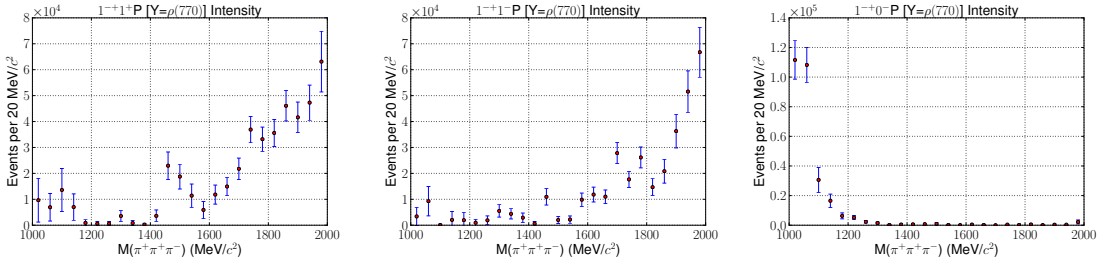

Figure B.44: 1^{-+} acceptance-corrected yields for Fit 10: $1^{-+}1^{+}P$ (**left**), $1^{-+}1^{-}P$ (**center**), and $1^{-+}0^{-}P$ (**right**) for data selected from the upper sideband of the neutron.

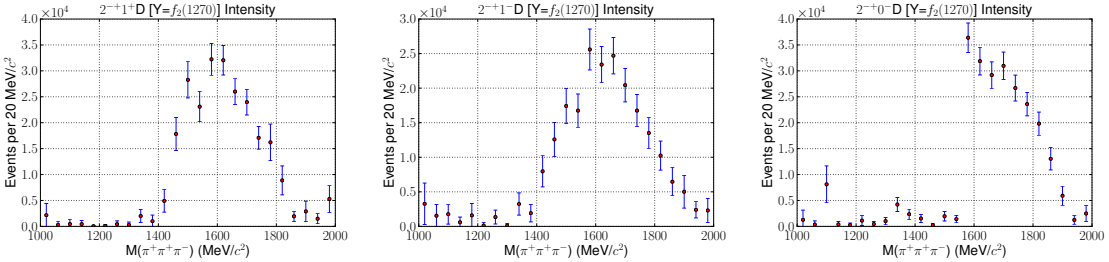

Figure B.45: 2^{-+} $[f_2(1270)\pi]_D$ acceptance-corrected yields for Fit 10: $2^{-+}1^{+}$ $[f_2\pi]_D$ (**left**), $2^{-+}1^{-}$ $[f_2\pi]_D$ (**center**), and $2^{-+}0^{-}$ $[f_2\pi]_D$ (**right**) for data selected from the upper sideband of the neutron.

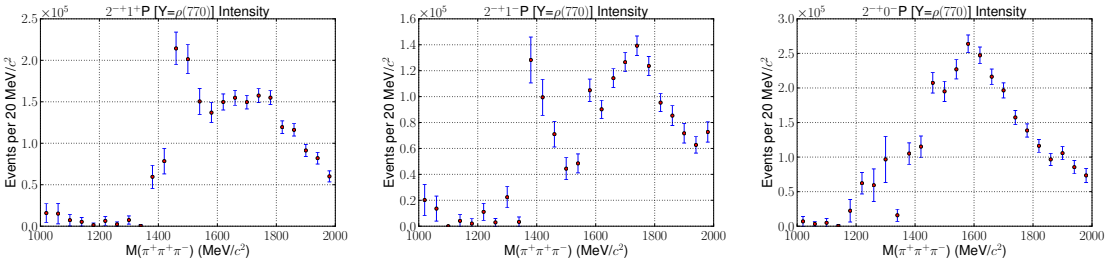

Figure B.46: 2^{-+} $[\rho\pi]_P$ acceptance-corrected yields for Fit 10: $2^{-+}1^{+}P$ (**left**), $2^{-+}1^{-}P$ (**center**), and $2^{-+}0^{-}P$ (**right**) for data selected from the upper sideband of the neutron.

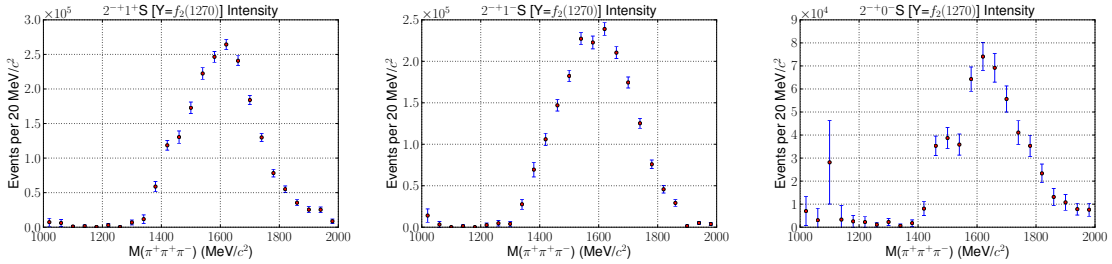

Figure B.47: 2^{-+} $[f_2(1270)\pi]_S$ acceptance-corrected yields for Fit 10: $2^{-+}1^+S$ (**left**), $2^{-+}1^-S$ (**center**), and $2^{-+}0^-S$ (**right**) for data selected from the upper sideband of the neutron.

B.8 10 MeV Bins in 3π Mass

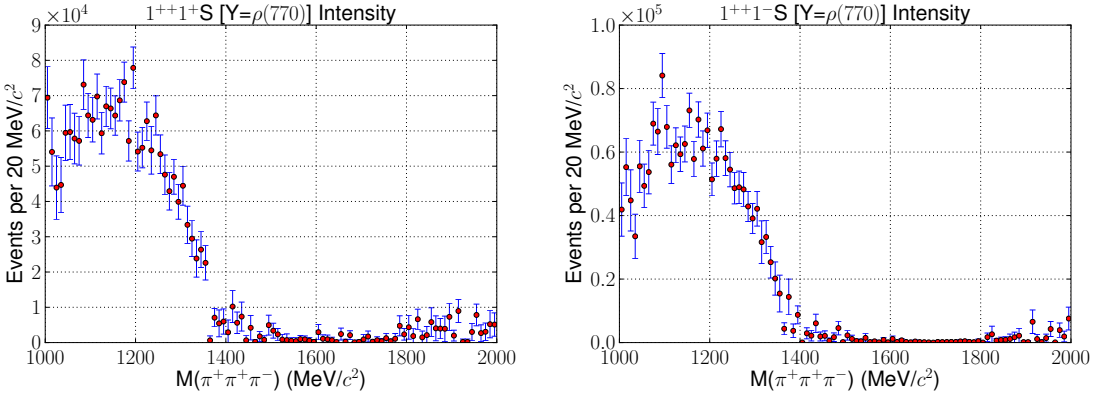

Figure B.48: 1^{++} acceptance-corrected yields for 10 MeV bins in 3π mass: $1^{++}1^+S$ (**left**) and $1^{++}1^-S$ (**right**).

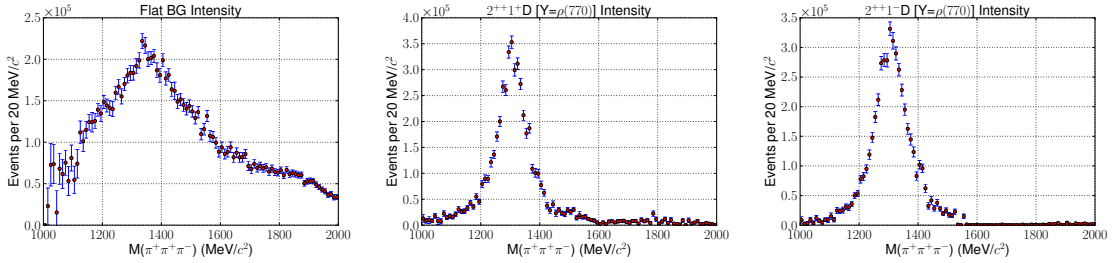

Figure B.49: Isotropic background (**left**) and 2^{++} acceptance-corrected yields for 10 MeV bins in 3π mass: $2^{++}1^+D$ (**center**) and $2^{++}1^-D$ (**right**).

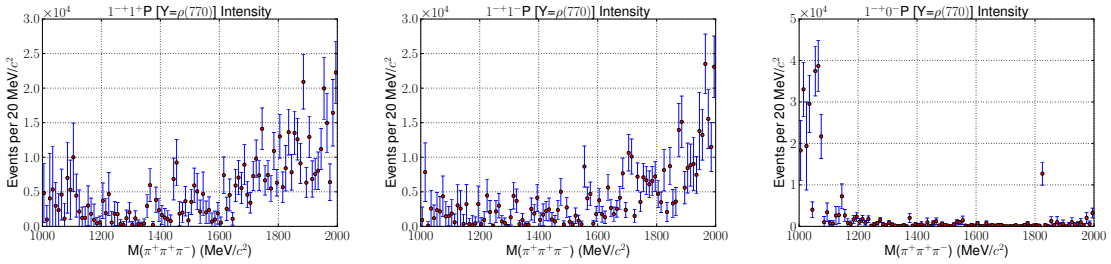

Figure B.50: 1^{-+} acceptance-corrected yields for 10 MeV bins in 3π mass: $1^{-+}1^{+}P$ (**left**), $1^{-+}1^{-}P$ (**center**), and $1^{-+}0^{-}P$ (**right**).

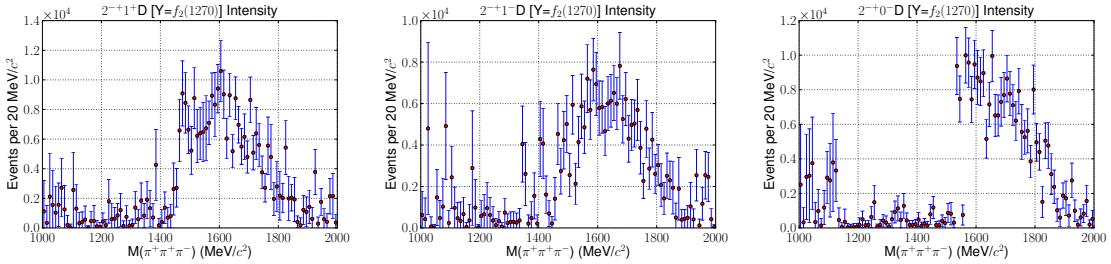

Figure B.51: $2^{-+}\ [f_2(1270)\pi]_D$ acceptance-corrected yields for 10 MeV bins in 3π mass: $2^{-+}1^{+}\ [f_2\pi]_D$ (**left**), $2^{-+}1^{-}\ [f_2\pi]_D$ (**center**), and $2^{-+}0^{-}\ [f_2\pi]_D$ (**right**).

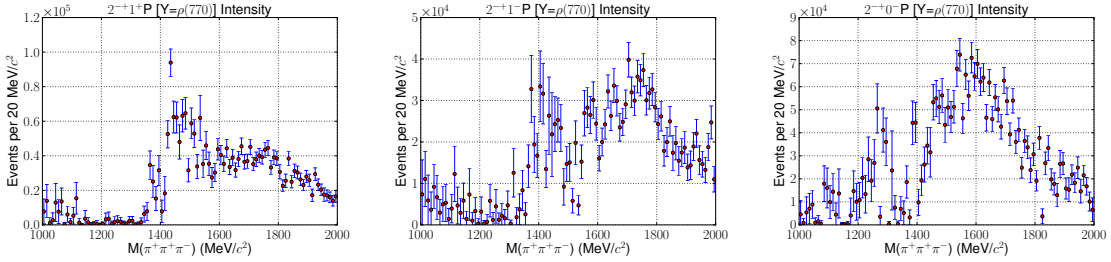

Figure B.52: $2^{-+}\ [\rho\pi]_P$ acceptance-corrected yields for 10 MeV bins in 3π mass: $2^{-+}1^{+}P$ (**left**), $2^{-+}1^{-}P$ (**center**), and $2^{-+}0^{-}P$ (**right**).

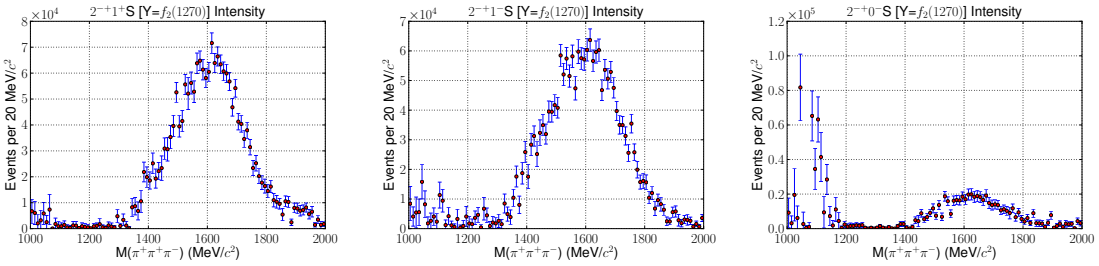

Figure B.53: $2^{-+}\,[f_2(1270)\pi]_S$ acceptance-corrected yields for 10 MeV bins in 3π mass: $2^{-+}1^{+}S$ (**left**), $2^{-+}1^{-}S$ (**center**), and $2^{-+}0^{-}S$ (**right**).

B.9 $1^{++}D$ Fit with ϕ_H Cut

The data sample in the fit described in this Section has had all events with $|\phi_H| < 25°$ for either isobar removed.

J^{PC}	M^{ϵ}	L	Y	Number of waves
1^{++}	$1^{\pm}$	S	$\rho(770)$	2
1^{++}	$0^{+}, 1^{\pm}$	D	$\rho(770)$	3
1^{-+}	$0^{-}, 1^{\pm}$	P	$\rho(770)$	3
2^{++}	$1^{\pm}$	D	$\rho(770)$	2
2^{-+}	$0^{-}, 1^{\pm}$	S, P, D	$f_2(1270)$, $\rho(770)$	9
isotropic background wave				

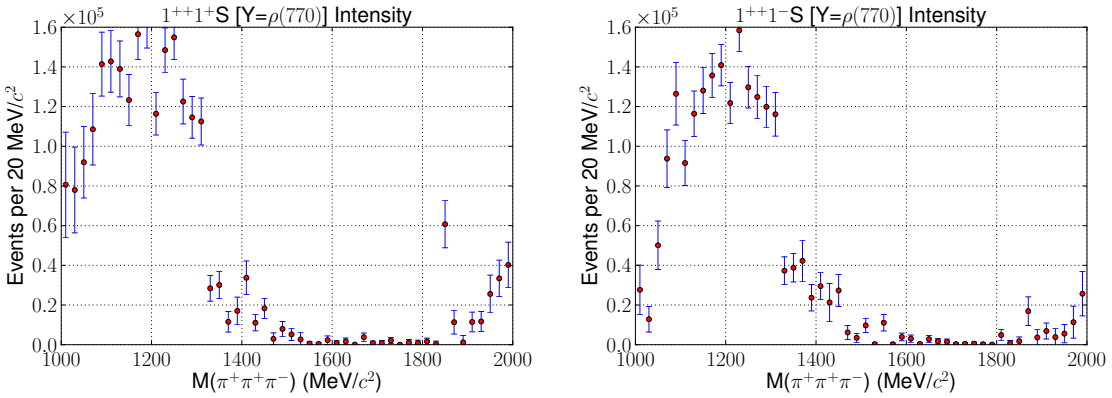

Figure B.54: $1^{++}S$ intensity with the region of $|\phi_H| < 25°$ removed: $1^{++}1^{+}S$ (**left**) and $1^{++}1^{-}S$ (**right**).

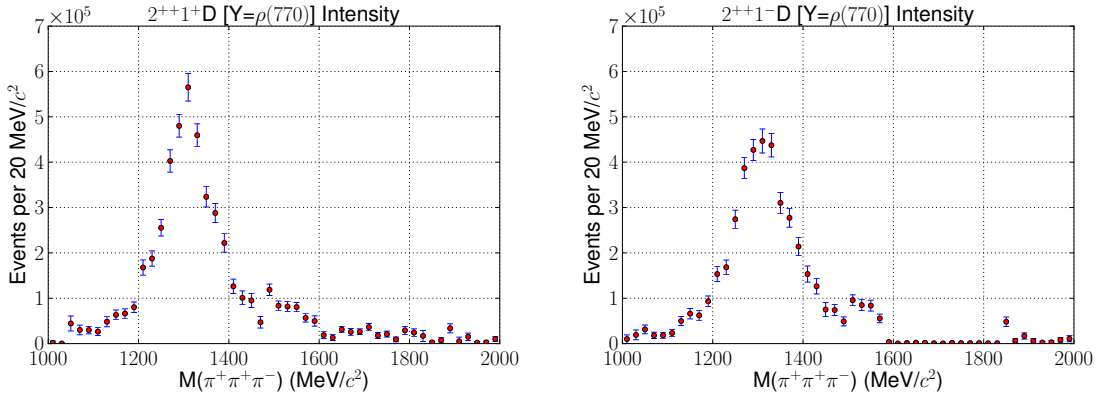

Figure B.55: $2^{++}D$ intensity with the region of $|\phi_H| < 25°$ removed: $2^{++}1^{+}D$ (**left**) and $2^{++}1^{-}D$ (**right**).

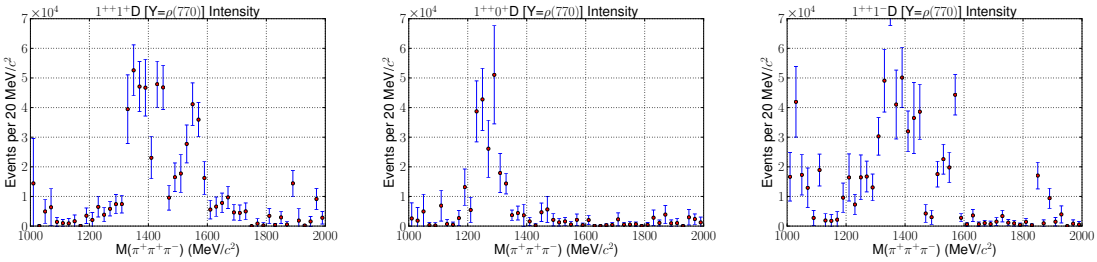

Figure B.56: $1^{++}D$ intensity when combined with our minimal waveset: $1^{++}1^{+}D$ (**left**), $1^{++}0^{+}D$ (**center**), and $1^{++}1^{-}D$ (**right**).

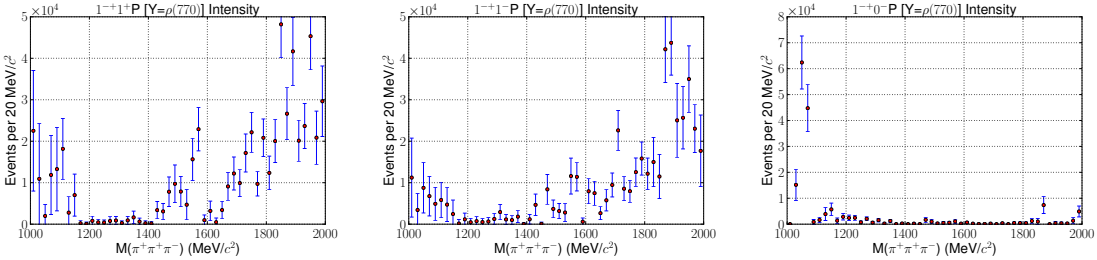

Figure B.57: 1^{-+} intensity spectra with the region of $|\phi_H| < 25°$ removed: $1^{-+}1^{+}P$ (**left**), $1^{-+}1^{-}P$ (**center**), and $1^{-+}0^{-}P$ (**right**).

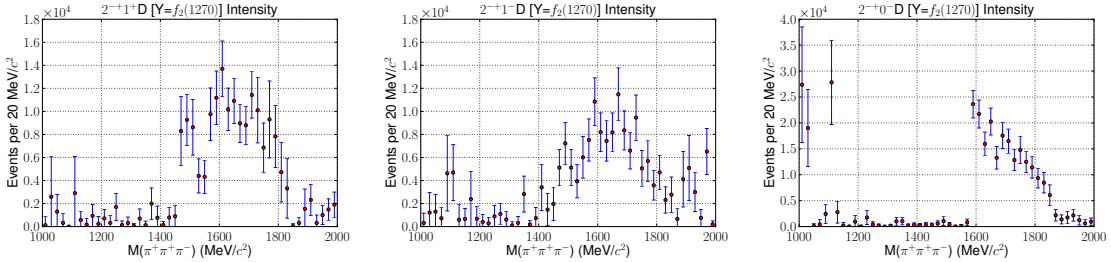

Figure B.58: 2^{-+} $[f_2(1270)\pi]_D$ intensity spectra with the region of $|\phi_H| < 25°$ removed: $2^{-+}1^{+}D$ (**left**), $2^{-+}1^{-}D$ (**center**), and $2^{-+}0^{-}D$ (**right**).

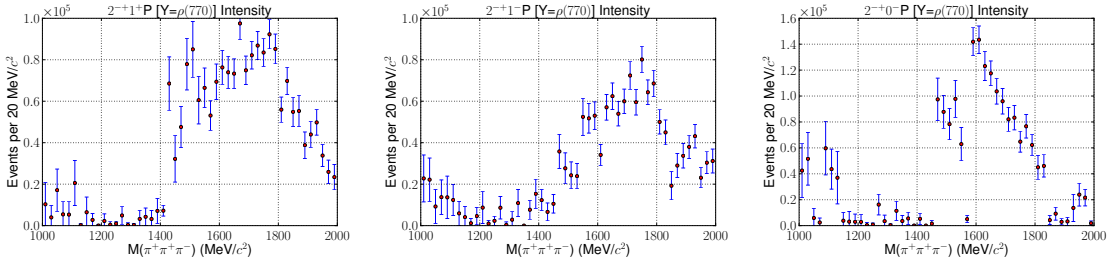

Figure B.59: 2^{-+} $[\rho\pi]_P$ intensity spectra with the region of $|\phi_H| < 25°$ removed: $2^{-+}1^{+}P$ (**left**), $2^{-+}1^{-}P$ (**center**), and $2^{-+}0^{-}P$ (**right**).

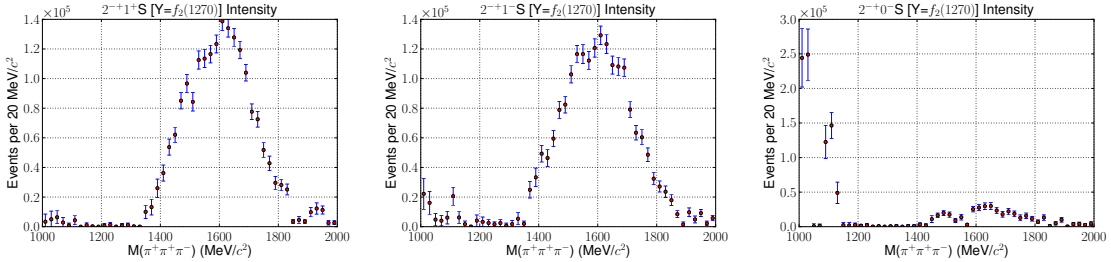

Figure B.60: 2^{-+} $[f_2(1270)\pi]_S$ intensity spectra with the region of $|\phi_H| < 25°$ removed: $2^{-+}1^{+}S$ (**left**), $2^{-+}1^{-}S$ (**center**), and $2^{-+}0^{-}S$ (**right**).

APPENDIX C

SYSTEMATIC EFFECTS ON FIT RESULTS

This section expands on the discussion in Section 5.3.9 of the stability of our fit results against changes in various parameters in our analysis.

C.1 Systematic Effects from Incidental Background

As shown in Section 3.1.6, we identify the neutron by its mass, using the momentum remaining after subtracting the momentum of the pions from the initial-state momentum. While our vertex and timing cuts greatly improved the signal-to-background ratio of the neutron peak, some background beneath the neutron still exists, and it is possible that some fraction of these events make it into our partial-wave analysis. To account for these events in the partial-wave analysis, we include an isotropic background wave in all of our fits, which when added in incoherently with all of our other waves, helps to absorb broken events which have a small overlap with the real states included in a given fit. In order to estimate how much incidental background we have, we can compare the accepted yield of the isotropic background wave in each bin to the number of events beneath the neutron in that bin. We determine the number of events beneath the neutron in the same manner as described in Section 3.1.3, using a Gaussian fit plus a polynomial background and integrating the polynomial over the selected region. The result is shown in Figure C.1. We see that the isotropic background wave is completely made up of incidental background in the low-mass region. As we increase in 3π mass, we see that the proportion drops, as we would expect for a gradually increasing level of baryon background.

However, the isotropic background wave only absorbs events which are not well-described by other amplitudes in our partial-wave basis. It is possible that events beneath the neutron have large overlaps with one or two non-isotropic waves in our basis, introducing a systematic bias into our fit results. In order to study this background more closely, we examine the *sidebands* of the neutron, where we select events just above and just below our nominal selection region. As our background is smoothly varying, these sideband events taken together should have similar characteristics to the events making up the background beneath the neutron.

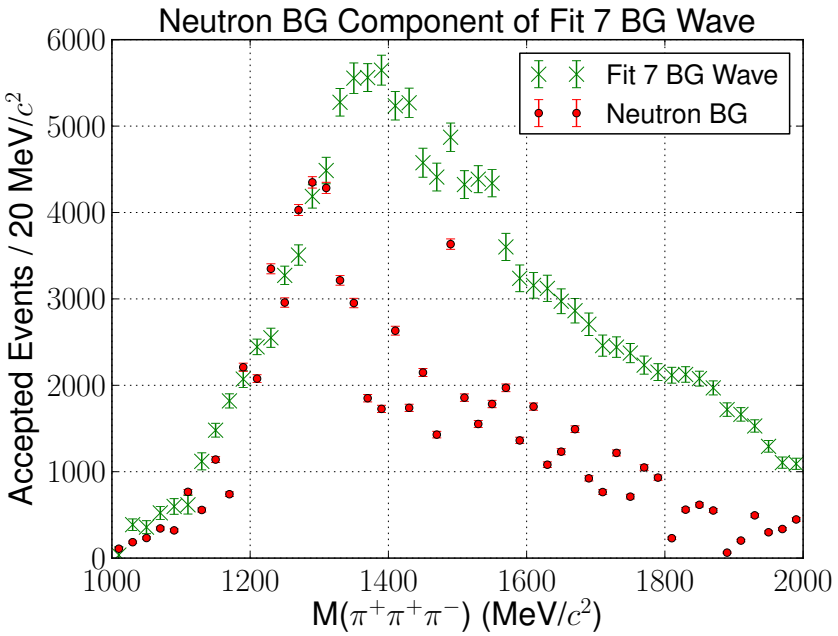

Figure C.1: An estimate of the fraction of the isotropic background wave for our minimal waveset which is due to events beneath the neutron in the event sample.

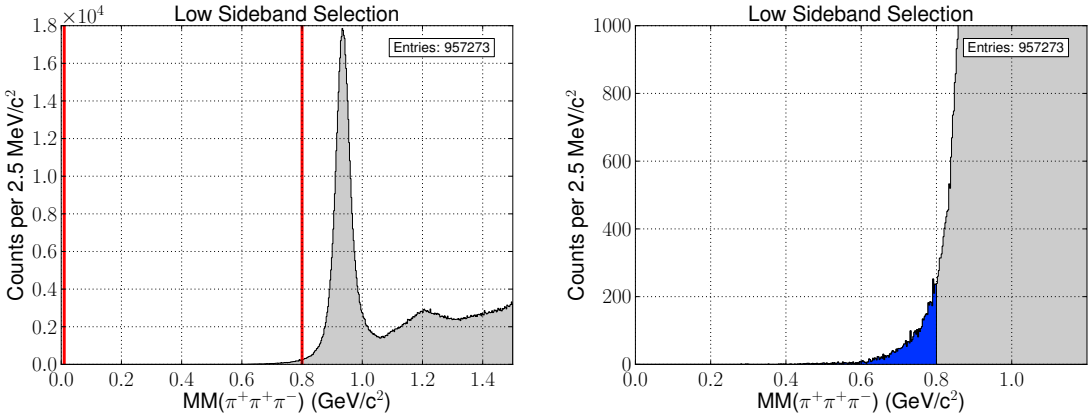

Figure C.2: On the left, the selected region for the low sideband of the neutron is between the two red lines; the right-hand plot shows a zoomed-in view, where the blue region is the selected region.

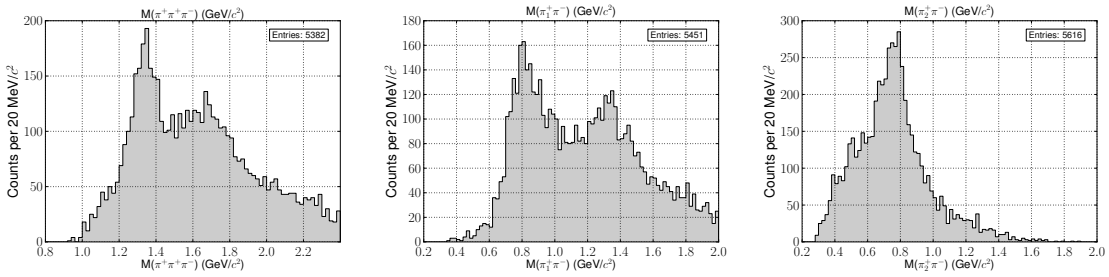

Figure C.3: Invariant masses for the 3π (**left**), $\pi_1^+\pi^-$ (**middle**), and $\pi_2^+\pi^-$ (**right**) systems for events in the lower sideband of the neutron.

C.1.1 Low Sideband

The low sideband of the neutron retains only 5616 events after our baryon-background rejection cuts. The selected region is shown in Figure C.2. Examining the 3π and $\pi^+\pi^-$ invariant masses for these events, all shown in Figure C.3, we see that we see features similar to those present in our regular data. The 3π invariant mass has a peak at 1.3 GeV and a shoulder at 1.6 GeV, and the di-pion masses show clear peaks for $\rho(770)$ and $f_2(1270)$ production. This indicates that while the neutron mass is incorrect, the majority of these events are still consistent with a $\gamma p \to \pi^+\pi^+\pi^- n$ process. The most likely cause for the low missing mass is that the photon that actually caused the event was not measured by the tagger, and we were forced to pick the wrong photon, which happened to be lower in energy than the trigger photon. Getting the energy and momentum balance for the event wrong means that our boosts into the various rest frames will be slightly off, blurring the angular distributions fit by the PWA. However as these events are present in low numbers and seem to be of the same production processes as our good events, we claim that the effect of these events on our PWA results is negligible.

C.1.2 High Sideband

The selection of the high sideband, from 1.04 to 1.15 GeV in missing mass, is shown in Figure C.4, and consists of 77K events. One can see that the next state to present itself in our missing-mass spectrum is the Δ^0, and we expect it to be the primary source of background from the high side. The three- and di-pion masses are shown in Figure C.5, and again, these show features consistent with our good $\gamma p \to \pi^+\pi^+\pi^- n$ events, with strong peaks for the a_2, f_2, and ρ in their respective mass combinations. These events are simply $\gamma p \to \pi^+\pi^+\pi^-\Delta^0$ events, which should be governed by the same physics as $\gamma p \to \pi^+\pi^+\pi^- n$ events. In fact producing the 3π system off the Δ might result in an even cleaner dataset than $\gamma p \to \pi^+\pi^+\pi^- n$, as the production mechanism is constrained to be pion exchange. The inclusion of these events beneath our neutron presents the same hazards as the low-mass sideband, in terms of our boosts being slightly incorrect and thus blurring our angular distributions. The presence of these events might lead us to an increased a_2 yield, but it should not affect an observation of the $\pi_1(1600)$, if present.

However, from the peak at 500 MeV, we can also see that our production of events with

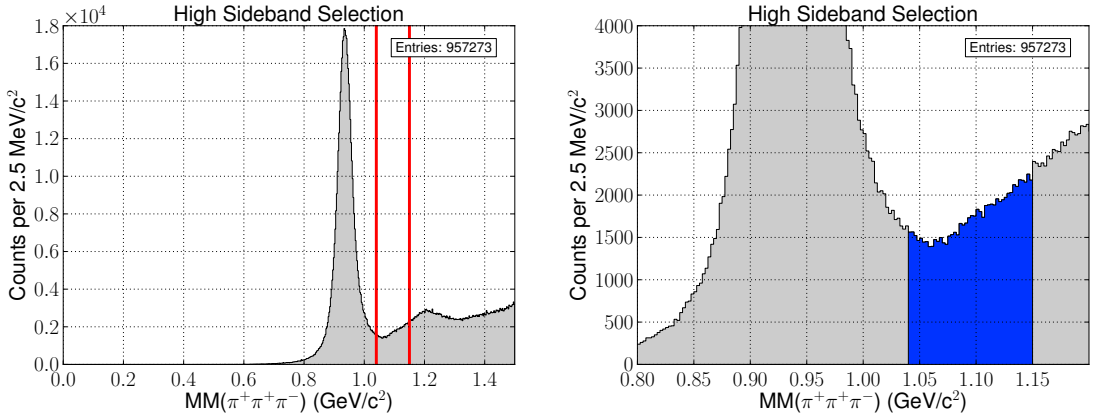

Figure C.4: On the left, the selected region for the high sideband of the neutron is between the two red lines; the right-hand plot shows a zoomed-in view, where the blue region is the selected region.

a K_S is significantly enhanced; this is due to events where the $\Lambda(1105)$ is within our missing mass selection. With a missing Λ, processes like $\gamma p \to \Sigma(1385)^+ K^0$ and $\gamma p \to \Lambda K^*(892)$ can make a contribution. While the K^* has $J^P = 1^-$, it is unlikely that these events will actually manifest in the 1^{-+} partial waves, as we do not have a K_S isobar in our basis, nor do we analyze events with $M_{3\pi}$ less than 1 GeV. While these events should be suppressed in our nominal sample by our missing mass selection, we will perform a PWA to examine any effect they may have on our results, as well as to confirm our assumptions about the effects of $\Delta\pi^+\pi^+\pi^-$ background.

We perform a PWA on these 77K sideband events using the same waves as included in our final waves. For normalization, we generate a separate set of monte-carlo with the same parameters as described in Section 3.4, but with a neutron mass of 1100 MeV rather than the nominal 939 MeV. 8M events were generated, and 149K were accepted after our cuts in t' and $\theta_{lab}\left[\pi_2^+\right]$.

The intensity is dominated by the isotropic background wave and the 2^{++} waves, shown in Figure C.6. The isotropic background wave peaks at 1.3 along with the 2^{++}, consistent with a mixture of events due to $a_2(1320)$ production with varying levels of distortion in their angular distributions. a_2 decays whose angles are severely affected by the incorrect kinematics are absorbed by the background, while those whose angles still overlap well enough with a $2^{++}D$ decay to produce a strong amplitude go into the 2^{++} wave. We see no features in any of the partial waves consistent with ΛK^* pollution. The rest of the intensities from this fit are shown in Appendix B.6.

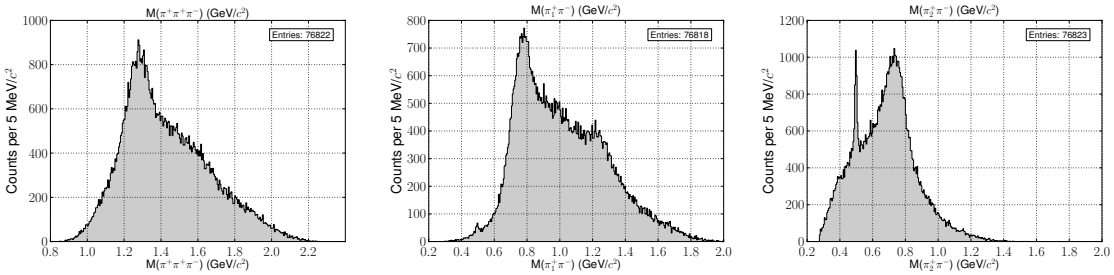

Figure C.5: Invariant masses for the 3π (**left**), $\pi_1^+\pi^-$ (**middle**), and $\pi_2^+\pi^-$ (**right**) systems for events in the upper sideband of the neutron. The peak for the K_S in the $\pi_2^+\pi^-$ mass (right) is quite pronounced compared to our good events, indicative of a tendency to accept events with a missing $\Lambda(1105)$ due to our higher missing-mass selection.

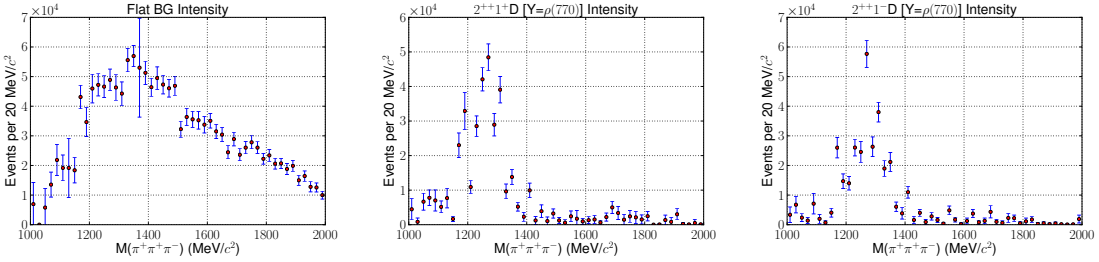

Figure C.6: Major waves in a PWA of the upper sideband of the neutron; the isotropic background wave (**left**), $2^{++}1^+$ (**center**), and $2^{++}1^+$ (**right**).

C.2 Rank Considerations

Throughout our analysis, we have experimented with fits of rank II in various configurations. The analysis in Ref. [51] justifies their use of a rank II fit by the peak in the isotropic background at 1.3 GeV. We have shown in Section C.1 that this background peak can be explained by the presence of poorly-measured $\gamma p \to \pi^+\pi^+\pi^-\Delta^0$ events leaking into our neutron mass selection. We find that adding a second rank does little to improve our fit results; leakage between waves is increased and features dominant in rank I are washed out.

To illustrate these effects, Figures C.7 through C.10 show a sample of the intensities of a rank II fit with the waveset of Appendix B.1. The isotropic background wave, shown in Figure C.7 along with the 2^{++} intensities, is reduced in size, but it continues to peak near the a_2 mass. The 2^{++} waves also acquire slightly more intensity, while the 1^{++} waves, shown in Figure C.8, are about the same size but with longer high-mass tails. However, in the high mass regime where the baryon background is more prevalent, the 2^{-+} waves, shown in Figure C.9, look highly disordered. Only the $2^{-+}S$ waves look similar to their rank I counterparts, albeit with long tails down into the low-mass region. The $2^{-+}D$ waves are plagued by leakage from the a_2 and show little symmetry between the two $M^\epsilon = 1^\pm$ intensities; the $2^{-+}P$ waves are broad across the entire 3π mass range, and the $2^{-+}0^-S$ shows signs of leakage from the 1^{++}.

The exotic waves, shown in Figure C.10, show a peak at 1.6 GeV in the $M = 0$ wave, whereas the $M^\epsilon = 1^\pm$ waves look similar to rank I, albeit with further signs of leakage at 1.2 GeV, likely from the 1^{++}.

The chaotic behavior of this fit at high mass is representative of many of our rank-II fits. In line with our expectations of our dataset being produced primarily through pion exchange, our physics seems to be best described by fits of rank I.

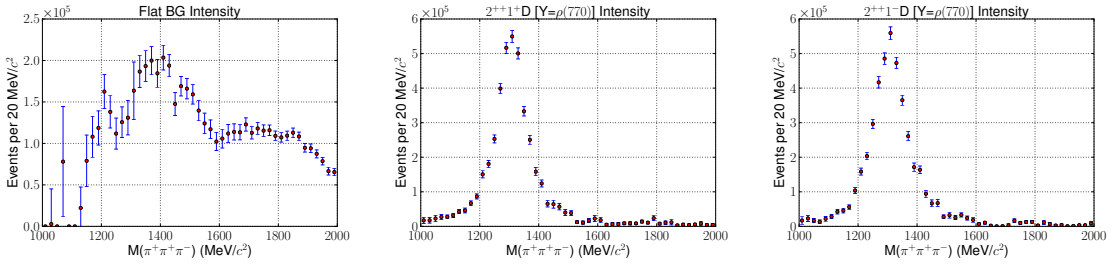

Figure C.7: Isotropic background (**left**) and 2^{++} acceptance-corrected yields for the rank-II fit: $2^{++}1^+D$ (**center**) and $2^{++}1^-D$ (**right**).

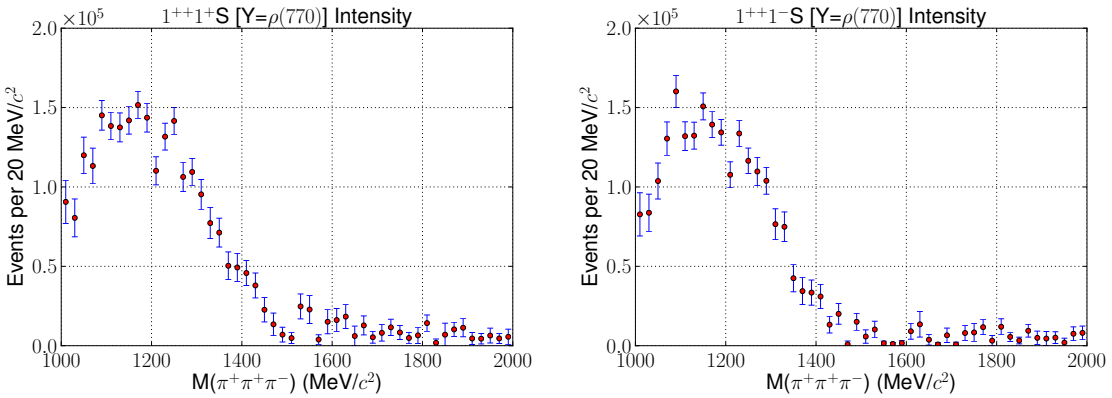

Figure C.8: 1^{++} acceptance-corrected yields for the rank-II fit: $1^{++}1^{+}S$ (**left**) and $1^{++}1^{-}S$ (**right**).

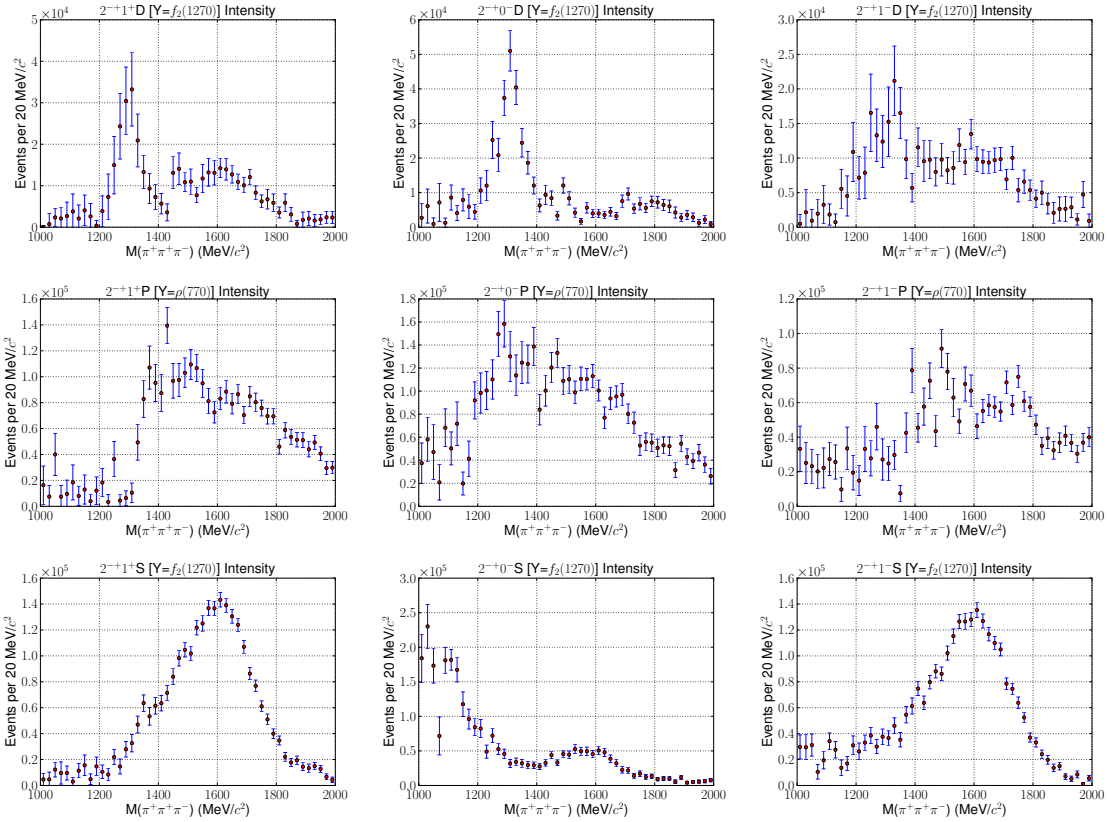

Figure C.9: Intensities for the 2^{-+} waves included in the rank-II fit: $2^{-+}1^{+}$ $[f_2\pi]_D$ (**top left**), $2^{-+}0^{-}$ $[f_2\pi]_D$ (**top center**), $2^{-+}1^{-}$ $[f_2\pi]_D$ (**top right**), $2^{-+}1^{+}$ $[\rho\pi]_P$ (**center left**), $2^{-+}0^{-}$ $[\rho\pi]_P$ (**dead center**), $2^{-+}1^{-}$ $[\rho\pi]_P$ (**center right**), $2^{-+}1^{+}$ $[f_2\pi]_S$ (**bottom left**), $2^{-+}0^{-}$ $[f_2\pi]_S$ (**bottom center**), and $2^{-+}1^{-}$ $[f_2\pi]_S$ (**bottom right**).

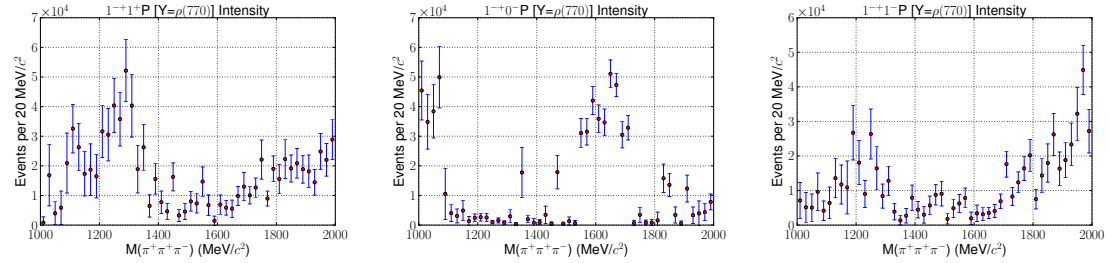

Figure C.10: Intensities for the exotic waves in the rank-II fit: $1^{-+}1^{+}$P (**left**), $1^{-+}0^{-}$P (**middle**), and $1^{-+}1^{-}$P (**right**).

C.3 Systematic Effects Due to Bin Size

As a check on the systematic dependence of our fit results on bin size, we performed two more fits with the basis in Appendix B.1 in 40 MeV and 10 MeV bins in 3π mass. The $1^{++}S$, $2^{++}D$, and $2^{-+}S$ intensities are compared in Figures C.11, C.12, and C.13, respectively. The results are quite robust across all waves despite the changes in binning, with very little in the way of statistical fluctuations. The complete set of intensity spectra for these fits are located in Appendix B.7 and B.8.

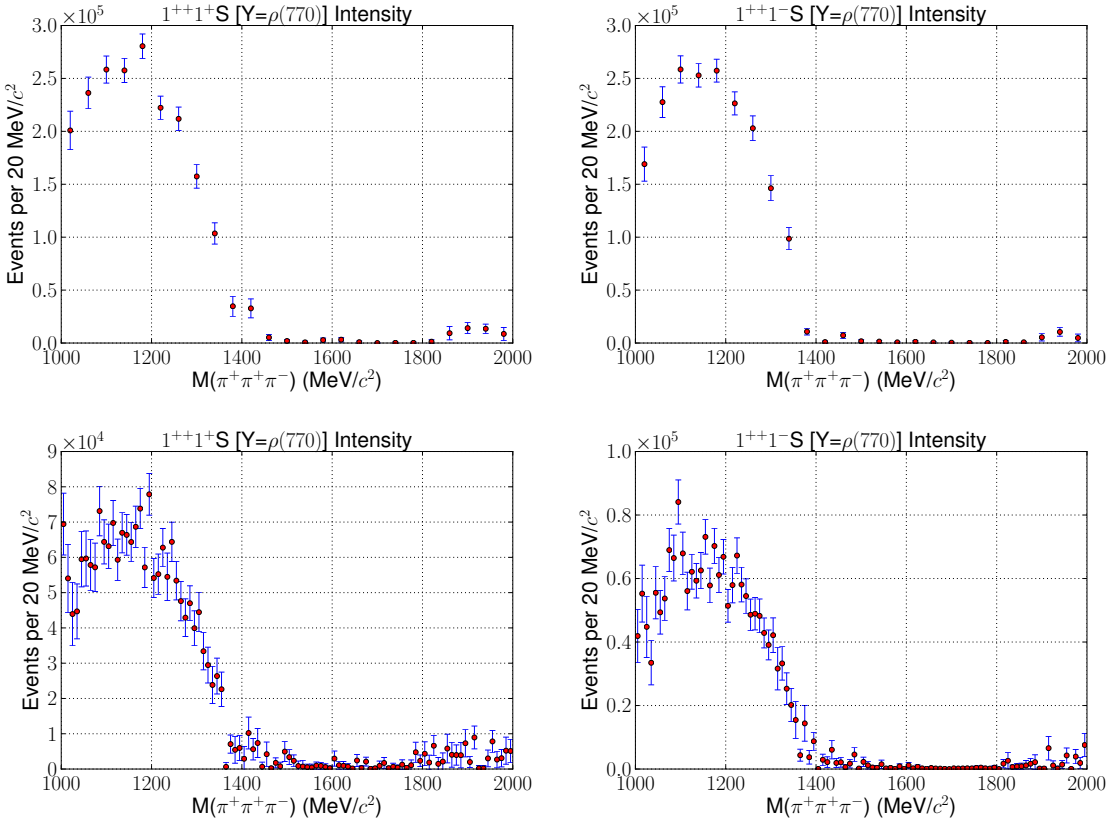

Figure C.11: The $1^{++}S$ acceptance-corrected yields for 40 MeV bins (**top**) and 10 MeV bins(**bottom**), with the $M^\epsilon = 1^+$ on the right and 1^- on the left.

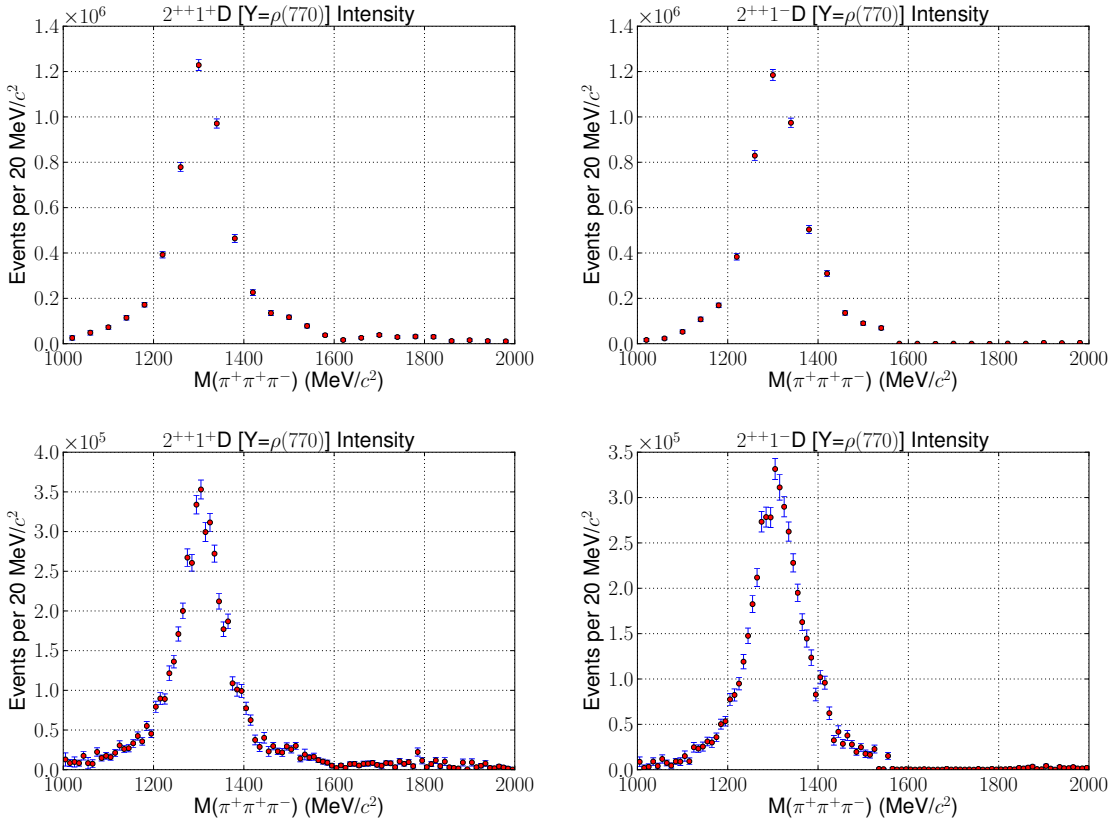

Figure C.12: The 2^{++} acceptance-corrected yields for 40 MeV bins (**top**) and 10 MeV bins(**bottom**), with the $M^{\epsilon} = 1^{+}$ on the right and 1^{-} on the left.

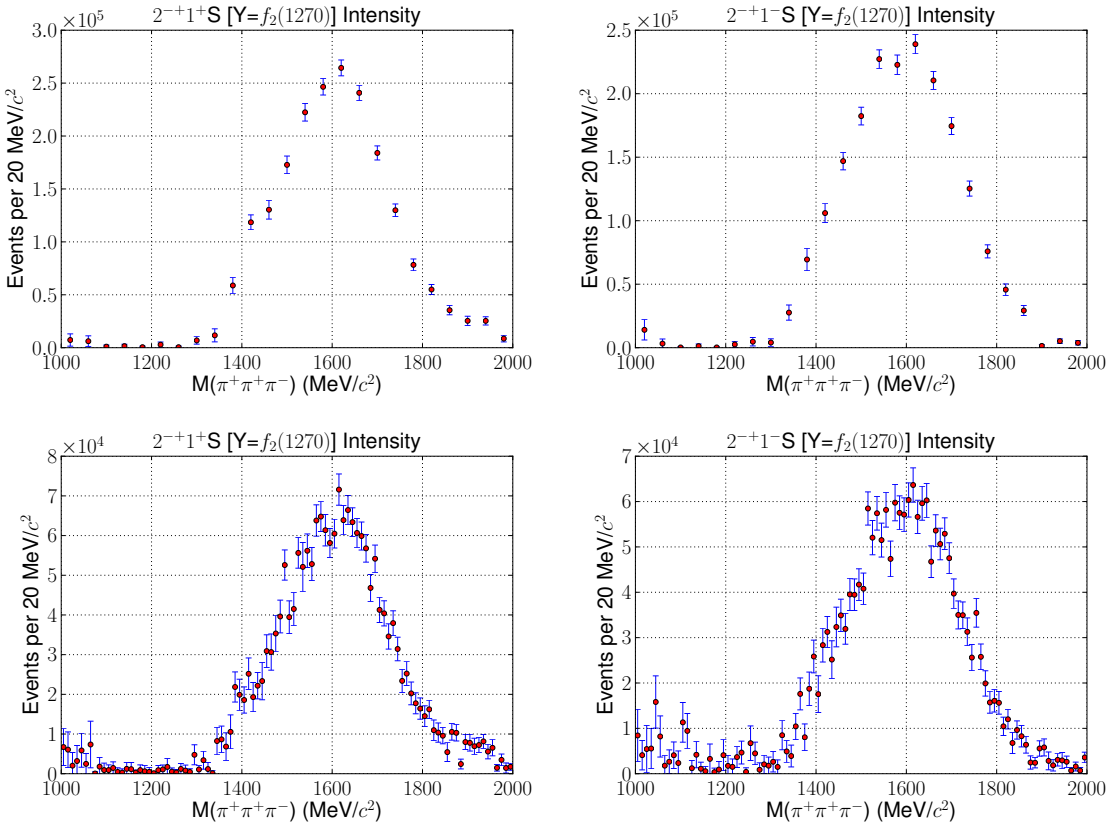

Figure C.13: The 2^{-+} acceptance-corrected yields for 40 MeV bins (**top**) and 10 MeV bins(**bottom**), with the $M^{\epsilon} = 1^{+}$ on the right and 1^{-} on the left.

C.4 Systematic Effects from Baryon Background

Here we examine the dependence of our fit results on the values of our cuts in t' and $\theta_{lab}\left[\pi_2^+\right]$.

C.4.1 Isotropic Background

We begin by examining the isotropic background wave as a function of our baryon background reduction (BBGR) cuts. We would expect the intensity of the isotropic background to increase in size as more of these events are introduced, as most are unlikely to have a strong overlap with any 3π meson resonance amplitudes. Figure C.14 shows the change in the isotropic background as the angular cuts are opened, while Figure C.15 shows the effects of opening the cut in $|t'|$. Starting with the background distribution peaked at 1.3 GeV, as discussed in C.1, one can see that as the cuts are opened, the isotropic background increases dramatically in the upper end of the 3π mass range, just as we would expect for increasing levels of t-channel baryon events.

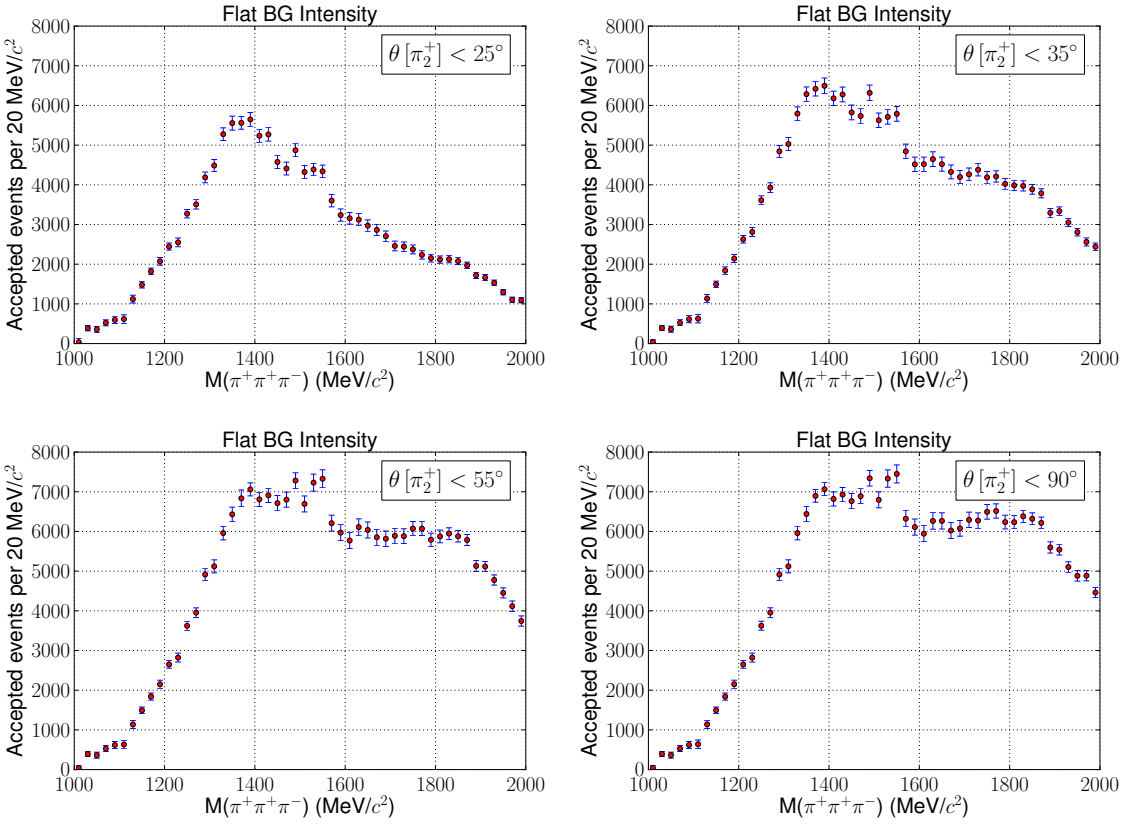

Figure C.14: Accepted intensities for the $1^{++}1^+S$ waves as a function of our cut in $\theta_{lab}\left[\pi_2^+\right]$. **Top left** has our nominal result from the minimal basis fit, and we open the cut on $\theta_{lab}\left[\pi_2^+\right]$ to 35° (**top right**), 55° (**bottom left**), and finally to 90° (**bottom right**).

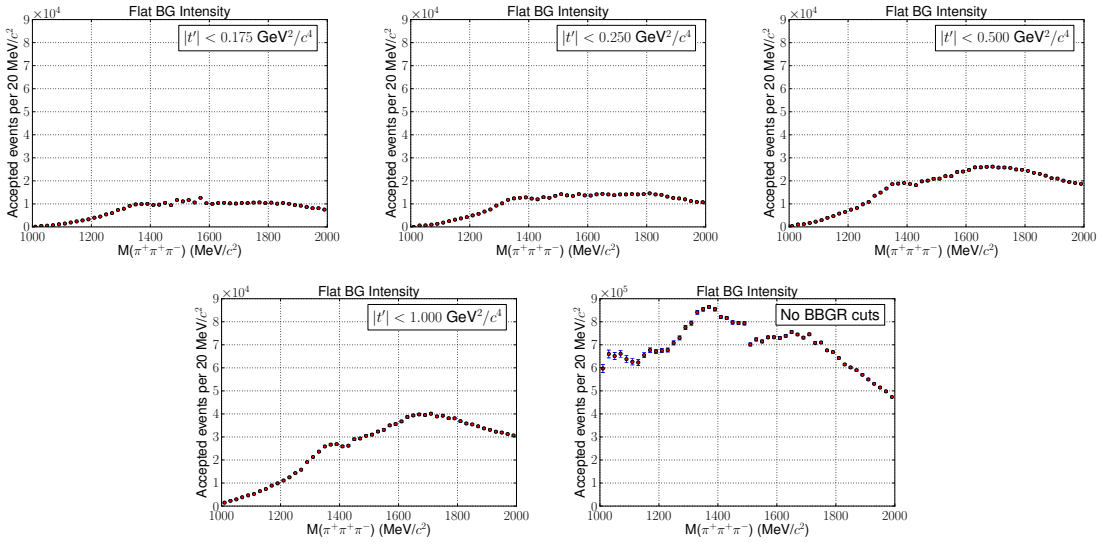

Figure C.15: Accepted intensities for the $1^{++}1^+S$ with no angle cut and opening the cut in $|t'|$, going from the nominal value of 0.1 GeV^2 to 0.175 (**top left**), 0.250 (**top center**), 0.5 (**top right**), 1.0 (**bottom left**), and finally no t' cut at all (**bottom right**).

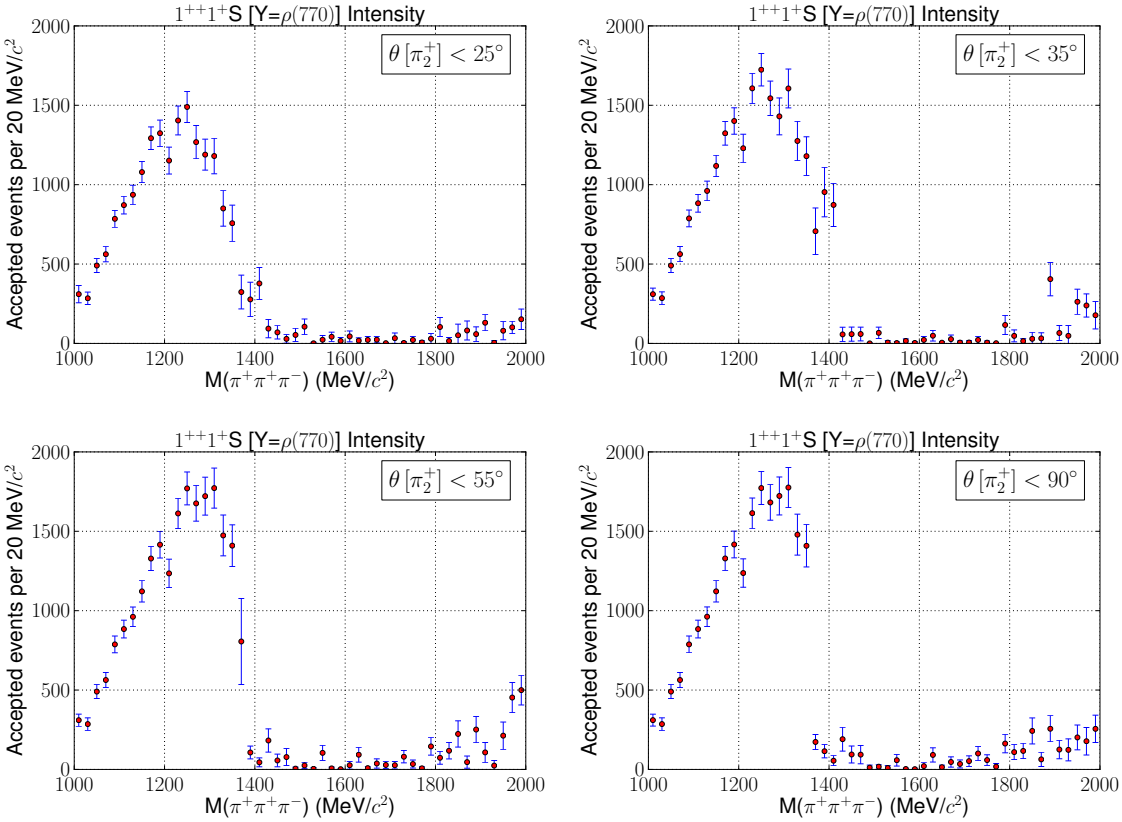

Figure C.16: Accepted intensities for the $1^{++}1^{+}S$ waves as a function of our cut in $\theta_{lab}\left[\pi_2^+\right]$. **Top left** has our nominal result from the minimal basis fit, and we open the cut on $\theta_{lab}\left[\pi_2^+\right]$ to 35° (**top right**), 55° (**bottom left**), and finally to 90° (**bottom right**).

C.4.2 $1^{++}\left[\rho(770)\pi\right]_S$

The $1^{++}\ [\rho\pi]_S$, the $M^\epsilon = 1^+$ dependence on the $\theta_{lab}\left[\pi_2^+\right]$ cut is shown in Figure C.16, and the dependence on t' in Figure C.17. The angular and t' dependence for the $M^\epsilon = 1^-$ is shown in Figures C.18 and C.19. Both reflectivities show a propensity to "lean" toward 1.3 GeV as more background is introduced. However, even a permissive cut in $|t'|$ makes a dramatic improvement on the shape of the 1^{++} intensity, as seen by the difference between the last two plots in Figure C.19.

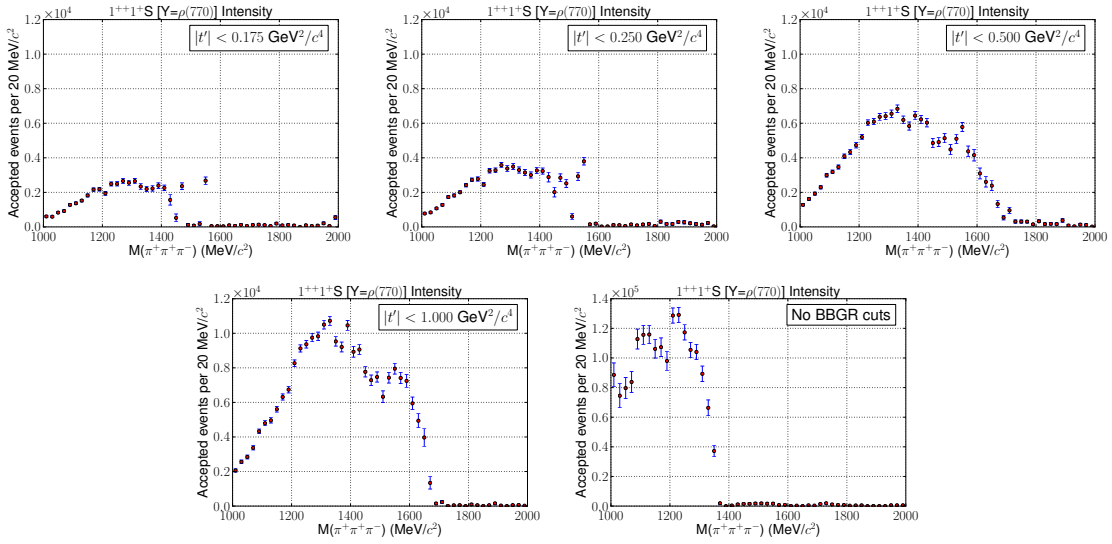

Figure C.17: Accepted intensities for the $1^{++}1^+S$ with no angle cut and opening the cut in $|t'|$, going from the nominal value of 0.1 GeV^2 to 0.175 (**top left**), 0.250 (**top center**), 0.5 (**top right**), 1.0 (**bottom left**), and finally no t' cut at all (**bottom right**).

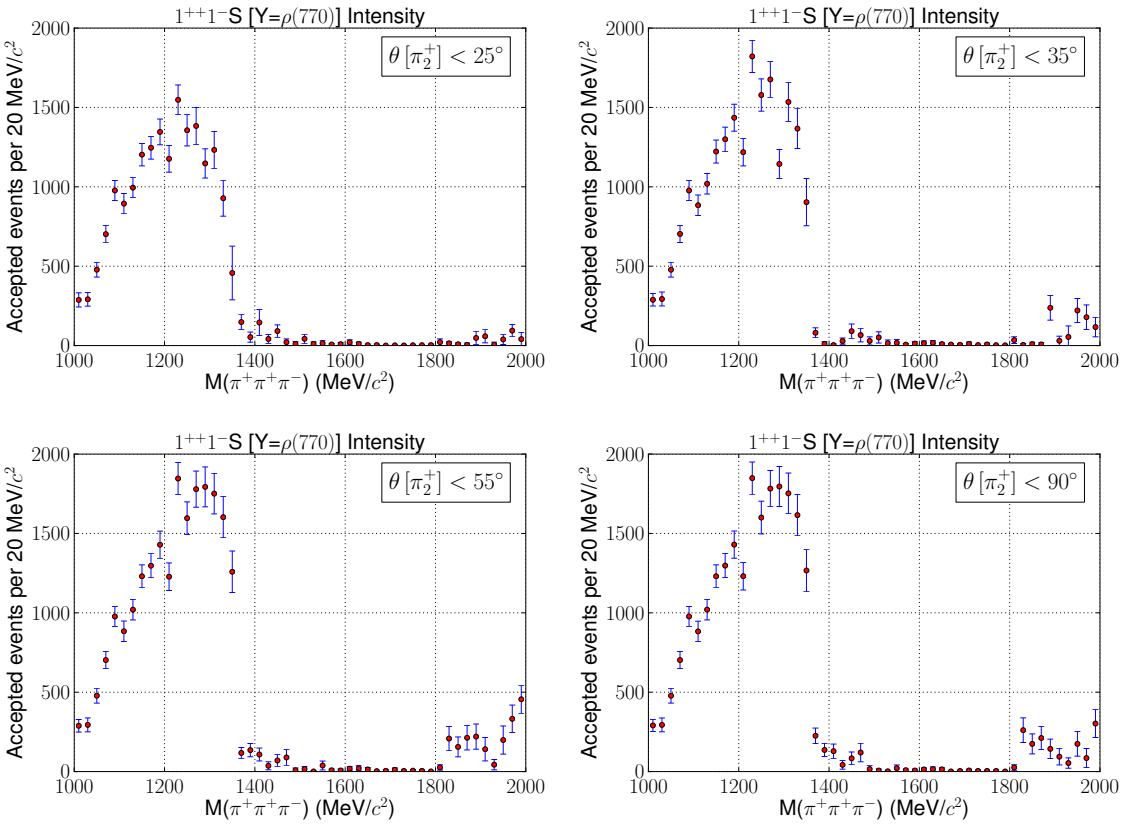

Figure C.18: Accepted intensities for the $1^{++}1^{-}S$ waves as a function of our cut in $\theta_{lab}\left[\pi_2^+\right]$. **Top left** has our nominal result from the minimal basis fit, and we open the cut on $\theta_{lab}\left[\pi_2^+\right]$ to 35° (**top right**), 55° (**bottom left**), and finally to 90° (**bottom right**).

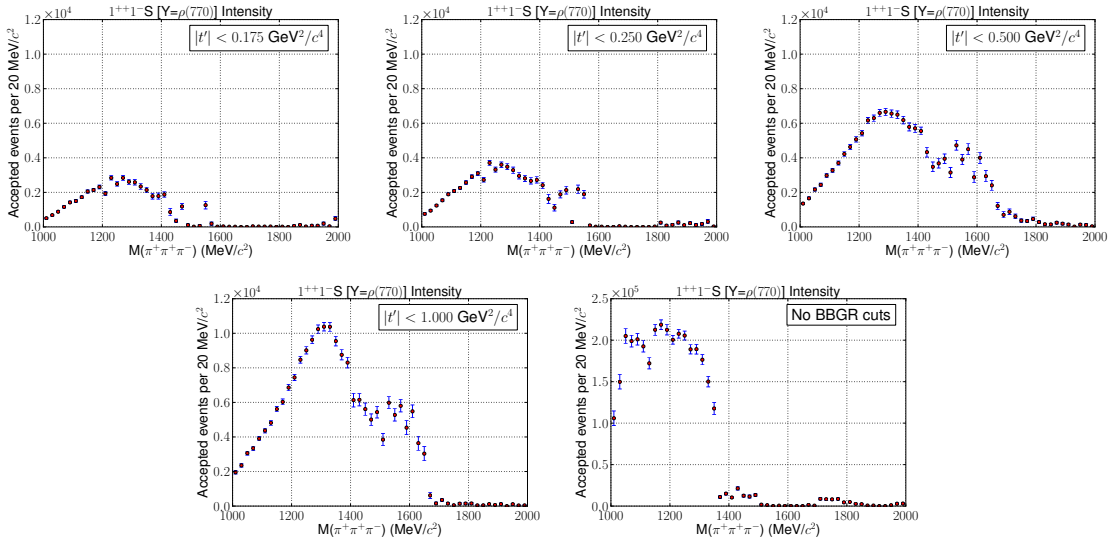

Figure C.19: Accepted intensities for the $1^{++}1^{-}S$ with no angle cut and opening the cut in $|t'|$, going from the nominal value of 0.1 GeV^2 to 0.175 (**top left**), 0.250 (**top center**), 0.5 (**top right**), 1.0 (**bottom left**), and finally no t' cut at all (**bottom right**).

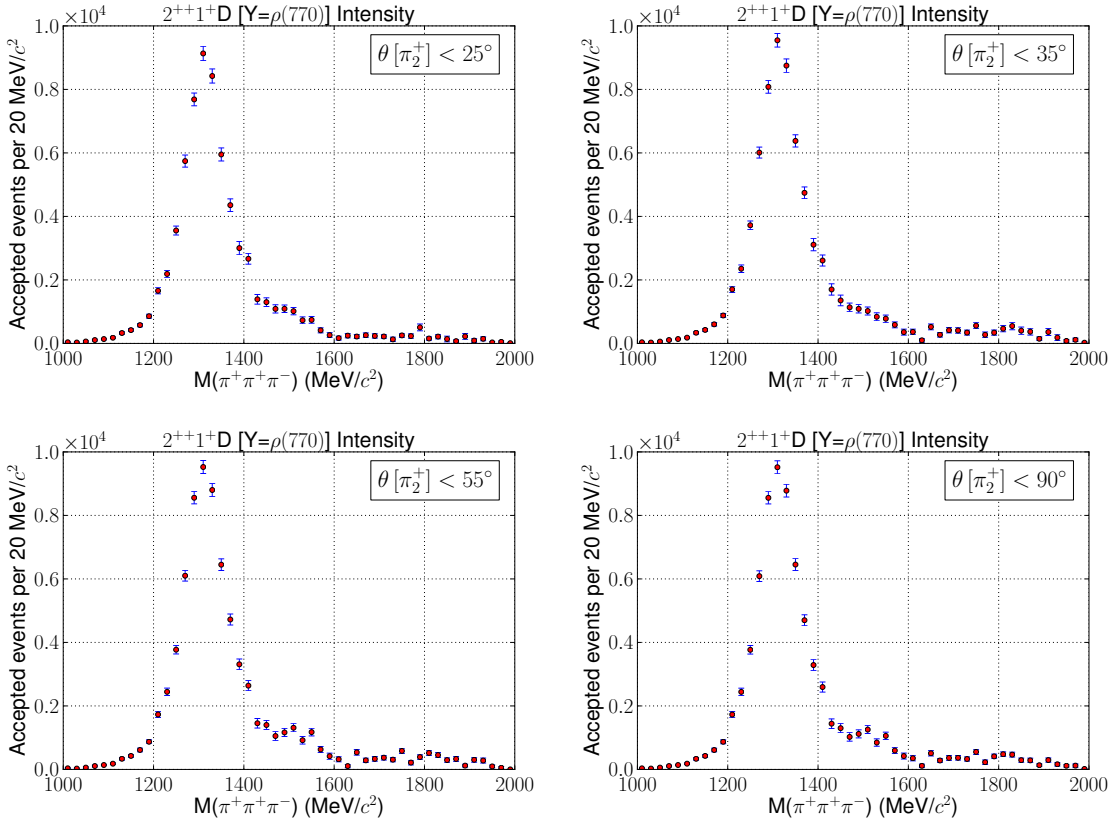

Figure C.20: Accepted intensities for the $2^{++}1^+D$ waves as a function of our cut in $\theta_{lab}\left[\pi_2^+\right]$. **Top left** has our nominal result from the minimal basis fit, and we open the cut on $\theta_{lab}\left[\pi_2^+\right]$ to 35° (**top right**), 55° (**bottom left**), and finally to 90° (**bottom right**).

C.4.3 $2^{++}\left[\rho(770)\pi\right]_D$

The $2^{++}\ \left[\rho\pi\right]_D$ dependence on our BBGR is shown in Figures C.20 and C.21 for the $M^\epsilon = 1^+$, and Figures C.22 and C.23 for the 1^-. The shape of the 2^{++} intensity is quite consistent for all cut values; only at very permissive limits in $|t'|$ do we see any distortion of the intensity. A noticeable preference for the 1^- does arise at the most permissive values of $|t'|$, consistent with our previous discussion of reflectivity asymmetry being related to the level of background in the sample.

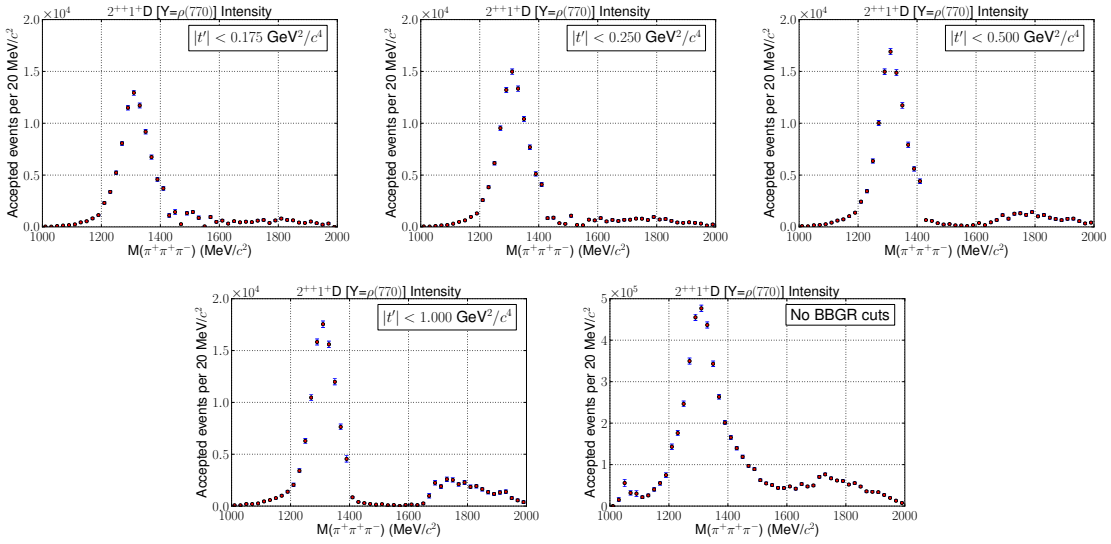

Figure C.21: Accepted intensities for the $2^{++}1^+D$ with no angle cut and opening the cut in $|t'|$, going from the nominal value of 0.1 GeV^2 to 0.175 (**top left**), 0.250 (**top center**), 0.5 (**top right**), 1.0 (**bottom left**), and finally no t' cut at all (**bottom right**).

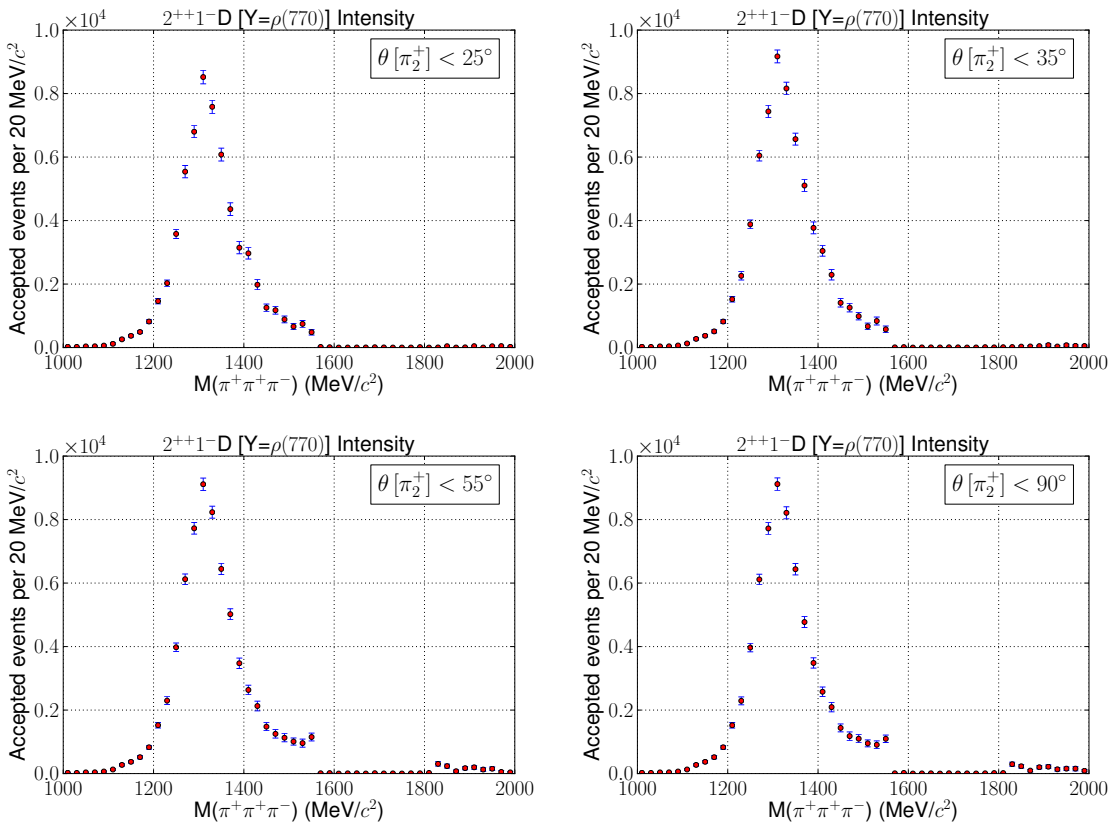

Figure C.22: Accepted intensities for the $2^{++}1^{-}D$ waves as a function of our cut in $\theta_{lab}\left[\pi_2^+\right]$. **Top left** has our nominal result from the minimal basis fit, and we open the cut on $\theta_{lab}\left[\pi_2^+\right]$ to 35° (**top right**), 55° (**bottom left**), and finally to 90° (**bottom right**).

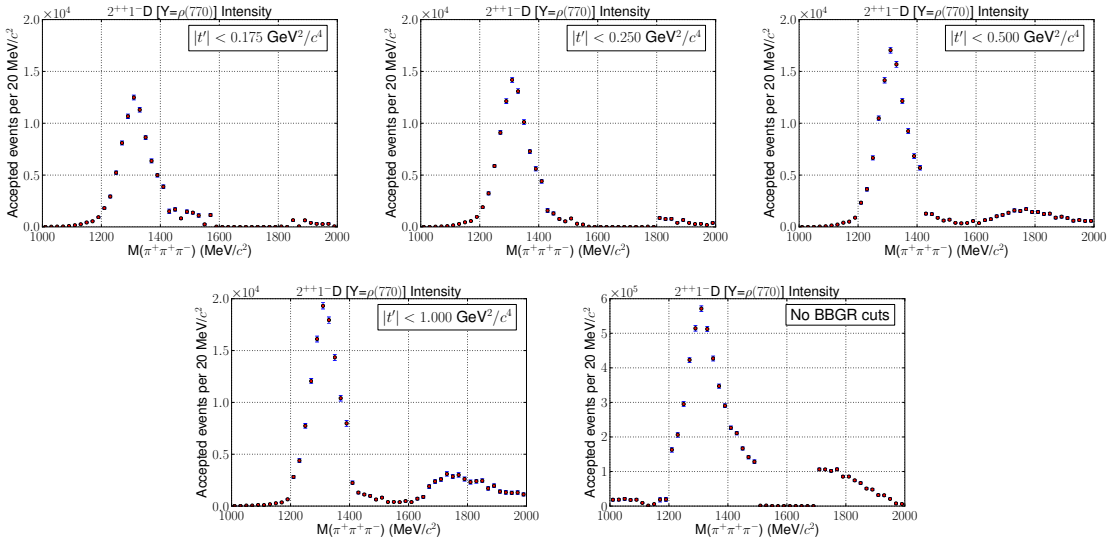

Figure C.23: Accepted intensities for the $2^{++}1^-D$ with no angle cut and opening the cut in $|t'|$, going from the nominal value of 0.1 GeV^2 to 0.175 (**top left**), 0.250 (**top center**), 0.5 (**top right**), 1.0 (**bottom left**), and finally no t' cut at all (**bottom right**).

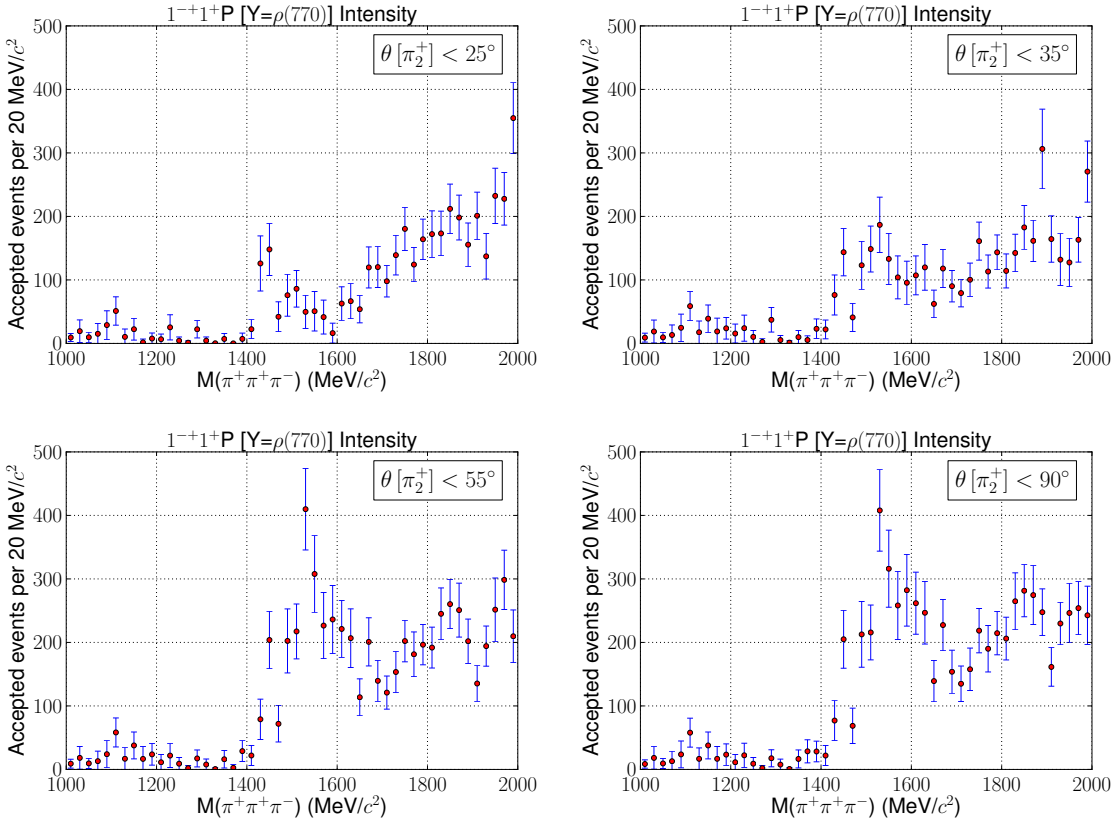

Figure C.24: Accepted intensities for the $1^{-+}1^+P$ waves as a function of our cut in $\theta_{lab}\left[\pi_2^+\right]$. **Top left** has our nominal result from the minimal basis fit, and we open the cut on $\theta_{lab}\left[\pi_2^+\right]$ to 35° (**top right**), 55° (**bottom left**), and finally to 90° (**bottom right**).

C.4.4 $1^{-+}\left[\rho(770)\pi\right]_P$

The systematic dependencies of the accepted intensity spectra of the exotic waves are shown in Figures C.24 and C.25 for the $M^\epsilon = 1^+$, C.26 and C.27 for the 1^-, and C.28 and C.29 for the 0^-. The $M^\epsilon = 1^\pm$ intensities show a peak as the cuts in angle are opened, first in the 1^+, and later followed by the 1^-. The peak is centered at about 1.5 to 1.55 GeV, appears during the opening of the angle cuts, before disappearing during the opening of the cuts in $|t'|$, and making a final appearance in the distribution with no BBGR cuts whatsoever (the last plot in Figures C.25 and C.27). The prominence of the peak in the uncut distribution, along with its inconsistent appearance among intensities with different values of cuts, makes it unlikely to be due to meson resonance production.

The $M^\epsilon = 0^-$ distribution shows very little change until the cuts in $|t'|$ are opened, and only then showing peaks at low mass, most likely to do leakage from the a_2, and a high-mass rise, most likely due to background pollution.

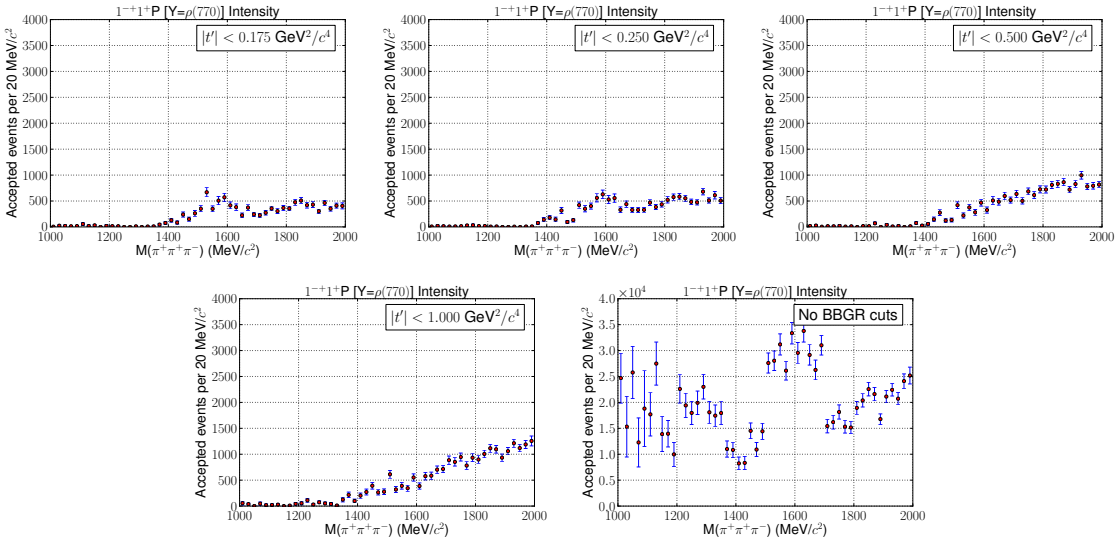

Figure C.25: Accepted intensities for the $1^{-+}1^{+}P$ with no angle cut and opening the cut in $|t'|$, going from the nominal value of 0.1 GeV^2 to 0.175 (**top left**), 0.250 (**top center**), 0.5 (**top right**), 1.0 (**bottom left**), and finally no t' cut at all (**bottom right**).

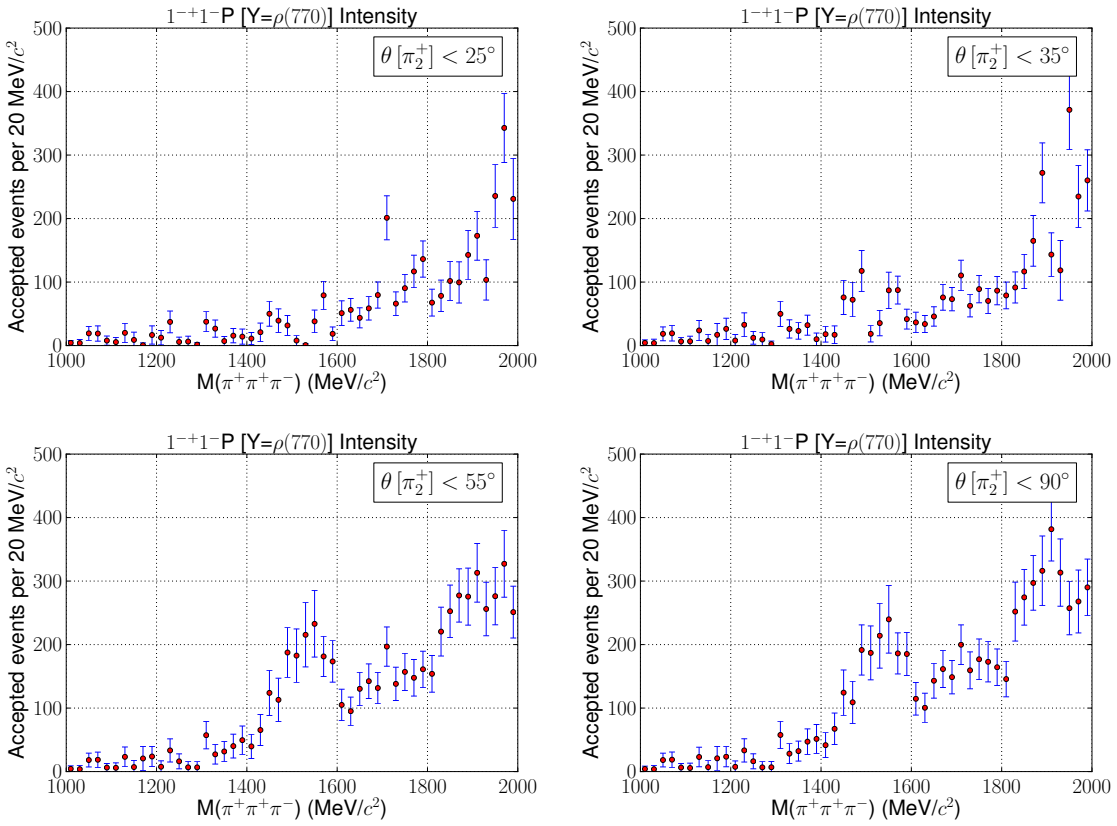

Figure C.26: Accepted intensities for the $1^{-+}1^{-}P$ waves as a function of our cut in $\theta_{lab}\left[\pi_2^+\right]$. **Top left** has our nominal result from the minimal basis fit, and we open the cut on $\theta_{lab}\left[\pi_2^+\right]$ to 35° (**top right**), 55° (**bottom left**), and finally to 90° (**bottom right**).

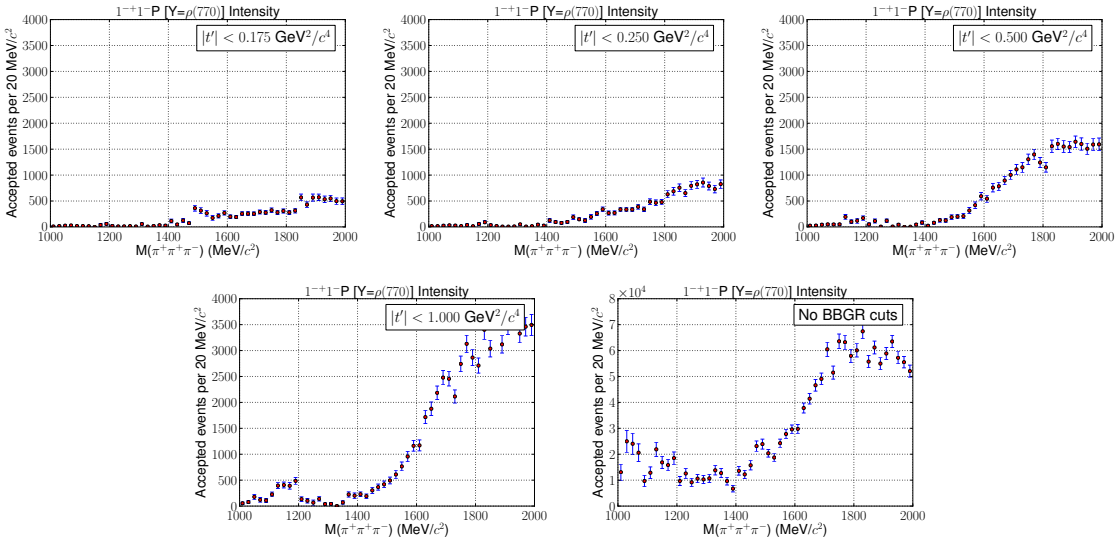

Figure C.27: Accepted intensities for the $1^{-+}1^{-}P$ with no angle cut and opening the cut in $|t'|$, going from the nominal value of 0.1 GeV^2 to 0.175 (**top left**), 0.250 (**top center**), 0.5 (**top right**), 1.0 (**bottom left**), and finally no t' cut at all (**bottom right**).

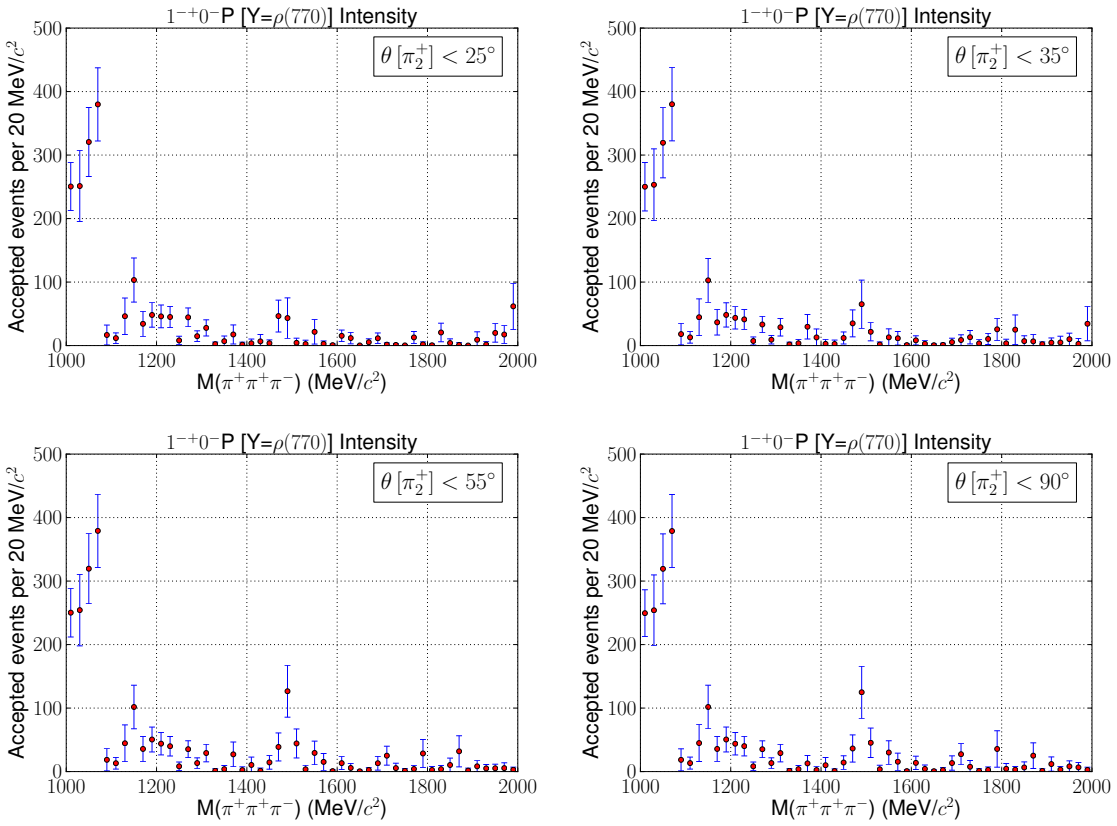

Figure C.28: Accepted intensities for the $1^{-+}0^{-}P$ waves as a function of our cut in $\theta_{lab}\left[\pi_2^+\right]$. **Top left** has our nominal result from the minimal basis fit, and we open the cut on $\theta_{lab}\left[\pi_2^+\right]$ to 35° (**top right**), 55° (**bottom left**), and finally to 90° (**bottom right**).

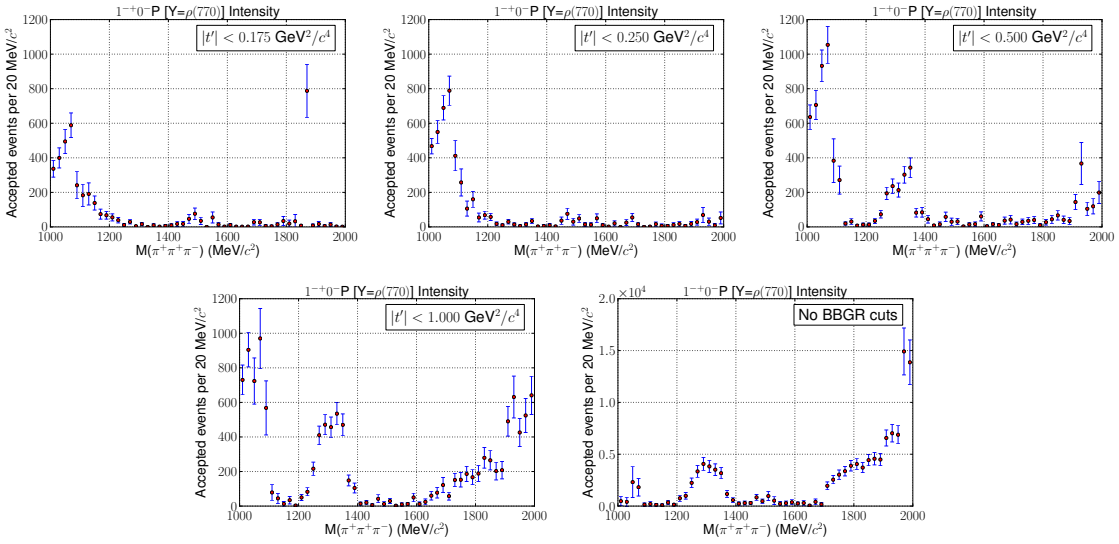

Figure C.29: Accepted intensities for the $1^{-+}0^{-}P$ with no angle cut and opening the cut in $|t'|$, going from the nominal value of 0.1 GeV^2 to 0.175 (**top left**), 0.250 (**top center**), 0.5 (**top right**), 1.0 (**bottom left**), and finally no t' cut at all (**bottom right**).

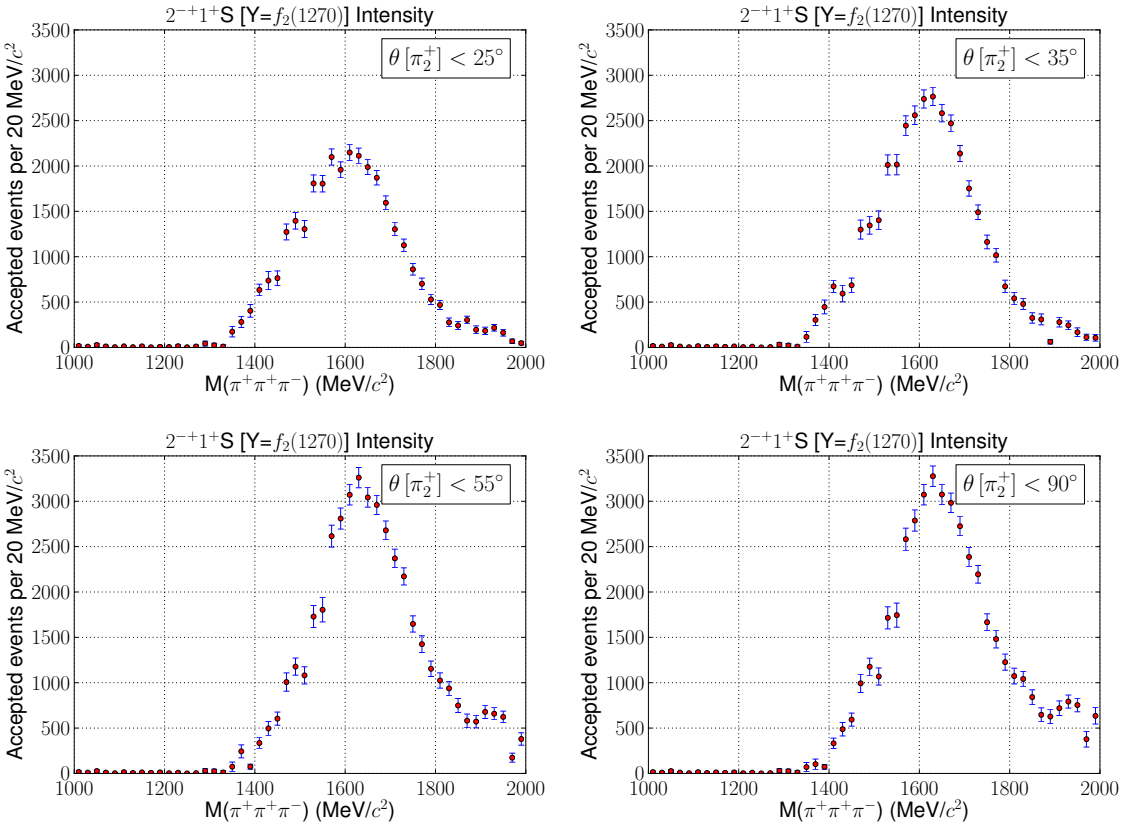

Figure C.30: Accepted intensities for the $2^{-+}1^+S$ waves as a function of our cut in $\theta_{lab}\left[\pi_2^+\right]$. **Top left** has our nominal result from the minimal basis fit, and we open the cut on $\theta_{lab}\left[\pi_2^+\right]$ to 35° (**top right**), 55° (**bottom left**), and finally to 90° (**bottom right**).

C.4.5 $2^{-+}\left[f_2(1270)\pi\right]_S$

The dependence of the 2^{-+} S-wave decays on the choice of BBGR cuts is shown in Figures C.30 and C.31 for the $M^\epsilon = 1^+$, Figures C.32 and C.35 for the 1^-, and C.30 and C.35 for the 0^-. Similar to the 2^{++}, the $2^{-+}S$ $M^\epsilon = 1^\pm$ shows good consistency across all values of BBGR cuts. The only change in shape is the rise of a flat shoulder on the high-mass side of the peak as the cuts are loosened.

The $M^\epsilon = 0^-$ shows dramatic change in scale as the cuts are opened, first peaking at $|t'| < 0.250$ GeV^2 before decreasing and then acquiring a peak in the same region as that in the 1^{-+} spectrum. This illustrates that the $M = 0$ projections in the high part of the 3π mass range are particularly susceptible to the introduction of baryon background into the sample.

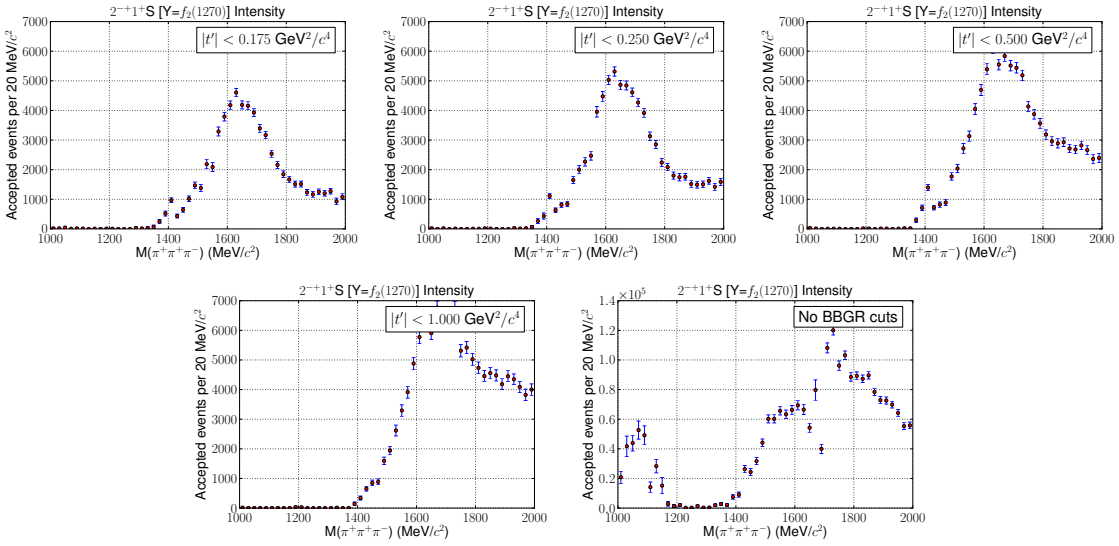

Figure C.31: Accepted intensities for the $2^{-+}1^{+}S$ with no angle cut and opening the cut in $|t'|$, going from the nominal value of 0.1 GeV^2 to 0.175 (**top left**), 0.250 (**top center**), 0.5 (**top right**), 1.0 (**bottom left**), and finally no t' cut at all (**bottom right**).

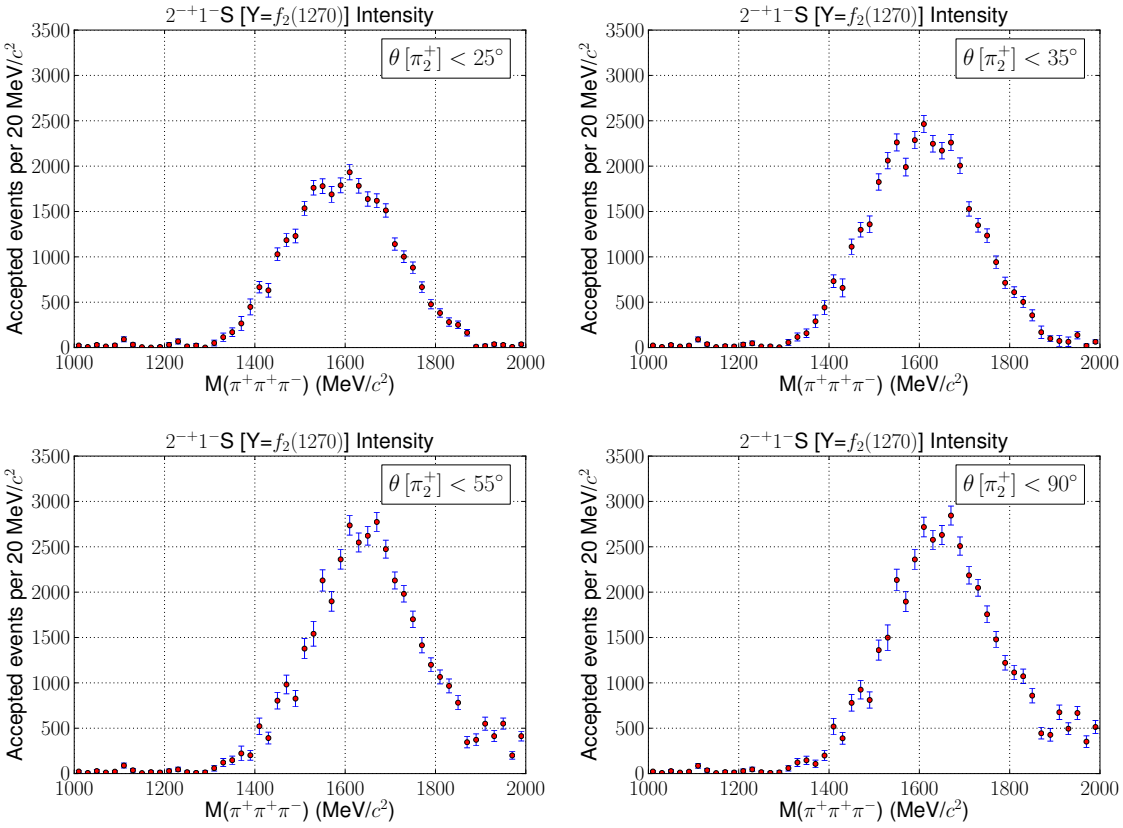

Figure C.32: Accepted intensities for the $2^{-+}1^{-}S$ waves as a function of our cut in $\theta_{lab}\left[\pi_2^+\right]$. **Top left** has our nominal result from the minimal basis fit, and we open the cut on $\theta_{lab}\left[\pi_2^+\right]$ to 35° (**top right**), 55° (**bottom left**), and finally to 90° (**bottom right**).

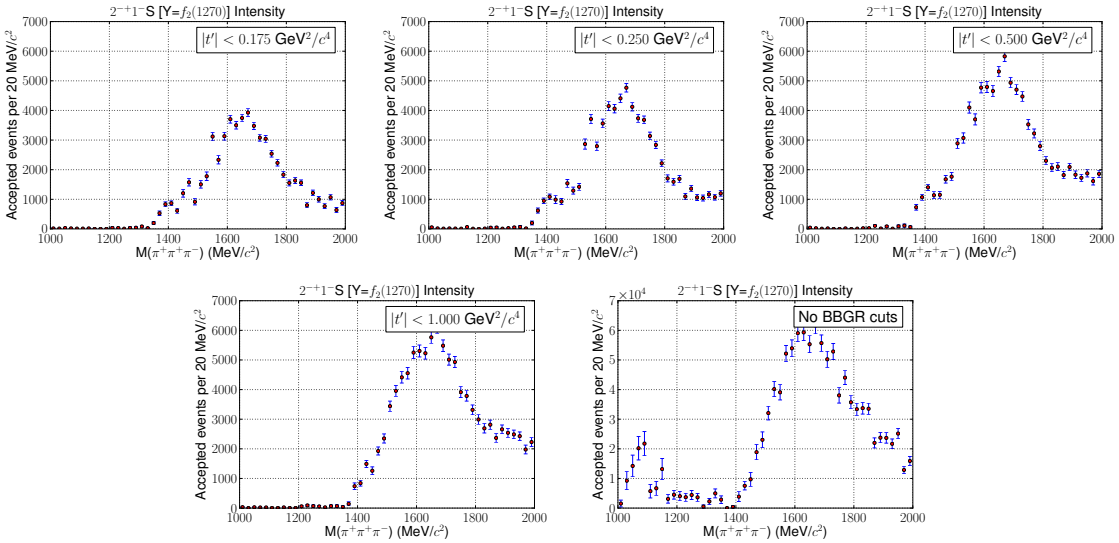

Figure C.33: Accepted intensities for the $2^{-+}1^-S$ with no angle cut and opening the cut in $|t'|$, going from the nominal value of 0.1 GeV^2 to 0.175 (**top left**), 0.250 (**top center**), 0.5 (**top right**), 1.0 (**bottom left**), and finally no t' cut at all (**bottom right**).

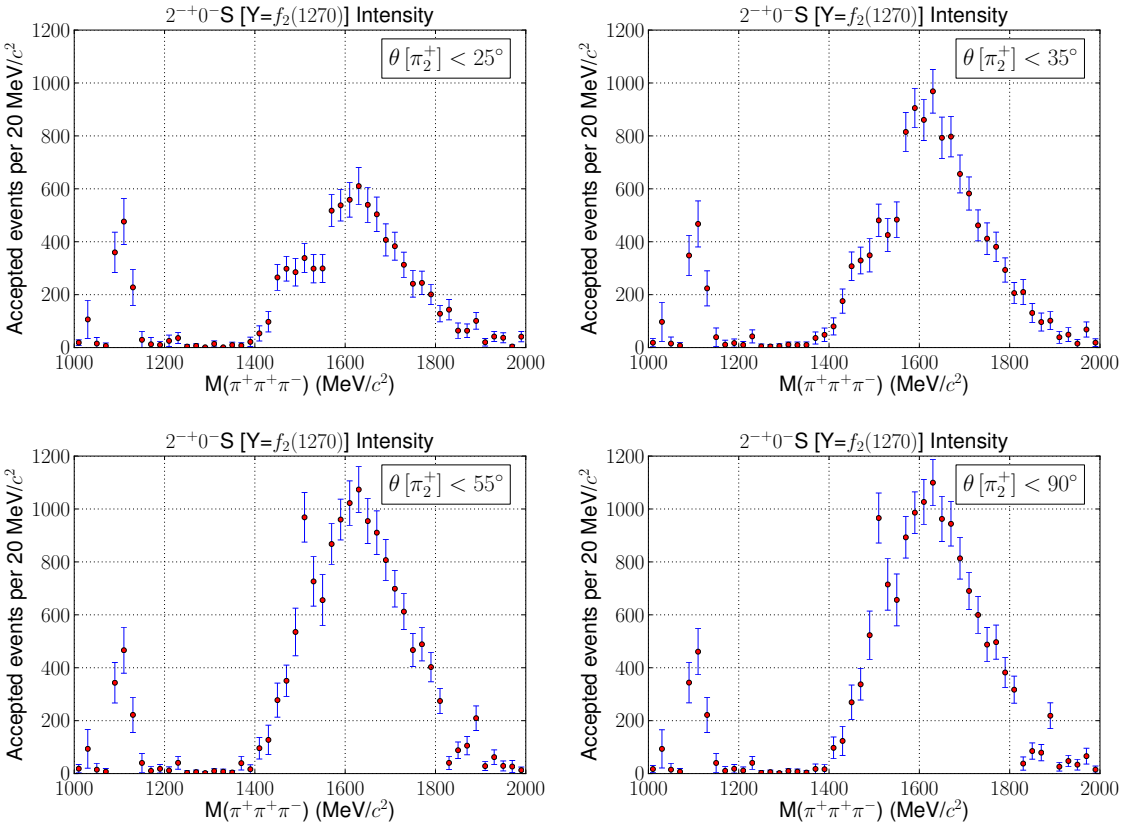

Figure C.34: Accepted intensities for the $2^{-+}0^{-}S$ waves as a function of our cut in $\theta_{lab}\left[\pi_2^+\right]$. **Top left** has our nominal result from the minimal basis fit, and we open the cut on $\theta_{lab}\left[\pi_2^+\right]$ to 35° (**top right**), 55° (**bottom left**), and finally to 90° (**bottom right**).

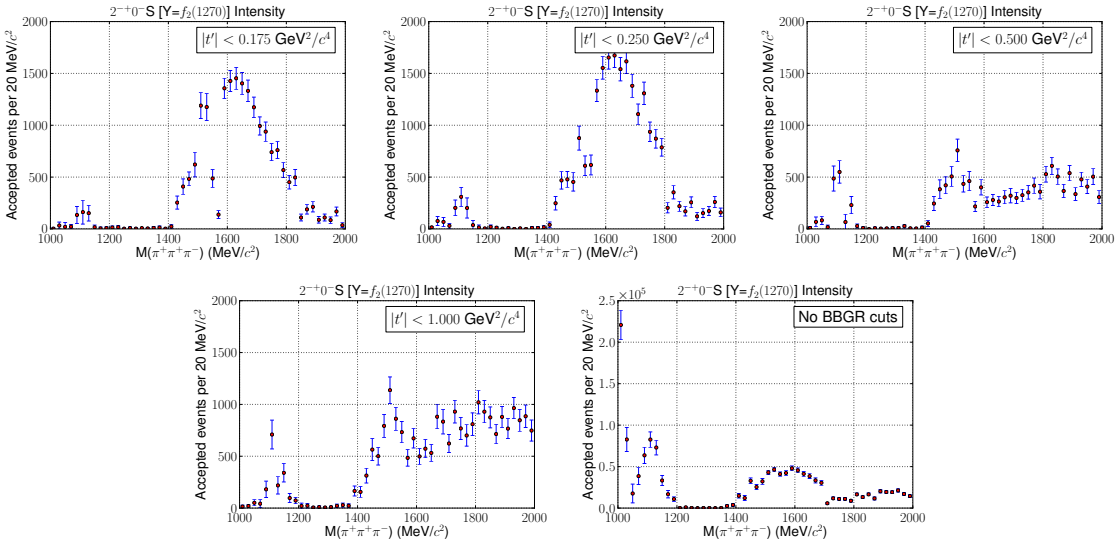

Figure C.35: Accepted intensities for the $2^{-+}0^{-}S$ with no angle cut and opening the cut in $|t'|$, going from the nominal value of 0.1 GeV^2 to 0.175 (**top left**), 0.250 (**top center**), 0.5 (**top right**), 1.0 (**bottom left**), and finally no t' cut at all (**bottom right**).

C.4.6 $2^{-+}\left[\rho(770)\pi\right]_P$

In Section 5.3.5, we saw that the $2^{-+}\left[\rho(770)\pi\right]_P$ exhibits some unexpected artifacts in its intensity at low mass. Figures C.36 and C.37, C.38 and C.39, and C.40 and C.41 illustrate the BBGR dependence of the $M^\epsilon = 1^+$, 1^-, and 0^-, respectively.

The $M^\epsilon = 1^\pm$ intensities show a clear difference in scale, with the 1^+ being favored over the 1^-. The angle cuts have a dramatic effect; whereas, with the low angle cut, some semblance of a resonant peak is visible at high mass where we expect to see the $\pi_2(1670) \to \rho\pi$ decay manifest itself, this feature quickly evaporates as the angle cut is opened up. Once it is removed, we see the $2^{-+}1^\pm P$ intensity spectra morph into something resembling a step function across 1.5 GeV, before becoming extremely complex with all cuts removed.

The 0^- wave shows a remarkably strong and well-shaped peak throughout the distributions up until the cut in $|t'|$ is opened up beyond 0.5 GeV^2. After that point, the distribution then acquires a very complex lineshape before settling into a shape similar to that of the $1^{-+}1^\pm$ spectra.

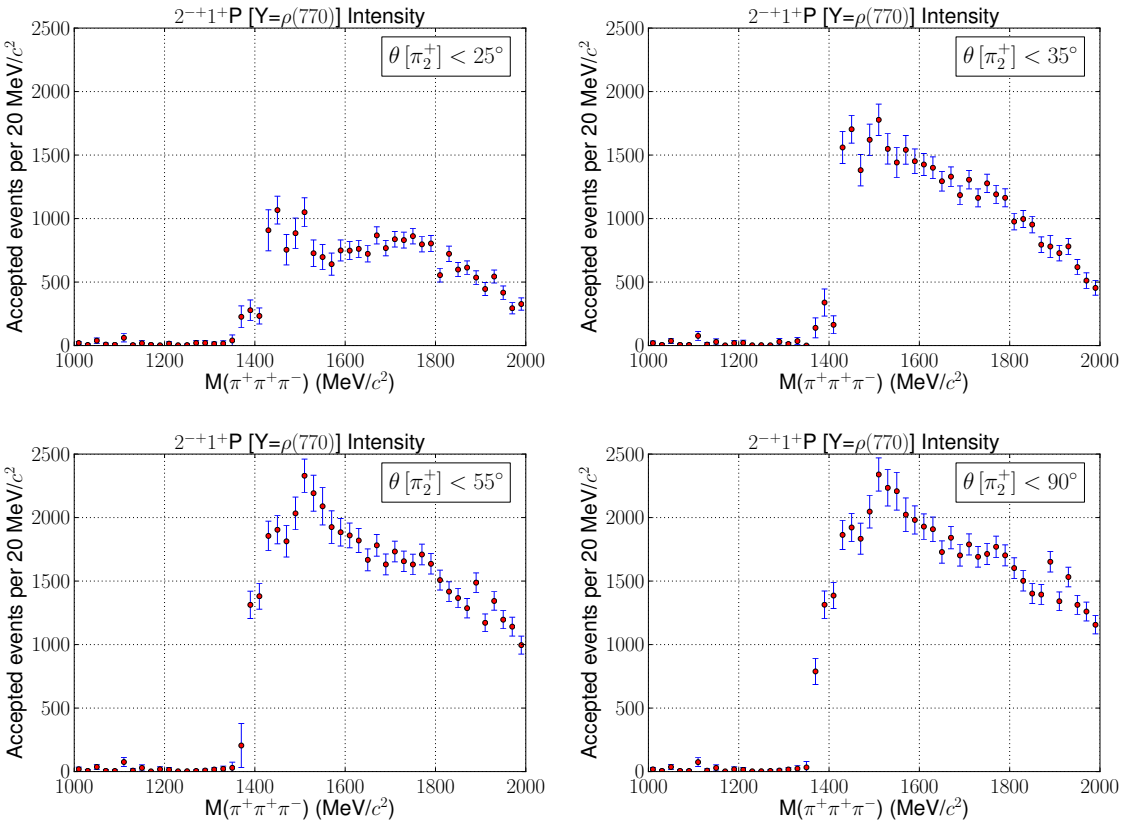

Figure C.36: Accepted intensities for the $2^{-+}1^{+}P$ waves as a function of our cut in $\theta_{lab}\left[\pi_2^+\right]$. **Top left** has our nominal result from the minimal basis fit, and we open the cut on $\theta_{lab}\left[\pi_2^+\right]$ to 35° (**top right**), 55° (**bottom left**), and finally to 90° (**bottom right**).

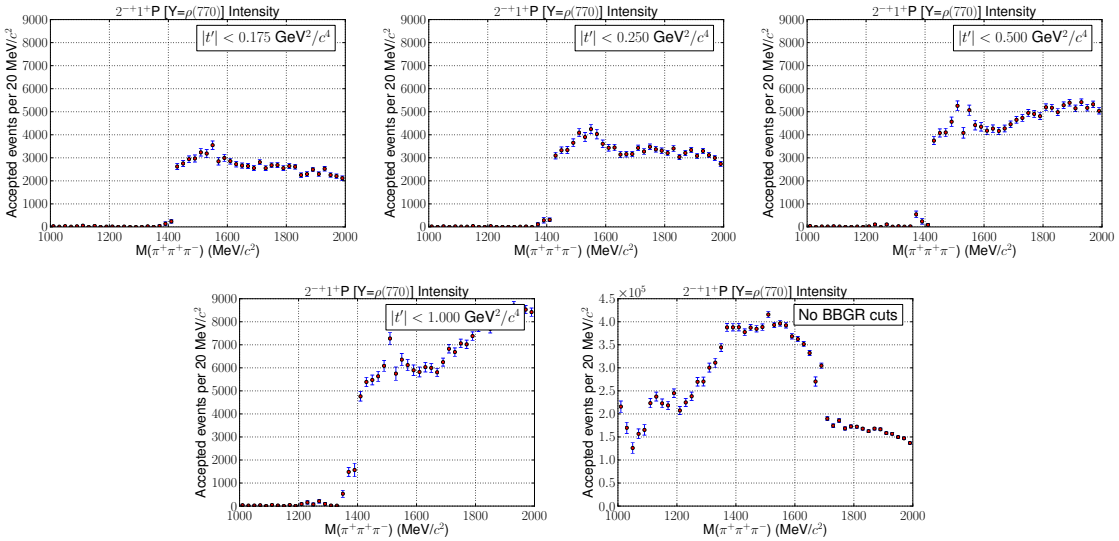

Figure C.37: Accepted intensities for the $2^{-+}1^+P$ with no angle cut and opening the cut in $|t'|$, going from the nominal value of 0.1 GeV^2 to 0.175 (**top left**), 0.250 (**top center**), 0.5 (**top right**), 1.0 (**bottom left**), and finally no t' cut at all (**bottom right**).

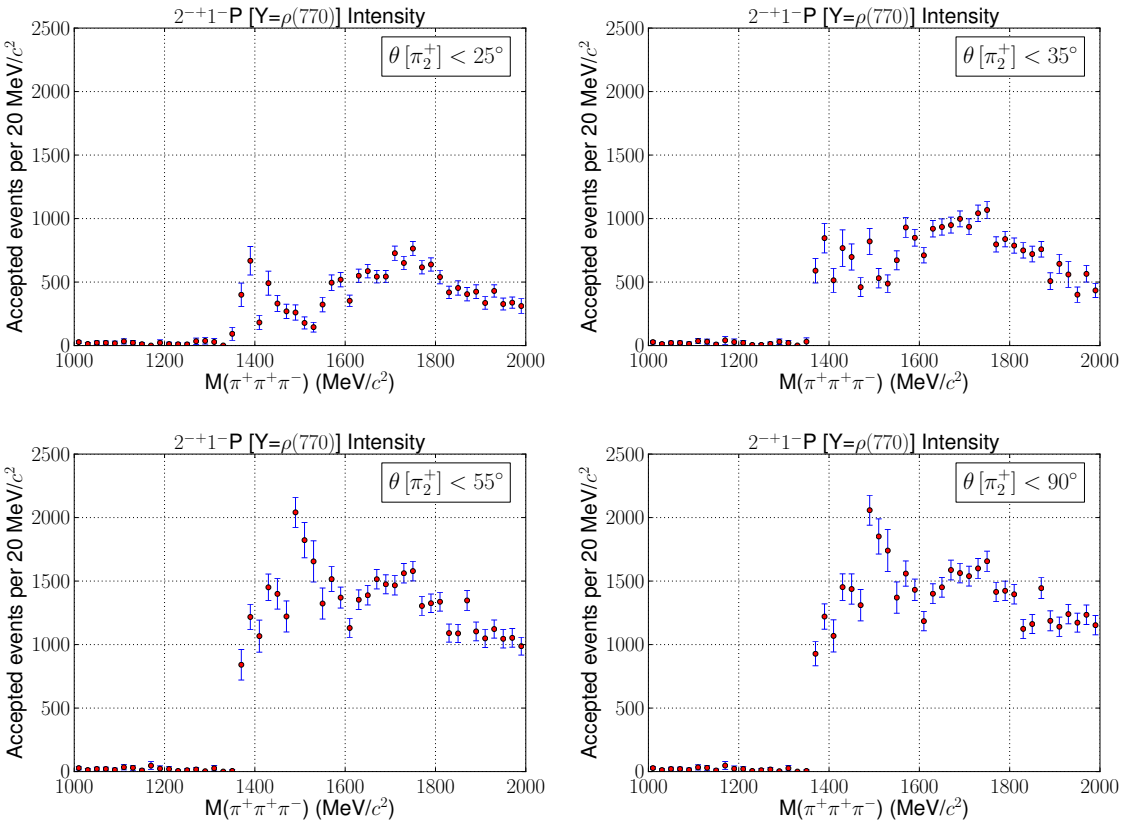

Figure C.38: Accepted intensities for the $2^{-+}1^{-}P$ waves as a function of our cut in $\theta_{lab}\left[\pi_2^+\right]$. **Top left** has our nominal result from the minimal basis fit, and we open the cut on $\theta_{lab}\left[\pi_2^+\right]$ to 35° (**top right**), 55° (**bottom left**), and finally to 90° (**bottom right**).

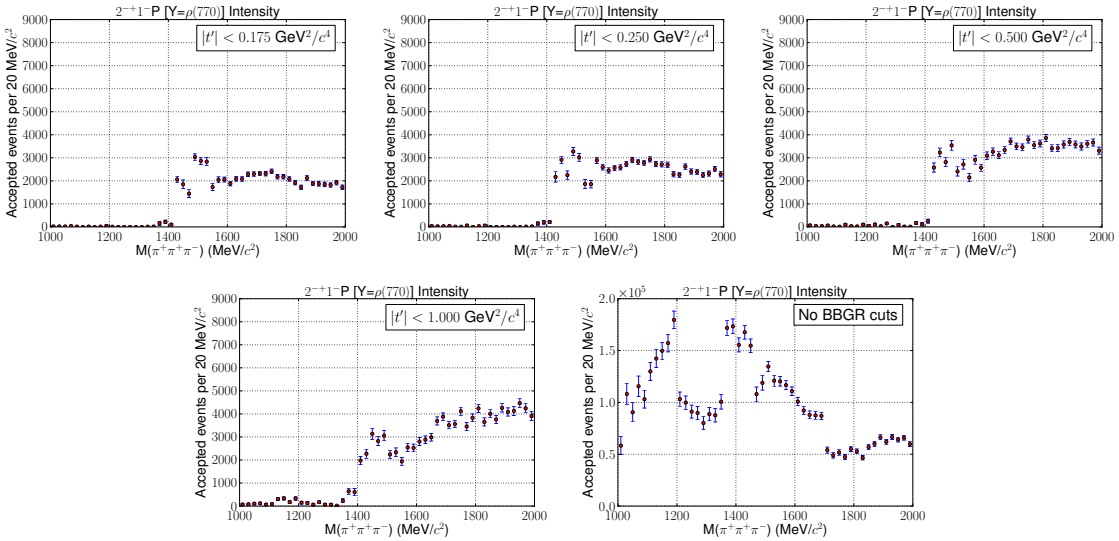

Figure C.39: Accepted intensities for the $2^{-+}1^{-}P$ with no angle cut and opening the cut in $|t'|$, going from the nominal value of 0.1 GeV^2 to 0.175 (**top left**), 0.250 (**top center**), 0.5 (**top right**), 1.0 (**bottom left**), and finally no t' cut at all (**bottom right**).

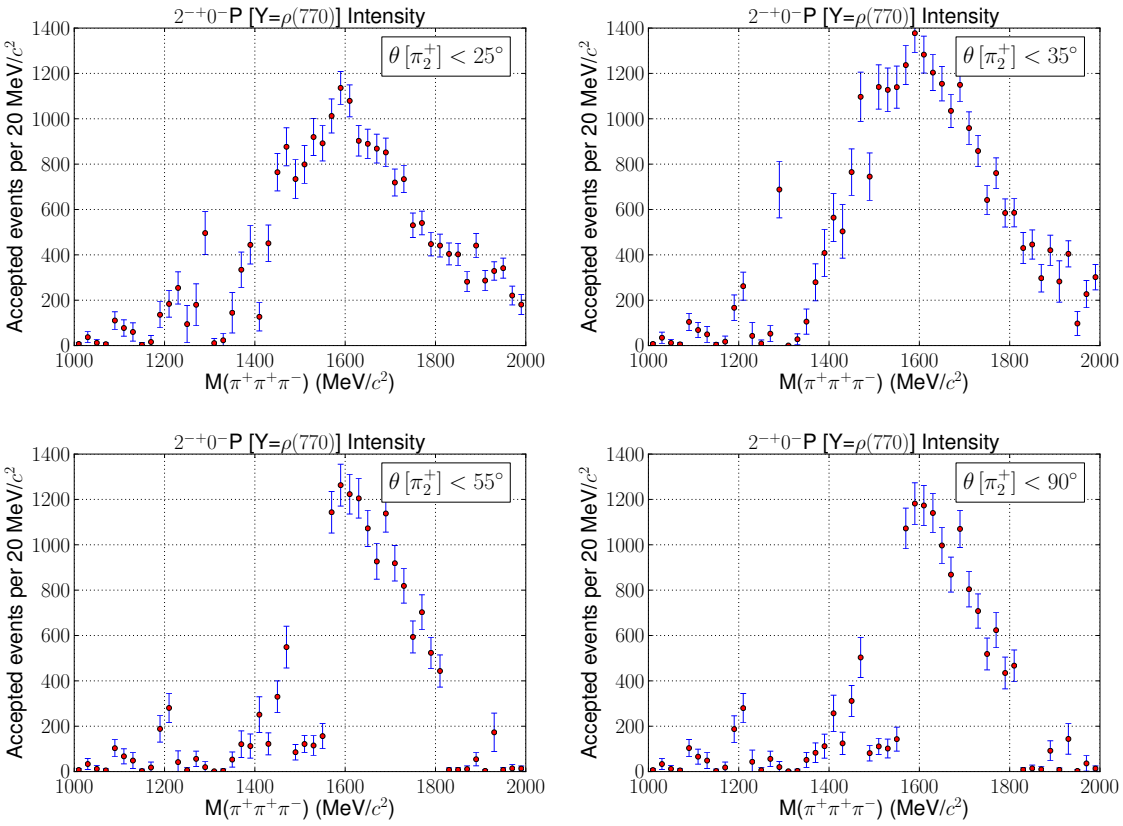

Figure C.40: Accepted intensities for the $2^{-+}0^{-}P$ waves as a function of our cut in $\theta_{lab}\left[\pi_2^+\right]$. **Top left** has our nominal result from the minimal basis fit, and we open the cut on $\theta_{lab}\left[\pi_2^+\right]$ to 35° (**top right**), 55° (**bottom left**), and finally to 90° (**bottom right**).

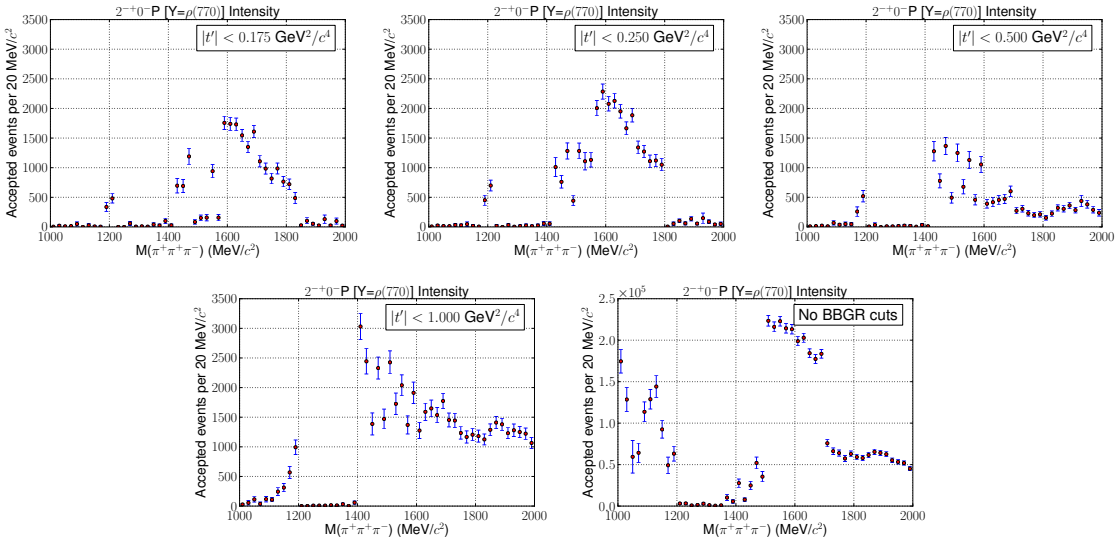

Figure C.41: Accepted intensities for the $2^{-+}0^{-}P$ with no angle cut and opening the cut in $|t'|$, going from the nominal value of 0.1 GeV^2 to 0.175 (**top left**), 0.250 (**top center**), 0.5 (**top right**), 1.0 (**bottom left**), and finally no t' cut at all (**bottom right**).

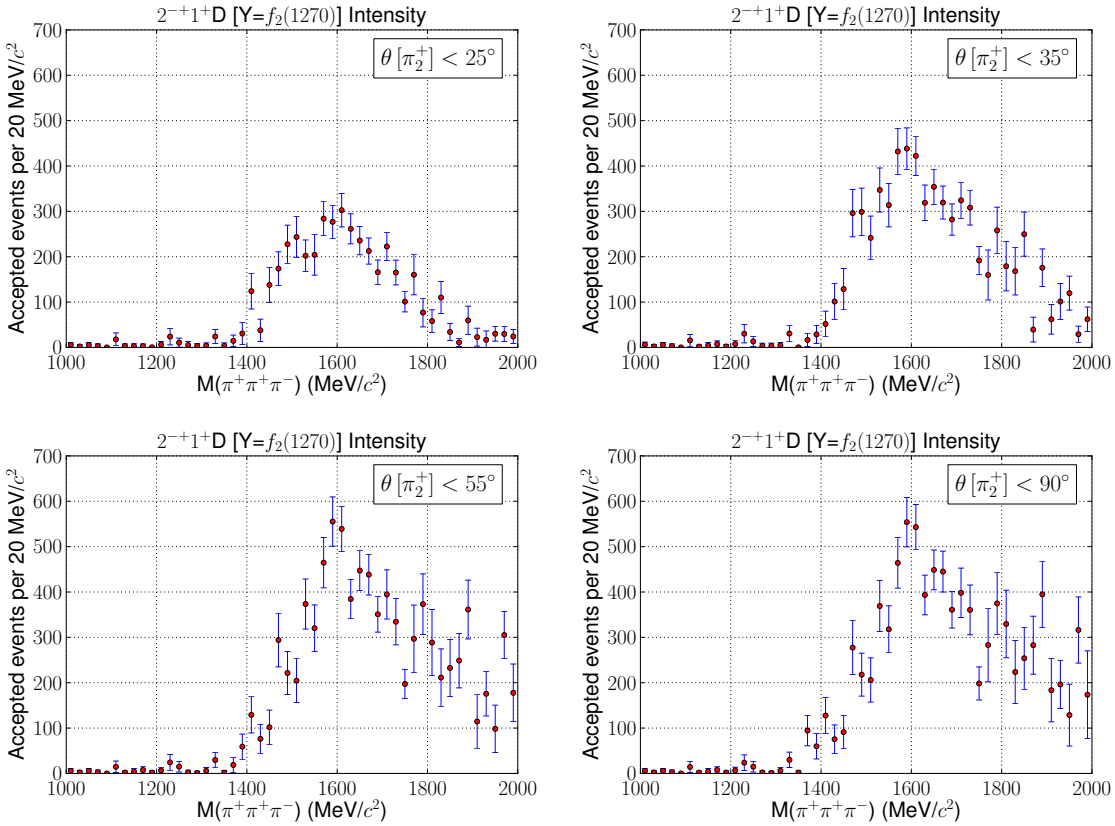

Figure C.42: Accepted intensities for the $2^{-+}1^{+}D$ waves as a function of our cut in $\theta_{lab}\left[\pi_2^+\right]$. **Top left** has our nominal result from the minimal basis fit, and we open the cut on $\theta_{lab}\left[\pi_2^+\right]$ to 35° (**top right**), 55° (**bottom left**), and finally to 90° (**bottom right**).

C.4.7 $2^{-+}\left[\rho(1270)\pi\right]_D$

The systematic dependencies of the $2^{-+}\left[\rho(1270)\pi\right]_D$ intensity spectra are shown in Figures C.42 and C.43, C.44 and C.45, and C.46 and C.47 for the $M^\epsilon = 1^+$, 1^-, and 0^-, respectively. All three waves tend to hang on to their defining features as the cuts are opened: the $M^\epsilon = 1^\pm$ waves to their peaks just above 1.6 GeV, and the 0^- its discontinuous distribution across 1.6 GeV. However as the cut in $|t'|$ opens past 0.25 GeV^2, the peak in the distribution shifts from 1.6 GeV to 1.8 GeV in all 3 spectra. Removing the cut in $|t'|$ destroys any features identifiable with meson resonance production.

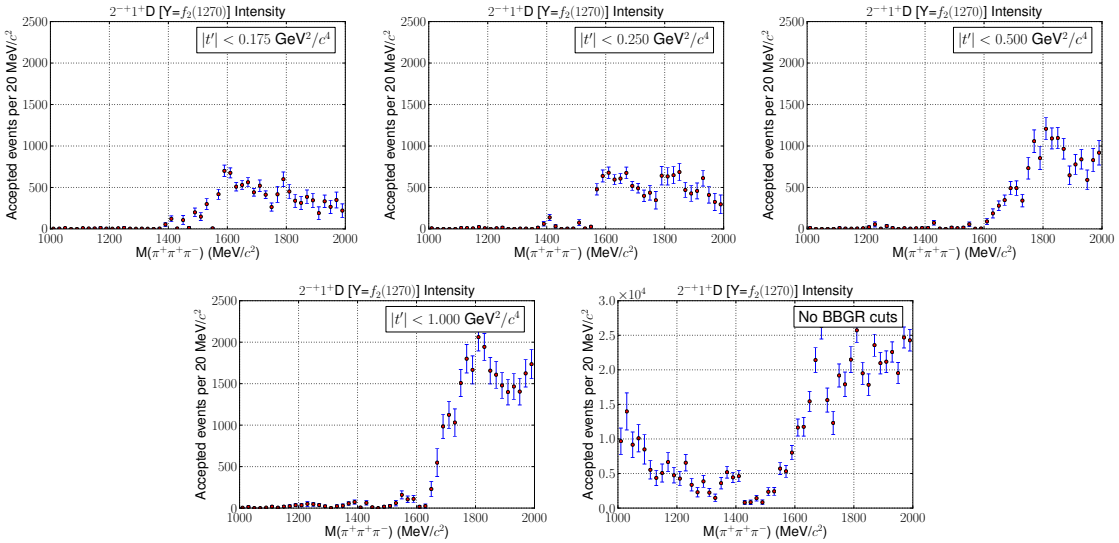

Figure C.43: Accepted intensities for the $2^{-+}1^{+}D$ with no angle cut and opening the cut in $|t'|$, going from the nominal value of 0.1 GeV^2 to 0.175 (**top left**), 0.250 (**top center**), 0.5 (**top right**), 1.0 (**bottom left**), and finally no t' cut at all (**bottom right**).

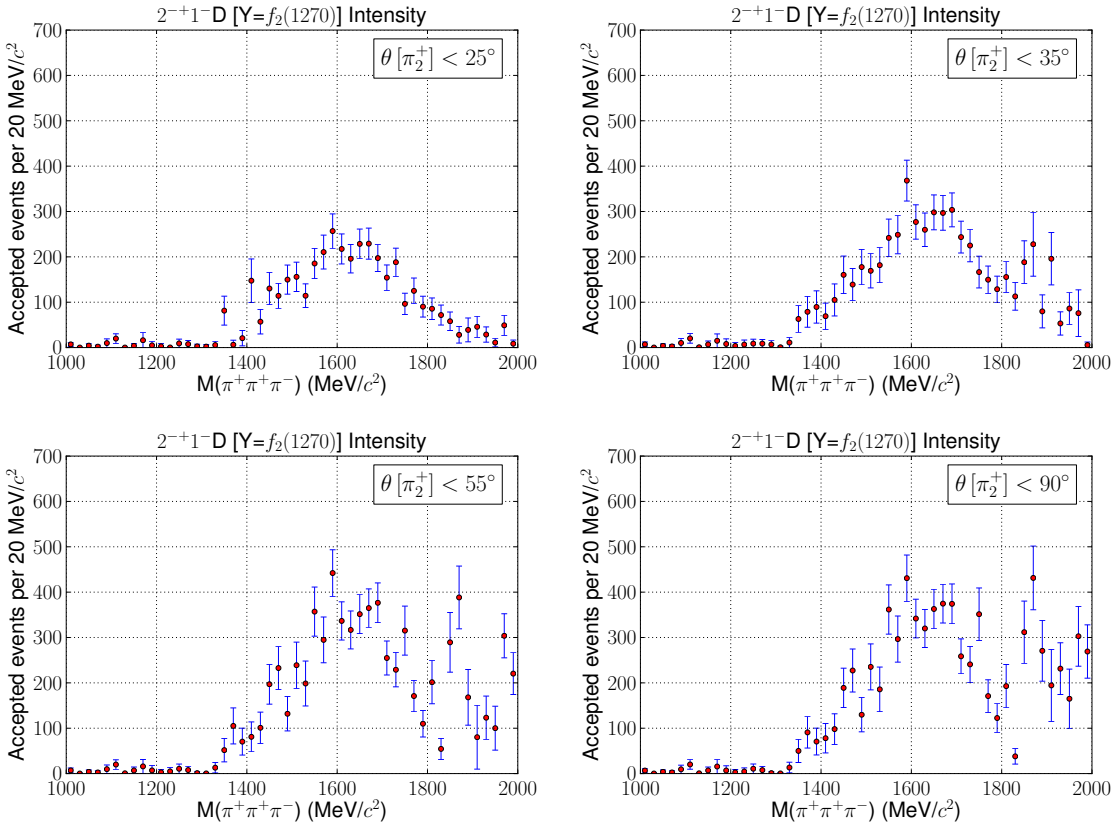

Figure C.44: Accepted intensities for the $2^{-+}1^{-}D$ waves as a function of our cut in $\theta_{lab}\left[\pi_2^+\right]$. **Top left** has our nominal result from the minimal basis fit, and we open the cut on $\theta_{lab}\left[\pi_2^+\right]$ to 35° (**top right**), 55° (**bottom left**), and finally to 90° (**bottom right**).

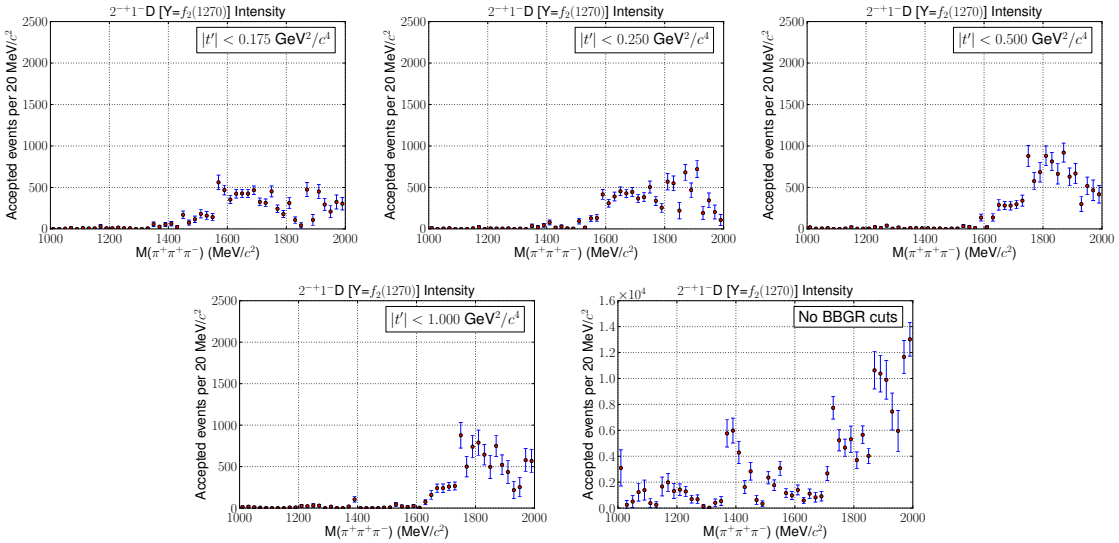

Figure C.45: Accepted intensities for the $2^{-+}1^-D$ with no angle cut and opening the cut in $|t'|$, going from the nominal value of 0.1 GeV^2 to 0.175 (**top left**), 0.250 (**top center**), 0.5 (**top right**), 1.0 (**bottom left**), and finally no t' cut at all (**bottom right**).

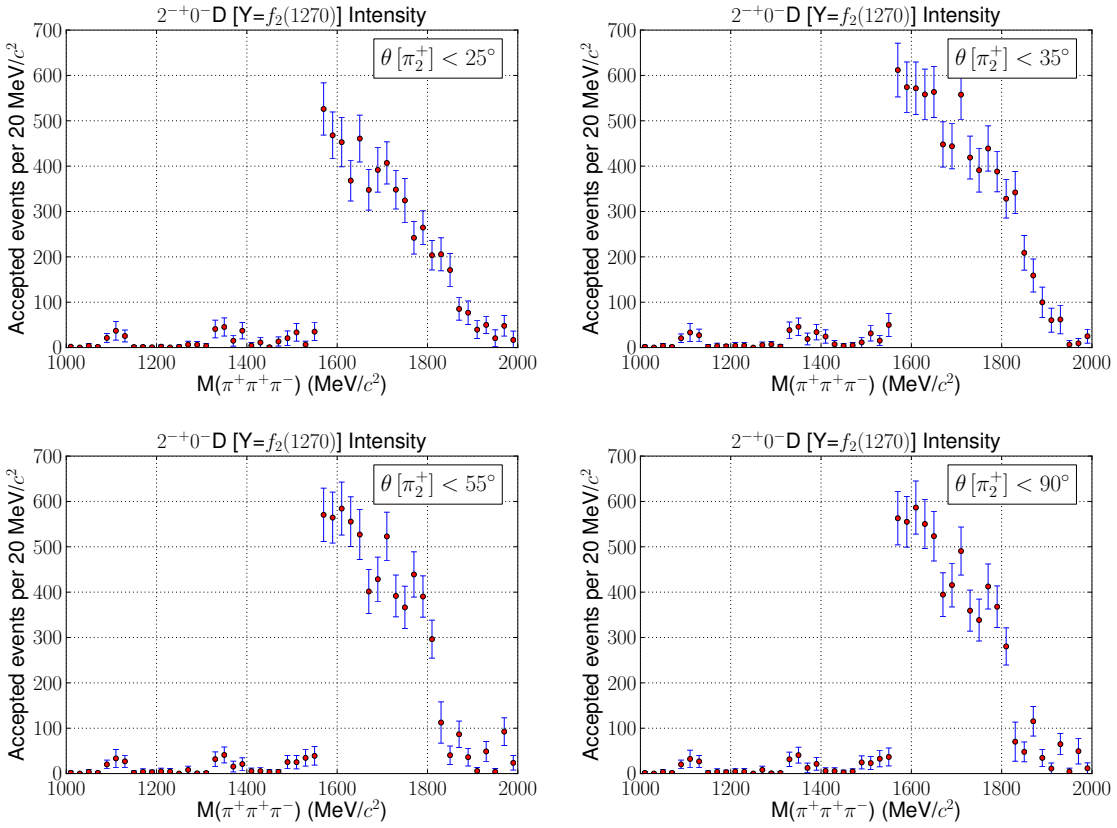

Figure C.46: Accepted intensities for the $2^{-+}0^{-}D$ waves as a function of our cut in $\theta_{lab}\left[\pi_2^+\right]$. **Top left** has our nominal result from the minimal basis fit, and we open the cut on $\theta_{lab}\left[\pi_2^+\right]$ to 35° (**top right**), 55° (**bottom left**), and finally to 90° (**bottom right**).

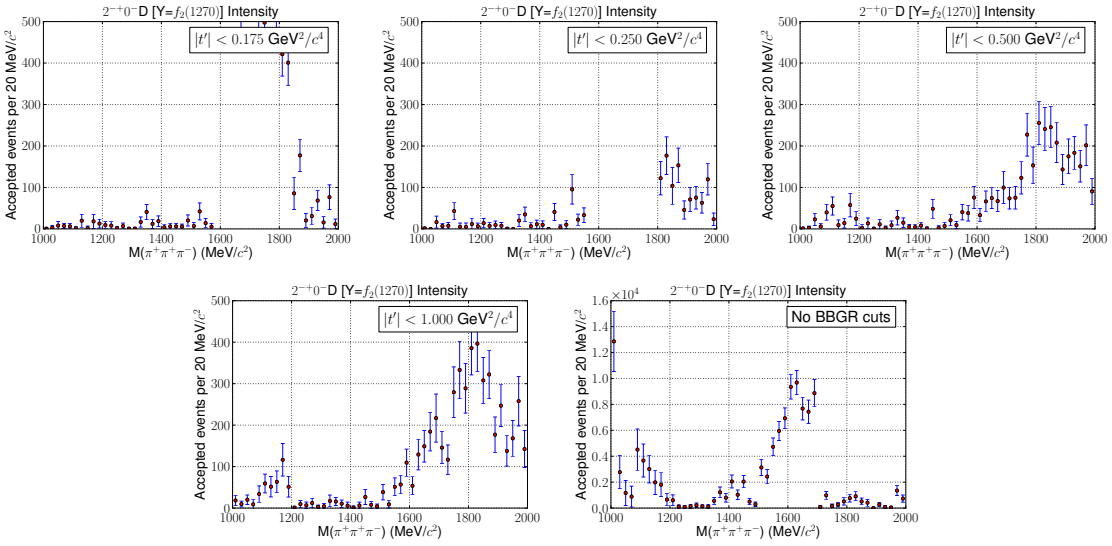

Figure C.47: Accepted intensities for the $2^{-+}0^{-}D$ with no angle cut and opening the cut in $|t'|$, going from the nominal value of 0.1 GeV^2 to 0.175 (**top left**), 0.250 (**top center**), 0.5 (**top right**), 1.0 (**bottom left**), and finally no t' cut at all (**bottom right**).

REFERENCES

[1] E. Rutherford. The scattering of α and β particles by matter and the structure of the atom. *Phil. Mag.*, 21:669–688, 1911.

[2] J. Chadwick. POSSIBLE EXISTENCE OF A NEUTRON. *Nature*, 129:312, 1932.

[3] Hideki Yukawa. On the interaction of elementary particles. *Proc. Phys. Math. Soc. Jap.*, 17:48–57, 1935.

[4] Carl D. Anderson and Seth H. Neddermeyer. Cloud Chamber Observations of Cosmic Rays at 4300 Meters Elevation and Near Sea-Level. *Phys. Rev.*, 50:263–271, 1936.

[5] C. M. G. Lattes, G. P. S. Occhialini, and C. F. Powell. OBSERVATIONS ON THE TRACKS OF SLOW MESONS IN PHOTOGRAPHIC EMULSIONS. 1. *Nature*, 160:453–456, 1947.

[6] C. M. G. Lattes, G. P. S. Occhialini, and C. F. Powell. OBSERVATIONS ON THE TRACKS OF SLOW MESONS IN PHOTOGRAPHIC EMULSIONS. 2. *Nature*, 160:486–492, 1947.

[7] G. D. Rochester and C. C. Butler. EVIDENCE FOR THE EXISTENCE OF NEW UNSTABLE ELEMENTARY PARTICLES. *Nature*, 160:855–857, 1947.

[8] Murray Gell-Mann. Symmetries of baryons and mesons. *Phys. Rev.*, 125:1067–1084, 1962.

[9] Murray Gell-Mann. A Schematic Model of Baryons and Mesons. *Phys. Lett.*, 8:214–215, 1964.

[10] V. E. Barnes et al. Observation of a Hyperon with Strangeness -3. *Phys. Rev. Lett.*, 12:204–206, 1964.

[11] E2m. The spin-0 nonet of mesons. `http://commons.wikimedia.org/wiki/File:Noneto_mes%C3%B4nico_de_spin_0.png`.

[12] E2m. The spin-1 nonet of mesons. `http://commons.wikimedia.org/wiki/File:Noneto_mes%C3%B4nico_de_spin_1.png`.

[13] M. Y. Han and Yoichiro Nambu. Three-triplet model with double SU(3) symmetry. *Phys. Rev.*, 139:B1006–B1010, 1965.

[14] O. W. Greenberg and A. M. L. Messiah. Selection rules for parafields and the absence of para particles in nature. *Phys. Rev.*, 138:B1155–B1167, 1965.

[15] W. Heisenberg. On the structure of atomic nuclei. *Z. Phys.*, 77:1–11, 1932.

[16] T. D. Lee and Chen-Ning Yang. CHARGE CONJUGATION, A NEW QUANTUM NUMBER G, AND SELECTION RULES CONCERNING A NUCLEON ANTINUCLEON SYSTEM. *Nuovo Cim.*, 10:749–753, 1956.

[17] W.-M. Yao, C. Amsler, D. Asner, R.M. Barnett, J. Beringer, P.R. Burchat, C.D. Carone, C. Caso, O. Dahl, G. D'Ambrosio, A. DeGouvea, M. Doser, S. Eidelman, J.L. Feng, T. Gherghetta, M. Goodman, C. Grab, D.E. Groom, A. Gurtu, K. Hagiwara, K.G. Hayes, J.J. Hernández-Rey, K. Hikasa, H. Jawahery, C. Kolda, Kwon Y., M.L. Mangano, A.V. Manohar, A. Masoni, R. Miquel, K. Mönig, H. Murayama, K. Nakamura, S. Navas, K.A. Olive, L. Pape, C. Patrignani, A. Piepke, G. Punzi, G. Raffelt, J.G. Smith, M. Tanabashi, J. Terning, N.A. Törnqvist, T.G. Trippe, P. Vogel, T. Watari, C.G. Wohl, R.L. Workman, P.A. Zyla, B. Armstrong, G. Harper, V.S. Lugovsky, P. Schaffner, M. Artuso, K.S. Babu, H.R. Band, E. Barberio, M. Battaglia, H. Bichsel, O. Biebel, P. Bloch, E. Blucher, R.N. Cahn, D. Casper, A. Cattai, A. Ceccucci, D. Chakraborty, R.S. Chivukula, G. Cowan, T. Damour, T. DeGrand, K. Desler, M.A. Dobbs, M. Drees, A. Edwards, D.A. Edwards, V.D. Elvira, J. Erler, V.V. Ezhela, W. Fetscher, B.D. Fields, B. Foster, D. Froidevaux, T.K. Gaisser, L. Garren, H.-J. Gerber, G. Gerbier, L. Gibbons, F.J. Gilman, G.F. Giudice, A.V. Gritsan, M. Grünewald, H.E. Haber, C. Hagmann, I. Hinchliffe, A. Höcker, P. Igo-Kemenes, J.D. Jackson, K.F. Johnson, D. Karlen, B. Kayser, D. Kirkby, S.R. Klein, K. Kleinknecht, I.G. Knowles, R.V. Kowalewski, P. Kreitz, B. Krusche, Yu.V. Kuyanov, O. Lahav, P. Langacker, A. Liddle, Z. Ligeti, T.M. Liss, L. Littenberg, L. Liu, K.S. Lugovsky, S.B. Lugovsky, T. Mannel, D.M. Manley, W.J. Marciano, A.D. Martin, D. Milstead, M. Narain, P. Nason, Y. Nir, J.A. Peacock, S.A. Prell, A. Quadt, S. Raby, B.N. Ratcliff, E.A. Razuvaev, B. Renk, P. Richardson, S. Roesler, G. Rolandi, M.T. Ronan, L.J. Rosenberg, C.T. Sachrajda, S. Sarkar, M. Schmitt, O. Schneider, D. Scott, T. Sjöstrand, G.F. Smoot, P. Sokolsky, S. Spanier, H. Spieler, A. Stahl, T. Stanev, R.E. Streitmatter, T. Sumiyoshi, N.P. Tkachenko, G.H. Trilling, G. Valencia, K. van Bibber, M.G. Vincter, D.R. Ward, B.R. Webber, J.D. Wells, M. Whalley, L. Wolfenstein, J. Womersley, C.L. Woody, A. Yamamoto, O.V. Zenin, J. Zhang, and R.-Y. Zhu. Review of Particle Physics. *Journal of Physics G*, 33:1+, 2006.

[18] P. Lacock and K. Schilling. Hybrid and orbitally excited mesons in full QCD. *Nucl. Phys. Proc. Suppl.*, 73:261–263, 1999.

[19] Zhong-Hao Mei and Xiang-Qian Luo. Exotic mesons from quantum chromodynamics with improved gluon and quark actions on the anisotropic lattice. *Int. J. Mod. Phys.*, A18:5713, 2003.

[20] J. N. Hedditch et al. 1^{-+} exotic meson at light quark masses. *Phys. Rev.*, D72:114507, 2005.

[21] C. Bernard et al. Lattice calculation of 1-+ hybrid mesons with improved Kogut-Susskind fermions. *Phys. Rev.*, D68:074505, 2003.

[22] C. McNeile and Christopher Michael. Decay width of light quark hybrid meson from the lattice. *Phys. Rev.*, D73:074506, 2006.

[23] Jozef J. Dudek, Robert G. Edwards, Michael J. Peardon, David G. Richards, and Christopher E. Thomas. Toward the excited meson spectrum of dynamical QCD. *Phys. Rev.*, D82:034508, 2010.

[24] C. A. Meyer and Y. Van Haarlem. The Status of Exotic-quantum-number Mesons. *Phys. Rev.*, C82:025208, 2010.

[25] A. Chodos, R. L. Jaffe, K. Johnson, Charles B. Thorn, and V. F. Weisskopf. A New Extended Model of Hadrons. *Phys. Rev.*, D9:3471–3495, 1974.

[26] Thomas A. DeGrand, R. L. Jaffe, K. Johnson, and J. E. Kiskis. Masses and Other Parameters of the Light Hadrons. *Phys. Rev.*, D12:2060, 1975.

[27] R. L. Jaffe and K. Johnson. Unconventional States of Confined Quarks and Gluons. *Phys. Lett.*, B60:201, 1976.

[28] Ted Barnes, F. E. Close, F. de Viron, and J. Weyers. Q anti-Q G Hermaphrodite Mesons in the MIT Bag Model. *Nucl. Phys.*, B224:241, 1983.

[29] Michael S. Chanowitz and Stephen R. Sharpe. Hybrids: Mixed States of Quarks and Gluons. *Nucl. Phys.*, B222:211, 1983. [ERRATUM-ibid.B228:588,1983].

[30] Nathan Isgur and Jack E. Paton. A Flux Tube Model for Hadrons in QCD. *Phys. Rev.*, D31:2910, 1985.

[31] D. Alde et al. Evidence for a 1-+ Exotic Meson. *Phys.Lett.*, B205:397, 1988.

[32] Yu. D. Prokoshkin and S. A. Sadovsky. Analysis of D wave in pi- p $\to$ a2(0) (1320) n reaction. *Phys. Atom. Nucl.*, 58:606–612, 1995. [Yad.Fiz.58N4:662-668,1995].

[33] G. M. Beladidze et al. Study of pi- N $\to$ eta pi- N and pi- N $\to$ eta-prime pi- N reactions at 37-GeV/c. *Phys. Lett.*, B313:276–282, 1993.

[34] H. Aoyagi et al. Study of the eta pi- system in the pi- p reaction at 6.3- GeV/c. *Phys. Lett.*, B314:246–254, 1993.

[35] D. R. Thompson et al. Evidence for exotic meson production in the reaction pi- p $\to$ eta pi- p at 18-GeV/c. *Phys. Rev. Lett.*, 79:1630–1633, 1997.

[36] A. Abele et al. Exotic eta pi state in anti-p d annihilation at rest into pi- pi0 eta p(spectator). *Phys. Lett.*, B423:175–184, 1998.

[37] Ted Barnes, F. E. Close, and E. S. Swanson. Hybrid and conventional mesons in the flux tube model: Numerical studies and their phenomenological implications. *Phys. Rev.*, D52:5242–5256, 1995.

[38] Adam P. Szczepaniak, Maciej Swat, Alex R. Dzierba, and Scott Teige. Study of the $\eta\pi$ and $\eta'\pi$ spectra and interpetation of possible exotic $J^{PC} = 1^{-+}$ mesons. *Phys. Rev. Lett.*, 91:092002, 2003.

[39] Robert T. Deck. Kinematical interpretation of the first pi - rho resonance. *Phys. Rev. Lett.*, 13:169–173, 1964.

[40] S. U. Chung et al. Exotic and qq resonances in the pi + pi - pi - system produced in pi -p collisions at 18 GeV/c. *Phys. Rev.*, D65:072001, 2002.

[41] A. R. Dzierba et al. A partial wave analysis of the $\pi^-\pi^-\pi^+$ and $\pi^-\pi 0\pi 0$ systems and the search for a $J^{PC} = 1^{-+}$ meson. *Phys. Rev.*, D73:072001, 2006.

[42] M. Alekseev et al. Observation of a JPC = 1-+ exotic resonance in diffractive dissociation of 190 GeV/c pi- into pi- pi- pi+. *Phys. Rev. Lett.*, 104:241803, 2010.

[43] E. I. Ivanov et al. Observation of exotic meson production in the reaction pi- p $\rightarrow$ eta' pi- p at 18-GeV/c. *Phys. Rev. Lett.*, 86:3977–3980, 2001.

[44] Joachim Kuhn et al. Exotic meson production in the f1(1285) pi- system observed in the reaction pi- p $\rightarrow$ eta pi+ pi- pi- p at 18-GeV/c. *Phys. Lett.*, B595:109–117, 2004.

[45] M. Lu et al. Exotic meson decay to omega pi0 pi-. *Phys. Rev. Lett.*, 94:032002, 2005.

[46] Frank E. Close and Philip R. Page. The Production and Decay of Hybrid Mesons by Flux-Tube Breaking. *Nucl. Phys.*, B443:233–254, 1995.

[47] Frank E. Close and Philip R. Page. The Photoproduction of hybrid mesons from CEBAF to HERA. *Phys. Rev.*, D52:1706–1709, 1995.

[48] F. E. Close and J. J. Dudek. The 'forbidden' decays of hybrid mesons to $\pi\rho$ can be large. *Phys. Rev.*, D70:094015, 2004.

[49] Murray Gell-Mann, D. Sharp, and W. G. Wagner. Decay rates of neutral mesons. *Phys. Rev. Lett.*, 8:261, 1962.

[50] Jozef J. Dudek, Robert Edwards, and Christopher E. Thomas. Exotic and excited-state radiative transitions in charmonium from lattice QCD. *Phys. Rev.*, D79:094504, 2009.

[51] M. Nozar et al. Search for the photo-excitation of exotic mesons in the pi+pi+pi- system. *Phys. Rev. Lett.*, 102:102002, 2009.

[52] F. E. Close and J. J. Dudek. Electroweak production of hybrid mesons in a flux-tube simulation of lattice QCD. *Phys. Rev. Lett.*, 91:142001, 2003.

[53] Adam P. Szczepaniak and Maciej Swat. Role of photoproduction in exotic meson searches. *Phys. Lett.*, B516:72–76, 2001.

[54] C. W. Leemann, D. R. Douglas, and G. A. Krafft. The Continuous Electron Beam Accelerator Facility: CEBAF at the Jefferson Laboratory. *Ann. Rev. Nucl. Part. Sci.*, 51:413–450, 2001.

[55] D. I. Sober et al. The bremsstrahlung tagged photon beam in Hall B at JLab. *Nucl. Instrum. Meth.*, A440:263–284, 2000.

[56] Y. G. Sharabian et al. A new highly segmented start counter for the CLAS detector. *Nucl. Instrum. Meth.*, A556:246–258, 2006.

[57] M. D. Mestayer et al. The CLAS drift chamber system. *Nucl. Instrum. Meth.*, A449:81–111, 2000.

[58] D. S. Carman et al. The region one drift chamber for the CLAS spectrometer. *Nucl. Instrum. Meth.*, A419:315–319, 1998.

[59] E. S. Smith et al. The time-of-flight system for CLAS. *Nucl. Instrum. Meth.*, A432:265–298, 1999.

[60] G. Adams et al. The CLAS Cherenkov detector. *Nucl. Instrum. Meth.*, A465:414–427, 2001.

[61] M. Amarian et al. The CLAS forward electromagnetic calorimeter. *Nucl. Instrum. Meth.*, A460:239–265, 2001.

[62] J. T. Goetz. Ξ *Hyperon Photoproduction from Threshold to 5.4 GeV with the* `CEBAF` *Large Acceptance Spectrometer*. PhD thesis, University of California Los Angeles, 2010.

[63] M. Williams, D. Applegate, and C. Meyer. Determining momentum and energy corrections for g1c using kinematic fitting. *CLAS NOTE*, 2004-017, 2004.

[64] M. Dugger and C. Hanretty. Corrections to the incident photon energy for g8b data. *CLAS NOTE*, 2009-030, 2009.

[65] R. Brun, F. Bruyant, M. Maire, M.C. McPherson, and P. Zanarini. *Geant3*. CERN.

[66] D. Herndon, P. Soding, and R. J. Cashmore. A GENERALIZED ISOBAR MODEL FORMALISM. *Phys. Rev.*, D11:3165, 1975.

[67] S. U. Chung. Formulas for Partial-Wave Analysis, Version II. Unpublished BNL preprint BNL-QGS-93-05, September 1999.

[68] Frank von Hippel and C. Quigg. Centrifugal-barrier effects in resonance partial decay widths, shapes, and production amplitudes. *Phys. Rev. D*, 5:624–638, Feb 1972.

[69] S. U. Chung and T. L. Trueman. Positivity Conditions on the Spin Density Matrix: A Simple Parametrization. *Phys. Rev.*, D11:633, 1975.

[70] John P. Cummings and Dennis P. Weygand. An object-oriented approach to partial wave analysis. eprint only, 2003.

[71] F. James and M. Roos. Minuit: A System for Function Minimization and Analysis of the Parameter Errors and Correlations. *Comput. Phys. Commun.*, 10:343–367, 1975.

[72] M. Williams, M. Bellis, and Meyer. ruby-pwa homepage.

[73] G. T. Condo et al. Further results from charge exchange photoproduction. *Phys. Rev.*, D48:3045–3047, 1993.

[74] A. Donnachie and P. V. Landshoff. Elastic Scattering and Diffraction Dissociation. *Nucl. Phys.*, B244:322, 1984.

[75] A. Donnachie and P. V. Landshoff. Dynamics of Elastic Scattering. *Nucl. Phys.*, B267:690, 1986.

[76] A. Donnachie and P. V. Landshoff. Total cross-sections. *Phys. Lett.*, B296:227–232, 1992.